# Performance Analysis of Reconfigurable Intelligent Surface Assisted Wireless Communications




Tianxiong Wang

Somerville College

Department of Engineering Science, University of Oxford

Supervised by Professor Justin P. Coon

*A thesis submitted to the University of Oxford for the degree of Doctor of Philosophy in Engineering Science*

Trinity 2023

# Abstract

**Thesis Title:** Performance Analysis of Reconfigurable Intelligent Surface Assisted Wireless Communications
**Name:** Tianxiong Wang
**College:** Somerville College
**Degree:** Doctor of Philosophy
**Term and Year of Submission:** Trinity 2023

The advent of the smart radio environment has challenged traditional wireless communication systems, and reconfigurable intelligent surfaces (RIS) have emerged as a promising solution to enhance the performance limits of wireless communications. This thesis aims to study RIS technology in future networks by examining the performance of four typical RIS-assisted communication systems, each featuring unique models and practical RIS characteristics. The research begins with the performance analysis of RIS-assisted wireless communication systems with phase errors in both line-of-sight (LoS) and Rayleigh fading scenarios. It investigates the impact of different types of phase errors and other system parameters on system performance. Next, the impact of channel correlations on RIS-assisted communication systems is examined by deriving closed-form expressions of outage probability and average achievable rates for both correlated Rayleigh fading and correlated Nakagami-$m$ fading models. The relationship between RIS size and performance degradation caused by channel correlations is explored. The study further investigates the application of RIS technology in more intricate wireless communication systems, specifically focusing on two spectrum efficiency techniques: non-orthogonal multiple access (NOMA) and full-duplex (FD) communications. For RIS-assisted NOMA, the research derives closed-form expressions for the outage probability of users with strong and weak channel conditions, while for RIS-assisted FD systems, the research proposes a setup where an FD transceiver serves uplink and downlink users simultaneously with two dedicated RISs and examines the impact of residual self-interference (SI). Finally, the performance of a RIS-assisted large-scale network is examined through stochastic geometry, assessing coverage probability and average achievable rate. The research discusses two association strategies: nearest and fixed association, and investigates the effects of increasing transmitter (TX) density and RIS association probability on system performance. This thesis provides valuable analytical resources on RIS-assisted wireless communications performance, laying a foundation for future research and application of RIS technology.

# Acknowledgements

First and foremost, I would like to express my profound gratitude to my supervisor, Prof. Justin Coon, for his invaluable guidance, support, and mentorship throughout my research journey. His expertise, patience, and encouragement have significantly contributed to my academic and personal growth.

I would also like to extend my sincere appreciation to Dr. Gaojie Chen from the University of Surrey and Dr. Mihai-Alin Badiu for their collaboration and insights on numerous projects. Their knowledge and experience have been instrumental in shaping my understanding of the research field.

My heartfelt thanks go to my colleagues Zijing Wang, Dr. Ferhat Yarkin, Dr. Sunghwan Cho, Tanmayee Deshprabhu, Martin Wafula, Amirmohammad Farzaneh, and Bradley Mee for creating a supportive and stimulating work environment. I also wish to acknowledge Nigel Tolson, a visiting scholar, for his unique insights during his time with us. The camaraderie, assistance, and friendships I have formed with all my colleagues have made my research journey a truly rewarding experience.

I would like to express my sincere gratitude to Prof. Dominic O'Brien and Prof. Tony Wilson. Their constructive comments and feedback during my transfer and confirmation interviews were instrumental in shaping the direction of my research and improving the quality of my thesis.

Lastly, I would like to express my deepest appreciation to my family, especially my father, mother, grandfather, and grandmother, for their unwavering love, support, and understanding throughout my academic pursuits. Their faith in my abilities and the sacrifices they have made for my education have been my source of strength and inspiration.

In conclusion, I am truly grateful for the opportunity to work with such an exceptional group of individuals and for the contributions each has made to my research and personal development.

# List of Publications

### Journal Papers

- **T. Wang**, G. Chen, M. -A. Badiu, and J. P, Coon, "Performance Analysis of RIS-Assisted Full-Duplex Communication over Correlated Nakagami-$m$ Fading Channel," in ***IEEE Transactions on Vehicular Technology*** (under review).
- **T. Wang**, G. Chen, M. -A. Badiu, and J. P, Coon, "Performance Analysis of RIS-Assisted Large-Scale Wireless Networks Using Stochastic Geometry," in ***IEEE Transactions on Wireless Communications***.
- **T. Wang**, M. -A. Badiu, G. Chen and J. P. Coon, "Performance Analysis of IOS-Assisted NOMA System With Channel Correlation and Phase Errors," in ***IEEE Transactions on Vehicular Technology***, vol. 71, no. 11, pp. 11861-11875, Nov. 2022.
- **T. Wang**, M. -A. Badiu, G. Chen and J. P. Coon, "Outage Probability Analysis of STAR-RIS Assisted NOMA Network With Correlated Channels," in ***IEEE Communications Letters***, vol. 26, no. 8, pp. 1774-1778, Aug. 2022.
- **T. Wang**, M. -A. Badiu, G. Chen and J. P. Coon, "Outage Probability Analysis of RIS-Assisted Wireless Networks With Von Mises Phase Errors," in ***IEEE Wireless Communications Letters***, vol. 10, no. 12, pp. 2737-2741, Dec. 2021.

### Conference Papers

- **T. Wang**, G. Chen, M. -A. Badiu and J. P. Coon, "Stochastic Geometry Analysis for RIS-Assisted Large-Scale Cellular Networks," ***2022 IEEE 96th Vehicular Technology Conference (VTC2022-Fall)***, London, United Kingdom, 2022, pp. 1-6.

- **T. Wang**, G. Chen, J. P. Coon and M. -A. Badiu, "Chernoff Bound and Saddlepoint Approximation for Outage Probability in IRS-Assisted Wireless Systems," ***2021 IEEE Globecom Workshops (GC Wkshps)***, Madrid, Spain, 2021, pp. 1-5.
- **T. Wang**, G. Chen, J. P. Coon and M. -A. Badiu, "Study of Intelligent Reflective Surface Assisted Communications with One-bit Phase Adjustments," ***2020 IEEE Global Communications Conference (GLOBECOM)***, Taipei, China, 2020, pp. 1-6.

# Acronyms

| | |
|---|---|
| **AP** | Access point |
| **AWGN** | Additive white Gaussian noise |
| **BPP** | Binomial Poisson process |
| **CDMA** | Code division multiple access |
| **CDF** | Cumulative distribution function |
| **CSCG** | Circularly symmetric complex Gaussian |
| **CSI** | Channel state information |
| **DC** | Direct current |
| **DL** | Downlink |
| **EM** | Electromagnetic |
| **FD** | Full-duplex |
| **FDMA** | Frequency-division multiple access |
| **FPGA** | Field-programmable gate arrays |
| **GCQ** | Gaussian Chebyshev quadrature |
| **GPP** | Gauss-Poisson process |
| **GPS** | Global positioning system |
| **HD** | Half-duplex |
| **HPPP** | Homogeneous Poisson point process |
| **IP** | Internet protocol |
| **IoT** | Internet of things |
| **ISAC** | Integrated sensing and communication |
| **ISI** | Inter-symbol interference |
| **i.i.d.** | Independent and identically distributed |

| | |
|---|---|
| **LEO** | Low earth orbit |
| **LoS** | Line-of-sight |
| **MIMO** | Multiple-input multiple-output |
| **mmWave** | Millimeter-wave |
| **MC** | Monte Carlo |
| $n$**G** | $n$th generation (network) |
| **NOMA** | Non-orthogonal multiple access |
| **OFDM** | Orthogonal frequency-division multiplexing |
| **OMA** | Orthogonal multiple access |
| **PCP** | Poisson cluster process |
| **PDF** | Probability density function |
| **PGFL** | Probability generating functional lemma |
| **PLS** | Physical layer security |
| **PPP** | Poisson point process |
| **PWM** | Pulse-width modulation |
| **RA** | Receive antenna |
| **RF** | Radio frequency |
| **RIS** | Reconfigurable intelligent surface |
| **RX** | Receiver |
| **SI** | Self-interference |
| **SIC** | Successive interference cancellation |
| **SINR** | Signal-to-interference-plus-noise ratio |
| **SNR** | Signal-to-noise ratio |
| **STAR-RIS** | Simultaneously transmitting and reflecting reconfigurable intelligent surface |
| **SWIPT** | Simultaneous wireless information and power transfer |
| **TA** | Transmit antenna |
| **TDMA** | Time-division multiple access |
| **TX** | Transmitter |

| | |
|---|---|
| **UAV** | Unmanned aerial vehicle |
| **UL** | Uplink |
| **UE** | User equipment |
| **VLC** | Visible light communications |
| **VR/AR** | Virtual/augmented reality |
| **WCDMA** | Wideband code division multiple access |
| **WSN** | Wireless sensor networks |

# Mathematical Notation

| | |
|---|---|
| $\mathbb{P}(\cdot)$ | Probability operator |
| $f_X(x)$ | Probability density function of a random variable $X$ |
| $F_X(x)$ | Cumulative distribution function of a random variable $X$ |
| $\bar{F}_X(x)$ | Complementary cumulative distribution function of a random variable $X$ |
| $D(\cdot\|\|\cdot)$ | Relative entropy function |
| $I(\cdot;\cdot)$ | Mutual information function |
| $\mathrm{Cov}\{X, Y\}$ | Covariance of random variables $X$ and $Y$ |
| $\Gamma(\cdot)$ | Gamma function |
| $\Gamma(\cdot,\cdot)$ | Upper incomplete gamma function |
| $\gamma(\cdot,\cdot)$ | Lower incomplete gamma function |
| $K_n(\cdot)$ | Modified Bessel function of the second kind with order $n$ |
| $\mathbb{E}[X]$ | Expectation of a random variable $X$ |
| $\mathrm{Var}[X]$ | Variance of a random variable $X$ |
| $\mathrm{mod}(a, b)$ | The remainder of division $a$ by $b$ |
| $\lfloor a \rfloor$ | Integer closet to $a$ that is less than or equal to $a$ |
| $\lfloor a \rceil$ | Integer closest to $a$ |
| $\mathbb{C}^{m\times n}$ | $m \times n$ complex space |
| $\mathbb{R}^{m\times n}$ | $m \times n$ real space |
| $(\cdot)^T$ | Transpose operator |
| $(\cdot)^H$ | Hermitian transpose operator |
| $(\cdot)^*$ | Conjugate operator |

| | |
|---|---|
| $\mathrm{diag}(\mathbf{a})$ | A diagonal matrix with the elements of $\mathbf{a}$ on its main diagonal |
| $\mathcal{CN}(\mu, \sigma^2)$ | Circularly symmetric complex Gaussian distribution with mean $\mu$ and variance $\sigma^2$ |
| $\mathcal{R}(\sigma)$ | Rayleigh distribution with the scale parameter $\sigma$ |
| $\mathrm{Nakagami}(m, \Omega)$ | Nakagami-$m$ distribution of shape parameter $m$ and scale parameter $\Omega$ |
| $\rightarrow$ | Approaching to a particular value |
| $\xrightarrow{P}$ | Convergence in probability |
| $\triangleq$ | Definition |
| $\sim$ | Asymptotic equivalence notation |
| $\|\cdot\|$ | Euclidean norm |
| $[\mathbf{A}]_{i,j}$ | $(i, j)$ entry of matrix $\mathbf{A}$ |
| ${}_2F_1(\cdot, \cdot; \cdot; \cdot)$ | Hypergeometric function |
| $\mathrm{erfc}(\cdot)$ | Complementary error function |
| $\mathrm{Ci}(\cdot)$ | Cosine integral function |
| $\mathrm{Si}(\cdot)$ | Sine integral function |

# Contents


**1 Introduction** **1**

1.1 Development of Wireless Communications . . . . . 1

1.2 Motivation for Using Reconfigurable Intelligent Surfaces . . . . . 3

1.3 Thesis Outline and Contributions . . . . . 6

**2 Research Background** **10**

2.1 Smart Radio Environment . . . . . 10

2.2 Basic Principles of RIS . . . . . 14

2.2.1 Hardware Structure . . . . . 14

2.2.2 Equivalent Circuit Model . . . . . 16

2.2.3 Geometric Interpretation of RIS . . . . . 19

2.2.4 CSI Acquisition of RIS-Assisted Communications . . . . . 21

2.2.4.1 Binary Reflection Enabled Channel Estimation . . . 22

2.2.4.2 Full Reflection Enabled Channel Estimation . . . . . 23

2.3 Stochastic Geometry for Large-Scale Network Modeling . . . . . 23

2.3.1 BPP . . . . . 25

2.3.1.1 Applications and Limitations of BPP . . . . . 26

2.3.2 HPPP . . . . . 27

2.3.2.1 Important Theorems about HPPP . . . . . 28

2.3.2.2 Applications and Limitations of HPPP . . . . . 29

2.3.3 PCP . . . . . 29

2.3.3.1 A Special Case of PCP: GPP . . . . . 30

2.4 Summary . . . . . 31

**3 RIS-Assisted Communications with Phase Errors** **33**

3.1 System Framework and Performance Metrics . . . . . 35

3.1.1 Channel and Signal Models . . . . . 35

3.1.1.1 LoS Scenario . . . . . 36

3.1.1.2 Fading Scenario . . . 37
3.1.2 Performance Metrics . . . 39
3.2 Analysis of LoS Scenario . . . 40
3.2.1 Path Loss Analysis . . . 40
3.2.2 Outage Probability Analysis with Phase Errors . . . 42
3.2.2.1 Distribution of the Composite Channel Gain . . . 43
3.2.2.2 Lower Tail Distribution Analysis . . . 46
3.2.2.3 Approximation Error Analysis . . . 48
3.2.2.4 Outage Probability and Diversity Order . . . 51
3.3 Analysis of Fading Scenario . . . 52
3.3.1 Perfect Phase Alignment . . . 52
3.3.1.1 Outage Probability Analysis . . . 52
3.3.1.2 Error Analysis . . . 54
3.3.1.3 Diversity Order . . . 54
3.3.2 One-bit Phase Adjustment . . . 56
3.3.2.1 Outage Probability Analysis . . . 56
3.3.2.2 Error Analysis . . . 58
3.3.2.3 Diversity Order . . . 59
3.4 Numerical Results . . . 60
3.4.1 Analysis of LoS Scenario . . . 60
3.4.2 Analysis of Fading Scenario . . . 63
3.4.2.1 Perfect Phase Alignment . . . 63
3.4.2.2 One-bit Phase Adjustment . . . 64
3.5 Summary . . . 65
3.6 Appendices . . . 66
3.6.1 Proof of the Lemma 2 . . . 66

**4 RIS-Assisted Communications over Correlated Channels 67**
4.1 System Framework and Performance Metrics . . . 69
4.1.1 RIS Implementations . . . 70
4.1.2 Channel and Signal Models . . . 70
4.1.2.1 Correlated Rayleigh Fading Channel Model . . . 71
4.1.2.2 Correlated Nakagami-$m$ Fading Channel Model . . . 73
4.1.3 Performance Metrics . . . 74
4.2 Outage Probability Analysis . . . 75
4.2.1 Analysis of Correlated Rayleigh Fading Channel . . . 75

4.2.2 Analysis of Correlated Nakagami-$m$ Fading Channel . . . . . 81
4.3 Average Achievable Rate Analysis . . . . . 86
4.3.1 Upper Bound Analysis . . . . . 86
4.3.2 Large Array Analysis . . . . . 87
4.3.3 Asymptotic Analysis . . . . . 88
4.4 Numerical Results . . . . . 91
4.4.1 Outage Probability Analysis . . . . . 92
4.4.2 Average Achievable Rate Analysis . . . . . 94
4.5 Summary . . . . . 96
4.6 Appendices . . . . . 98
4.6.1 Proof of the Proposition 3 . . . . . 98

**5 RIS-Assisted Spectral Efficiency Techniques 101**
5.1 System Framework . . . . . 104
5.1.1 RIS-Assisted NOMA Communication . . . . . 104
5.1.2 RIS-Assisted FD Communication . . . . . 108
5.2 Analysis of RIS-Assisted NOMA . . . . . 113
5.2.1 Outage Probability Analysis . . . . . 114
5.2.1.1 Channel Distribution Analysis . . . . . 114
5.2.1.2 Outage Probability of $U_t$ . . . . . 116
5.2.1.3 Outage Probability of $U_r$ . . . . . 117
5.2.2 NOMA and OMA Comparison . . . . . 117
5.2.2.1 Average Achievable Rates of NOMA . . . . . 118
5.2.2.2 Average Achievable Rates of OMA . . . . . 119
5.2.2.3 Sum Rate Comparison . . . . . 120
5.3 Analysis of RIS-Assisted FD . . . . . 121
5.3.1 Channel Distribution Analysis . . . . . 121
5.3.2 Outage Probability of UL and DL Users . . . . . 122
5.3.2.1 Outage Probability of $U_A$ . . . . . 122
5.3.2.2 Outage Probability of $U_B$ . . . . . 123
5.3.3 Discussion of HD Communication . . . . . 126
5.4 Numerical Results . . . . . 128
5.4.1 RIS-Assisted NOMA . . . . . 129
5.4.2 RIS-Assisted FD . . . . . 131
5.5 Summary . . . . . 135

**6 RIS-Assisted Large-Scale Networks** **137**
6.1 System Framework . . . 140
6.1.1 Channel Model . . . 141
6.1.2 Signal Model . . . 143
6.1.3 Performance Metrics . . . 145
6.1.3.1 Coverage Probability . . . 145
6.1.3.2 Average Achievable Rate . . . 146
6.2 Signal Power Analysis . . . 146
6.2.1 Distribution with RIS-Assisted Transmission . . . 146
6.2.2 Distribution without RIS Beamforming . . . 148
6.3 Interference Power Analysis . . . 149
6.3.1 Interference Power Distribution Analysis . . . 149
6.3.1.1 Interference from TX with Assisting RIS . . . 149
6.3.1.2 Interference from TX without Assisting RIS . . . 150
6.3.2 Laplace Transform of the Interference Power . . . 150
6.3.2.1 Fixed Association Strategy . . . 151
6.3.2.2 Nearest Association Strategy . . . 151
6.4 Performance Analysis . . . 152
6.4.1 Coverage Probability Analysis . . . 152
6.4.1.1 Fixed Association with Assisting RIS . . . 152
6.4.1.2 Fixed Association without Assisting RIS . . . 153
6.4.1.3 Nearest Association Strategy . . . 154
6.4.2 Average Achievable Rate Analysis . . . 157
6.5 Numerical Results . . . 159
6.5.1 Fixed Association Strategy Analysis . . . 160
6.5.2 Nearest Association Strategy Analysis . . . 163
6.6 Summary . . . 164
6.7 Appendices . . . 166
6.7.1 Proof of the Proposition 8 . . . 166
6.7.2 Proof of the Proposition 10 . . . 167
6.7.3 Proof of the Proposition 12 . . . 169

**7 Conclusions and Future Work** **170**
7.1 Thesis Summary . . . 170
7.2 Future Directions . . . 173
7.2.1 Analysis of RIS-Assisted MIMO Systems . . . 173

7.2.2 New Designs of RIS to Achieve Full Coverage . . . . . 174
7.2.3 Analysis of RIS-Assisted OFDM . . . . . 175
7.2.4 Standardization and Regulation . . . . . 175
7.3 Outlook on RIS Technology . . . . . 176

**Bibliography** **178**

# List of Figures


2.1 The concept of a smart radio environment. . . . . 11
2.2 Applications of RIS-empowered smart radio networks. . . . . 12
2.3 Typical structure of a RIS. . . . . 15
2.4 Typical structure of an element. . . . . 16
2.5 Equivalent circuit model of an element. . . . . 18
2.6 Phase shift $\arg(v)$ versus the effective capacitance $C$. . . . . 19
2.7 Composite channel gains with mirror limit $\beta$, mirror-mimicking phases $\beta_1$, and optimal phases $\beta_2$. . . . . 21

3.1 System model. . . . . 36
3.2 Relative entropy $D(f_{W_n}||f_{\text{app}})$. The "ref" curves corresponds to the relative entropy of Student's $t$-distribution with $N$ degrees of freedom and its normal approximation. . . . . 55
3.3 Outage probability versus transmit SNR $\gamma_t$ for different $\kappa$ in LoS scenario. 61
3.4 Outage probability versus transmit SNR $\gamma_t$ for different SNR threshold $\bar{\gamma}$ in LoS scenario. . . . . 62
3.5 Outage probability versus transmit SNR $\gamma_t$ for different $N$ in LoS scenario. . . . . 62
3.6 Outage probability versus transmit SNR $\gamma_t$ for different $N$ without phase errors in Rayleigh fading scenario. . . . . 63
3.7 Outage probability versus transmit SNR $\gamma_t$ for different $N$ with one-bit phase adjustment in Rayleigh fading scenario. . . . . 64
3.8 Outage probability versus transmit SNR $\gamma_t$ for different bits of phase adjustment in Rayleigh fading scenario. . . . . 65

4.1 System model. . . . . 69
4.2 RIS structure. . . . . 69
4.3 Outage probability versus transmit power $P$ for different $N$ over correlated Rayleigh fading channels. . . . . 93

4.4 Outage probability versus transmit power $P$ for different $N$ over correlated Nakagami-$m$ fading channels. . . . . 94
4.5 Average achievable rates versus transmit power $P$ for different $N$ over correlated Rayleigh fading channels. . . . . 95
4.6 Average achievable rates versus transmit power $P$ for different shape parameters over correlated Nakagami-$m$ fading channels. . . . . 96
4.7 Average achievable rates versus the number of RIS elements $N$ over correlated and uncorrelated Rayleigh fading channels. . . . . 97
4.8 Average achievable rates versus the number of RIS elements $N$ over correlated and uncorrelated Nakagami-$m$ fading channels. . . . . 97

5.1 System model of RIS-assisted NOMA communication system. . . . . 105
5.2 System model of RIS-assisted FD communication system. . . . . 109
5.3 Outage probability of $U_t$ versus the transmit power $P$ for different Nakagami-$m$ shape parameters and number of RIS elements $N$. . . . 130
5.4 Outage probability of $U_r$ versus the transmit power $P$ for different number of RIS elements $N$. . . . . 130
5.5 Average achievable rate of $U_t$ versus the transmit power $P$ for different number of RIS elements $N$. . . . . 131
5.6 Average achievable rate of $U_r$ versus the transmit power $P$. . . . . 132
5.7 Sum rate versus the transmit power $P$ for NOMA and OMA. . . . . 132
5.8 Outage probability of $U_A$ versus the transmit power $P_A$ with different $\epsilon$. 133
5.9 Outage probability of $U_B$ versus the transmit power $P_T$ with different number of elements. . . . . 134
5.10 Relative error of the GCQ based approximation. . . . . 135
5.11 FD and HD Communications Comparison. Average achievable rate of $U_A$ with FD and HD schemes. . . . . 136

6.1 System model of RIS assisted large-scale network. . . . . 141
6.2 Coverage probability versus transmit power with different densities of TXs. Fixed association strategy with assisting RIS. . . . . 161
6.3 Coverage probability versus transmit power with different densities of TXs. Fixed association strategy without assisting RIS. . . . . 162
6.4 Coverage probability versus transmit power with different RIS association probabilities. Fixed association strategy with assisting RIS. . . 162
6.5 Average achievable versus transmit power with different densities of TXs. Fixed association strategy. . . . . 163

6.6 Coverage probability versus transmit power with different densities of TXs. Nearest association strategy. . . . . 164
6.7 Average achievable rate and coverage probability versus RIS association probability. Nearest association strategy. . . . . 165

# Chapter 1

# Introduction

## 1.1 Development of Wireless Communications

The development of wireless communications has been regarded as a significant achievement in the history of technology, changing the way that people connect with each other over long distances. The concept of wireless communications refers to data transmission without the use of any cables or wires. The development of wireless communications can be dated back to the invention of radiotelegraphy in the late 19th century by Guglielmo Marconi [1]. And, the first important breakthrough took place when Guglielmo Marconi transmitted a signal across the Atlantic Ocean in the early 20th century, demonstrating the feasibility of wireless signal transmission over long distances [2]. The beginning of the theoretical analysis of wireless communications was marked by the information theory developed by Claude E. Shannon in 1948. Prior to Shannon's work, design and optimization of wireless communication systems were largely based on empirical results. Shannon realized the limitations of this sort of method, and focused on a rigorous mathematical framework for understanding the information transmitted through communication channels [3]. The 1948 paper titled "A Mathematical Theory of Communication", by Claude E. Shannon, is now widely

regarded as the foundation of the modern study of communication technology [4].

The commercialization and industrialization of wireless communication networks can be traced back to the deployment of the first-generation (1G) wireless communication networks. The evolution of wireless communication networks has gone through five generations up to the present, depending on not only the development of communication theories, but also the progress of the communication hardware. The 1G wireless communication networks emerged in the 1980s. This technology utilized analog signals to convey information, and allowed wireless voice calls by using frequency-division multiple access (FDMA) [5]. However, due to the limitations regarding spectrum efficiency, quality of service, and security issues, 1G was replaced by second-generation (2G) wireless networks in the 1990s. Relying on digital technology, 2G wireless networks offered improved communication quality and supported some additional data services, such as text messages [6]. In the early 2000s, due to the significant increase of mobile communication devices, third-generation (3G) wireless networks were introduced, which have been viewed as a remarkable progression over 2G. Based on packet switching, code division multiple access (CDMA), and wideband code division multiple access (WCDMA) technologies, 3G was able to provide much higher date rates and support a much more diverse range of services, such as Internet browsing, global positioning system (GPS) applications, mobile apps, etc [7]. At the same time, due to the advent of smartphones, mobile data traffic soared. With the development of orthogonal frequency-division multiplexing (OFDM), multiple-input-multiple-output (MIMO) and some other sophisticated technologies, fourth-generation (4G) wireless networks provided wireless communication services with higher data rates and lower latency, making high-quality video streaming, online gaming and real-time video conferencing possible on mobile devices [8]. Recently, fifth-generation (5G) wireless communication networks have been widely deployed in many countries in the 2020s. As the latest and most advanced wireless

technology, 5G promises to provide greater connectivity, faster data speeds and lower latency than its predecessors. With a number of key technologies including massive MIMO, millimeter-wave (mmWave) communications, network slicing, etc, 5G is able to support a range of new technologies, such as the Internet of Things (IoT), autonomous driving, virtual/augmented reality (VR/AR), etc [9].

It is understood that wireless communication networks evolve around every ten years to satisfy the growing requirements on communication services. Meanwhile, wireless connectivity and mobile data traffic will continue to grow dramatically in the future. As per predictions, global Internet protocol (IP) data traffic is expected to grow by 55% annually, reaching 5016 exabytes per year between 2020 and 2030 [10]. Furthermore, the number of connected mobile devices is projected to reach 25.9 billion by 2025 [10]. To overcome these new challenges, academia and industry have already started the early-stage investigation and research pertaining to the next-generation wireless communication network, namely, the sixth-generation (6G). A number of new potential technologies, including visible light communications (VLC) [11], integrated sensing and communications (ISAC) [12], semantic communications [13], and low earth orbit (LEO) satellite networks [14], have been extensively studied recently.

## 1.2 Motivation for Using Reconfigurable Intelligent Surfaces

Since current wireless networks are not able to satisfy the ever-growing demands on wireless communication services, a novel wireless communication network with brand new communication technologies must be developed and implemented to meet these challenging demands. Among potential physical layer technologies for next-generation wireless networks, reconfigurable intelligent surface (RIS) assisted wireless communication has gained enormous research interest and has been regarded as a

promising physical layer technology for future wireless communication networks [15].

One of the key benefits of RIS technology is the ability to improve spectrum efficiency[1], which is an essential factor in wireless communications. The wireless propagation environment is inherently random and uncontrollable, making it challenging to ensure reliable and efficient wireless communications [16]. Traditionally, researchers have designed a wide range of transmission and reception techniques to combat the negative effects brought by the randomness of wireless channels. Contrary to existing technologies, RIS can offer a potential solution to create a controllable wireless propagation environment. Specifically, a RIS is a planar array consisting of a large number of reflecting elements. With the development of metamaterials and metasurfaces, each element is controlled by the RIS controller to perform real-time independent phase shifting of the incident signals [17]. Using channel state information (CSI), a RIS is capable of reconfiguring the wireless propagation environment intelligently by adjusting the phase shifts of all the elements such that the signals can be combined constructively towards specific directions to achieve spatial signal enhancement, thus enhancing the spectrum efficiency [18].

Another attractive benefit of RIS is the passive nature of this technology. Increased power consumption is a critical issue in today's wireless networks. For example, MIMO systems usually should have complex signal processing capabilities, leading to not only complicated hardware designs, but also high energy consumption [18]. Thus, the application of MIMO can be particularly challenging for energy-constrained networks. Unlike the traditional amplifiers, a RIS is a nearly passive device, resulting in significant energy savings compared to traditional wireless communication devices [19]. As reported in [16], each RIS element only consumes 8 $\mu$W when powered. This feature makes RIS technology particularly useful in various applications. For example, in IoT networks and wireless sensor networks (WSN), enhancing energy

[1]It is a performance metric to evaluate the amount of information that can be transmitted over a unit bandwidth

efficiency can ensure longer battery life and lower operating costs [20]. Similarly, in wireless communication systems for industrial automation, enhancing energy efficiency can ensure more efficient and sustainable production processes, leading to reduced costs and environmental impacts. Moreover, it is worth noting that a RIS does not require power amplifiers, which theoretically eliminates the issue of noise enhancement at the RIS [21].

Integrating RISs into wireless communication networks also bring benefits from the perspective of low hardware costs [22]. Compared with MIMO, for which each antenna requires a costly radio frequency (RF) chain, a RIS can be manufactured by using low-cost materials. The passive nature of the RIS eliminates the need for active components such as power amplifiers and filters which are common in traditional wireless communication devices [21]. Thus, the hardware cost is significantly reduced. Additionally, the RIS technology can be easily deployed and integrated into existing wireless communication systems, saving the costs for significant hardware upgrades.

Furthermore, RIS is able to extend the service coverage of wireless communications. By adjusting the phase shifts of the RIS properly, the signals incident on the RIS can be redirected towards different directions, overcoming the obstacles and signal attenuation [23]. Considering a device located in a wireless dead zone where the direct link between the device and its serving access point (AP) is blocked, traditional wireless systems will increase the transmit power to ensure reliable communication is achieved. However, these types of methods will lead to not only high power consumption, but also significant interference. In contrast, deploying a RIS between the device and its AP can help to bypass the blocks and extend wireless coverage. The extended wireless coverage brought by RIS technology can have significant implications. For example, in rural areas, the access to reliable wireless communications is essential but often limited by geography and infrastructure. Also, mmWave communications can benefit from this feature since the channels for high-frequency signals are very

vulnerable to blockages [24].

As a brand new technology with the above attractive advantages, an essential task in academia is to analyze RIS-assisted wireless communications rigorously from the perspective of the communication theory. Physical characteristics of RIS should be properly modeled, and the performance gain that can be brought by this technology should be carefully exploited. Therefore, we choose to focus on the performance analysis of RIS-assisted wireless communication systems in this thesis.

## 1.3 Thesis Outline and Contributions

In the above sections, we have introduced the evolution of wireless communication technology and explained the motivation of carrying out performance analysis of RIS-assisted communication networks. In this thesis, we focus on four different and important RIS systems, which have different system models and practical RIS characteristics. To provide a logical roadmap for readers, the organization of the rest of the thesis and the technical contributions of each chapter are set out as follows. Note that the majority of the mathematical notations and nomenclatures used in this thesis are defined and used separately in each chapter to ensure clarity. The analytical results presented in this thesis are obtained manually or with the assistance of Mathematica, while special notes and/or references are provided in other cases. The numerical results are obtained through Monte Carlo simulations using MATLAB.

Chapter 2 establishes the foundation for the research conducted in this thesis by exploring key elements of the performance analysis of RIS-assisted communications. It starts by introducing the concept of smart radio environments and discussing the potential applications of RIS technology in fostering intelligent wireless propagation. Subsequently, it delves into the fundamental principles of RIS, providing readers with essential background knowledge and a comprehensive understanding of this technol-

ogy's basic concepts. Additionally, the chapter briefly touches upon stochastic geometry, an important and practical mathematical approach for analyzing large-scale wireless networks.

Chapter 3 is the first of four research chapters. This chapter presents a comprehensive analysis of the performance of RIS-assisted wireless communication systems with phase errors. Both the line-of-sight (LoS) and Rayleigh fading scenarios are considered. In the LoS scenario, a path loss model is introduced, and the outage probability of the system with Von Mises distributed phase errors is derived by using the theory of directional statistics and Laplace's method. The derived outage probability is proved to be asymptotically equivalent for a large number of RIS elements. In the Rayleigh fading scenario, the outage probability of perfect phase alignment and one-bit phase adjustment schemes are derived in a closed form and an integral form, respectively. Through a more accurate asymptotic analysis, the diversity orders of these two phase adjustment schemes are obtained. Impacts of different types of phase errors and other system parameters on the system performance are explored and discussed in this chapter. The research results of this chapter have been published in IEEE Wireless Communications Letters and Proc. IEEE Globecom 2020.

Chapter 4 delves into the impact of channel correlations on RIS systems. As RIS elements are sub-wavelength, channel correlation is an unavoidable issue in practical scenarios, making it critical to analyze. This chapter presents performance analysis under two channel models, correlated Rayleigh fading and correlated Nakagami-$m$ fading, with closed form expressions of outage probability and average achievable rates derived for both models. Additionally, the chapter reveals the channel hardening effect in the RIS-assisted communication system with correlated channels, which is used to derive approximate expressions of the average achievable rates. Notably, it is demonstrated that the average achievable rate with correlated channels is asymptotically equivalent to that with uncorrelated channels for a large number of RIS

elements. This important result shows that even though channel correlations degrade system performance, increasing the number of elements can offset the performance loss. The research of this chapter has been published in IEEE Transactions on Vehicular Technology, IEEE Communications Letters, and submitted for possible publication in IEEE Transactions on Vehicular Technology.

Chapter 5 studies RIS in more complex wireless communication systems, and considers two spectrum efficiency techniques, namely, non-orthogonal multiple access (NOMA) and full-duplex (FD) communications. For RIS-assisted NOMA, a priority-oriented phase shifting scheme is applied at the RIS, and closed-form expressions for the outage probability of users with strong and weak channel conditions are derived. To compare the performance of RIS-assisted NOMA and RIS-assisted TDMA, this chapter also gives upper bounds on average achievable rates for NOMA and TDMA transmission schemes, and a mathematical condition is given for when RIS-assisted NOMA has a higher sum rate. For RIS-assisted FD, a system with an FD transceiver serving uplink and downlink users simultaneously is proposed, with two RISs set up to serve the users individually. The outage probability of the uplink and downlink transmissions are obtained in closed form, and the impact of residual self-interference (SI) is explored. The residual SI threshold below which the FD communication outperforms the HD counterpart is given in closed form and verified through simulations. The research of this chapter has been published in IEEE Transactions on Vehicular Technology, IEEE Communications Letters, and submitted for possible publication in IEEE Transactions on Vehicular Technology.

In Chapter 6, we investigate the performance of a RIS-assisted large-scale network by characterizing the coverage probability and the average achievable rate using the theory of stochastic geometry. Considering the spatial correlation between transmitters (TXs) and RISs, their locations are jointly modelled by a Gauss-Poisson process (GPP). Two association strategies, i.e., nearest association and fixed association, are

both discussed. For the RIS-aided transmission, the signal power distribution is characterized, and the Laplace transform of the aggregate interference power is derived in closed form. Based on these expressions, we analyze the coverage probability, and the average achievable rate of the typical user. We derive the coverage probability expressions for the fixed association strategy and the nearest association strategy in an interference-limited scenario in closed form. Theoretical and numerical results provide practical insights, including the independence between the system performance and the density of TXs with the nearest association strategy in the interference-limited scenario. The research of this chapter has been published in IEEE Transactions on Wireless Communications.

Finally, Chapter 7 summarizes the main findings of the thesis and highlights potential avenues for future research.

# Chapter 2

# Research Background

## 2.1 Smart Radio Environment

Reconfigurable intelligent surface (RIS) is envisaged to play a pivotal role in establishing a smart radio environment in next-generation wireless communication networks [25]. The concept of a smart radio environment is an emerging trend in the field of wireless communication. A wireless environment is a collection of physical objects that can have a significant impact on the transmission of electromagnetic (EM) waves between devices. The waves are typically subject to attenuation and multi-path propagation, which can seriously affect the communication performance. Attenuation occurs due to material absorption and path loss, while multi-path propagation is caused by reflection, diffraction, and refraction in the propagation environment, leading to small-scale fading and inter-symbol interference (ISI) [26]. The wireless environment is determined by the location, materials, and geometry of physical objects, which cannot be dynamically modified or modeled to adapt to communication services. Several advanced communication techniques have been implemented on the device side to mitigate the effects of the unpredictable wireless environment. For instance, in certain scenarios, massive multiple-input multiple-output (MIMO) and

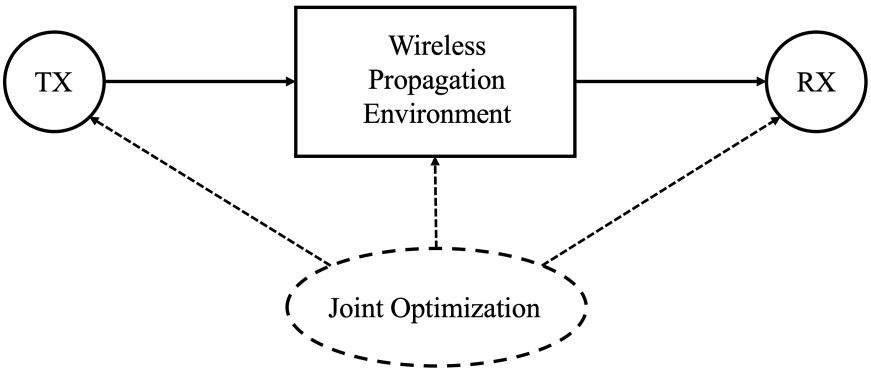



Figure 2.1: The concept of a smart radio environment.

relays have been utilized [27]. Nevertheless, these methods can lead to hardware scalability and mobility concerns [28]. Consequently, the wireless environment as a whole remains ignorant of the ongoing communications within it, and the wireless propagation environment is still far from being considered "smart" .

In contrast, upcoming sixth-generation (6G) communication networks are expected to challenge long-standing assumptions by asserting that the wireless environment can be controlled to achieve significant performance improvements [29]. Fig. 2.1 illustrates the conceptual vision of a smart radio environment, where the transmitter, receiver and wireless environment can be jointly optimized to improve the communication performance. One promising approach to develop a smart radio environment is to utilize software-controlled RISs to cover the physical objects in the environment, including walls, furniture, and other elements [30]. By doing so, these RISs can be programmed to dynamically shape the radio environment to fulfill various performance requirements.

A few applications of RIS-empowered smart radio networks are illustrated in Fig. 2.2. One potential application involves a user situated in a wireless dead zone where the direct link between the user and its associated access point (AP) is absent due to obstacles. In such a scenario, deploying a RIS that has direct links with both the user and the AP can facilitate smart signal reflection, thus establishing a virtual

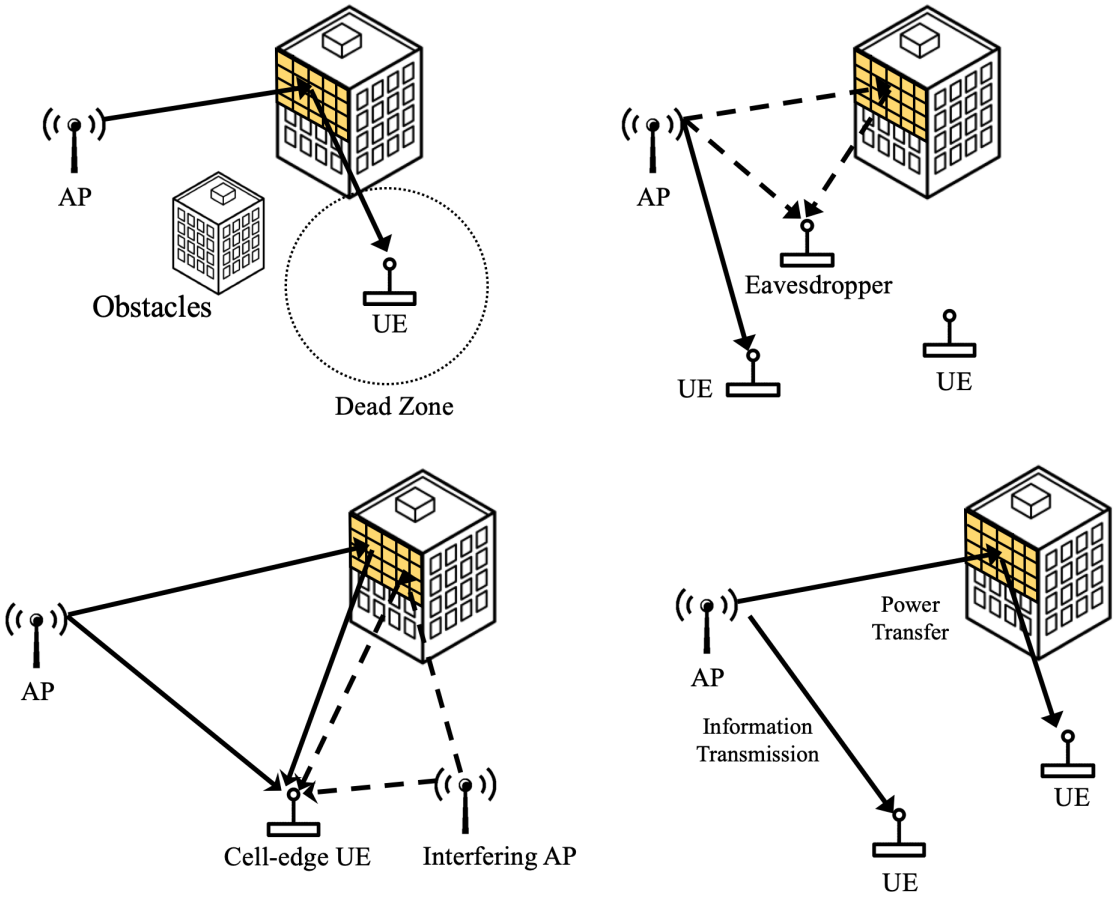



Figure 2.2: Applications of RIS-empowered smart radio networks.

line-of-sight (LoS) link between the two. This application can be especially beneficial for extending coverage of millimeter-wave (mmWave) communication networks that suffer from serious attenuation. By strategically placing RISs throughout the environment, the wireless signals can be intelligently redirected to bypass obstructions and establish a reliable connection between the user and the AP, thereby enhancing the overall communication performance.

Another potential application is for enhancing the physical layer security (PLS) of wireless communication [31]. In scenarios where an eavesdropper is located closer to the AP than the legitimate user, or when the eavesdropper is located in the same direction as the legitimate user, it is challenging to achieve high secrecy communication rates, even with the use of transmit beamforming at the AP. However, deploying an

RIS in the vicinity of the eavesdropper can enable intelligent signal reflection, whereby the signal reflected by the RIS can be adjusted to cancel out the received signal at the eavesdropper through the direct link. As a result, the information leakage can be significantly reduced. Such applications have the potential to revolutionize the way we think about wireless communication, offering new avenues for enhancing both the reliability and security of wireless networks.

The third application of RIS in smart radio networks is for improving the communication performance of a cell-edge user that experiences both serious signal attenuation due to long propagation distance and severe inter-cell interference from a neighboring AP. In this case, a RIS can be set up at the cell edge to boost the desired signal power and mitigate the interference by strategically designing the phase shifting scheme. With the help of the RIS, the cell-edge user can achieve a higher signal-to-interference-plus-noise ratio (SINR), leading to enhanced communication performance. This application demonstrates the potential of RISs in enhancing the coverage and capacity of cellular networks, particularly in areas with poor signal quality and/or high interference levels.

The last use case for RISs is to enable simultaneous wireless information and power transfer (SWIPT) in an Internet of things (IoT) network [32]. In such scenarios, where IoT devices are located far away from the power source, RISs can be employed to compensate for power loss due to the long distance by passive beamforming to improve the wireless power transfer efficiency of nearby IoT devices. This approach can help IoT devices become more self-sufficient by enabling them to harvest energy from the environment and reduce their reliance on batteries.

Analysis of the four aforementioned RIS use cases indicates that RISs have the potential to play an important role in the future smart radio environment, and can enable the manipulation of EM wave propagation in wireless networks. The technical principles and specifics of RIS will be elaborated on below.

## 2.2 Basic Principles of RIS

### 2.2.1 Hardware Structure

RIS, also known as metasurfaces, is a recently developed category of planar metamaterials that can interact with incident EM waves in a precisely controlled way [33]. A RIS usually consists of a large number elements, and the fundamental idea involves modifying the EM properties of each element to adjust the incident waves on the RIS. Specifically, when the EM waves impinge on the RIS, the waves will generate induction currents in each element. If the element is static, the current pattern is entirely determined by the geometry structure and material of the element. However, if the EM property of each element can be changed artificially, the current pattern in each element can be controlled [34]. Thus, the reflected waves from the RIS can be adjusted for different functionalities, such as combining the signals from different elements constructively and destructively towards different directions.

Typically, a RIS can be considered as a multi-layered structure, with each layer consisting of various physical and virtual components as shown in Fig. 2.3 [15]. The outermost layer of the RIS is typically referred to as the metamaterial layer, which directly interacts with the incident signals. In this layer, a large number of elements are fabricated on a dielectric substrate. The dimension of each element is sub-wavelength in size, falling within the range of $\lambda/8$ to $\lambda/2$, where $\lambda$ represents the wavelength. In practice, RIS elements are usually fabricated using metallic patches and varactor diodes. Fig. 2.4 shows a typical RIS element, which consists of a pair of metallic patches connected by a varactor diode. The external bias voltage can be used to control the junction capacitance. Two metallic via-holes are drilled in the dielectric substrate to connect the pair of metallic patches, which are used to input the direct current (DC) voltage bias. By applying different biased voltages, the properties of the varactor diode can be adjusted, resulting in the artificial modification of the EM

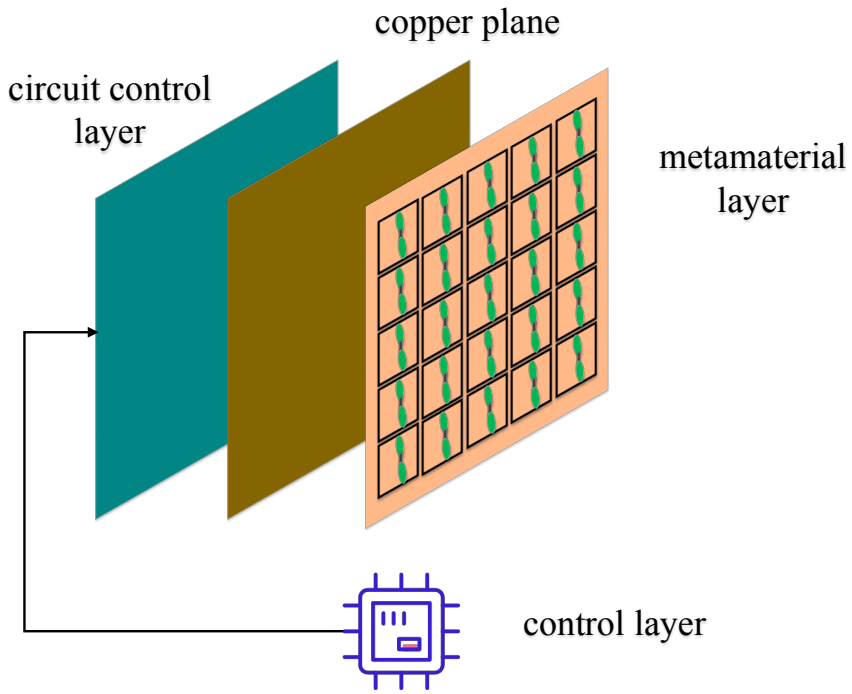



Figure 2.3: Typical structure of a RIS.

properties of the element [35]. The design and fabrication of the RIS metamaterial layer are critical in achieving the desired signal manipulation characteristics. There is also a copper plane under the dielectric substrate to reduce the energy leakage.

The second layer of the RIS is the circuit control layer, which is an important layer responsible for the control and operation of the RIS. It is composed of various electronic components that are arranged in a specific pattern and configuration to form a circuit. The circuit control layer enables independent phase shifting control of each element, which is necessary to achieve the desired signal reflection pattern. The circuit control layer is usually connected to the metamaterial layer through the via-holes in the dielectric substrate.

The innermost layer of the RIS is the control layer, which plays a crucial role in the operation and coordination of the entire system. The control layer typically consists of an intelligent controller, which can be implemented using various technologies, such

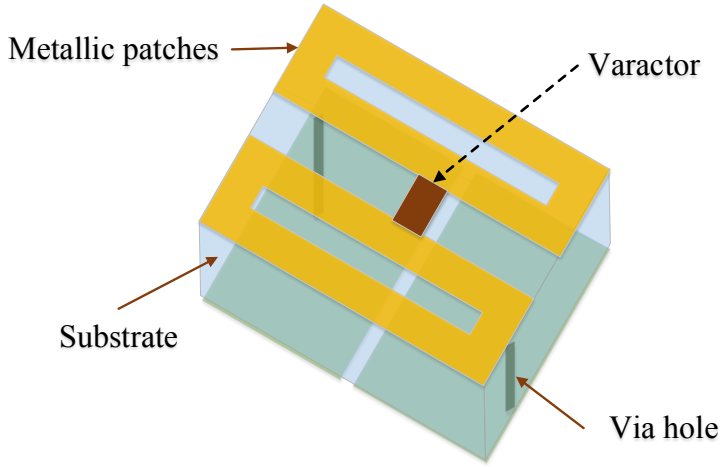



Figure 2.4: Typical structure of an element.

as field-programmable gate arrays (FPGAs) [36]. The controller generates control signals that are transmitted to the circuit control layer to adjust the phase shifts of the individual RIS elements. Moreover, the control layer serves as a communication gateway, facilitating the coordination between the RIS and other network components. For instance, the control layer can obtain channel state information (CSI) from APs or users through wireless links with low information exchange rates. This information can then be used to optimize the phase shifting scheme of the RIS and improve the overall system performance.

### 2.2.2 Equivalent Circuit Model

As introduced above, a RIS element is comprised of metallic patches placed on the top layer of the dielectric substrate, and a copper plane on the bottom layer. A semiconductor device, such as a varactor diode, is integrated into the metallic patches to enable real-time adjustment of the EM response of the element by controlling the bias voltage over the semiconductor device. This implies that, with the geometrical parameters of the element fixed, the semiconductor device has control over the phase shift of the element. As the dimension of a single element is sub-wavelength, the EM

response of an element can be described by an equivalent circuit model, regardless of its specific geometry [37]. The equivalent circuit model for an element is shown in Fig. 2.5 as a parallel resonant circuit, with the impedance given by [38]:

$$Z(C,R) = \frac{j\omega L_1 \left(j\omega L_2 + \frac{1}{j\omega C} + R\right)}{j\omega L_1 + \left(j\omega L_2 + \frac{1}{j\omega C} + R\right)}, \tag{2.1}$$

where $L_1$, $L_2$, $C$, $R$, and $\omega$ represent the bottom layer inductance, top layer inductance, effective capacitance, effective resistance, and angular frequency of the transmitted signal, respectively. It should be noted that $R$ characterizes the power dissipation caused by the losses in metals and semiconductor devices. In practice, this value can be very low, so the amplitude of the reflection coefficient of each element is often assumed to be equal to one in existing literature. On the other hand, $C$ relates to the charge accumulation associated with the geometrical parameters of the element and the bias voltage over the semiconductor device. As per the model illustrated in Fig. 2.5, the reflection coefficient of an element, denoted as $v$, can be given as the fraction of the reflected EM wave due to the impedance discontinuity between the element impedance $Z(C,R)$ and the free space impedance $Z_0$. Thus, $v$ can be given as

$$v = \frac{Z(C,R) - Z_0}{Z(C,R) + Z_0}. \tag{2.2}$$

Since $v$ is a function of the effective capacitance $C$, the reflected EM waves by the element can be precisely controlled and programmed by adjusting the value of $C$ in the RIS element.

Fig. 2.6 investigates the relationship between an element's phase shift, denoted as $\arg(v)$, and the effective capacitance $C$. As per the simulation setup in [38], the effective capacitance varies in $C \in (0.5\,\text{pF}, 2.5\,\text{pF})$. The bottom and top layer inductance are given as $L_1 = 2.5\text{nH}$ and $L_2 = 0.7\text{nH}$. The free space impedance is $Z_0 = 377\,\Omega$, and $\omega = 2\pi \times 2.4 \times 10^9$. It is learned that a RIS element can achieve

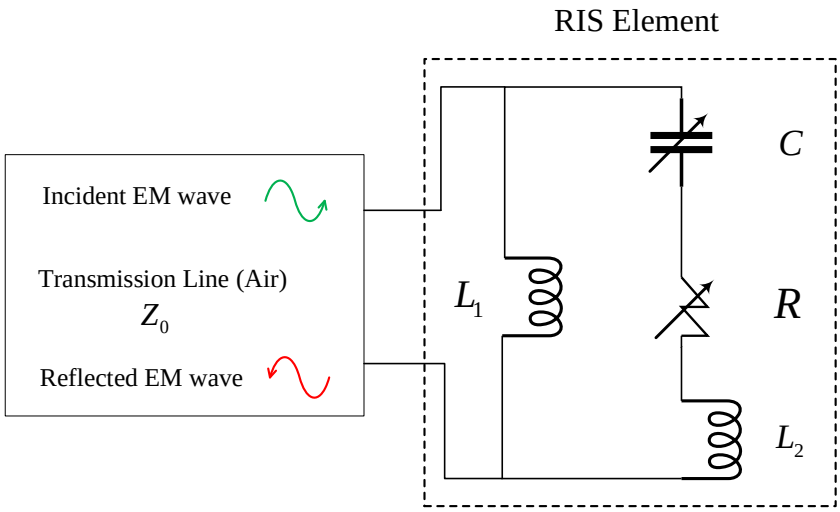



Figure 2.5: Equivalent circuit model of an element.

almost $2\pi$ phase shifting by adjusting the effective capacitance.

The effective capacitance of a RIS element can be continuously adjusted by varying the bias voltage over the varactor diode, allowing for continuous phase adjustment. One approach proposed in the literature is the use of micro-controllers to generate pulse-width modulation (PWM) signals, which are then low-pass filtered to create bias voltages that can be continuously varied from 0 to 5 V [39]. However, this method requires generating a separate PWM signal for each element, and integrating a corresponding low-pass filter circuit in each element, resulting in increased hardware complexity and cost when building large-scale RISs. To address this issue, low-precision RISs have been developed that use biased diodes with only two states, i.e., on and off [40]. While these RISs cannot achieve continuous phase adjustment, they still allow for discrete phase adjustments that are sufficient for many practical applications. Additionally, their simpler design and lower hardware cost make them a more attractive option for large-scale RISs.

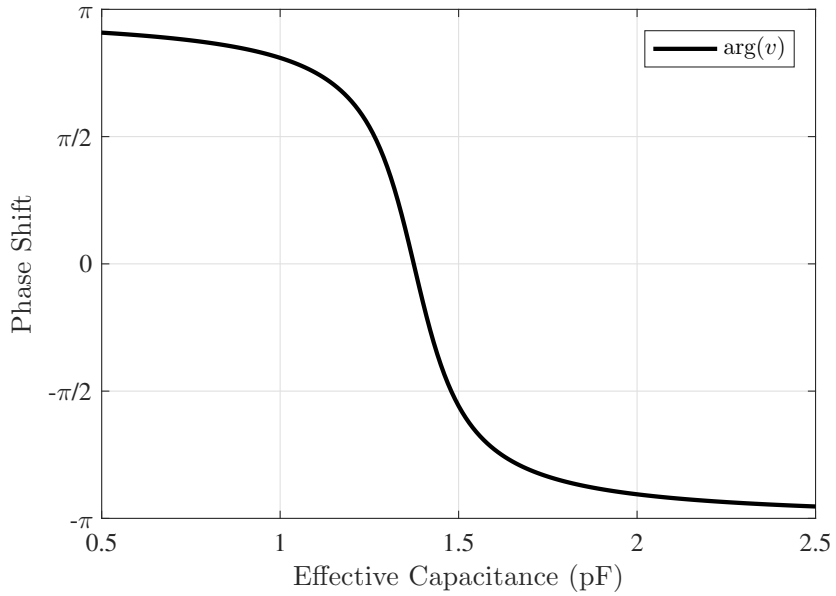



Figure 2.6: Phase shift $\arg(v)$ versus the effective capacitance $C$.

### 2.2.3 Geometric Interpretation of RIS

Many existing studies describe the role of RIS as an anomalous mirror, which implies that the RIS reflects incoming signals toward the destination similarly to a flat and perfectly rotated plane mirror. Under this assumption, the total channel gain of a RIS system converges to

$$\beta = \left( \frac{\lambda}{4\pi(d_1 + d_2)} \right)^2, \tag{2.3}$$

as the RIS size increases. Here, $\lambda$ represents the signal's wavelength, while $d_1$ and $d_2$ indicate the distances between the transmitter (TX) and RIS, and the RIS and receiver (RX), respectively.

However, the authors in [41] challenge this interpretation. They argue that if a plane wave impinges on a plane mirror, the reflection is also a plane wave. Conversely, if a plane wave impinges on a RIS with $N$ elements, each element scatters a portion of the wave with a specific phase shift. By optimizing phase shifts so that the $N$ scattered waves constructively combine at the destination, the RIS essentially functions as a concave mirror, focusing the incident wave at the destination.

The authors in [41] thoroughly investigate the path loss of a RIS-assisted communication link where both the TX and RX are equipped with lossless isotropic antennas. Their analytical results support the 'concave mirror' interpretation and are confirmed by numerical simulations. Assuming a LoS scenario with a RIS equipped with $N$ elements, the TX-RIS and RIS-RX channels are denoted as $\mathbf{h} = [|h_1|e^{j\phi_1}, ..., |h_N|e^{j\phi_N}]$ and $\mathbf{g} = [|g_1|e^{j\varphi_1}, ..., |g_N|e^{j\varphi_N}]$, respectively. The phase shift for the $n$th RIS element is $\theta_n$. Each element measures $\frac{\lambda}{4} \times \frac{\lambda}{4}$, with $\lambda = 0.1, \mathrm{m}$. Both TX and RX are centered in front of the RIS at distances of $d_1 = 25, \mathrm{m}$ and $d_2 = 2.5, \mathrm{m}$. Given the TX and RX locations, a mirror-mimicking RIS has $\theta_n = 0$ for all $n$, and the composite channel gain can be expressed as

$$\beta_1 = \left| \sum_{n=1}^{N} |h_n||g_n| e^{j(\phi_n + \varphi_n)} \right|^2 . \tag{2.4}$$

For an optimally phase-shifted RIS, where $\theta_n = -\phi_n - \varphi_n$, the composite channel gain is

$$\beta_2 = \left( \sum_{n=1}^{N} |h_n||g_n| \right)^2 . \tag{2.5}$$

Fig. 2.7 displays the composite channel gains $\beta$, $\beta_1$, and $\beta_2$ as functions of the number of RIS elements. For small RISs, there is no significant difference between $\beta_1$ and $\beta_2$ because, when TX and RX are in the far-field, focusing the incident plane waves on a distant point is roughly equivalent to mimicking a plane mirror that reflects the signal towards a distant point in the same direction. However, as the number of RIS elements increases, $\beta_1$ converges to $\beta$, while $\beta_2$ continues to grow, demonstrating that an optimized RIS cannot generally be characterized as an anomalous mirror, and the performance of an optimized RIS will exceed the mirror limit. Moreover, the curve for $\beta_2$ starts to flatten as the number of elements grows larger. This is due to the energy conservation law, which is discussed in more detail in [41] and lies beyond the scope of this thesis.

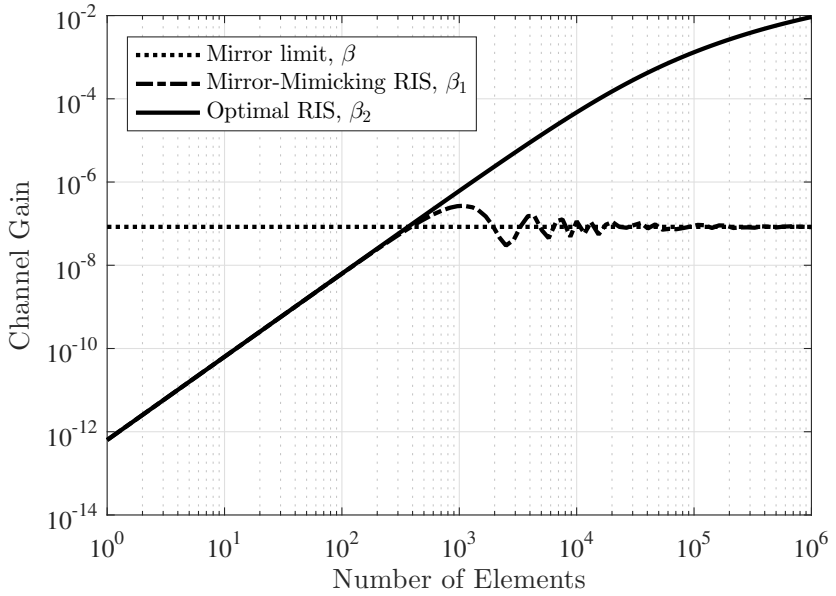



Figure 2.7: Composite channel gains with mirror limit $\beta$, mirror-mimicking phases $\beta_1$, and optimal phases $\beta_2$.

### 2.2.4 CSI Acquisition of RIS-Assisted Communications

While the focus of this thesis is not on the channel estimation problem in RIS-assisted communication systems, it is still worth briefly discussing this topic in this subsection. In the context of RIS-assisted communications, obtaining the accurate CSI is crucial to achieve the optimal active beamforming design at the transmitter, optimal phase shifting design at the RIS, and the information decoding at the receiver. However, obtaining CSI in RIS-assisted systems presents a significant challenge. Unlike active devices, the RIS is nearly passive with a large number of RIS elements, which renders traditional CSI acquisition methods ineffective. Additionally, estimating the transmitter-RIS channel and RIS-receiver channel separately can be challenging due to their coupling with the RIS reflecting coefficient matrix. Moreover, the large number of elements results in a high training overhead.

For example, we consider a RIS-assisted communication link where both the TX and the RX are equipped with a single antenna, and the RIS is equipped with $N$ elements. Denote the channels from the TX to the RIS, and from the RIS to the RX

as $\mathbf{h} \in \mathbb{C}^{N\times 1}$, and $\mathbf{g} \in \mathbb{C}^{N\times 1}$, respectively. The direct link between TX and RX is $h_d \in \mathbb{C}$. Thus, the composite channel gain from TX to the RX can be given as

$$H = \mathbf{h}^T \text{diag}\left(\boldsymbol{\Theta}\right) \mathbf{g} + h_d \tag{2.6a}$$

$$= \boldsymbol{\Theta} \text{diag}\left(\mathbf{h}^T\right) \mathbf{g} + h_d, \tag{2.6b}$$

where $\boldsymbol{\Theta} = [\theta_1, \theta_2, ..., \theta_N]$ is the reflecting coefficient vector of the RIS. The CSI of the direct link can be estimated using conventional channel estimation techniques. Upon observing (2.6b), it is obvious that the optimal design of the reflecting coefficient matrix $\boldsymbol{\Theta}$ does not necessitate the precise knowledge of channel links $\mathbf{h}$ and $\mathbf{g}$, but rather relies only on the CSI of the direct link and the cascaded channel

$$\mathbf{H}_1 = \text{diag}\left(\mathbf{h}^T\right) \mathbf{g}. \tag{2.7}$$

There have been a number of proposed methods for estimating the cascaded channel $\mathbf{H}_1$ in RIS-assisted communication. These methods can typically be categorized into two groups.

#### 2.2.4.1 Binary Reflection Enabled Channel Estimation

In [42], a binary reflection method was proposed for estimating a RIS-assisted communication system. This method sequentially activates only one element for each pilot symbol, and an extra training symbol is required to estimate the direct link between the TX and the RX when all RIS elements are turned off. However, the on/off switching of a large number of RIS elements can be costly, and the channel estimation accuracy is reduced as only a single element is activated at each time resulting in low received power of the pilot symbol. To address these challenges, another binary reflection scheme based on sub-groups of RIS elements was proposed in a paper by [43] for RIS-assisted systems, utilizing the spatial correlations among adjacent elements.

In this method, the RIS elements are divided into multiple sub-groups, and each subgroup consisting of adjacent elements shares a common reflecting coefficient.

#### 2.2.4.2 Full Reflection Enabled Channel Estimation

The binary reflection method, while easy to implement, has drawbacks such as large training overhead and low received power for channel estimation. To address these issues, several existing studies have focused on the design of full reflection based channel estimation schemes, in which all RIS elements are activated during the channel estimation process. The fundamental idea for channel estimation in a RIS system with $N$ elements involves adjusting the reflecting coefficient patterns of the RIS to alternate between $N$ mutually orthogonal patterns. The authors in [44] proposed a full reflection based approach and designed the training reflecting coefficient patterns based on the minimum variance unbiased estimation principle. To further enhance efficiency, the method presented in [45] integrates the grouping idea into full reflection based channel estimation techniques. Moreover, some studies have also harnessed the capabilities of deep learning to obtain the CSI in RIS-assisted communication networks [46, 47].

## 2.3 Stochastic Geometry for Large-Scale Network Modeling

Apart from conducting the link-level analysis in this thesis, we also study RIS-assisted large-scale communication networks, where inter-cell interference caused by interfering TXs and RISs is considered in the analysis. Stochastic geometry is an essential tool for modelling and analyzing large-scale wireless networks with spatial uncertainty [48]. Unlike the traditional analytical models that assume a deterministic node placement, the fundamental concept of stochastic geometry is to model the spa-

tial distributions of wireless nodes as a random process, which allows researchers to study the average behavior over many spatial realizations of a network whose nodes are placed according to some random point patterns [49]. Stochastic geometry is useful for large-scale wireless network modeling since the exact locations of the wireless nodes are often uncertain and can vary from one deployment to another. Moreover, stochastic geometry can be used to investigate various network performance metrics.

In stochastic geometry, different types of wireless nodes are typically modeled as independent point or cluster processes. These processes can be generated according to various process patterns, such as Binomial point process (BPP), homogeneous Poisson point process (HPPP), Poisson cluster process (PCP), etc. Once the process is established, the network's characteristics can be analyzed using a variety of mathematical tools. These tools enable the study of the behavior of the network under various conditions, such as varying node densities, network topologies, or propagation environments [50].

One of the key advantages of stochastic geometry is the ability to capture the effect of spatial randomness on network performance metrics such as coverage probability and spectrum efficiency [51]. These metrics are often crucial for the design and optimization of wireless networks, and their accurate evaluation requires accounting for the randomness in the network topology and propagation environment. By providing a rigorous mathematical framework, stochastic geometry facilitates the derivation of analytical expressions for these performance metrics.

In addition, the stochastic geometry approach is also flexible and versatile. It can be applied to model a wide range of wireless networks, including cellular networks, ad-hoc networks, wireless sensor networks, and IoT networks [52]. Moreover, it can model various network topologies, ranging from dense urban environments to sparse rural areas. By accurately modeling the randomness of node placements, stochastic geometry allows for more realistic analysis of network performance.

Furthermore, stochastic geometry is able to capture the dynamics of wireless networks. Wireless networks are inherently dynamic, with nodes constantly moving and the environment changing over time. Stochastic geometry can account for this dynamic nature by modeling node mobility as a random process. This allows for the study of the properties of time-varying networks and provides insights into how network performance varies over time [53]. Overall, the stochastic geometry approach is a powerful and flexible tool for modeling and analyzing wireless networks, enabling researchers to gain a deeper understanding of network behavior and performance in various environments and scenarios.

In the following section, we will introduce two commonly used point processes, i.e., BPP and HPPP, as well as a cluster process PCP.

### 2.3.1 BPP

The BPP, is a widely used spatial point process in stochastic geometry for modeling the locations of wireless nodes in large-scale wireless networks. It is a discrete point process that characterizes the distribution of random points in a bounded area, and is defined by two properties: the number of points and the geometry of the bounded area.

Specifically, given a space $A \subset \mathbb{R}^2$, the BPP refers to a point process $X$ consisting of a fixed number of $n$ i.i.d. random points that are uniformly distributed in $A$. The density function of the points on $A$ is given by

$$f(x) = \frac{1}{L(A)}, \quad x \in A, \tag{2.8}$$

where $L(A)$ is the area of $A$. This means that the locations of the points are randomly distributed in a given bounded area, without any preferential bias towards certain locations, and the probability of finding a point in any subregion of $A$ is proportional

to the area of that subregion. Specifically, for any bounded set $B \subset A$ and a randomly selected point $X_i$, the probability that $X_i$ belongs to $B$ is given by

$$\mathbb{P}(X_i \in B) = \frac{L(B)}{L(A)}. \tag{2.9}$$

Furthermore, the probability of having $k$ points in $B$ can be expressed as

$$\mathbb{P}\left(\Phi(B) = k\right) = \binom{n}{k} \left(\frac{L(B)}{L(A)}\right)^k \left(1 - \frac{L(B)}{L(A)}\right)^{n-k}, \tag{2.10}$$

where $\Phi(B)$ represents the number of points in $B$. This formula gives the probability that out of the $n$ points in the BPP, exactly $k$ points lie in the region $B$. The first term in the equation is the binomial coefficient that counts the number of ways to choose $k$ points out of $n$. The second term is the probability of having $k$ points in $B$, and the third term is the probability of having the remaining $n-k$ points outside $B$.

#### 2.3.1.1 Applications and Limitations of BPP

The uniform BPP is a popular choice for modeling the locations of a fixed number of nodes in a finite wireless network. This model is particularly useful for studying the performance of a user across all locations, since interference and SINR can vary between the center and boundary of the network. For instance, in [54], the authors used the uniform BPP to study the performance of a reference receiver located at any point within a circular region, under uniform and $k$-closest transmitter selection policies. Similarly, in [55], a BPP was employed to model a finite network of unmanned aerial vehicles (UAVs) serving a given area, and the downlink coverage probability for a reference receiver at any ground location was derived assuming Nakagami-$m$ fading for all wireless links.

Despite its usefulness, the BPP has some limitations. First, it requires a known number of nodes, which may not be available in practical networks where only the

average number of users is known. Second, the analytic complexity associated with deriving performance metrics is often challenging due to boundary effects. Furthermore, the BPP also has limitations in modeling networks where nodes are spatially correlated with each other or networks where nodes are clustered in certain areas. To overcome these issues, researchers often use alternative models such as HPPPs and PCPs.

### 2.3.2 HPPP

The HPPP is the most widely used point process in the modeling and analysis of large-scale wireless communication networks. It is a special case of the Poisson point process (PPP), where the density of points is uniform throughout the spatial domain. In wireless networks, the HPPP can be used to model the spatial distribution of nodes in a variety of scenarios, such as ad hoc networks, cellular networks, and wireless sensor networks. Compared to the BPP, which requires a known number of nodes, the HPPP can be used to model networks where the number of nodes is not known a priori. This flexibility allows for more realistic modeling of practical communication scenarios. Furthermore, the HPPP enables the derivation of analytical expressions for key performance metrics more easily.

The HPPP is defined over the entire plane. A point process $\Lambda$ in $\mathbb{R}^2$ is considered a HPPP if it satisfies two properties. Firstly, for any two disjoint regions $A_1 \subset \mathbb{R}^2$ and $A_2 \subset \mathbb{R}^2$, the random variables $\Phi(A_1)$ and $\Phi(A_2)$ describing the number of points in $\Lambda$ falling in these regions are independent. Secondly, the number of points $\Phi(A)$ falling in a bounded region $A$ follows a Poisson distribution with parameter $\lambda L(A)$, where $\lambda$ is the intensity of the process, i.e., the expected number of points per unit area, and $L(A)$ is the area of $A$. This can be mathematically represented as follows:

$$\mathbb{P}(\Phi(A) = n) = e^{-\lambda L(A)} \frac{(\lambda L(A))^n}{n!}, \quad n \in \mathbb{N}_0. \tag{2.11}$$

In other words, a HPPP is a completely random point process where the locations of points are independent of each other and the probability of finding a point in any region of a fixed area is proportional to the area of that region. The properties of homogeneity, isotropy, and independence make the analysis of Poisson processes relatively straightforward. These properties also imply that the process is the same with respect to rotation around an arbitrarily chosen origin.

#### 2.3.2.1 Important Theorems about HPPP

The HPPP has two important theorems associated with it, namely Campbell's theorem and the probability generating functional lemma (PGFL).

The Campbell's theorem states that, for a HPPP $\Lambda$ of density $\lambda$ and a real-valued function $f(x) : \mathbb{R}^2 \to \mathbb{R}^+$, we have [56]

$$\mathbb{E}\left[\sum_{x\in\Lambda} f(x)\right] = \lambda \int_{\mathbb{R}^2} f(x)\,\mathrm{d}x. \tag{2.12}$$

The PGFL states that, for a HPPP $\Lambda$ of density $\lambda$ and a real-valued function $f(x) : \mathbb{R}^2 \to [0, 1]$, we have [56]

$$\mathbb{E}\left[\prod_{x\in\Lambda} f(x)\right] = \exp\left(-\lambda \int_{\mathbb{R}^2} (1 - f(x))\ \mathrm{d}x\right). \tag{2.13}$$

These two theorems are fundamental to the analysis of large-scale networks modeled as HPPPs and provide tools for evaluating expectations of random sums and products over the process. They have broad applications in the stochastic geometry analysis of large-scale wireless networks, enabling the computation of coverage probabilities, spectral efficiency, and other performance metrics.

#### 2.3.2.2 Applications and Limitations of HPPP

The HPPP has emerged as a popular model for analyzing various components of communication networks, such as the locations of users and APs, owing to its ability to provide tractable analytical expressions for specific performance metrics, such as coverage probability. The independence between different points and the simplicity of the PGFL are key factors that enable HPPP models to yield meaningful results. In early studies [57], a communication system with HPPP-modeled base stations was found to provide a lower bound to a hexagonal cellular system in terms of connection probability under normal shadow fading conditions, and a good approximation under high shadow fading scenarios. HPPP is also widely used in the study of RIS-assisted large-scale wireless networks. For example, the authors in [58] employed two independent HPPPs to model the locations of APs and RISs, respectively, and investigate the communication performance of a typical user.

While the HPPP is a widely-used model in communication network analysis, it has limitations in certain scenarios. One limitation is that the HPPP assumes that the locations of points are completely independent and randomly distributed, which may not accurately reflect the real-world behavior of wireless nodes. In situations where nodes tend to cluster together due to physical proximity or due to network protocol requirements, the HPPP may not be an appropriate model. Furthermore, in RIS-assisted communication networks where RISs may be deployed close to APs or users, the HPPP may not capture the spatial coupling between nodes that can significantly impact network performance. To model non-uniform behavior of wireless nodes, alternative point process models, such as the PCP, may be more appropriate.

### 2.3.3 PCP

The PCP is an alternative process model used for network modeling in scenarios where the locations of nodes exhibit correlation or non-uniform behavior. The PCP

combines the parent process and the offspring process, where the parent process is generated from the realizations of a HPPP and the offspring process is a finite point process. Unlike the HPPP, the PCP can capture the spatial coupling between nodes, making it a more appropriate model for certain scenarios. In general, the PCP is a collection of cluster processes, including Neyman-Scott process, Mat'ern cluster process, modified Thomas cluster process, etc. The PGFL can also be applied in the analysis of large-scale networks modeled by PCPs. In this thesis, the Gauss-Poisson process (GPP) is utilized, which is a special case of PCP.

#### 2.3.3.1 A Special Case of PCP: GPP

The GPP is defined over the entire plane $\mathbb{R}^2$, where the parent process is a HPPP denoted as $\Lambda_p$ with a density of $\lambda_p$. In a GPP, each cluster can contain one or two points with probabilities $1-p$ and $p$, respectively. If a cluster has a single point, it is situated at the parent's position. On the other hand, if a cluster contains two points, the first point is at the parent's position, while the second point is uniformly distributed along a circle centered at the parent's position with a radius $d$ [59].

Applying the GPP in a RIS-assisted communication network, clusters consisting of one point correspond to transmitters without assisting RISs, represented by $\Lambda^{(1)} = \{x\}$, while clusters consisting of two points correspond to transmitters with assisting RISs, represented by $\Lambda^{(2)} = \{x, x+u\}$, where $u$ is a translation vector of length $d = |u|$ in any direction. Therefore, we have $\Lambda = \Lambda^{(1)} \cup \Lambda^{(2)}$ and the GPP's density is $\lambda = (1+p)\lambda_p$.

For a GPP $\Lambda$ of parent process density $\lambda_p$ and a real-valued function $f(x) : \mathbb{R}^2 \rightarrow$

$[0,1]$, the PGFL of the GPP is given by [60]

$$\mathbb{E}\left[\prod_{x\in\Lambda} f(x)\right] = \exp\left(\lambda_p \int_{\mathbb{R}^2}\left((1-p)f(x) + pf(x)\int_0^{2\pi} \frac{f(x+d\,w(\psi))}{2\pi}\,\mathrm{d}\psi - 1\right)\,\mathrm{d}x\right), \tag{2.14}$$

where $w(\psi) = (\cos(\psi), \sin(\psi))$; $x$ is defined in Cartesian coordinate system.

Overall, the PCP can capture spatial clustering and heterogeneity among nodes, which makes it more appropriate for modeling certain communication network scenarios. The GPP is a specific instance of the PCP and has been used extensively in network modeling [60]. The PGFL can also be applied in the analysis of large-scale networks modeled by PCPs [48]. In practice, the choice of point or cluster process models should be carefully considered based on the specific characteristics and requirements of the network being modeled.

## 2.4 Summary

This chapter provided the necessary background for the research presented in this thesis by examining several key aspects of RIS-assisted communication performance analysis. The concept of the smart radio environment was first introduced, highlighting the motivation for investigating RIS technology as a promising means to achieve intelligent radio propagation in the future. Subsequently, the fundamental principles of RIS were presented, including hardware structure, equivalent circuit model, geometric interpretation, and channel estimation. These discussions served to elucidate how RIS operates in wireless communication systems. Moreover, the theory of stochastic geometry, an important mathematical method for analyzing large-scale wireless communication networks, was briefly introduced. Based on this comprehensive overview and existing research on RIS-assisted wireless communication, the

subsequent chapters focus on analyzing four distinct scenarios, examining the impact of RIS characteristics on system performance and the potential performance gains RIS can offer future wireless networks.

# Chapter 3

# RIS-Assisted Communications with Phase Errors

Due to the rapid development of metamaterials and metasurfaces, RIS-assisted wireless communications have become an important academic research topic. By tuning the phases of the channels dynamically, a RIS is able to create a controllable wireless propagation environment with low hardware cost and energy consumption.

The first work dedicated to the performance analysis of RIS-assisted communications is presented in [61]. A RIS-assisted communication link over the Rayleigh fading channels is analyzed by using the central limit theorem, and several performance metrics, e.g., outage probability, average achievable rate, and average symbol error rate, are derived. The phase alignment of the RIS and channel estimation are both assumed to be accurate. However, perfect phase adjustment and accurate channel estimation cannot be achieved in practice. Physically, the most common configuration of a RIS element is that planar metallic patches are connected with biased diodes. Different phase shifting levels of a RIS element can be generated by changing the input biasing direct current (DC) voltage through the DC feeding lines. Although the continuous phase adjustment scheme is beneficial for communication performance, it

cannot be realized in practice since building high-precision RIS elements requires high hardware costs and complicated system structures. For example, to realize a 4-bit (16 levels) phase shifting scheme, four biased diodes are required to be integrated into a sub-wavelength RIS element, making the system design challenging, especially when the number of RIS elements is significant. Therefore, it is more reasonable and cost-effective to implement low-precision RIS elements, and the 1-bit (2 levels) phase shifting is the most common phase shifting scheme in practice. On the other hand, even though many research efforts have been devoted to the channel estimation of RIS-assisted wireless communication systems, accurate channel estimation cannot be guaranteed in practice. Furthermore, a RIS is a nearly passive device, and it is not equipped with radio frequency (RF) chains that can be used to estimate the channels associated with the RIS. These properties make the acquisition of accurate channel state information (CSI) even more difficult. Therefore, it is important to include channel estimation errors in the performance analysis.

Motivated by the above issues, the performance of a RIS-assisted wireless communication system with phase errors is analyzed in this chapter. Particularly, several important performance metrics are derived, e.g., outage probability and diversity order, and the impact of phase errors on communication performance is investigated. The main contributions of this chapter can be summarized as follows:

- The path loss of a RIS-assisted communication link in a line-of-sight (LoS) scenario is introduced. Then, the outage probability of the system with phase errors is derived. The phase errors are modeled by a Von Mises distribution, a common distribution to model the channel estimation errors.

- To provide an ideal performance benchmark, we analyze the performance of a RIS-assisted communication link over the Rayleigh fading channels without phase errors. A moment-matching approach based on the gamma distribution is proposed to approximate the composite channel gain as a gamma random

variable, which is shown to have high approximation accuracy. Then, the outage probability of the system is derived, and the diversity order is obtained through an asymptotic analysis.

- Considering the 1-bit phase shifting scheme, we investigate a RIS-assisted communication link over Rayleigh fading channels. The outage probability expression is derived in an integral form, and the diversity order is obtained. Further, the performance degradation due to discrete phase quantization is discussed.

## 3.1 System Framework and Performance Metrics

In this chapter, we study a RIS-assisted downlink communication system, where a single-antenna transmitter (TX) communicates with a single-antenna user equipment (UE), aided by a RIS with $N$ elements, labeled as $(R_1, R_2, ..., R_N)$. Each element is of size $s_0 = l_0 w_0$, where $l_0$ and $w_0$ denote the length and width of each element. All the elements are placed in a rectangular array with $N_l$ elements per row and $N_w$ elements per column, such that $N = N_l N_w$. The RIS is operating in the far field of both TX and UE. As shown in Fig. 3.1, the direct link between TX and UE is absent due to obstacles, shadowing effects, and/or deep fading.

### 3.1.1 Channel and Signal Models

Let $\mathbf{h} = (h_1, ..., h_N)^T \in \mathbb{C}^{N\times 1}$ and $\mathbf{g} = (g_1, ..., g_N)^T \in \mathbb{C}^{N\times 1}$ represent the complex attenuation vectors of the TX-RIS and RIS-UE channels, respectively. Under this model, the received signal at UE can be given as

$$y = \sum_{n=1}^{N} h_n e^{j\theta_n} g_n \sqrt{P} s + n_0, \tag{3.1}$$

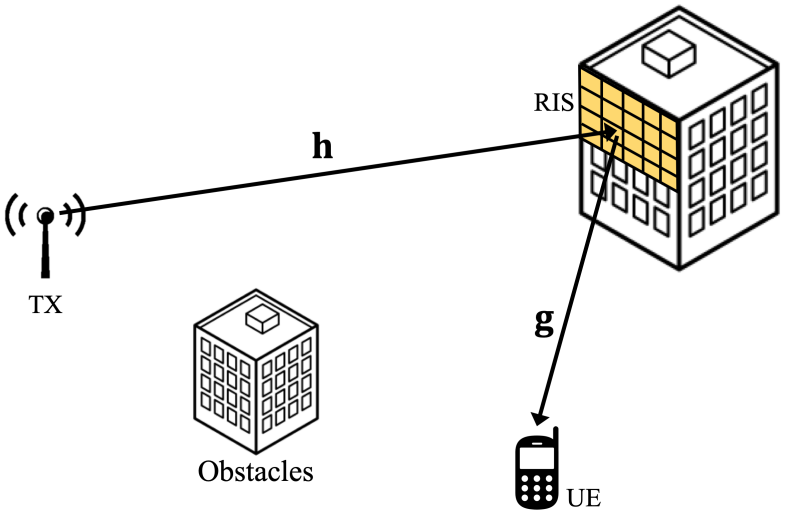



Figure 3.1: System model.

where $\theta_n$, $n \in \{1, ..., N\}$ is the phase shifting level of the $n$th RIS element; $P$ is the transmit power of TX; $n_0 \sim \mathcal{CN}(0, \sigma_0^2)$ is the additive white Gaussian noise (AWGN) at UE with zero mean and variance $\sigma_0^2$; $s$ is the unit power transmit constellation symbol, such that $\mathbb{E}[|s|^2] = 1$.

#### 3.1.1.1 LoS Scenario

In a LoS propagation scenario without small scale fading, the received signal can be rewritten as

$$y = \sqrt{\beta_1} \left( \sum_{n=1}^{N} \tilde{h}_n e^{j\theta_n} \tilde{g}_n \right) \sqrt{P} s + n_0, \tag{3.2}$$

where $\beta_1$ is the path loss between TX and UE through the RIS in a LoS set-up; $\tilde{h}_n = e^{j\phi_{h,n}}$ and $\tilde{g}_n = e^{j\phi_{g,n}}$ denote the normalized LoS channel coefficients of the TX-$R_n$ and $R_n$-UE channels, respectively. $\phi_{h,n}$ and $\phi_{g,n}$ are the phases of the corresponding channels, such that

$$\phi_{h,n} = -\frac{2\pi d_h}{\lambda}, \quad \phi_{g,n} = -\frac{2\pi d_g}{\lambda}, \tag{3.3}$$

where $d_h$ and $d_g$ are the distances of the TX-RIS and RIS-UE channels, respectively; $\lambda$ is the wavelength of the transmit signal.

Ideally, to optimize the communication system performance, the RIS is supposed to align the phases of all the channels by setting $\theta_n = -\phi_{h,n} - \phi_{g,n}$. Therefore, in this case, the received signal at UE can be written as

$$y = N\sqrt{\beta_1 P}s + n_0. \tag{3.4}$$

However, in a practical system, imperfect channel estimation will lead to phase errors. Mathematically, the resulting phase shift of the $n$th RIS element is

$$\theta_n = -\phi_{h,n} - \phi_{g,n} + \tilde{\theta}_n, \tag{3.5}$$

where $\tilde{\theta}_n$ is the phase error inherent in each RIS element, which is commonly modeled by mutually independent and identical distributed (i.i.d.) Von Mises random variables. Assuming that $\tilde{\theta}_n$ follows the Von Mises distribution with zero mean and concentration parameter $\kappa$, the probability density function (PDF) of $\tilde{\theta}_n$ is given by

$$f_{\tilde{\theta}_n}(\theta) = \frac{e^{\kappa\cos(\theta)}}{2\pi I_0(\kappa)}, \qquad -\pi < \theta < \pi, \tag{3.6}$$

where $I_0(\cdot)$ is the modified Bessel function of the first kind of order zero. Thus, the received signal at UE in a LoS scenario with channel estimation errors can be written as

$$y = \sqrt{\beta_1 P}H_1 s + n_0, \tag{3.7}$$

where

$$H_1 = \sum_{n=1}^{N} e^{j\tilde{\theta}_n}. \tag{3.8}$$

#### 3.1.1.2 Fading Scenario

In a rich scattering propagation environment without stable LoS links, the Rayleigh fading is commonly used to model the channels in the proposed system. Thus, the

received signal at UE in a Rayleigh fading scenario can be written as

$$y = \sqrt{\beta_2} \left( \sum_{n=1}^{N} \bar{h}_n e^{j\theta_n} \bar{g}_n \right) \sqrt{P} s + n_0, \tag{3.9}$$

where $\beta_2$ is the path loss of the TX-RIS-UE channel; $\bar{h}_n$ and $\bar{g}_n$, $n \in \{1, ..., N\}$ denote the normalized small scale fading of the TX-$R_n$ and $R_n$-UE channels, respectively. $\bar{h}_n$ and $\bar{g}_n$, $n \in \{1, ..., N\}$ are i.i.d. circularly symmetric complex Gaussian (CSCG) random variables with zero mean and unit variance, such that $\bar{h}_n, \bar{g}_n \sim \mathcal{CN}(0, 1)$. Thus, the magnitudes of $\bar{h}_n$ and $\bar{g}_n$ are Rayleigh distributed, i.e., $|\bar{h}_n|, |\bar{g}_n| \sim \mathcal{R}(\sqrt{2}/2)$.

Assuming that channel estimation is accurate and the RIS is able to perform perfect continuous phase adjustment, the phase shifts of the RIS are controlled to co-phase all the channels such that

$$\theta_n = -\arg(\bar{h}_n) - \arg(\bar{g}_n). \tag{3.10}$$

In this case, the received signal at UE can be rewritten as

$$y = \sqrt{\beta_2 P} H_2 s + n_0, \tag{3.11}$$

where

$$H_2 = \sum_{n=1}^{N} |\bar{h}_n||\bar{g}_n|. \tag{3.12}$$

However, the phases of the RIS elements cannot be set precisely in reality due to the finite precision inherent in the phase alignment operation. Mathematically, the resulting phase adjustment at the $n$th element can be written as

$$\theta_n = -\arg(\bar{h}_n) - \arg(\bar{g}_n) + \bar{\theta}_n, \tag{3.13}$$

where $\bar{\theta}_n$ denotes the phase error introduced through phase quantization at the $n$th

element. We assume that each element of the RIS is a 1-bit phase shifter, either leaving the phase of the incident wave unaltered or shifting it by $\pi$ radians. It follows that the phase errors $\bar{\theta}_n,\ n \in \{1, ..., N\}$ are mutually independent and uniformly distributed on the interval $[-\pi/2, \pi/2]$. In this case, the received signal at UE is

$$y = \sqrt{\beta_2 P} H_3 s + n_0, \tag{3.14}$$

where

$$H_3 = \sum_{n=1}^{N} |\bar{h}_n||\bar{g}_n| e^{j\bar{\theta}_n}. \tag{3.15}$$

The key difference between the channel gain in LoS and fading scenarios is the level of fluctuation. In a LoS scenario, the composite channel gain is primarily dependent on path loss, which is relatively stable. However, in a fading scenario, the channel gain fluctuates over time, and this fluctuation is characterized by random variables in system modeling.

### 3.1.2 Performance Metrics

The received signal-to-noise ratio (SNR) of UE is defined as the ratio of desired signal power to noise power. Therefore, the received SNR of UE in a LoS propagation scenario with channel estimation errors is given by

$$\gamma_1 = \gamma_t \beta_1 |H_1|^2, \tag{3.16}$$

where $\gamma_t = P/\sigma_0^2$ is the transmit SNR of TX. The received SNR of UE in a Rayleigh fading scenario can be given as

$$\gamma_u = \gamma_t \beta_2 |H_u|^2, \tag{3.17}$$

where $u \in \{2, 3\}$ represents the cases without and with phase shifting errors, respectively.

The outage probability is an important performance metric used to evaluate the reliability of a communication system. It is equivalent to the received SNR distribution and is defined as the probability that the received SNR falls below a SNR threshold $\bar{\gamma}$:

$$P_w(\bar{\gamma}) = \mathbb{P}(\gamma_w < \bar{\gamma}), \quad w \in \{1, 2, 3\}, \tag{3.18}$$

where $\gamma_w$, $w \in \{1, 2, 3\}$ is the received SNR of UE defined in (3.16) and (3.17).

Based on the outage probability, the diversity order of a communication system refers to the slope of the outage probability decreasing with the increase of the transmit SNR in the log-log scale as the transmit SNR becomes large. Mathematically, the diversity order is defined as

$$d_w = \lim_{\gamma_t \to \infty} -\frac{\log P_w(\bar{\gamma})}{\log \gamma_t}, \quad w \in \{1, 2, 3\}. \tag{3.19}$$

## 3.2 Analysis of LoS Scenario

This section analyzes the outage probability of a RIS-assisted communication system over LoS channels. The path loss of the system is introduced first, followed by the outage probability analysis with Von Mises phase errors.

### 3.2.1 Path Loss Analysis

A RIS consists of a large number of elements to reconfigure the phases of the incoming electromagnetic (EM) waves. The incoming EM waves can induce a surface electric current in the RIS. By adjusting the surface impedance of each element, we can obtain a local surface phase shifting profile required by the generalized Snell's law and thereby obtain scattered EM waves in a certain direction [34]. If we want to use

a RIS with $N$ elements to reflect the incoming signals towards the direction $\psi_r$ and follow the generalized Snell's law, the path loss in the far field of distance $d_g$ can be given as [62]

$$\beta_s = \frac{G_t G_r}{(4\pi)^2} \left( \frac{N l_0 w_0}{d_h d_g} \right)^2 \cos^2(\psi_i) \left( \frac{\sin\left(\frac{\pi w_0}{\lambda}(\sin(\psi_s) - \sin(\psi_r))\right)}{\frac{\pi w_0}{\lambda}(\sin(\psi_s) - \sin(\psi_r))} \right)^2, \tag{3.20}$$

where $G_t$ and $G_r$ are the antenna gains of the transmit and receive antennas, respectively; $\psi_i$ is the incident angle; $\psi_s$ is the observation angle; $\lambda$ is the wavelength of the incoming waves; $d_h$ is the distance between the transmitter and the RIS.

The behavior of each element can be analyzed based on (3.20). If the dimension of each element is sub-wavelength such that $l_0, w_0 \ll \lambda$, no matter the phase shift of the element, the path loss between the transmitter and receiver through the element is independent of $\psi_r$ in the far field, such that

$$\beta_1 = \frac{G_t G_r}{(4\pi)^2} \left( \frac{l_0 w_0}{d_h d_g} \right)^2 \cos^2(\psi_i). \tag{3.21}$$

In other words, a RIS can be regarded as a collection of diffuse scatters, of which the phase shifts can be controlled to achieve directional signal enhancement or nulling. The received signal model over LoS channels given in (3.2) is based on (3.21), and a more concise form of writing $\beta_1$ is

$$\beta_1 = \frac{\Lambda_1}{d_h^2 d_g^2}, \tag{3.22}$$

where $\Lambda_1$ is the path loss per unit distance in the LoS scenario. Similarly, the path loss in the fading scenario is given as [63]

$$\beta_2 = \frac{\Lambda_2}{d_h^\chi d_g^\chi}, \tag{3.23}$$

where $\Lambda_2$ is the path loss per unit distance in the fading scenario, and $\chi$ is the path loss exponent.

### 3.2.2 Outage Probability Analysis with Phase Errors

In this subsection, we study the outage probability of a RIS-assisted communication system over LoS channels with Von Mises phase errors. The set-up reflects scenarios with a dominant LoS component, e.g., a RIS equipped on an unmanned aerial vehicle (UAV). Based on experimental measurements, the channels in such scenarios usually consist of a strong LoS component and few weak scattered components. Hence, the channels can be assumed to experience no small scale fading. On the other hand, as introduced in some papers on UAV communications, imperfect channel knowledge is often considered since UAVs may shake and jitter due to unpleasant weather conditions, such as on windy days. Although the movements due to jittering are negligible compared to the distances of the TX-RIS and RIS-UE channels, they may cause significant phase shifts to the channels when displacement is on the order of the wavelength. Therefore, we use a general Von Mises distribution to model the phase errors. As introduced above, the shape of the Von Mises distribution is determined by a concentration parameter $\kappa$, and the phase error $\tilde{\theta}_n$ gets more concentrated around zero with the increase of $\kappa$, standing for higher accuracy in channel estimation.

The distribution of the composite channel gain is studied first by deriving the PDF and cumulative distribution function (CDF) in integral forms. Then, an asymptotic analysis regarding the lower tail distribution of the composite channel gain is carried out by using Laplace's method, and closed form expressions of the PDF and CDF of the lower tail are derived. Finally, the outage probability and diversity order of the system are discussed.

#### 3.2.2.1 Distribution of the Composite Channel Gain

As discussed in [64], for a two-dimensional random variable $(x, y)$, if

$$x = r\cos(\theta), \quad y = r\sin(\theta), \tag{3.24}$$

and the characteristic function of $(x, y)$ is $\varphi(t_1, t_2)$, then the characteristic function of $(r, \theta)$ is

$$\tilde{\varphi}(\rho, \Phi) = \int_0^{\infty} \int_0^{2\pi} e^{i\rho r\cos(\theta-\Phi)} f(r, \theta)\, \mathrm{d}\theta\, \mathrm{d}r, \tag{3.25}$$

where $f(r, \theta)$ is the joint distribution function of $(r, \theta)$. Conversely, the joint distribution of $(r, \theta)$ can be derived from $\tilde{\varphi}(\rho, \Phi)$ as

$$f(r, \theta) = \frac{1}{4\pi^2} r \int_0^{\infty} \int_0^{2\pi} e^{-i\rho r\cos(\theta-\Phi)} \tilde{\varphi}(\rho, \Phi)\rho\, \mathrm{d}\Phi\, \mathrm{d}\rho. \tag{3.26}$$

Before analyzing the general Von Mises random vectors, we first consider a special case of $\kappa = 0$, i.e., $\tilde{\theta}_n$ follows the uniform distribution within $[-\pi, \pi)$. The analysis for $\kappa = 0$ is then generalized to the case of $\kappa > 0$. Defining

$$R = |H_1|, \quad \Theta = \arg(H_1), \tag{3.27}$$

it is possible to rewrite $H_1$ in polar coordinates as

$$H_1 = \sum_{n=1}^{N} \cos(\tilde{\theta}_n) + j \sum_{n=1}^{N} \sin(\tilde{\theta}_n) = R\cos(\Theta) + jR\sin(\Theta). \tag{3.28}$$

Then, the characteristic function of $(1, \tilde{\theta}_n)$ can be given as

$$\begin{aligned} \tilde{\varphi}_n(\rho, \Phi) &= \int_0^{\infty} \int_{-\pi}^{\pi} e^{i\rho r\cos(\tilde{\theta}_n-\Phi)} f_{\tilde{\theta}_n}(\tilde{\theta}_n)\delta(r-1)\, \mathrm{d}\tilde{\theta}_n\, \mathrm{d}r \\ &= J_0(\rho), \end{aligned} \tag{3.29}$$

where $f_{\tilde{\theta}_n}(\tilde{\theta}_n)$ is the PDF of $\tilde{\theta}_n$ defined in (3.6). Due to independence, we have the characteristic function of $(R, \Theta)$ as

$$\tilde{\varphi}^*(\rho, \Phi) = \left(J_0(\rho)\right)^N . \tag{3.30}$$

Taking the inversion formula, the joint distribution of $(R, \Theta)$ can be calculated to be

$$\begin{aligned} f_{R,\Theta}(r, \theta) &= \frac{1}{4\pi^2} r \int_0^\infty \int_0^{2\pi} e^{-i\rho r \cos(\theta - \Phi)} \left(J_0(\rho)\right)^n \rho \, \mathrm{d}\Phi \, \mathrm{d}\rho \\ &= \frac{1}{2\pi} r \int_0^\infty J_0(\rho r) \left(J_0(\rho)\right)^n \rho \, \mathrm{d}\rho \\ &= \frac{1}{2\pi} r \psi(r^2) \end{aligned} \tag{3.31}$$

where

$$\psi(r^2) = \int_0^\infty J_0(\rho r) \left(J_0(\rho)\right)^N \rho \, \mathrm{d}\rho \tag{3.32}$$

Integrating over $\Theta$, we have the distribution of $R$ as

$$f_R(r) = r\psi(r^2). \tag{3.33}$$

Denoting $R\cos(\Theta)$ and $R\sin(\Theta)$ as $A$ and $B$ respectively, and using (3.31), the joint distribution of $A$ and $B$ can be given as

$$f_{A,B}(a, b) = \frac{1}{2\pi} \psi(a^2 + b^2). \tag{3.34}$$

These result will be used for determining the distribution of $|H_1|$ for $\kappa > 0$.

If $\tilde{\theta}_n$, $n \in \{1, ..., N\}$, follows an i.i.d. Von Mises distribution with zero mean and

concentration parameter $\kappa$, then the joint distribution of $(A, B)$ can be written as

$$\begin{aligned} f_{A,B}(a,b;\kappa) &= \int_{\tilde{\theta}_1 \in S_1} \cdots \int_{\tilde{\theta}_n \in S_n} \prod_{n=1}^{N} f_{\tilde{\theta}_n}(\tilde{\theta}_n)\, \mathrm{d}\tilde{\theta}_n \cdots \mathrm{d}\tilde{\theta}_1 \\ &= \int_{\tilde{\theta}_1 \in S_1} \cdots \int_{\tilde{\theta}_n \in S_n} \left(\frac{1}{2\pi}\right)^N \frac{1}{I_0(\kappa)^N} e^{\kappa \sum_{n=1}^{N} \cos(\tilde{\theta}_n)}\, \mathrm{d}\tilde{\theta}_n \cdots \mathrm{d}\tilde{\theta}_1. \end{aligned} \tag{3.35}$$

The integral is taken over the values of $\tilde{\theta}_1, ..., \tilde{\theta}_n$ that satisfy

$$a = \sum_{n=1}^{N} \cos(\tilde{\theta}_n), \quad b = \sum_{n=1}^{N} \sin(\tilde{\theta}_n). \tag{3.36}$$

Taking $\kappa$ in (3.35) as 0 and using the result in (3.34), we have

$$\int_{\tilde{\theta}_1 \in S_1} \cdots \int_{\tilde{\theta}_n \in S_n} \left(\frac{1}{2\pi}\right)^N \mathrm{d}\tilde{\theta}_n \cdots \mathrm{d}\tilde{\theta}_1 = \frac{1}{2\pi}\psi(a^2 + b^2). \tag{3.37}$$

Therefore, (3.35) can be simplified as

$$f_{A,B}(a,b;\kappa) = \frac{1}{2\pi I_0(\kappa)^N} e^{\kappa a} \psi(a^2 + b^2). \tag{3.38}$$

Since

$$A = R\cos(\Theta), \qquad B = R\sin(\Theta), \tag{3.39}$$

we can further arrive at the joint distribution of $(R, \Theta)$:

$$f_{R,\Theta}(r,\theta) = \frac{r}{2\pi I_0(\kappa)^N} e^{\kappa r \cos(\theta)} \psi(r^2). \tag{3.40}$$

Integrating over $\Theta$ gives the PDF of $R$ as

$$\begin{aligned} f_R(r) &= \frac{r}{I_0(\kappa)^N} I_0(\kappa r) \psi(r^2) \\ &= \frac{r}{I_0(\kappa)^N} I_0(\kappa r) \int_0^\infty J_0(\rho r) \left(J_0(\rho)\right)^N \rho\, \mathrm{d}\rho. \end{aligned} \tag{3.41}$$

Then, the CDF of $R$ is given by

$$F_R(r) = \int_0^r \int_0^\infty \frac{r}{I_0(\kappa)^N} I_0(\kappa r) J_0(\rho r) \left(J_0(\rho)\right)^N \rho \, \mathrm{d}\rho \, \mathrm{d}r. \tag{3.42}$$

Changing the order of integration and evaluating the inner integral, we arrive at

$$\begin{aligned} F_R(r) &= \frac{r\kappa I_1(\kappa r)}{I_0(\kappa)^N} \mathcal{I}_1(r) + \frac{r I_0(\kappa r)}{I_0(\kappa)^N} \mathcal{I}_2(r) \\ &= \frac{r\kappa I_1(\kappa r)}{I_0(\kappa)^N} \int_0^\infty \frac{J_0(\rho)^N J_0(\rho r)\rho}{\kappa^2 + \rho^2} \, \mathrm{d}\rho + \frac{r I_0(\kappa r)}{I_0(\kappa)^N} \int_0^\infty \frac{J_0(\rho)^N J_1(\rho r)\rho^2}{\kappa^2 + \rho^2} \, \mathrm{d}\rho. \end{aligned} \tag{3.43}$$

(3.43) gives the CDF of $R$, i.e., $|H_1|$, in an integral form, which can be evaluated numerically by software.

#### 3.2.2.2 Lower Tail Distribution Analysis

The PDF of $R$ in (3.41) can be analyzed asymptotically based on the Laplace's method. We denote by $\mathcal{I}(r)$ the integral in (3.41) and rewrite it as

$$\mathcal{I}(r) = \int_0^\infty \rho J_0(\rho r) \exp\left(N \ln\left(J_0(\rho)\right)\right) \, \mathrm{d}\rho. \tag{3.44}$$

Based on the theory of Laplace's method, the integral is dominated for large $N$ by the absolute maximum point of $\ln\left(J_0(\rho)\right)$. Denoting the absolute maximum point of $\ln\left(J_0(\rho)\right)$ by $\hat{\rho}$, we have that

$$-\frac{J_1(\hat{\rho})}{J_0(\hat{\rho})} = 0. \tag{3.45}$$

Therefore, the local maxima of $\ln\left(J_0(\rho)\right)$ are the zero points of $J_1(\rho)$. When $\hat{\rho} = 0$, $\ln\left(J_0(\rho)\right)$ reaches its global maximum. Furthermore, $\rho J_0(\rho r)$ and $\ln\left(J_0(\rho)\right)$ can be

approximated by the first terms of their Taylor series as

$$\rho J_0(\rho r) = \rho + O\left(\rho^3\right), \qquad \rho \to 0, \tag{3.46a}$$

$$\ln\left(J_0(\rho)\right) = -\frac{\rho^2}{4} + O\left(\rho^4\right), \quad \rho \to 0. \tag{3.46b}$$

Taking (3.46a) and (3.46b) into (3.44) and evaluating the integral yields the approximation to $f_R(r)$ as

$$\tilde{f}_R(r) = \frac{2rI_0(\kappa r)}{NI_0(\kappa)^N}. \tag{3.47}$$

Then, the approximation to the CDF of $R$ is obtained as

$$\tilde{F}_R(r) = \frac{2rI_1(\kappa r)}{\kappa NI_0(\kappa)^N}. \tag{3.48}$$

It should be noted that the CDF expression of $R$ in (3.43) can also be analyzed by using Laplace's method. Following the same procedure, we get the approximations to $\mathcal{I}_1(r)$ and $\mathcal{I}_2(r)$ as

$$\tilde{\mathcal{I}}_1(r) = \frac{2}{\kappa^2 N}, \quad \tilde{\mathcal{I}}_2(r) = \frac{4r}{\kappa^2 N^2}. \tag{3.49}$$

Taking (3.49) into (3.43), we get the approximation to $F_R(r)$ as

$$\hat{F}_R(r) = \frac{2rI_1(\kappa r)}{\kappa NI_0(\kappa)^N} + \frac{4r^2 I_0(\kappa r)}{\kappa^2 N^2 I_0(\kappa)^N}. \tag{3.50}$$

**Remark 1.** *When $r \in (0, N^\epsilon)$ for $0 < \epsilon < 1$ and $N$ is large, we have*

$$\begin{aligned}\hat{F}_R(r) &= \tilde{F}_R(r)\left(1 + \frac{2rI_0(\kappa r)}{\kappa NI_1(\kappa r)}\right) \\ &= \tilde{F}_R(r)\left(1 + O\left(\frac{1}{N^{1-\epsilon}}\right)\right), \; N \to \infty.\end{aligned} \tag{3.51}$$

*Therefore, for large $N$, $\hat{F}_R(r)$ and $\tilde{F}_R(r)$ give the same approximation to the probability of $R$ when $R \in (0, N^\epsilon)$.*

**Remark 2.** *If $\kappa = 0$, (3.47) becomes $\tilde{f}_R(r) = 2r/N$. Integrating over $r$, we have the asymptotic approximation to the lower tail probability of $R$ for $\kappa = 0$: $\tilde{F}_R(r) = r^2/N$.*

#### 3.2.2.3 Approximation Error Analysis

We analyze the error of the proposed approximation and prove that $\tilde{f}_R(r)$ and $\tilde{F}_R(r)$ given in (3.47) and (3.48) are asymptotically equivalent in $N$ for the lower tail of the distribution of $R$. The approximation errors arise from the higher order terms of the Taylor series of $\rho J_0(\rho r)$ and $\ln(J_0(\rho))$:

$$\rho J_0(\rho r) = \rho + A(\rho), \quad \ln(J_0(\rho)) = -\frac{\rho^2}{4} + B(\rho), \tag{3.52}$$

where

$$A(\rho) = \rho J_0(\rho r) - \rho = \sum_{k=1}^{\infty} a_k r^{2k} \rho^{2k+1}, \tag{3.53a}$$

$$B(\rho) = \ln(J_0(\rho)) + \frac{\rho^2}{4} = \sum_{j=2}^{\infty} b_j \rho^{2j}, \tag{3.53b}$$

where $k \geq 1$ and $j \geq 2$ are non-negative integers; $a_k$ and $b_j$ are coefficients of the series expansion. Hence, $\mathcal{I}(r)$ can be rewritten as

$$\mathcal{I}(r) = \int_0^{\infty} (\rho + A(\rho)) \exp\left(-\frac{N\rho^2}{4}\right) \exp(N \times B(\rho)) \, \mathrm{d}\rho. \tag{3.54}$$

The exponential factor $\exp(N \times B(\rho))$ can be further expanded as

$$\exp(N \times B(\rho)) = 1 + C(\rho), \tag{3.55}$$

where

$$C(\rho) = \sum_{i=1}^{\infty} \frac{1}{i!} (N \times B(\rho))^i = \sum_{i=1}^{\infty} \frac{1}{i!} \left(N \sum_{j=2}^{\infty} b_j \rho^{2j}\right)^i, \tag{3.56}$$

where $i \geq 1$ is a non-negative integer. Therefore, $\mathcal{I}(r)$ can be transformed as

$$\begin{aligned}\mathcal{I}(r) &= \int_0^\infty \exp\left(-\frac{N\rho^2}{4}\right)(\rho + A(\rho))\,(1 + C(\rho))\,\mathrm{d}\rho \\ &= \mathcal{I}_a(r) + \mathcal{I}_b(r) + \mathcal{I}_c(r) + \mathcal{I}_d(r),\end{aligned} \tag{3.57}$$

where

$$\begin{aligned}\mathcal{I}_a(r) &= \int_0^\infty \rho \exp\left(-\frac{N\rho^2}{4}\right)\mathrm{d}\rho, \\ \mathcal{I}_b(r) &= \int_0^\infty \rho C(\rho) \exp\left(-\frac{N\rho^2}{4}\right)\mathrm{d}\rho, \\ \mathcal{I}_c(r) &= \int_0^\infty A(\rho) \exp\left(-\frac{N\rho^2}{4}\right)\mathrm{d}\rho, \\ \mathcal{I}_d(r) &= \int_0^\infty A(\rho)C(\rho) \exp\left(-\frac{N\rho^2}{4}\right)\mathrm{d}\rho.\end{aligned} \tag{3.58}$$

First, we give the following two lemmas regarding asymptotic equivalence and the convergence of the four integrals in (3.58).

**Lemma 1.** *Define $f(x)$ as an integrable function of the variable $x > 0$ with asymptotic expansion*

$$f(x) \sim \sum_{m=0}^{\infty} \alpha_m x^m, \quad x \to 0^+, \tag{3.59}$$

*where $\alpha_m$ denotes the coefficient of the Taylor series of $f(x)$ at zero; $0^+$ means approaching $0$ from the right side of the number line. If there exists a positive number $q^*$ such that, for any $q > q^*$, the integral $\mathcal{J} = \int_0^\infty f(x)e^{-qx^2}\,\mathrm{d}x$ converges, then $\mathcal{J}$ has the asymptotic behavior*

$$\mathcal{J} = \int_0^\infty f(x)e^{-qx^2}\,\mathrm{d}x \sim \sum_{m=0}^{\infty} \frac{\alpha_m \Gamma((1+m)/2)}{2q^{(1+m)/2}}, \quad q \to \infty, \tag{3.60}$$

*where $\Gamma(\cdot)$ denotes the gamma function.*

*Proof.* Similar to the proof of [65, Lemma 1.2]. □

**Lemma 2.** *There exists a positive number $N^*$ such that, any $N > N^*$, the four integrals $\mathcal{I}_a$, $\mathcal{I}_b$, $\mathcal{I}_c$ and $\mathcal{I}_d$ all converge.*

*Proof.* See Appendix 3.6.1. □

Next, we analyze the four equations in (3.58) as follows.

- We evaluate $\mathcal{I}_a(r) = 2/N$, which gives (3.47).

- Using the multinomial theorem and Lemma 1, we have

$$\mathcal{I}_b(r) \sim \sum_{i\geq 1}\sum_{j\geq 2}\sum_{u\geq 0} d_{i,j,u}^{(b)} \frac{\Gamma\left(ji+u+1\right)}{N^{(j-1)i+u+1}}, \quad N\to\infty, \tag{3.61}$$

  where the non-negative integer $u$ comes from the expansion of the power of the multinomial; $d_{i,j,u}^{(b)}$ is the coefficient of each term. Therefore, we can find that $\mathcal{I}_b(r) = O\left(\frac{1}{N^2}\right),\ N\to\infty$.

- The asymptotic expansion of $\mathcal{I}_c(r)$ is given by

$$\mathcal{I}_c(r) \sim \sum_{k\geq 1} d_k^{(c)} \frac{r^{2k}\Gamma\left(k+1\right)}{N^{k+1}}, \quad N\to\infty. \tag{3.62}$$

  $d_k^{(c)}$ is the coefficient of each team. For $r\in(0, N^\alpha)$ and $0<\alpha<\frac{1}{2}$,

$$\mathcal{I}_c(r) < \sum_{k\geq 1} \frac{d_k^{(c)}\Gamma(k+1)}{N^{k(1-2\alpha)+1}}, \qquad N\to\infty. \tag{3.63}$$

  Therefore, $\mathcal{I}_c(r) = O\left(1/N^{2-2\alpha}\right),\ N\to\infty$.

- Similarly, the asymptotic expansion of $\mathcal{I}_d(r)$ is

$$\mathcal{I}_d(r) \sim \sum_{i\geq 1}\sum_{j\geq 2}\sum_{u\geq 0}\sum_{k\geq 1} d_{i,j,u,k}^{(d)} \frac{r^{2k}\Gamma\left(ji+u+k+1\right)}{N^{(j-1)i+u+k+1}}, N\to\infty. \tag{3.64}$$

$d_{i,j,u,k}^{(d)}$ is the coefficient of each term. For $r \in (0, N^{\alpha})$ and $0 < \alpha < \frac{1}{2}$, $\mathcal{I}_d(r) = O\left(1/N^{3-2\alpha}\right)$, $N \to \infty$.

Therefore, we obtain that, if $r \in (0, N^{\alpha})$ with $0 < \alpha < \frac{1}{2}$,

$$\mathcal{I}(r) = \frac{2}{N} + O\left(\frac{1}{N^{2-2\alpha}}\right), \quad N \to \infty. \tag{3.65}$$

This result shows that (3.48) gives an asymptotic approximation to the lower tail of the distribution of $R$, which is particularly important for the outage probability of the proposed system.

#### 3.2.2.4 Outage Probability and Diversity Order

The outage probability is defined as the probability that the received SNR given by (3.16) falls below a threshold SNR $\bar{\gamma}$. The approximate outage probability as a function of $\gamma_t$ is obtained as

$$\begin{aligned} P_1(\bar{\gamma}) &= \tilde{F}_R\left(\sqrt{\frac{\overline{\gamma}}{\beta_1 \gamma_t}}\right) \\ &= \begin{cases} \dfrac{2\sqrt{\bar{\gamma}}\, I_1\left(\kappa\sqrt{\frac{\bar{\gamma}}{\beta_1\gamma_t}}\right)}{\sqrt{\beta_1\gamma_t}\kappa N I_0(\kappa)^N}, & \text{If } \kappa > 0, \gamma_t > \dfrac{\bar{\gamma}}{\beta_1 N^{2\alpha}} \\ \dfrac{\bar{\gamma}}{\beta_1 \gamma_t N}, & \text{If } \kappa = 0, \gamma_t > \dfrac{\bar{\gamma}}{\beta_1 N^{2\alpha}}. \end{cases} \end{aligned} \tag{3.66}$$

**Remark 3.** *For $\kappa > 0$, the outage probability is proportional to $\exp\left[-N \ln\left(I_0(\kappa)\right)\right]/N$. The exponential decay rate is $\ln\left(I_0(\kappa)\right)$, which increases with $\kappa$.*

**Remark 4.** *For $\kappa > 0$, it can be proved that (3.66) is a decreasing function of $\kappa$ by calculating the derivative of (3.66) with respect to $\kappa$. Thus, increasing the phase adjustment accuracy, i.e., $\kappa$, will lower the outage probability.*

Based on [66], the diversity order is

$$d_1 = \lim_{\gamma_t \to \infty} -\frac{\log P_1(\bar{\gamma})}{\log \gamma_t} = 1. \tag{3.67}$$

**Remark 5.** *The diversity order of the system is one, which is due to the fact that the system model does not have $N$ independent fading channels. The proposed system model corresponds to the scenario without multipath components, e.g., RIS on UAV.*

## 3.3 Analysis of Fading Scenario

In this section, we study the outage probability and diversity order of a RIS-assisted communication system over Rayleigh fading channels. The case of perfect phase alignment is discussed first, which can be regarded as an ideal benchmark that cannot be achieved in practice. Then, the case of 1-bit phase adjustment is investigated to figure out the impact of phase quantization errors on communication performance.

### 3.3.1 Perfect Phase Alignment

The outage probability is characterized by using a moment-matching method based on gamma distribution, followed by a brief error analysis showing the high approximation accuracy numerically. We also study the diversity order of the system through an asymptotic analysis.

#### 3.3.1.1 Outage Probability Analysis

Let $W_n = \left|\bar{h}_n\right| |\bar{g}_n|$. $W_n$ follows a double Rayleigh distribution, and the PDF of $W_n$ is given by [67]

$$f_{W_n}(x) = 4xK_0(2x). \tag{3.68}$$

Unfortunately, continuing with this form of the calculation will prove fruitless; hence, we adopt a moment-matching approximation method for the PDF of $W_n$ by using the gamma distribution. In existing works, the gamma distribution is often applied to fit some sophisticated distributions due to its advantages in terms of convenient parameter calculations and high accuracy. The gamma distribution has the freedom of adjusting two parameters, with the concise forms of the mean and variance, resulting in tractable parameter computations. Since the mean and variance of $W_n$ are

$$\mathbb{E}[W_n] = \frac{\pi}{4}, \quad \mathrm{Var}[W_n] = \frac{16-\pi^2}{16}, \tag{3.69}$$

we can use the moment-matching method to approximate the distribution of $W_n$ to a gamma distribution as

$$f_{\mathrm{app}}(x) = \frac{x^{k-1}e^{-\frac{x}{\omega}}}{\omega^k \Gamma(k)} \tag{3.70}$$

where

$$k = \frac{\pi^2}{16-\pi^2}, \quad \omega = \frac{16-\pi^2}{4\pi}. \tag{3.71}$$

Since $W_n$, $n \in \{1, ..., N\}$, are i.i.d., we can approximate the PDF and CDF of $H_2 = \sum_{n=1}^{N} \left|\bar{h}_n\right| |\bar{g}_n|$ as

$$f_{H_2}(x) \approx \frac{x^{Nk-1}e^{-\frac{x}{\omega}}}{\omega^{Nk}\Gamma(Nk)}, \tag{3.72a}$$

$$F_{H_2}(x) \approx \frac{1}{\Gamma(Nk)} \gamma\left(Nk, \frac{x}{\omega}\right). \tag{3.72b}$$

Hence, the outage probability of UE can be approximated as

$$P_2(\bar{\gamma}) \approx F_{H_2}\left(\sqrt{\frac{\bar{\gamma}}{\gamma_t \beta_2}}\right). \tag{3.73}$$

#### 3.3.1.2 Error Analysis

The above approximation arises from using the gamma distribution to approximate the double Rayleigh distribution. To explore the accuracy of the approximation, we compute the relative entropy of the true distribution and the approximation. The relative entropy of the exact distribution and the approximate (gamma) distribution in this case is defined as

$$D(f_{W_n}||f_{\text{app}}) = \int_0^\infty f_{W_n}(x) \log \frac{f_{W_n}(x)}{f_{\text{app}}(x)} \, \mathrm{d}x, \tag{3.74}$$

where $f_{W_n}(x)$ is defined in (3.68) and $f_{\text{app}}(x)$ is the gamma approximation of $f_{W_n}(x)$ with the parameters $k$ and $\omega$. Fig. 3.2 illustrates the relative entropy. For comparison, we also plot the relative entropy of Student's $t$-distribution with $N$ degrees of freedom and its normal approximation ("ref" in the legend). As $N \to \infty$, Student's $t$-distribution approaches the normal distribution [68], but it is very accurate even for $N > 10$. As can be seen from the figure, $D(f_{W_n}||f_{\text{app}})$ is smaller than the the relative entropy of Student's $t$-distribution and its normal approximation for reasonably large values of $N$. This brief analysis suggests that the accuracy of the approximation resulting from the rounding operation and the use of the gamma distribution is quite high.

#### 3.3.1.3 Diversity Order

We analyze $F_{H_2}(t)$ when $t$ approaches zero. The PDF of $W_n$ can be expanded about zero to yield $f_{W_n}(x) = -4x \ln x + O(x)$. Performing an $N$-fold convolution and taking the leading term every time, we obtain the leading order of the PDF of $H_2$:

$$f_{H_2}(x) = \frac{2^{2N} x^{2N-1}}{(2N-1)!} \left( \ln \frac{1}{x} \right)^N + o\left( x^{2N-1} (\ln x)^N \right). \tag{3.75}$$

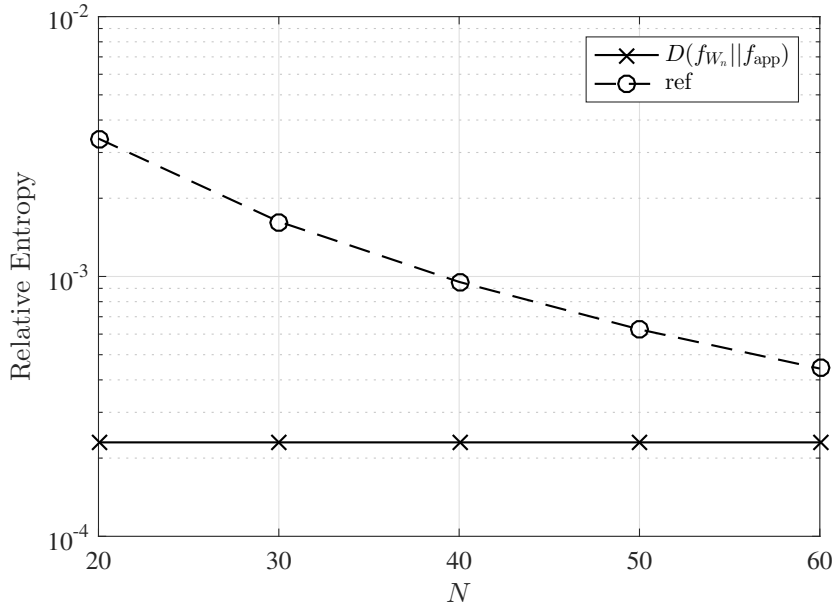



Figure 3.2: Relative entropy $D(f_{W_n}||f_{\text{app}})$. The "ref" curves corresponds to the relative entropy of Student's $t$-distribution with $N$ degrees of freedom and its normal approximation.

Eq. (3.75) can be proved by induction. Hence, the CDF of $H_2$, to leading order, can be written as

$$\begin{aligned} F_{H_2}(t) &= \int_0^t f_{H_2}(x)\,\mathrm{d}x \\ &= \frac{2^{2N-1}t^{2N}\left(\ln\frac{1}{t}\right)^N}{N(2N-1)!} + o(t^{2N}(\ln t)^N). \end{aligned} \tag{3.76}$$

Based on the definition of diversity order in (3.19), we find that the diversity order under perfect phase alignment is

$$d_2 = N. \tag{3.77}$$

This is entirely expected, since the assumption of the model we consider is that all $N$ spatial channels are independent.

### 3.3.2 One-bit Phase Adjustment

We now treat the case where each RIS element is able to adjust the phase of the incident wave by $\pi$ only (or leave it unaltered). Similar to the case of perfect phase adjustment, an approximate outage probability expression is presented first, followed by a numerical error analysis and the calculation of the diversity order.

#### 3.3.2.1 Outage Probability Analysis

$H_3$ can be rewritten as

$$\begin{aligned} H_3 &= \sum_{n=1}^{N} |h_n|\,|g_n|\, e^{j\bar{\theta}_n} \\ &= \sum_{n=1}^{N} |h_n|\,|g_n| \cos(\bar{\theta}_n) + j \sum_{n=1}^{N} |h_n|\,|g_n| \sin(\bar{\theta}_n) \\ &= \sum_{n=1}^{N} X_n + j \sum_{n=1}^{N} Y_n \\ &= X + jY. \end{aligned} \tag{3.78}$$

As noted earlier, $\bar{\theta}_n$ is uniformly distributed on the interval $[-\pi/2, \pi/2]$. As a result, the PDF of $\cos(\bar{\theta}_n)$ is

$$f_{\cos(\bar{\theta}_n)}(x) = \frac{2}{\pi\sqrt{1-x^2}}, \quad 0 \le x \le 1. \tag{3.79}$$

We can use (3.68) and (3.79) to obtain the PDF of $X_n$:

$$\begin{aligned} f_{X_n}(z) &= \int_0^1 \frac{1}{x} f_{\cos(\phi_n)}(x) f_{H_n}\left(\frac{z}{x}\right) \mathrm{d}x \\ &= 2\exp(-2z), \qquad z \ge 0. \end{aligned} \tag{3.80}$$

Similarly, the PDF of $\sin(\bar{\theta_n})$ is

$$f_{\sin(\bar{\theta}_n)}(x) = \frac{1}{\pi\sqrt{1-x^2}}, \quad -1 \leq x \leq 1, \tag{3.81}$$

and the PDF of $Y_n$ can be calculated to be

$$f_{Y_n}(z) = \exp(-2\,|z|), \quad z \in \mathbb{R}. \tag{3.82}$$

Since $X_n$ and $Y_n$ are i.i.d. for all $n$, the PDF of $X$ and $Y$ can be calculated to be [69, ch. 7] [70, ch. 2]

$$f_X(x) = \frac{2^N \exp(-2x) x^{N-1}}{(N-1)!}, \quad x \geq 0 \tag{3.83}$$

and

$$f_Y(y) = \frac{\exp\left(-2\,|y|\right)}{2^{N-1}(N-1)!} \sum_{m=0}^{N-1} \frac{2^{N-1-2m}(N-1+m)!|y|^{N-1-m}}{m!(N-1-m)!}, \quad y \in \mathbb{R}. \tag{3.84}$$

Since $|H_3|^2 = X^2 + Y^2$, we can state an approximation[1] for the CDF of $|H_3|^2$ as

$$\begin{aligned} F_{|H_3|^2}(t) &= \mathbb{P}\left(X^2 + Y^2 < t\right) \\ &= \int_{-\sqrt{t}}^{\sqrt{t}} F_X\left(\sqrt{t-y^2}\right) f_Y(y)\,\mathrm{d}y \\ &= \int_{-\sqrt{t}}^{\sqrt{t}} \frac{\gamma\left(N, 2\sqrt{t-y^2}\right)}{\Gamma(N)} f_Y(y)\,\mathrm{d}y. \end{aligned} \tag{3.85}$$

Eq.(3.85) can be evaluated numerically in efficient ways, and the outage probability of UE can be given as

$$P_3(\bar{\gamma}) = F_{|H_3|^2}\left(\frac{\bar{\gamma}}{\gamma_t \beta_2}\right). \tag{3.86}$$

[1]The approximation is due to the assumption that $X$ and $Y$ are independent.

#### 3.3.2.2 Error Analysis

Note that the above approximation does not arise from the use of a moment-matched gamma distribution, but rather from the assumption that $X$ and $Y$ are independent. It can be proved that $X_n$ and $Y_n$ are uncorrelated. Indeed, when the PDF of $\bar{\theta}_n$ is even, we have

$$\mathrm{E}[\cos(\bar{\theta}_n)\sin(\bar{\theta}_n)] = \frac{1}{2}\mathrm{E}[\sin(2\bar{\theta}_n)] = 0 = \mathrm{E}[\cos(\bar{\theta}_n)]\mathrm{E}[\sin(\bar{\theta}_n)], \tag{3.87}$$

since $\mathrm{E}[\sin(\bar{\theta}_n)] = 0$. The relative entropy of the exact distribution and the approximate distribution is just the mutual information between the random variables $X_n$ and $Y_n$:

$$I(X_n; Y_n) = h(X_n) + h(Y_n) - h(X_n, Y_n), \tag{3.88}$$

where $h(\cdot)$ represents the differential entropy here. The joint PDF of $(X_n, Y_n)$ can be obtained by performing a transformation of variables:

$$\begin{aligned} f_{X_n,Y_n}(x,y) &= \det(J(x,y)) f_{W_n}(a(x,y)) f_{\bar{\theta}_n}(\bar{\theta}_n(x,y)) \\ &= \frac{4}{\pi} K_0(2\sqrt{x^2+y^2}), \end{aligned} \tag{3.89}$$

where $J(x,y) = \partial(a, \bar{\theta}_n)/\partial(x,y)$ is the Jacobian matrix for the transformation $\{x = a\cos(\bar{\theta}_n),\ y = a\sin(\bar{\theta}_n)\}$.

By computing numerically, we have that $I(X_n; Y_n) \approx 0.04441$. The small value indicates the dependence between $X_n$ and $Y_n$ is small. While this analysis applies for a single reflecting path, it is worth noting that the dependence between $X = \sum_n X_n$ and $Y = \sum_n Y_n$ will decrease as the number of elements grows. Indeed, as the number of terms in each sum increases, central limit effects take hold and $X$ and $Y$ become approximately independent since the two random variables are (nearly) Gaussian and uncorrelated.

#### 3.3.2.3 Diversity Order

In a similar manner as was done for the case of perfect phase alignment, we start by analyzing $F_{|H_3|^2}(t)$ when $t$ approaches zero. Note that in this case the PDF of $X$ has the simple (exact) form given by (3.83). Computing the PDF of $X^2$, expanding about zero, and retaining the leading order, we can obtain

$$f_{X^2}(x) = \frac{2^{N-1} x^{\frac{N-2}{2}}}{(N-1)!} + o\left(x^{\frac{N-2}{2}}\right). \tag{3.90}$$

Similarly, we can write the leading order term of the PDF of $Y^2$ in the succinct form

$$f_{Y^2}(y) = \frac{(2N-2)!}{2^{2N-2}(\Gamma(N))^2\sqrt{y}} + O(1). \tag{3.91}$$

Invoking the assumption that the real and imaginary parts of the channel gain are independent, we arrive at the following approximation for the leading order of the CDF of $|G|^2$:

$$\begin{aligned} F_{|H_3|^2}(t) &\approx \int_0^t \int_0^{t-y} f_{Y^2}(y) f_{X^2}(x)\, \mathrm{d}x\, \mathrm{d}y \\ &\approx \frac{\sqrt{\pi}(2N-2)!\Gamma\left(\frac{N}{2}+1\right)}{2^{N-2}N(\Gamma(N))^3\Gamma\left(\frac{N+3}{2}\right)} t^{\frac{N+1}{2}}. \end{aligned} \tag{3.92}$$

The inner integral above can be evaluated directly, and the outer integral results from [71, eq. 3.191.1]. By using (3.92), along with the definitions of the outage probability and diversity order given in (3.18) and (3.19) respectively, we can derive the diversity order as

$$d_3 = \frac{N+1}{2}. \tag{3.93}$$

## 3.4 Numerical Results

In this section, the outage probability and diversity order of the system are analyzed, and the proposed analytical results are evaluated via Monte Carlo (MC) simulations. Unless otherwise stated, the distances of the TX-RIS and RIS-UE channels are set as $d_h = 10\,\mathrm{m}$ and $d_g = 15\,\mathrm{m}$. The path loss per unit distance of the LoS and Rayleigh fading scenarios are given as $\Lambda_1 = \Lambda_2 = -20\,\mathrm{dB}$. The path loss exponent of the fading scenario is $\chi = 3$. The outage SNR threshold is $\bar{\gamma} = 0\,\mathrm{dB}$.

### 3.4.1 Analysis of LoS Scenario

The outage probability versus the transmit SNR $\gamma_t$ for different $\kappa$ is plotted in Fig. 3.3 for $N = 8$. As $\kappa$ increases, the distribution becomes more concentrated about zero, which means higher phase adjustment accuracy in practical systems. As expected, increasing the phase adjustment accuracy can significantly reduce the required transmit SNR for given outage probability. For example, when the outage probability is $10^{-3}$, $\gamma_t$ is 60 dB and 75 dB for $\kappa = 2$ and $\kappa = 1$, respectively. The case of $\kappa = 0$ is given as a benchmark, which refers to a RIS-assisted communication system that only reflects signals but does not perform any phase adjustment. We can observe that imperfect phase adjustment can bring significant performance gains compared with simple signal reflection. It also can be seen that the asymptotic expression given in (3.48) is very accurate in the large transmit SNR regime and the diversity order of the system is one, which confirms our analysis. It is worth noting that the proposed outage probability is valid for $\gamma_t > \frac{\bar{\gamma}}{\beta N^{2\alpha}}$, $0 < \alpha < \frac{1}{2}$. Under the current simulation setting, the valid SNR range for $N = 8$ is $\gamma_t > 58\,\mathrm{dB}$. However, when $\kappa = 4$ and $\gamma_t > 58\,\mathrm{dB}$, the outage probability is already lower than $10^{-5}$. Therefore, the analysis does not match well with the simulations for $\kappa = 4$.

Fig. 3.4 illustrates the outage probability as a function of the transmit SNR $\gamma_t$

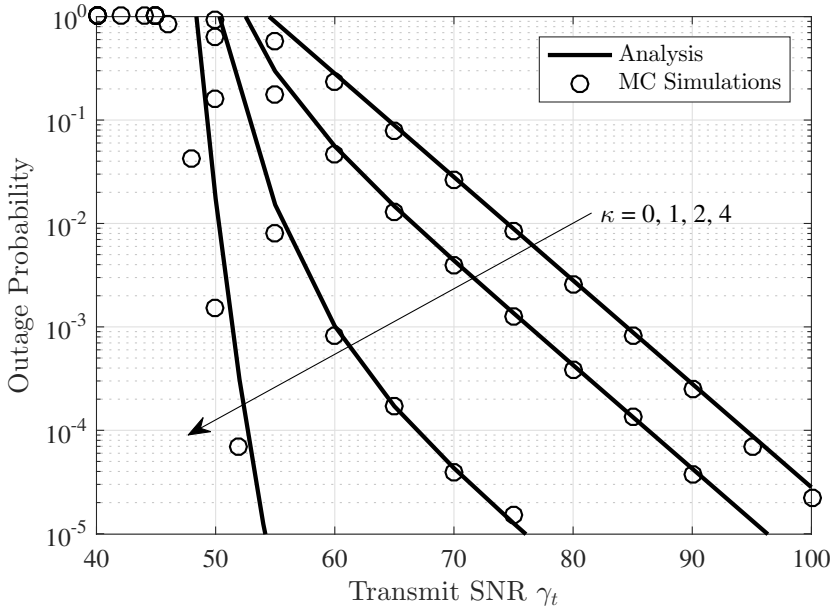



Figure 3.3: Outage probability versus transmit SNR $\gamma_t$ for different $\kappa$ in LoS scenario.

for different SNR thresholds $\bar{\gamma}$. We have set $\kappa = 1$ and $N = 8$. The SNR thresholds considered are $\bar{\gamma} \in \{0\,\text{dB}, 10\,\text{dB}, 20\,\text{dB}, 30\,\text{dB}\}$. Notably, altering the SNR threshold $\bar{\gamma}$ corresponds to shifting the outage probability curve along the horizontal axis. To maintain the same outage probability, we observe that increasing $\bar{\gamma}$ by 10 dB requires a 10 dB increment in the transmit SNR $\gamma_t$. For example, when the outage probability is $10^{-3}$, $\gamma_t$ is 75 dB and 85 dB when $\bar{\gamma}$ is 0 dB and 10 dB, respectively.

Fig. 3.5 illustrates the outage probability against $\gamma_t$ for different numbers of RIS elements $N$ when $\kappa = 1$. Again, the theoretical analysis is in good agreement with the MC simulations at high transmit SNR regime. The valid SNR range for $N = 64$ is $\gamma_t > 49\,\text{dB}$, which cannot be shown in the figure. Therefore, the analysis does not approximate the simulations well for $N = 64$. For larger $N$, the outage probability will decay so quickly that the valid SNR range will start at a lower outage probability (smaller than $10^{-5}$) that cannot be shown in the figure. It can be observed that increasing the number of RIS elements can greatly improve system performance. For example, to achieve an outage probability lower than $10^{-4}$, the transmit SNR should be larger than 58 dB and 75 dB for $N = 32$ and $N = 16$, respectively.

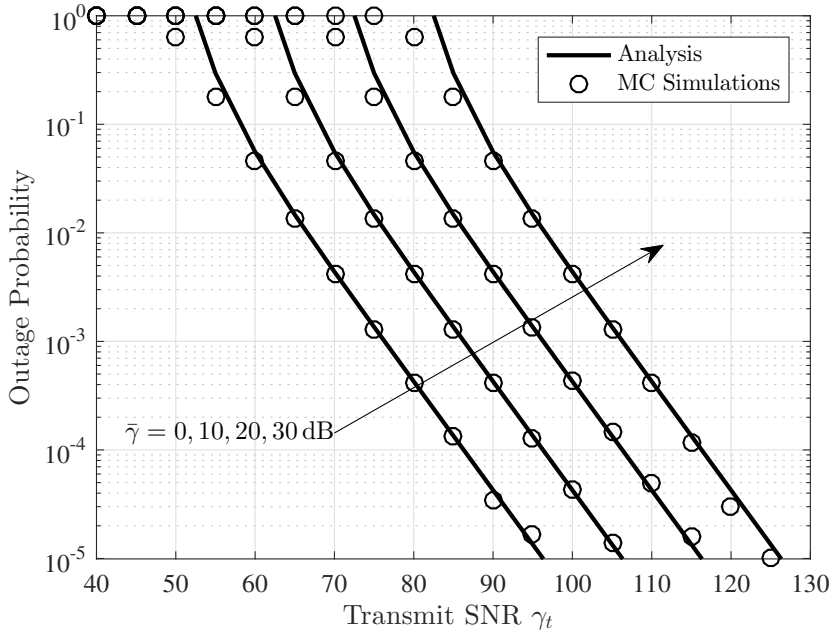



Figure 3.4: Outage probability versus transmit SNR $\gamma_t$ for different SNR threshold $\bar{\gamma}$ in LoS scenario.

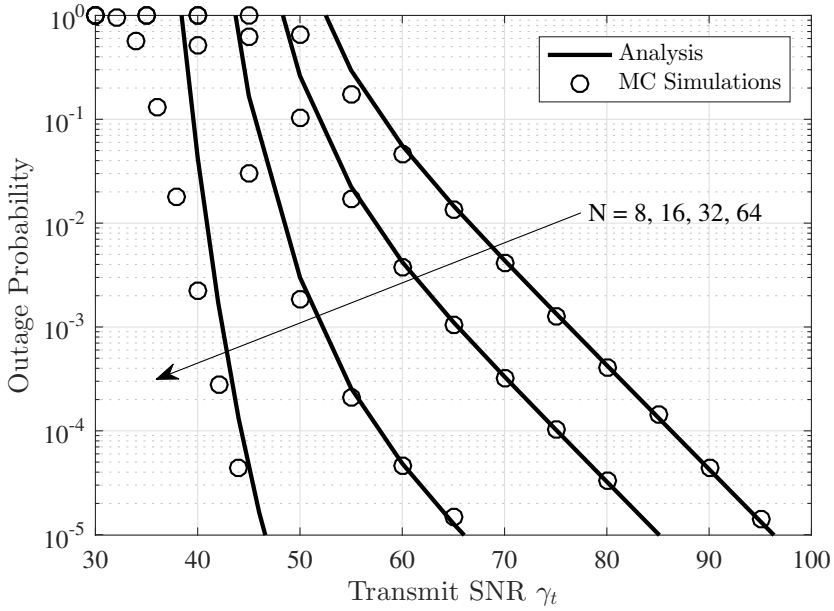



Figure 3.5: Outage probability versus transmit SNR $\gamma_t$ for different $N$ in LoS scenario.

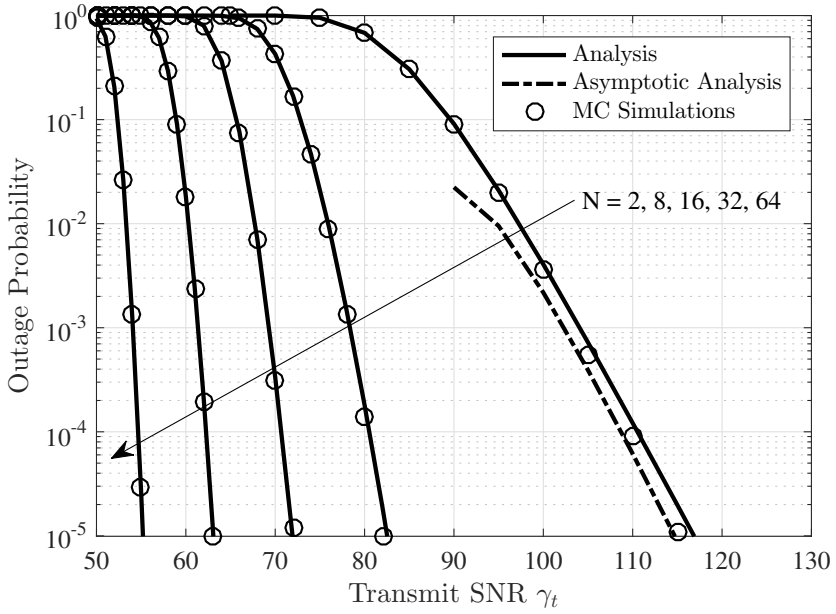



Figure 3.6: Outage probability versus transmit SNR $\gamma_t$ for different $N$ without phase errors in Rayleigh fading scenario.

### 3.4.2 Analysis of Fading Scenario

#### 3.4.2.1 Perfect Phase Alignment

The outage probability is plotted against the transmit SNR $\gamma_t$ when there are no phase errors in Fig. 3.6. In particular, the outage probability of the proposed approximation is compared with the MC simulations. We observe that the derived outage probability expression matches well with the simulation results. Fig. 3.6 also illustrates that with an increasing number of RIS elements, the outage probability decreases significantly for the same transmit SNR. For example, when $\gamma_t = 70\,\text{dB}$, the outage probability is 0.4 for $N = 8$ and $5 \times 10^{-4}$ for $N = 16$. To verify the diversity order of the system equals to the number of RIS elements, the asymptotic outage probability is also given for $N = 2$, and the asymptotic result is accurate in the large transmit SNR regime.

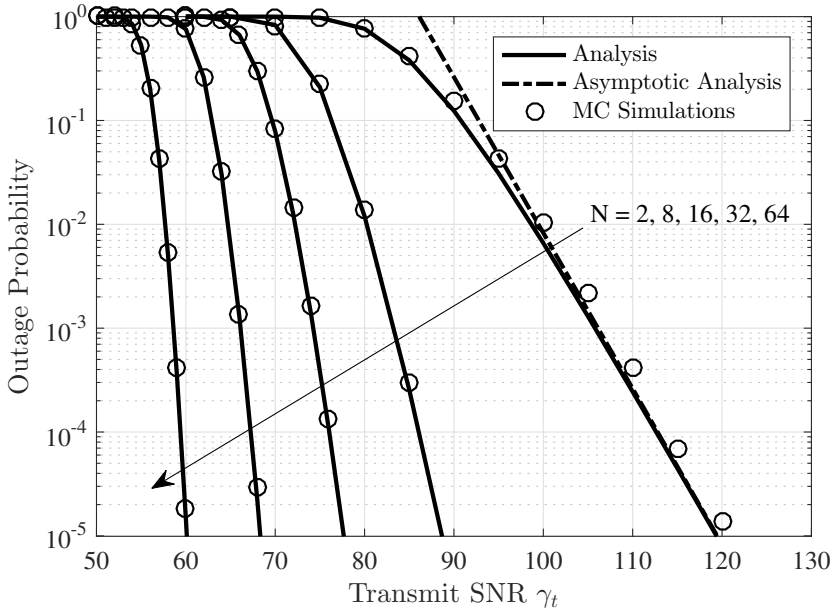



Figure 3.7: Outage probability versus transmit SNR $\gamma_t$ for different $N$ with one-bit phase adjustment in Rayleigh fading scenario.

#### 3.4.2.2 One-bit Phase Adjustment

Fig. 3.7 illustrates the outage probability under the condition of one-bit phase adjustment. Similar to the case without phase errors, our analysis is in good agreement with the simulations. Comparing the results in Figs. 3.6 and 3.7, it can be seen that phase errors lead to a performance loss with the gap being about 5 dB. For example, when $N = 8$, the transmit SNRs required to achieve an outage probability of $10^{-2}$ are 75 dB and 80 dB for perfect and imperfect phase alignment, respectively. The asymptotic outage probability is plotted for $N = 2$ in this example as well. This curve is included to illustrate that the approximate asymptotic analysis resulting from the independence assumption is reasonably accurate. Hence, we can be fairly confident that the diversity order is indeed $(N + 1)/2$ in this case. As a step further, Fig. 3.8 compares the outage probability of different phase adjustment schemes. The number of RIS elements varies in $N \in \{8, 32\}$. It turns out that two-bit phase adjustment can already achieve the outage performance very close to the ideal benchmark.

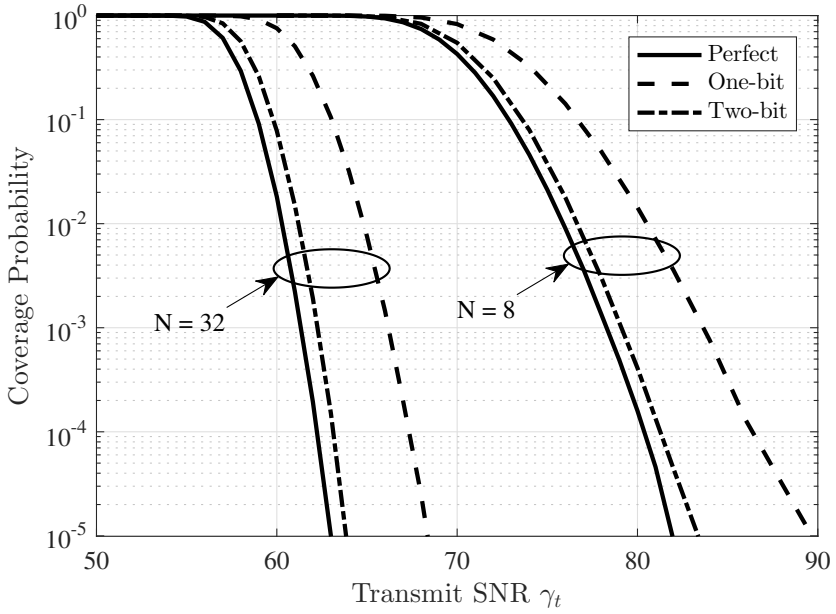



Figure 3.8: Outage probability versus transmit SNR $\gamma_t$ for different bits of phase adjustment in Rayleigh fading scenario.

## 3.5 Summary

In this chapter, we studied the performance of a RIS-assisted communication system with phase errors. Regarding the LoS propagation scenario, the path loss model was first introduced. Then, the outage probability and diversity order of the system over LoS channels with Von Mises phase errors were analyzed. This set-up could represent imperfect phase estimation in a scenario without multi-path propagation. It was shown that increasing the number of reflecting elements and improving the accuracy of phase adjustment can significantly improve the system performance. Also, we investigated the outage probability and diversity order of a RIS-assisted communication system over Rayleigh fading channels. The performance of perfect phase alignment and one-bit phase adjustment were compared. It was shown that one can expect a penalty of approximately 5 dB when a one-bit phase adjustment is made at each RIS element, and the two-bit phase adjustment scheme can lead to nearly optimal performance. Through a more accurate asymptotic analysis, we conjectured that the diversity order of a one-bit phase adjustment system is $(N + 1)/2$.

## 3.6 Appendices

### 3.6.1 Proof of the Lemma 2

We obtain $\mathcal{I}_a(r) = \frac{2}{N}$ and $\mathcal{I}_c(r) = \frac{2}{N}\left(\exp(-r^2/N) - 1\right)$ [72, Eq.11.4.29]. Also since $\mathcal{I}_a(r) + \mathcal{I}_b(r) + \mathcal{I}_c(r) + \mathcal{I}_d(r)$ corresponds to the PDF in (3.41), which also converges, we only need to prove $\mathcal{I}_b(r)$ converges. $\mathcal{I}_b(r)$ can be rewritten as

$$\begin{aligned}\mathcal{I}_b(r) &= \int_0^\infty \rho\left(\exp\left(N \times B(\rho)\right) - 1\right)\exp\left(-\frac{N\rho^2}{4}\right)\mathrm{d}\rho \\ &= \int_0^\infty \rho J_0(\rho)^N \,\mathrm{d}\rho - \frac{2}{N}.\end{aligned} \tag{3.94}$$

An upper bound of the Bessel function of the first kind was given in [73] as $|J_0(x)| \leq \min\{1, c\,|x|^{-1/3}\}$, where $c = 0.786$. Hence, an upper bound of the first term in (3.94) can be constructed as

$$\int_0^\infty \rho J_0(\rho)^N \,\mathrm{d}\rho < \int_0^a \rho J_0(\rho)^N \,\mathrm{d}\rho + \int_a^\infty c^N \frac{1}{\rho^{\frac{N}{3}-1}}\,\mathrm{d}\rho. \tag{3.95}$$

We can easily observe that $\mathcal{I}_b(r)$ converges for $N > 6$. Thus, we complete the proof.

# Chapter 4

# RIS-Assisted Communications over Correlated Channels

In Chapter 3, we analyze the performance of a RIS-assisted communication system with phase errors. Through analytical and numerical results, we show that the performance loss of about 5 dB in terms of the transmit signal-to-noise ratio (SNR) can appear if the one-bit phase adjustment scheme is applied. Moreover, if the two-bit phase adjustment is made at each element, we can obtain a performance close to the optimal performance. However, all the analysis in Chapter 3 assumes the independent Rayleigh fading channel model. Since all the RIS elements are sub-wavelength and closely spaced in a rectangular array, the independent fading channel model is not accurate in a practical RIS system[1]. The channel correlation effect in a RIS system was first pointed out in [76], where the authors proposed a correlated Rayleigh fading channel model in a RIS-assisted communication system. Following this pioneering work, the authors in [77] analyzed the outage probability of a RIS-aided communication system over correlated Rayleigh fading channels with a random phase shifting

[1]The small distance between adjacent elements will also lead to the mutual coupling effect, which is out of the scope of this thesis, and requires further investigation in the future. Furthermore, some works have been working on reducing the mutual coupling effect in RIS system [74, 75].

scheme. However, the random phase shifting scheme leads to poor performance since the RIS performs phase adjustments arbitrarily without knowledge of the channel state information (CSI). Furthermore, a correlated Rayleigh fading channel model can only capture the rich scattering propagation environment without a stable line-of-sight (LoS) link. The correlated Nakagami-$m$ fading channel model is a more general and accurate channel model for many propagation environments; however, it requires more investigation and is an open area of study.

To fill the research gap and investigate the impact of channel correlation on communication performance, we analyze the performance of a RIS-assisted communication system over correlated fading channels. Specifically, we derive the closed form expressions of the outage probability and average achievable rates of the system under two different channel models: the correlated Rayleigh fading model and the correlated Nakagami-$m$ fading model. The main contributions of this chapter are listed as follows:

- A correlated Rayleigh fading channel model and an exponential decay power correlation Nakagami-$m$ fading channel model are presented. Outage probability and upper bounds on the average achievable rates of the downlink transmission are derived for these two models.

- We reveal the channel hardening effect in the RIS-assisted communication system with correlated channels. Then, using the results of the channel hardening effect, approximate expressions of the average achievable rates are obtained.

- The upper bound and the approximation of the average achievable rates are both proved to be asymptotically equivalent. Moreover, it is demonstrated that the average achievable rate with correlated channels is asymptotically equivalent to that with uncorrelated channels for a large number of elements.

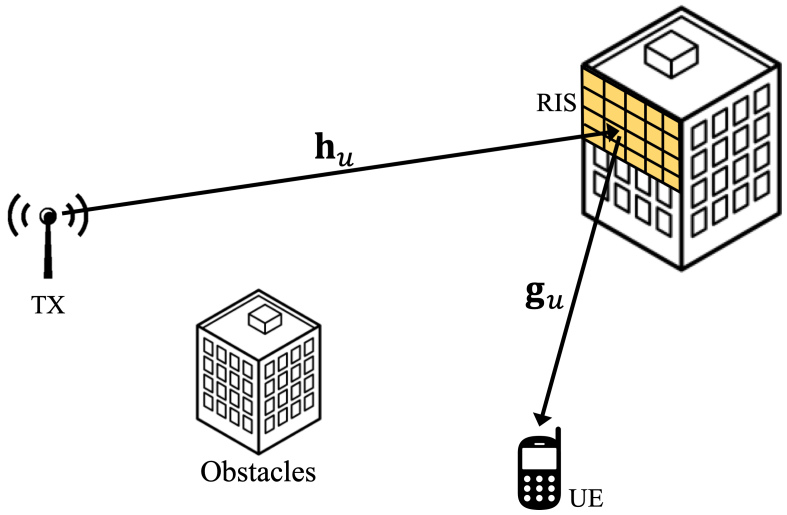



Figure 4.1: System model.

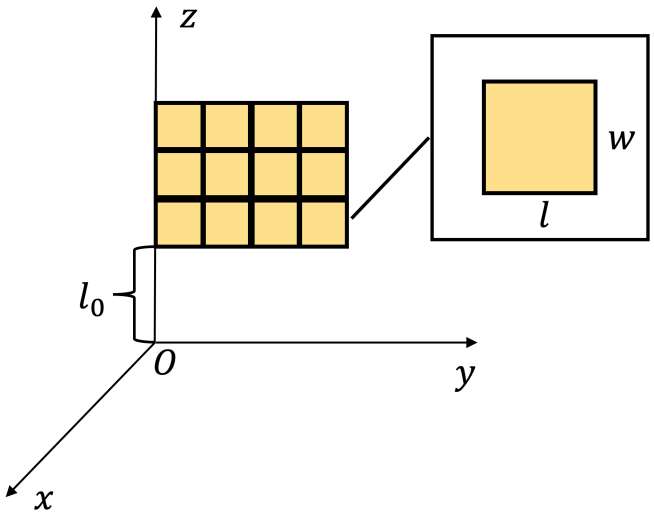



Figure 4.2: RIS structure.

## 4.1 System Framework and Performance Metrics

In this chapter, we consider a RIS-assisted communication network, where a single-antenna transmitter (TX) communicates with a single-antenna user equipment (UE). As shown in Fig. 4.1, it is assumed that obstacles block the direct link from TX to UE.

### 4.1.1 RIS Implementations

We consider a RIS with $N = N_h N_v$ elements placed in a planar rectangular array. As illustrated in Fig. 4.2, the RIS is on the $yOz$ plane with $N_h$ elements per row and $N_v$ elements per column. We assume each element is of size $S = l \times w$, where $l$ and $w$ are the horizontal and vertical lengths of each element. The RIS is equipped on a building of height $l_0$, and the coordinate of the $n$th element can be written as

$$\mathbf{a}_n = [0, y(n)l, z(n)w + l_0], \tag{4.1}$$

where

$$y(n) = \mathrm{mod}(n-1, N_h), \quad z(n) = \lfloor \frac{n-1}{N_h} \rfloor. \tag{4.2}$$

$y(n)$ and $z(n)$ are the indexes of the $n$th element on the $y$-axis and $z$-axis.

Each RIS element is able to adjust phase shift for the user. Denoting the phase shift imposed on the incident signal by the $n$th element as $\theta_n$, the reflecting coefficient matrix can be written as

$$\mathbf{\Theta} = \mathrm{diag}\left(e^{j\theta_1}, ..., e^{j\theta_N}\right). \tag{4.3}$$

The RIS is assumed to be passive with no energy dissipation.

### 4.1.2 Channel and Signal Models

In this subsection, we introduce the channel and signal models over the correlated Rayleigh and correlated Nakagami-$m$ fading channels subsequently. While the Rayleigh fading is a special case of the Nakagami-$m$ fading [78], we introduce the two models separately because they follow different correlation profiles. The correlated Rayleigh fading model follows the Clarke's model for 3D spaces [79]. It is assumed that the RIS is placed in an isotropic scattering environment without stable LoS links, and the

multipath components are uniformly distributed over the half-space in front of the RIS. In contrast, the correlated Nakagami-$m$ fading model follows the exponential decay power correlation model.

#### 4.1.2.1 Correlated Rayleigh Fading Channel Model

Let $\mathbf{h}_A = (h_{A,1}, ..., h_{A,N})^T \in \mathbb{C}^{N\times 1}$ and $\mathbf{g}_A = (g_{A,1}, ..., g_{A,N})^T \in \mathbb{C}^{N\times 1}$ denote the normalized small scale fading of the TX-RIS and RIS-UE channels, respectively. RIS operates in the far-field of TX and UE, thus the electromagnetic (EM) waves impinging on the RIS are plane waves with the wave vector [80]

$$\mathbf{v}(\varrho, \varphi) = \frac{2\pi}{\lambda} \left[\cos(\varrho)\cos(\varphi), \sin(\varrho)\cos(\varphi), \sin(\varphi)\right], \tag{4.4}$$

where $\varrho$ and $\varphi$ are the azimuth and elevation angles; $\lambda$ is the wavelength.

Due to multi-path propagation, the small scale fading $\mathbf{h}_A$ is a superposition of the independent array response of each multi-path component $\mathbf{c}_k$ as [26]

$$\mathbf{h}_A = \sum_{k=1}^{K} \mathbf{c}_k = \sum_{k=1}^{K} \frac{l_k}{\sqrt{K}} \hat{\mathbf{c}}_k, \tag{4.5}$$

where $l_k/\sqrt{K}$ is a complex random variable that stands for the attenuation and phase-rotation of the $k$th multi-path component and

$$\hat{\mathbf{c}}_k = \left[\exp\left(j\mathbf{v}\mathbf{a}_1^T\right), \exp\left(j\mathbf{v}\mathbf{a}_2^T\right), ..., \exp\left(j\mathbf{v}\mathbf{a}_N^T\right)\right]^T. \tag{4.6}$$

In non-LoS scenarios, $l_k$, $k \in \{1, 2, ..., K\}$, are i.i.d. random variables with zero mean and unit variance. In a rich scattering environment, there are an infinite number of multi-path components ($K \to \infty$). Hence, with the help of the central limit theorem [76], we have

$$\mathbf{h}_A \sim \mathcal{CN}\left(\mathbf{0}_N, \mathbf{R}_A\right), \tag{4.7}$$

where $\mathbf{R}_A$ is the covariance matrix of $\mathbf{h}_A$, defined as

$$\mathbf{R}_A = \mathbb{E}\left[\mathbf{h}_A \mathbf{h}_A^H\right] = \mathbb{E}\left[\sum_{k=1}^{K} \mathbf{c}_k \mathbf{c}_k^H\right] \tag{4.8}$$

Using the result in [76, Prop. 1], each element in $\mathbf{R}_A$ can be written as

$$[\mathbf{R}_A]_{m,n} = \frac{\sin\left(\frac{2\pi}{\lambda} \parallel \mathbf{a}_m - \mathbf{a}_n \parallel\right)}{\frac{2\pi}{\lambda} \parallel \mathbf{a}_m - \mathbf{a}_n \parallel}. \tag{4.9}$$

In a similar way, we have

$$\mathbf{g}_A \sim \mathcal{CN}\left(\mathbf{0}_N, \mathbf{R}_A\right). \tag{4.10}$$

Hence, the received signal at UE over correlated Rayleigh fading channels can be written as

$$y_A = \sqrt{\beta_A} \mathbf{g}_A^T \mathbf{\Theta} \mathbf{h}_A \sqrt{P} s + n_0, \tag{4.11}$$

where $P$ is the transmit power of TX; $n_0$ is the additive white Gaussian noise (AWGN) with zero mean and variance $\sigma_0^2$, i.e., $n_0 \sim \mathcal{CN}(0, \sigma_0^2)$. $\beta_A$ is the path loss of the TX-RIS-UE channel, and it is defined as

$$\beta_A = \frac{\Lambda_A}{d_h^\chi d_g^\chi}, \tag{4.12}$$

where $\Lambda_A$ stands for the path loss of the unit distance of the TX-RIS-UE link; $\chi$ is the path loss exponent; $d_h$, $d_g$ denote the distances of the TX-RIS and RIS-UE links, respectively.

We assume that the RIS is able to perform continuous phase adjustment without phase errors. Thus, the optimal phase shift can be given as

$$\theta_n = -\arg(h_{A,n}) - \arg(g_{A,n}). \tag{4.13}$$

After phase adjustment, the received signal at UE can be written as

$$y_A = \sqrt{\beta_A} H_A \sqrt{P} s + n_0, \tag{4.14}$$

where

$$H_A = \sum_{n=1}^{N} |h_{A,n}||g_{A,n}|. \tag{4.15}$$

#### 4.1.2.2 Correlated Nakagami-$m$ Fading Channel Model

The normalized small scale fading of the TX-RIS and RIS-UE channels are denoted as $\mathbf{h}_B = (h_{B,1}, ..., h_{B,N})^T \in \mathbb{C}^{N\times 1}$ and $\mathbf{g}_B = (g_{B,1}, ..., g_{B,N})^T \in \mathbb{C}^{N\times 1}$, respectively. Since the correlated Nakagami-$m$ fading channel model is applied, $\mathbf{h}_B$ and $\mathbf{g}_B$ satisfy

$$|h_{B,n}| \sim \text{Nakagami}(a_{h,B}, 1), \tag{4.16}$$

$$|g_{B,n}| \sim \text{Nakagami}(a_{g,B}, 1). \tag{4.17}$$

where $n \in \{1, ..., N\}$; $a_{h,B}$ and $a_{g,B}$ are the shape parameters of the corresponding channels. $|h_{B,n}|$ and $|g_{B,n}|$ have the same unit scale parameters. The channel correlation is characterized by the well-known exponential decay power correlation model as introduced in many related studies such as [81–83]. Under this model, for the channel TX-RIS, we can write the power correlation coefficient of $|h_{B,m}|$ and $|h_{B,n}|$ where $m, n \in \{1, 2, ..., N\}$ as

$$\rho_{m,n} = \frac{\text{Cov}\left(|h_{B,m}|^2, |h_{B,n}|^2\right)}{\sqrt{\text{Var}(|h_{B,m}|^2)\,\text{Var}(|h_{B,n}|^2)}} = \rho^{\frac{\|\mathbf{a}_m - \mathbf{a}_n\|}{a_0}}, \tag{4.18}$$

where $0 < \rho < 1$ is the power correlation coefficient of the channels associated with the nearest neighboring elements on the RIS; $\| \mathbf{a}_m - \mathbf{a}_n \|$ is the distance between the $m$th and $n$th elements on the RIS; $a_0$ is the smallest element spacing of the RIS. Under the same framework, it can be learned that (4.18) also applies to the power

correlation coefficients of $|g_{B,m}|$ and $|g_{B,n}|$, such that

$$\rho_{m,n} = \frac{\mathrm{Cov}\left(|g_{B,m}|^2, |g_{B,n}|^2\right)}{\sqrt{\mathrm{Var}(|g_{B,m}|^2)\,\mathrm{Var}(|g_{B,n}|^2)}}. \tag{4.19}$$

Similarly, the received signal at UE with perfect phase adjustment over correlated Nakagami-$m$ fading channels can be written as

$$y_B = \sqrt{\beta_B} H_B \sqrt{P} s + n_0, \tag{4.20}$$

where

$$H_B = \sum_{n=1}^{N} |h_{B,n}||g_{B,n}|. \tag{4.21}$$

$\beta_B$ is the path loss of the TX-RIS-UE channel, defined as

$$\beta_B = \frac{\Lambda_B}{d_h^{\chi} d_g^{\chi}}, \tag{4.22}$$

where $\Lambda_B$ is the path loss per unit distance.

### 4.1.3 Performance Metrics

Two performance metrics, i.e., outage probability and average achievable rate, are studied. According to the channel and signal models, the received SNR can be written as

$$\gamma_u = \gamma_t \beta_u H_u^2, \quad u \in \{A, B\}, \tag{4.23}$$

where $\gamma_t = P/\sigma_0^2$ is the transmit power; $u \in \{A, B\}$ stands for the cases of correlated Rayleigh fading and correlated Nakagami-$m$ fading, respectively. The outage probability is a performance metric to evaluate the reliability of a communication system, and it is defined as the probability that the received SNR falls below a SNR threshold

$\bar{\gamma}$ such that

$$P_u(\bar{\gamma}) = \mathbb{P}(\gamma_u < \bar{\gamma}), \quad u \in \{A, B\}. \tag{4.24}$$

On the other hand, the average achievable rate is used to evaluate the communication efficiency, and it is defined as per Shannon's law as

$$R_u = \mathbb{E}\left[\log_2\left(1 + \gamma_u\right)\right] \quad u \in \{A, B\}. \tag{4.25}$$

## 4.2 Outage Probability Analysis

In this section, the outage probabilities for the proposed communication system over correlated Rayleigh fading channels and correlated Nakagami-$m$ fading channels are derived subsequently. Since the exact characterization of the channel distribution is mathematically intractable, the exact mean and variance of the composite channel gain are computed first, followed by fitting the composite channel gain as a gamma random variable.

### 4.2.1 Analysis of Correlated Rayleigh Fading Channel

The random variable $H_A$ is the sum of products of correlated Rayleigh random variables. The exact distribution of $H_A$ cannot be obtained in closed form. Therefore, in this case, we analyzed the mean and variance of $H_A$ first. The mean of $H_A$ can be calculated directly as

$$\mathbb{E}[H_A] = \mathbb{E}\left[\sum_{n=1}^{N} |h_{A,n}||g_{A,n}|\right] = \frac{\pi}{4}N. \tag{4.26}$$

Regarding the variance of $H_A$, it can be manipulated as

$$\begin{aligned}
&\mathrm{Var}[H_A] = \mathbb{E}[(H_A - \mathbb{E}[H_A])^2] \\
&= \mathbb{E}\left[\left(\sum_{n=1}^{N}\left(|h_{A,n}||g_{A,n}| - \mathbb{E}[|h_{A,n}||g_{A,n}|]\right)\right)^2\right] \\
&= \mathbb{E}\left[\sum_{i=1}^{N}\sum_{j=1}^{N}\left(|h_{A,i}||g_{A,i}| - \frac{\pi}{4}\right)\left(|h_{A,j}||g_{A,j}| - \frac{\pi}{4}\right)\right] \\
&= \sum_{i=1}^{N}\sum_{j=1}^{N}\left(\mathbb{E}\left[|h_{A,i}||h_{A,j}|\right]\mathbb{E}\left[|g_{A,i}||g_{A,j}|\right]\right) - \frac{\pi^2}{16}N^2.
\end{aligned} \tag{4.27}$$

Thus, the key problem lies in characterizing $\mathbb{E}\left[|w_{A,i}|\,|w_{A,j}|\right]$, where $w \in \{h, g\}$ and $i, j \in \{1, ..., N\}$. The result is summarized in the following proposition.

**Proposition 1.** *For $i \neq j$, $\mathbb{E}\left[|w_{A,i}|\,|w_{A,j}|\right]$, $w \in \{h, g\}$, can be expressed in terms of $\mathbb{E}\left[w_{A,i}w_{A,j}^*\right]$ as*

$$\mathbb{E}\left[|w_{A,i}|\,|w_{A,j}|\right] = \left(\frac{\left|\mathbb{E}[w_{A,i}w_{A,j}^*]\right|^2}{2} - \frac{1}{2}\right)K\left(\left|\mathbb{E}[w_{A,i}w_{A,j}^*]\right|^2\right) + E\left(\left|\mathbb{E}[w_{A,i}w_{A,j}^*]\right|^2\right). \tag{4.28}$$

*For $i = j$,*

$$\mathbb{E}\left[|w_{A,i}|\,|w_{A,j}|\right] = 1. \tag{4.29}$$

*$K(\cdot)$ and $E(\cdot)$ are the complete elliptic integral of the first kind and the second kind, respectively.*

*Proof.* In the proposed system, $w_{A,i}$ can be written as

$$w_{A,i} = R_i \exp\left(j\vartheta_i\right) = X_i + jY_i,\ i \in \{1, 2, ..., N\}, \tag{4.30}$$

where $R_i$, $\vartheta_i$, $X_i$ and $Y_i$ denote the amplitude, phase angle, real part and imaginary part of $w_{A,i}$, respectively; $X_i$ and $Y_i$ are uncorrelated normal random variables, each

with zero mean and variance as

$$\tau \triangleq \mathrm{Var}[X_i] = \mathrm{Var}[Y_i] = \frac{1}{2}. \tag{4.31}$$

For the channels associated with two different RIS elements, it can be obtained that

$$\mathbb{E}\left[X_i X_j\right] = \mathbb{E}\left[|w_{A,i}||w_{A,j}|\cos(\vartheta_i)\cos(\vartheta_j)\right], \tag{4.32a}$$

$$\begin{aligned}\mathbb{E}\left[Y_i Y_j\right] &= \mathbb{E}\left[|w_{A,i}||w_{A,j}|\sin(\vartheta_i)\sin(\vartheta_j)\right] \\ &= \mathbb{E}\left[|w_{A,i}||w_{A,j}|\cos(\vartheta_i+\pi/2)\cos(\vartheta_j+\pi/2)\right].\end{aligned} \tag{4.32b}$$

Since $\vartheta_i$, $i \in \{1, 2, ..., N\}$, are uniformly distributed over $[-\pi, \pi)$ and the above functions are periodic, we have

$$\tau_1 \triangleq \mathbb{E}\left[X_i X_j\right] = \mathbb{E}\left[Y_i Y_j\right]. \tag{4.33}$$

Similarly,

$$\mathbb{E}\left[X_i Y_j\right] = \mathbb{E}\left[|w_{A,i}||w_{A,j}|\cos(\vartheta_i)\sin(\vartheta_j)\right], \tag{4.34a}$$

$$\begin{aligned}\mathbb{E}\left[Y_i X_j\right] &= \mathbb{E}\left[|w_{A,i}||w_{A,j}|\sin(\vartheta_i)\cos(\vartheta_j)\right] \\ &= -\mathbb{E}\left[|w_{A,i}||w_{A,j}|\cos(\vartheta_i+\pi/2)\sin(\vartheta_j+\pi/2)\right].\end{aligned} \tag{4.34b}$$

Hence,

$$\tau_2 \triangleq \mathbb{E}\left[X_i Y_j\right] = -\mathbb{E}\left[Y_i X_j\right]. \tag{4.35}$$

For $i \neq j$, the joint distribution of $(X_i, Y_i, X_j, Y_j)$ can be written as

$$f(x_i, y_i, x_j, y_j) = \frac{1}{(2\pi)^2\sqrt{\det\mathbf{C}}}\exp\left(-\frac{1}{2}\mathbf{v}\mathbf{C}^{-1}\mathbf{v}^T\right), \tag{4.36}$$

where $\mathbf{v} = [x_i, y_i, x_j, y_j]$; $\mathbf{C}$ is the covariance matrix of $\{X_i, Y_i, X_j, Y_j\}$, given by

$$\mathbf{C} = \begin{pmatrix} \tau & 0 & \tau_1 & \tau_2 \\ 0 & \tau & -\tau_2 & \tau_1 \\ \tau_1 & -\tau_2 & \tau & 0 \\ \tau_2 & \tau_1 & 0 & \tau \end{pmatrix}. \tag{4.37}$$

The determinant and inverse of $\mathbf{C}$ can be calculated as

$$\det\{\mathbf{C}\} = (\tau^2 - \tau_1^2 - \tau_2^2)^2, \tag{4.38}$$

$$\mathbf{C}^{-1} = \begin{pmatrix} \frac{\tau}{\tau^2-\tau_1^2-\tau_2^2} & 0 & \frac{-\tau_1}{\tau^2-\tau_1^2-\tau_2^2} & \frac{-\tau_2}{\tau^2-\tau_1^2-\tau_2^2} \\ 0 & \frac{\tau}{\tau^2-\tau_1^2-\tau_2^2} & \frac{\tau_2}{\tau^2-\tau_1^2-\tau_2^2} & \frac{-\tau_1}{\tau^2-\tau_1^2-\tau_2^2} \\ \frac{-\tau_1}{\tau^2-\tau_1^2-\tau_2^2} & \frac{\tau_2}{\tau^2-\tau_1^2-\tau_2^2} & \frac{\tau}{\tau^2-\tau_1^2-\tau_2^2} & 0 \\ \frac{-\tau_2}{\tau^2-\tau_1^2-\tau_2^2} & \frac{-\tau_1}{\tau^2-\tau_1^2-\tau_2^2} & 0 & \frac{\tau}{\tau^2-\tau_1^2-\tau_2^2} \end{pmatrix}. \tag{4.39}$$

Taking (4.38) and (4.39) into (4.36), the joint distribution of $(X_i, Y_i, X_j, Y_j)$ can be obtained. Then, using the theorem of the transformation of random variables:

$$f(r_i, r_j, \vartheta_i, \vartheta_j) = |\det(J(r_i, r_j, \vartheta_i, \vartheta_j))|\, f(x_i, y_i, x_j, y_j), \tag{4.40}$$

where

$$J(r_i, r_j, \vartheta_i, \vartheta_j) = \frac{\partial(x_i, y_i, x_j, y_j)}{\partial(r_i, r_j, \vartheta_i, \vartheta_j)} \tag{4.41}$$

is the Jacobian matrix for the transformation

$$\begin{aligned} \{&x_i = r_i \cos(\vartheta_i), y_i = r_i \sin(\vartheta_i), \\ &x_j = r_j \cos(\vartheta_j), y_j = r_j \sin(\vartheta_j)\}, \end{aligned} \tag{4.42}$$

we can derive the joint distribution of $(R_i, R_j, \vartheta_i, \vartheta_j)$ as [84]

$$\begin{aligned} f(r_i, r_j, \vartheta_i, \vartheta_j) &= \frac{r_i r_j}{(2\pi)^2(\tau^2 - q^2)} \\ &\times \exp\left[-\frac{\tau\left(r_i^2 + r_j^2\right) - 2r_i r_j q \cos\left(\vartheta_j - \vartheta_i - \xi\right)}{2\left(\tau^2 - q^2\right)}\right], \end{aligned} \tag{4.43}$$

where

$$\xi = \arctan\left(\frac{\tau_2}{\tau_1}\right), \tag{4.44a}$$

$$q^2 = \tau_1^2 + \tau_2^2 = \frac{\left|\mathbb{E}[w_{A,i} w_{A,j}^*]\right|^2}{4}. \tag{4.44b}$$

After some mathematical manipulation, $\mathbb{E}[R_i R_j]$ can be expressed as [71, eq.6.631.1, eq.7.621.4]

$$\begin{aligned} \mathbb{E}[R_i R_j] &= \int_0^\infty \int_0^\infty \int_0^{2\pi} \int_0^{2\pi} r_i r_j f(r_i, r_j, \vartheta_i, \vartheta_j)\, \mathrm{d}\vartheta_i\, \mathrm{d}\vartheta_j\, \mathrm{d}r_i\, \mathrm{d}r_j \\ &= \left(\frac{q^2}{\tau} - \tau\right) K\left(\frac{q^2}{\tau^2}\right) + 2\tau E\left(\frac{q^2}{\tau^2}\right). \end{aligned} \tag{4.45}$$

For $i = j$, we can directly write

$$\mathbb{E}\left[R_i R_j\right] = 1, \quad i = j. \tag{4.46}$$

Thus, the proof is complete. □

For notational simplicity, we can define

$$\bar{\mathbf{R}}_A = \mathbb{E}[|\mathbf{h}_A||\mathbf{h}_A|^T] = \mathbb{E}[|\mathbf{g}_A||\mathbf{g}_A|^T], \tag{4.47}$$

in which

$$\left[\bar{\mathbf{R}}_A\right]_{i,j} = \frac{\left|[\mathbf{R}_A]_{i,j}\right|^2 - 1}{2} K\left(\left|[\mathbf{R}_A]_{i,j}\right|^2\right) + E\left(\left|[\mathbf{R}_A]_{i,j}\right|^2\right), \quad i \neq j, \tag{4.48a}$$

$$\left[\bar{\mathbf{R}}_A\right]_{i,j} = 1, \quad i = j. \tag{4.48b}$$

Thus, the variance of $H_A$ can be written as

$$\begin{aligned} \mathrm{Var}[H_A] &= \sum_{i=1}^{N}\sum_{j=1}^{N}\left(\left[\bar{\mathbf{R}}_A\right]_{i,j}\right)^2 - \frac{\pi^2}{16}N^2 \\ &= \mathbf{tr}\left(\bar{\mathbf{R}}_A\bar{\mathbf{R}}_A\right) - \frac{\pi^2}{16}N^2. \end{aligned} \tag{4.49}$$

With the mean and variance of $H_A$ given in (4.26) and (4.49) respectively, the moment-matching approach can be utilized to analyze the distribution of $H_A$ by matching the expectation and variance of $H_A$ to a gamma random variable with mean $\kappa_A\omega_A$ and variance $\kappa_A\omega_A^2$. As introduced in [67], the gamma distribution can be used to approximate complicated SNR distributions with high accuracy and tractable parameter computation. Thus, $H_A$ can be approximated as a gamma random variable with shape parameter $\kappa_A$ and scale parameter $\omega_A$:

$$\kappa_A = \frac{\mathbb{E}^2[H_A]}{\mathrm{Var}[H_A]}, \quad \omega_A = \frac{\mathrm{Var}[H_A]}{\mathbb{E}[H_A]}. \tag{4.50}$$

The probability density function (PDF) and cumulative distribution function (CDF) of $H_A$ can be approximated as

$$f_{H_A}(x) \approx \frac{x^{\kappa_A - 1}\exp\left(-\frac{x}{\omega_A}\right)}{\Gamma(\kappa_A)\,\omega_A^{\kappa_A}}, \tag{4.51a}$$

$$F_{H_A}(x) \approx \frac{1}{\Gamma(\kappa_A)}\gamma\left(\kappa_A, \frac{x}{\omega_A}\right), \tag{4.51b}$$

where $\Gamma(\cdot)$ is gamma function and $\gamma(\cdot,\cdot)$ is lower incomplete gamma function. Hence,

the outage probability of UE can be written as

$$P_A(\bar{\gamma}) = F_{H_A}\left(\sqrt{\frac{\bar{\gamma}}{\gamma_t \beta_A}}\right) \approx \frac{1}{\Gamma(\kappa_A)}\gamma\left(\kappa_A, \sqrt{\frac{\bar{\gamma}}{\gamma_t \beta_A \omega_A^2}}\right). \tag{4.52}$$

### 4.2.2 Analysis of Correlated Nakagami-$m$ Fading Channel

The composite channel gain $H_B$ of the correlated Nakagami-$m$ fading channel model is the sum of products of correlated Nakagami-$m$ random variables. Similar to the case of correlated Rayleigh fading model, the mean of $H_B$ can be given as

$$\mathbb{E}[H_B] = \mathbb{E}\left[\sum_{n=1}^{N} |h_{B,n}||g_{B,n}|\right] = N\frac{\Gamma\left(a_{h,B}+\frac{1}{2}\right)\Gamma\left(a_{g,B}+\frac{1}{2}\right)}{\Gamma(a_{h,B})\Gamma(a_{g,B})}\left(\frac{1}{a_{h,B}a_{g,B}}\right)^{\frac{1}{2}}. \tag{4.53}$$

The variance of $H_B$ is the difference between the second order raw moment of $H_B$ and the square of the mean of $H_B$, and is given as

$$\begin{aligned}\mathrm{Var}[H_B] &= \mathbb{E}[H_B^2] - (\mathbb{E}[H_B])^2 \\ &= \mathbb{E}\left[\left(\sum_{n=1}^{N} |h_{B,n}||g_{B,n}|\right)^2\right] - (\mathbb{E}[H_B])^2 \\ &= \sum_{i=1}^{N}\sum_{j=1}^{N}\left(\mathbb{E}\left[|h_{B,i}|\,|h_{B,j}|\right]\mathbb{E}\left[|g_{B,i}|\,|g_{B,j}|\right]\right) - (\mathbb{E}[H_B])^2.\end{aligned} \tag{4.54}$$

The mean of $|w_{B,i}||w_{B,j}|$, $w \in \{h, g\}$, $i, j \in \{1, ..., N\}$, is summarized in the following proposition.

**Proposition 2.** *$\mathbb{E}\left[|w_{B,i}||w_{B,j}|\right]$, $w \in \{h, g\}$, can be expressed in terms of $\rho_{i,j}$ as*

$$\mathbb{E}[|w_{B,i}||w_{B,j}|] = \frac{\Gamma^2\left(a_{w,B}+\frac{1}{2}\right)}{a_{w,B}\Gamma^2\left(a_{w,B}\right)}\,{}_2F_1\left(-\frac{1}{2}, -\frac{1}{2}, a_{w,B}, \rho_{i,j}\right). \tag{4.55}$$

*Proof.* $|w_{B,i}|$ and $|w_{B,j}|$, $w \in \{h, g\}$, are two correlated Nakagami-$m$ random variables

such that

$$|w_{B,i}| \sim \text{Nakagami}(a_{w,B}, 1), \tag{4.56a}$$

$$|w_{B,j}| \sim \text{Nakagami}(a_{w,B}, 1), \tag{4.56b}$$

$$\frac{\text{Cov}(|w_{B,i}|^2, |w_{B,j}|^2)}{\sqrt{\text{Var}(|w_{B,i}|^2)\,\text{Var}(|w_{B,j}|^2)}} = \rho_{i,j}. \tag{4.56c}$$

Denoting $|w_{B,i}|^2$ and $|w_{B,j}|^2$ as $H_{B,i}$ and $H_{B,j}$ respectively, and using the property of Nakagami-$m$ distribution, $H_{B,i}$ and $H_{B,j}$ can be written as the sum of squares of independent Rayleigh random variables as

$$H_{B,i} = \sum_{a=1}^{a_{w,B}} R_{a,B,i}^2 = R_{1,B,i}^2 + R_{2,B,i}^2 + ... + R_{a_{w,B},B,i}^2, \tag{4.57a}$$

$$H_{B,j} = \sum_{a=1}^{a_{w,B}} R_{a,B,j}^2 = R_{1,B,j}^2 + R_{2,B,j}^2 + ... + R_{a_{w,B},B,j}^2, \tag{4.57b}$$

where

$$R_{a,B,i} \sim \mathcal{R}\left(\frac{1}{\sqrt{2a_{w,B}}}\right), \quad R_{a,B,j} \sim \mathcal{R}\left(\frac{1}{\sqrt{2a_{w,B}}}\right), \quad a \in \{1, 2, ..., a_{w,B}\}, \tag{4.58}$$

$$\begin{cases} \dfrac{\text{Cov}(R_{a,B,i}^2, R_{a',B,j}^2)}{\sqrt{\text{Var}(R_{a,B,i}^2)\,\text{Var}(R_{a',B,j}^2)}} = \rho_{i,j}, \quad a = a', \\ \dfrac{\text{Cov}(R_{a,B,i}^2, R_{a',B,j}^2)}{\sqrt{\text{Var}(R_{a,B,i}^2)\,\text{Var}(R_{a',B,j}^2)}} = 0 \quad a \neq a', \end{cases} \tag{4.59}$$

such that

$$\text{Cov}\left(H_{B,i}, H_{B,j}\right) = a_{w,B}\text{Cov}\left(R_{a,B,i}^2, R_{a,B,j}^2\right), \tag{4.60a}$$

$$\text{Var}\left(H_{B,i}\right) = \text{Var}\left(H_{B,j}\right) = a_{w,B}\text{Var}\left(R_{a,B,i}^2\right) = a_{w,B}\text{Var}\left(R_{a,B,j}^2\right), \tag{4.60b}$$

where $a \in \{1, 2, ..., a_{w,B}\}$. Following the discussion in [85], the joint distribution of

$(R_{a,B,i}, R_{a,B,j})$ can be written as

$$f_{R_{a,B,i},R_{a,B,j}}(x,y) = \frac{4a_{w,B}^2 xy}{(1-\rho_{i,j})} \exp\left(-\frac{a_{w,B}(x^2+y^2)}{(1-\rho_{i,j})}\right) I_0\left(\frac{2a_{w,B}\sqrt{\rho_{i,j}}xy}{(1-\rho_{i,j})}\right). \quad (4.61)$$

Applying the transformation of variables, the joint distribution of $\left(R_{a,B,i}^2, R_{a,B,j}^2\right)$ can be directly obtained as

$$f_{R_{a,B,i}^2,R_{a,B,j}^2}(x,y) = \frac{a_{w,B}^2}{(1-\rho_{i,j})} \exp\left(-\frac{a_{w,B}(x+y)}{(1-\rho_{i,j})}\right) I_0\left(\frac{2a_{w,B}\sqrt{\rho_{i,j}xy}}{(1-\rho_{i,j})}\right) \quad (4.62)$$

Further, the two dimensional Laplace transform of $\left(R_{a,B,i}^2, R_{a,B,j}^2\right)$ is derived as follows:

$$\begin{aligned}\psi_{R_{a,B,i}^2,R_{a,B,j}^2}(s_1,s_2) &= \int_0^\infty \int_0^\infty e^{-s_1x-s_2y} f_{R_{a,B,i}^2,R_{a,B,j}^2}(x,y)\,\mathrm{d}x\,\mathrm{d}y \\ &= \frac{a_{w,B}^2}{(1-\rho_{i,j})}\left(\left(s_1+\frac{a_{w,B}}{1-\rho_{i,j}}\right)\left(s_2+\frac{a_{w,B}}{1-\rho_{i,j}}\right)-\frac{a_{w,B}^2\rho_{i,j}}{(1-\rho_{i,j})^2}\right)^{-1}. \quad (4.63)\end{aligned}$$

Using the properties of Laplace transforms, the two dimensional Laplace transform of $(H_{B,i}, H_{B,j})$ is

$$\begin{aligned}\psi_{H_{B,i},H_{B,j}}(s_1,s_2) &= \left(\psi_{R_{a,B,i}^2,R_{a,B,j}^2}(s_1,s_2)\right)^{a_{w,B}} \\ &= \left(\frac{a_{w,B}^2}{(1-\rho_{i,j})}\right)^{a_{w,B}}\left(\left(s_1+\frac{a_{w,B}}{1-\rho_{i,j}}\right)\left(s_2+\frac{a_{w,B}}{1-\rho_{i,j}}\right)-\frac{a_{w,B}^2\rho_{i,j}}{(1-\rho_{i,j})^2}\right)^{-a_{w,B}}. \quad (4.64)\end{aligned}$$

Taking the inverse two dimensional Laplace transform [86], the joint distribution of $(H_{B,i}, H_{B,j})$ is derived as

$$\begin{aligned}f_{H_{B,i},H_{B,j}}(x,y) &= \frac{1}{(j2\pi)^2}\int_{c_1-\infty}^{c_1+\infty}\int_{c_2-\infty}^{c_2+\infty} e^{s_1x+s_2y}\psi_{H_{B,i},H_{B,j}}(s_1,s_2)\,\mathrm{d}s_2\,\mathrm{d}s_1 \\ &= \left(\frac{a_{w,B}^2}{(1-\rho_{i,j})}\right)^{a_{w,B}} \frac{(xy)^{\frac{a_{w,B}-1}{2}}(1-\rho_{i,j})^{(a_{w,B}-1)}}{\Gamma(a_{w,B})(\sqrt{\rho_{i,j}}a_{w,B})^{(a_{w,B}-1)}} \\ &\quad \times \exp\left(-\frac{a_{w,B}}{(1-\rho_{i,j})}(x+y)\right) I_{a_{w,B}-1}\left(\frac{2\sqrt{\rho_{i,j}}a_{w,B}}{1-\rho_{i,j}}\sqrt{xy}\right). \quad (4.65)\end{aligned}$$

$\psi_{H_{B,i},H_{B,j}}(s_1, s_2)$ is an analytic function for all $s_1$ and $s_2$ in a region confined by $\mathrm{Re}(s_1) \geq c_1$ and $\mathrm{Re}(s_2) \geq c_2$, where $c_1$ and $c_2$ are real constants chosen properly. Applying the transformation of variables again leads to the joint distribution of $(|w_{B,i}|, |w_{B,j}|)$ such that

$$f_{|w_{B,i}|,|w_{B,j}|}(x,y) = \frac{4(xy)^{a_{w,B}} a_{w,B}^{(a_{w,B}+1)}}{\Gamma(a_{w,B})(1-\rho_{i,j})\rho_{i,j}^{\frac{a_{w,B}-1}{2}}} \times \exp\left(-\frac{a_{w,B}}{(1-\rho_{i,j})}(x^2+y^2)\right) I_{a_{w,B}-1}\left(\frac{2\sqrt{\rho_{i,j}}a_{w,B}}{1-\rho_{i,j}}xy\right). \quad (4.66)$$

As per the joint distribution of $(|w_{B,i}|, |w_{B,j}|)$, the mean of $|w_{B,i}|\,|w_{B,j}|$ can be computed as

$$\begin{aligned}\mathbb{E}[|w_{B,i}||w_{B,j}|] &= \int_0^\infty \int_0^\infty xy f_{|w_{B,i}|,|w_{B,j}|}(x,y)\,\mathrm{d}x\,\mathrm{d}y \\ &= \frac{\Gamma^2\left(a_{w,B}+\frac{1}{2}\right)}{a_{w,B}\Gamma^2\left(a_{w,B}\right)}\,{}_2F_1\left(-\frac{1}{2},-\frac{1}{2},a_{w,B},\rho_{i,j}\right). \end{aligned} \quad (4.67)$$

Thus, the proof is complete. □

For notational simplicity, we can define

$$\mathbf{R}_{h,B} = \mathbb{E}[|\mathbf{h}_B||\mathbf{h}_B|^T], \quad (4.68)$$

$$\mathbf{R}_{g,B} = \mathbb{E}[|\mathbf{g}_B||\mathbf{g}_B|^T], \quad (4.69)$$

in which

$$[\mathbf{R}_{h,B}]_{i,j} = \frac{\Gamma^2\left(a_{h,B}+\frac{1}{2}\right)}{a_{h,B}\Gamma^2\left(a_{h,B}\right)}\,{}_2F_1\left(-\frac{1}{2},-\frac{1}{2},a_{h,B},\rho_{i,j}\right), \quad (4.70a)$$

$$[\mathbf{R}_{g,B}]_{i,j} = \frac{\Gamma^2\left(a_{g,B}+\frac{1}{2}\right)}{a_{g,B}\Gamma^2\left(a_{g,B}\right)}\,{}_2F_1\left(-\frac{1}{2},-\frac{1}{2},a_{g,B},\rho_{i,j}\right). \quad (4.70b)$$

Hence, the variance of $H_B$ is

$$\begin{aligned}\mathrm{Var}[H_B] &= \sum_{i=1}^{N}\sum_{j=1}^{N}[\mathbf{R}_{h,B}]_{i,j}[\mathbf{R}_{g,B}]_{i,j} - \frac{N^2}{a_{h,B}a_{g,B}}\left(\frac{\Gamma\left(a_{h,B}+\frac{1}{2}\right)\Gamma\left(a_{g,B}+\frac{1}{2}\right)}{\Gamma(a_{h,B})\Gamma(a_{g,B})}\right)^2 \\ &= \mathbf{tr}\left(\mathbf{R}_{h,B}\mathbf{R}_{g,B}\right) - \frac{N^2}{a_{h,B}a_{g,B}}\left(\frac{\Gamma\left(a_{h,B}+\frac{1}{2}\right)\Gamma\left(a_{g,B}+\frac{1}{2}\right)}{\Gamma(a_{h,B})\Gamma(a_{g,B})}\right)^2. \end{aligned} \tag{4.71}$$

As per the mean and variance of $H_B$ given in (4.53) and (4.71) respectively, the moment-matching approach can be utilized to fit the distribution of $H_B$ to a gamma random variable with mean $\kappa_B\omega_B$ and variance $\kappa_B\omega_B^2$, such that

$$\kappa_B = \frac{\mathbb{E}^2[H_B]}{\mathrm{Var}[H_B]}, \quad \omega_B = \frac{\mathrm{Var}[H_B]}{\mathbb{E}[H_B]}. \tag{4.72}$$

The PDF and CDF of $H_B$ can be approximated as

$$f_{H_B}(x) \approx \frac{x^{\kappa_B-1}\exp\left(-\frac{x}{\omega_B}\right)}{\Gamma(\kappa_B)\,\omega_B^{\kappa_B}}, \tag{4.73a}$$

$$F_{H_B}(x) \approx \frac{1}{\Gamma(\kappa_B)}\gamma\left(\kappa_B, \frac{x}{\omega_B}\right), \tag{4.73b}$$

Hence, the outage probability of UE can be approximated as

$$\begin{aligned} P_B(\bar{\gamma}) &= F_{H_B}\left(\sqrt{\frac{\bar{\gamma}}{\gamma_t\beta_B}}\right) \\ &\approx \frac{1}{\Gamma(\kappa_B)}\gamma\left(\kappa_B, \sqrt{\frac{\bar{\gamma}}{\gamma_t\beta_B\omega_B^2}}\right). \end{aligned} \tag{4.74}$$

**Remark 6.** *If $a_{h,B} = a_{g,B} = 1$, the exponential decay power correlated Nakagami-m fading model is specialized to the exponential decay power correlated Rayleigh fading model.*

## 4.3 Average Achievable Rate Analysis

In this section, the average achievable rates of the proposed communication system over two different correlated channel models are analyzed. We first proposed upper bounds on the average achievable rates over two channel models. Then, channel hardening is shown to occur in the proposed system, based on which we derive approximations of the average achievable rates. The analytical results illustrate that the proposed upper bounds and approximations on the average achievable rates are asymptotically equivalent in the number of elements.

### 4.3.1 Upper Bound Analysis

An upper bound on the average achievable rate of UE is derived with the well-known Jensen's inequality [87], such that

$$\mathbb{E}[f(X)] \leq f\left(\mathbb{E}[X]\right), \tag{4.75}$$

for any random variable $X$ and concave function $f(x)$. The Jensen's inequality is commonly used to study the average achievable rate of RIS-assisted wireless communication systems since it is a tight bound and asymptotically equivalent when the number of elements is large. According to the theorem given in [88, Theorem 4], for a sequence of positive independent and identically distributed (i.i.d.) random variables $\{X_n\}$ with finite mean value $\mu_n$ and variance $\sigma_n^2$, and satisfying $\mu_n \to \infty$ and $\frac{\sigma_n}{\mu_n} \to 0$ as $n \to \infty$, we have:

$$\frac{\mathbb{E}[\log(1+X_n)]}{\log(1+\mathbb{E}[X_n])} \to 1. \tag{4.76}$$

In the following, we will demonstrate that the average achievable rate of the RIS-assisted communication system over correlated channels satisfies the theorem.

Regarding the case of correlated Rayleigh fading channel model, an upper bound

$R_A^*$ on the average achievable rate of UE can be derived as

$$\begin{aligned} R_A^* &= \log_2\left(1+\mathbb{E}[\gamma_A]\right) \\ &= \log_2\left(1+\gamma_t\beta_A\mathbb{E}[H_A^2]\right) \\ &= \log_2\left(1+\gamma_t\beta_A\mathbf{tr}\left(\bar{\mathbf{R}}_A\bar{\mathbf{R}}_A\right)\right). \end{aligned} \tag{4.77}$$

Following similar procedures, an upper bound $R_B^*$ on the average achievable rate of UE over correlated Nakagami-$m$ fading channels can be written as

$$\begin{aligned} R_B^* &= \log_2\left(1+\gamma_t\beta_B\mathbb{E}[H_B^2]\right) \\ &= \log_2\left(1+\gamma_t\beta_B\mathbf{tr}\left(\mathbf{R}_{h,B}\mathbf{R}_{g,B}\right)\right). \end{aligned} \tag{4.78}$$

### 4.3.2 Large Array Analysis

In this subsection, we show that the channel hardening effect appears in the proposed system and revisit the average achievable rates for a large number of RIS elements.

As defined in [76], the channel hardening effect in a RIS-assisted system refers to the case when the received SNR variations average out and the received SNR is approximately equal to $N^2$ times a constant as $N$ goes large. The channel hardening effect in the proposed system model over correlated channels is presented in the following proposition.

**Proposition 3.** *The composite channel gains of UE over correlated Rayleigh and correlated Nakagami-m fading channel models, namely $H_A$ and $H_B$, satisfy*

$$\frac{1}{N}H_A \xrightarrow{P} \frac{\pi}{4}, \quad N\to\infty, \tag{4.79a}$$

$$\frac{1}{N}H_B \xrightarrow{P} \frac{\Gamma\left(a_{h,B}+\frac{1}{2}\right)\Gamma\left(a_{g,B}+\frac{1}{2}\right)}{\Gamma(a_{h,B})\Gamma(a_{g,B})}\left(\frac{1}{a_{h,B}a_{g,B}}\right)^{\frac{1}{2}}, \quad N\to\infty, \tag{4.79b}$$

*with the convergence in probability*[2]*. Hence,* $H_A^2$ *and* $H_B^2$ *can be approximated by constants as*

$$H_A^2 \approx \frac{\pi^2}{16} N^2, \tag{4.80a}$$

$$H_B^2 \approx \frac{N^2}{a_{h,B} a_{g,B}} \left( \frac{\Gamma\left(a_{h,B} + \frac{1}{2}\right) \Gamma\left(a_{g,B} + \frac{1}{2}\right)}{\Gamma(a_{h,B}) \Gamma(a_{g,B})} \right)^2, \tag{4.80b}$$

*when the number of elements is large.*

*Proof.* See Appendix 4.6.1. □

**Remark 7.** *It is worth noting that the channel correlation does not play a role in the conclusion of Proposition 3. And, in the case of uncorrelated channels, the same approximations on* $H_A$ *and* $H_B$ *can be derived by using the conventional law of large numbers.*

We revisit the average achievable rates when the number of elements is large. By using (4.80a) and (4.80b), the average achievable rates of UE over correlated Rayleigh and correlated Nakagami-$m$ fading channel models can be approximated as

$$R_A \approx R_A^+ = \log_2 \left( 1 + \frac{\gamma_t \beta_A \pi^2 N^2}{16} \right), \tag{4.81}$$

$$R_B \approx R_B^+ = \log_2 \left( 1 + \frac{\gamma_t \beta_B N^2}{a_{h,B} a_{g,B}} \left( \frac{\Gamma\left(a_{h,B} + \frac{1}{2}\right) \Gamma\left(a_{g,B} + \frac{1}{2}\right)}{\Gamma(a_{h,B}) \Gamma(a_{g,B})} \right)^2 \right). \tag{4.82}$$

### 4.3.3 Asymptotic Analysis

Relations between $R_A^*$ and $R_A^+$ as well as between $R_B^*$ and $R_B^+$ are analyzed and summarized in the following proposition.

**Proposition 4.** *For a large number of elements, the following asymptotic equivalence*

[2]Convergence in probability is a type of convergence in probability theory. A sequence of random variables $X_1, X_2, ..., X_n$ converges to a random variable $X$ in probability if, for any $\epsilon > 0$, $\lim_{n\to\infty} P(|X_n - X| > \epsilon) = 0$.

*relations hold:*

$$R_A^* \sim R_A^+, \quad N \to \infty, \tag{4.83a}$$

$$R_B^* \sim R_B^+, \quad N \to \infty. \tag{4.83b}$$

*Proof.* The Rayleigh fading model is analyzed first. The expectation of $H_A$ is

$$\mathbb{E}[H_A] = \frac{\pi}{4}N. \tag{4.84}$$

$\mathbb{E}[H_A^2]$ can be written as

$$\mathbb{E}[H_A^2] = (\mathbb{E}[H_A])^2 + \mathrm{Var}[H_A] \tag{4.85}$$

As shown in Lemma 3 in Appendix 4.6.1, the variance of $H_A$ scales with $N$. Thus, $\mathbb{E}[H_A^2]$ satisfies the asymptotic equivalence as

$$\mathbb{E}[H_A^2] \sim \frac{\pi^2}{16}N^2, \quad N \to \infty. \tag{4.86}$$

Thus, we obtain (4.83a) in Proposition 4. Following similar procedures, (4.83b) can be derived as well. □

Next, the relations between $R_A$ and $R_A^*$ as well as between $R_B$ and $R_B^*$ are investigated and summarized in the following proposition.

**Proposition 5.** *For a large number of elements, $R_A$ and $R_A^*$ satisfy asymptotic equivalence, i.e.,*

$$R_A \sim R_A^*, \quad N \to \infty. \tag{4.87}$$

*Similarly, $R_B$ and $R_B^*$ are also asymptotically equivalent, i.e.,*

$$R_B \sim R_B^*, \quad N \to \infty. \tag{4.88}$$

*Further, due to the transitive property of asymptotic analysis and Proposition 4, we have*

$$R_A \sim R_A^+, \quad N \to \infty, \tag{4.89a}$$

$$R_B \sim R_B^+, \quad N \to \infty. \tag{4.89b}$$

*Proof.* As shown in Proposition 3, the random variable

$$G_N = \frac{1}{N^2} H_A^2 \tag{4.90}$$

satisfies

$$G_N \xrightarrow{P} \frac{\pi^2}{16}, \quad N \to \infty, \tag{4.91}$$

with the convergence in probability. As shown in Proposition 4 and its proof, the expectation and variance of $G_N$ satisfy

$$\mathbb{E}[G_N] \to \frac{\pi^2}{16}, \quad \mathrm{Var}[G_N] \to 0, \quad N \to \infty. \tag{4.92}$$

Thus, the expectation and variance of $H_A^2$ satisfy

$$\frac{\mathrm{Var}\left[H_A^2\right]}{\mathbb{E}^2\left[H_A^2\right]} \to 0, \quad N \to \infty. \tag{4.93}$$

Invoking [88, Theorem 4], the asymptotic equivalence of $R_A$ and $R_A^*$ can be obtained. Following similar procedures, the asymptotic equivalence of $R_B$ and $R_B^*$ also holds. □

With the conclusions in Propositions 4 and 5, the relations between the average achievable rates of UE over correlated channels, i.e., $R_A$ and $R_B$, and uncorrelated channels, i.e., $R_{A,u}$ and $R_{B,u}$, are presented in the following proposition.

**Proposition 6.** *For a large number of elements, $R_A$ and $R_B$ are asymptotically equivalent to $R_{A,u}$ and $R_{B,u}$, respectively, such that*

$$R_A \sim R_{A,u}, \quad N \to \infty. \tag{4.94a}$$

$$R_B \sim R_{B,u}, \quad N \to \infty. \tag{4.94b}$$

*Proof.* Denote the approximate expression of $R_{A,u}$ derived from the channel hardening effect as $R_{A,u}^{+}$. Referring to Remark 7, we have $R_A^{+} = R_{A,u}^{+}$. Then, following similar procedures as in Propositions 4 and 5, we can obtain $R_A \sim R_{A,u}$ as $N \to \infty$. Following similar procedures, the asymptotic equivalence of $R_B$ and $R_{B,u}$ also holds. □

## 4.4 Numerical Results

In this section, we present numerical results to evaluate the accuracy of the proposed analysis by Monte Carlo (MC) simulations and show the impact of channel correlation on the system performance. Unless otherwise stated, the distances of the TX-RIS and RIS-UE channels are set as $d_h = 10\,\text{m}$ and $d_g = 15\,\text{m}$. The path loss per unit distance of the LoS and Rayleigh fading scenarios are given as $\Lambda_A = \Lambda_B = -20\,\text{dB}$. The path loss exponent of the fading scenario is $\chi = 3$. The outage SNR threshold is $\bar{\gamma} = 0\,\text{dB}$. The carrier frequency is 3 GHz with the wavelength $\lambda = 0.1\,\text{m}$. Each RIS element is of size $l = \frac{\lambda}{4}$ and $w = \frac{\lambda}{4}$. The AWGN power is $\sigma_0^2 = -50\,\text{dBm}$. The correlated Rayleigh random variables can be generated by generating the correlated Gaussian random variables following the method proposed in [89]. The correlated Nakagami-$m$ random

variables can be generated by using the property of the Nakagami-$m$ distribution. Since the square of a Nakagami-$m$ random variable can be written as the sum of the squares of the Rayleigh random variables, the correlated Nakagami-$m$ random variable can be generated by using the correlated Rayleigh random variables. The detailed procedures are given in [90].

### 4.4.1 Outage Probability Analysis

Fig. 4.3 illustrates the outage probability versus the transmit power of the proposed RIS-assisted communication system over correlated Rayleigh fading channels. RIS elements are assumed to be placed in a uniform rectangular array with five elements per column, i.e., $N_v = 5$. The number of elements per row varies in $N_h \in \{10, 20\}$. Hence, the number of RIS elements varies in $N \in \{50, 100\}$. The outage probability of UE when the channels are assumed to be uncorrelated is given as a benchmark. As shown in Fig. 4.3, channel correlations deteriorate the outage performance. For example, when the transmit power is $P = 0\,\text{dBm}$ and $N = 100$, the outage probability is $10^{-4}$ and 0.02 for uncorrelated channels and correlated channels, respectively. To illustrate the impact of element spacing, we fix the element size and increase the inter-element distance by 1 cm. The outage curves for larger element spacing are labelled 'Larger Distance'. Increasing the spacing will lead to better outage performance.

Fig. 4.4 shows the outage probability verses the transmit power of UE over correlated Nakagami-$m$ fading channels. RIS elements are deployed in a compact rectangular array with five elements per column, i.e., $N_v = 5$. The number of RIS elements per row varies in $N_h \in \{10, 20\}$. The Nakagami-$m$ shape parameters are set to be $a_{h,B} = a_{g,B} = 2$. The power correlation coefficient of the channels associated with the nearest neighboring elements varies in $\rho \in \{0.3, 0.5\}$. To illustrate the impact of channel correlations on the communication performance, a benchmark that all the channels are assumed to be uncorrelated is given for comparison. As illustrated in

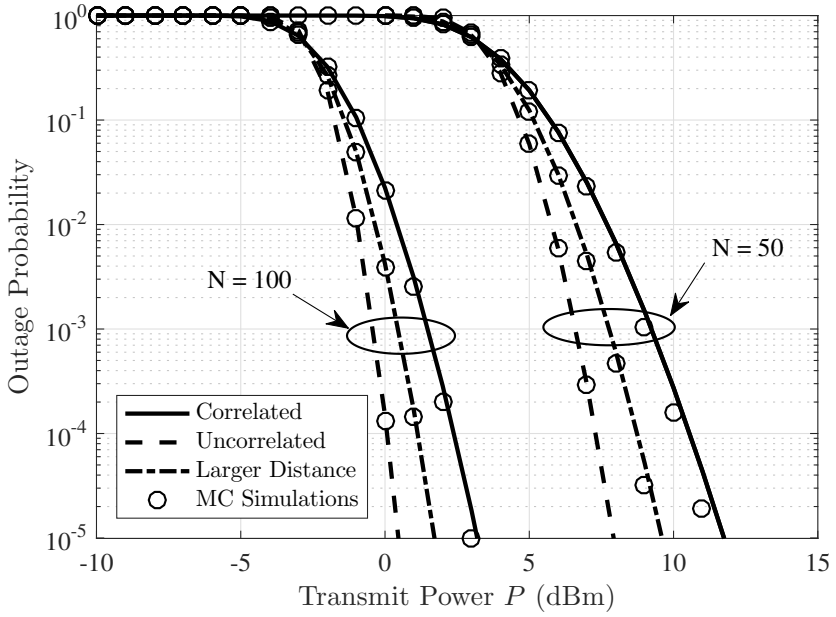



Figure 4.3: Outage probability versus transmit power $P$ for different $N$ over correlated Rayleigh fading channels.

Fig. 4.4, increasing the number of RIS elements can improve the communication performance. In other words, the lower outage probability can be achieved with a larger number of RIS elements. For example, to achieve the outage probability of $10^{-3}$ when $\rho = 0.3$, the required transmit power is $P = 6\,\text{dBm}$ and $P = -1\,\text{dBm}$ for $N = 50$ and $N = 100$, respectively. As expected, channel correlation has a negative impact on the system performance, and decreasing $\rho$ is beneficial for the communication performance. When the transmit power is $P = 5\,\text{dBm}$ and the number of elements is $N = 50$, the outage probability is 0.06, 0.01, and $5 \times 10^{-5}$ for $\rho = 0.5$, $\rho = 0.3$, and uncorrelated channels, respectively. It is worth noting that the proposed gamma approximation is more accurate for the case of uncorrelated channels than the case of correlated channels, especially in the large transmit power regime. And, the approximation is more accurate for a larger number of RIS elements. This is due to not only the approximation errors arising from approximating the composite channel gain as a gamma random variable, but also the errors brought by the correlated Nakagami-$m$ random variables generation method [90]. However, the proposed method already

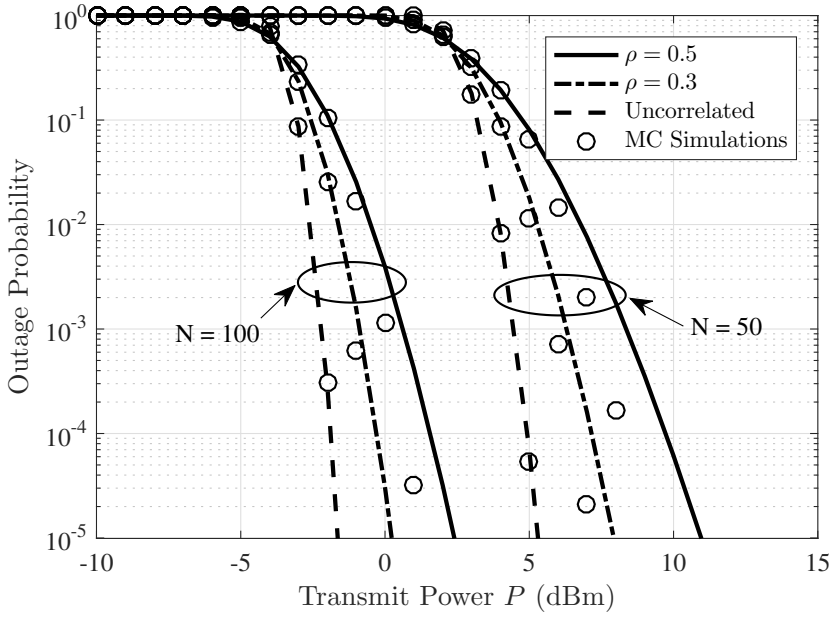



Figure 4.4: Outage probability versus transmit power $P$ for different $N$ over correlated Nakagami-$m$ fading channels.

provided us with expressions in concise form, which can demonstrate the impacts of channel correlations on the system performance. The approximation gap is less than 1 dBm for the same outage probability when $N = 100$.

### 4.4.2 Average Achievable Rate Analysis

The relation between the average achievable rates and the transmit power of UE over correlated Rayleigh fading channels is explored in Fig. 4.5. Regarding the RIS, the number of elements per column is $N_v = 5$, and the number of elements per row varies in $N_h \in \{10, 15, 20\}$. In the legend, 'Upper Bound' and 'Approximation' represent the upper bound and approximation derived in (4.77) and (4.81), respectively. As illustrated in Fig. 4.5, the proposed upper bound and approximation are both very accurate, matching very well with the MC simulation results. The average achievable rate of UE increases with the transmit power, and increasing the number of RIS elements will lead to better communication performance. For example, when the transmit power is $P = 15$ dBm, the average achievable rates are 4 bits/s/Hz and

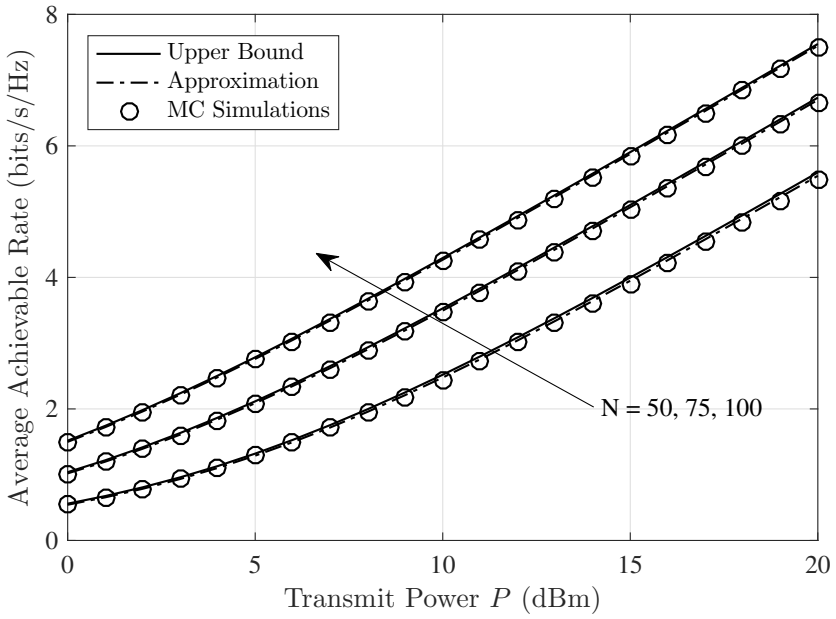



Figure 4.5: Average achievable rates versus transmit power $P$ for different $N$ over correlated Rayleigh fading channels.

6 bits/s/Hz for $N = 50$ and $N = 100$, respectively.

Similarly, Fig. 4.6 shows the average achievable rates versus the transmit power of UE over correlated Nakagami-$m$ fading channels. The RIS configuration is $N_v = 5$ and $N_h = 10$. The shape parameters of the Nakagami-$m$ distribution vary in $a_{h,B}, a_{g,B} \in \{2, 4\}$, and $\rho = 0.5$. Similar to the case of Rayleigh fading channels, the proposed upper bound and approximation are in good agreement with the simulation results for the correlated Nakagami-$m$ fading channels. As expected, larger Nakagami-$m$ shape parameters will lead to better communication performance due to better channel conditions. For example, when the transmit power is $P = 10$ dBm, the average achievable rates are 2.7 bits/s/Hz and 2.9 bits/s/Hz for $a_{h,B} = a_{g,B} = 2$ and $a_{h,B} = a_{g,B} = 4$, respectively.

Fig. 4.7 investigates the asymptotic behavior of the average achievable rates over correlated and uncorrelated Rayleigh fading channels. The number of elements per column is $N_v = 5$, and the number of elements per row varies in $N_h \in (2, 20)$. $P = 20$ dBm. As shown in Fig. 4.7, the average achievable rates of uncorrelated and

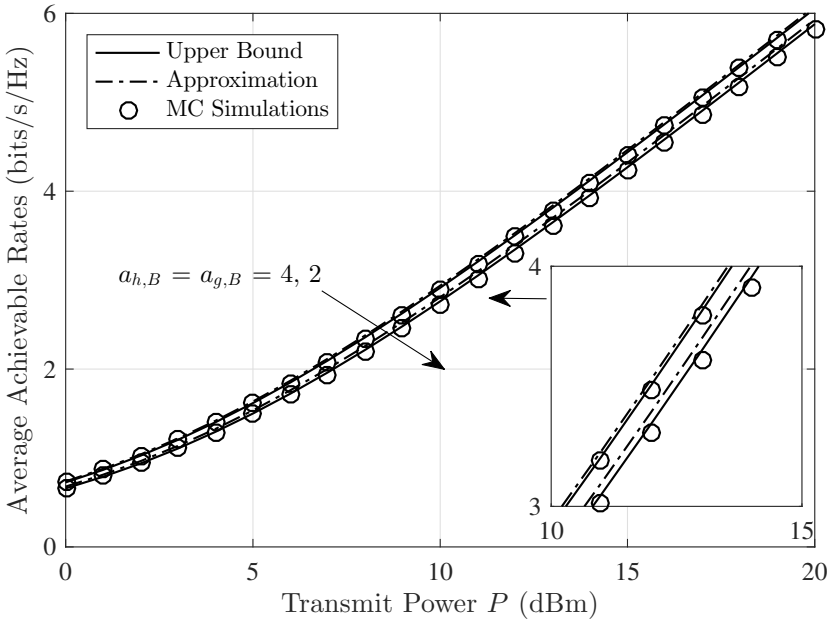



Figure 4.6: Average achievable rates versus transmit power $P$ for different shape parameters over correlated Nakagami-$m$ fading channels.

correlated channels are close to each other, even for a small number of elements. For example, when $N = 20$, the performance gap is 0.042 bit/s/Hz. Moreover, the performance gap of the average achievable rates between uncorrelated and correlated channels decreases with an increase in the number of elements, as expected from Proposition 6. For example, for $N = 90$, the performance gap decreases to 0.021 bit/s/Hz. Similar phenomenon also can be observed from Fig. 4.8, which shows the average achievable rates over correlated and uncorrelated Nakagami-$m$ fading channels. The performance gap decreases from 0.055 bit/s/Hz to 0.038 bit/s/Hz when the number of elements increases from $N = 20$ to $N = 60$.

## 4.5 Summary

In this chapter, we studied the performance of a RIS-assisted communication system over correlated channels. Two channel models, i.e., Rayleigh fading channel model and Nakagami-$m$ fading channel model, were both considered. Specifically, the out-

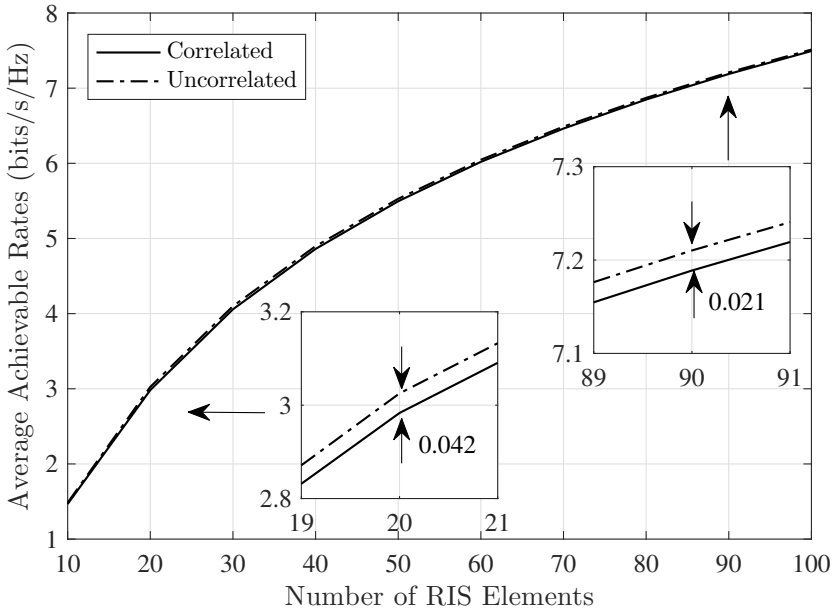



Figure 4.7: Average achievable rates versus the number of RIS elements $N$ over correlated and uncorrelated Rayleigh fading channels.

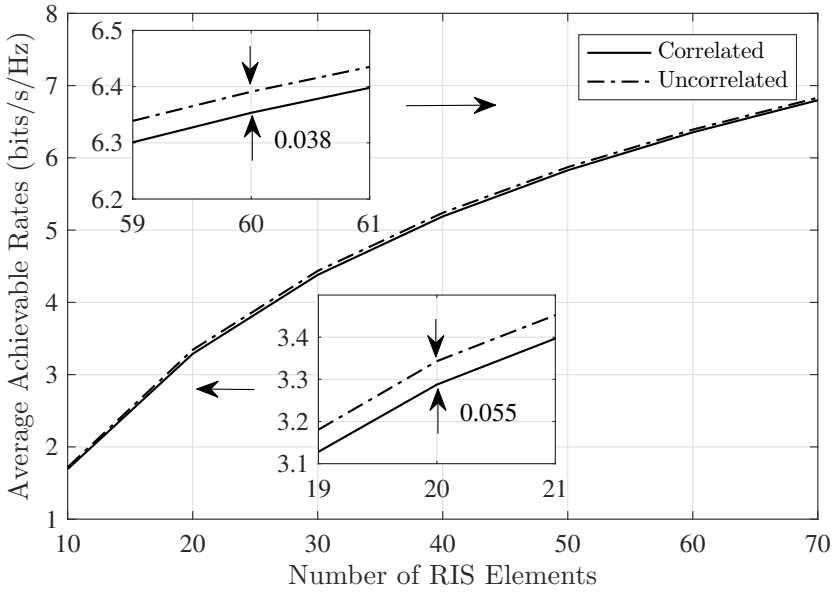



Figure 4.8: Average achievable rates versus the number of RIS elements $N$ over correlated and uncorrelated Nakagami-$m$ fading channels.

age probability expressions were derived using a moment-matching method based on gamma distribution. Also, we investigated an upper bound on the average achievable rates using Jensen's inequality. The channel hardening effect in the proposed system was exploited, from which an approximation on the average achievable rates was derived. The proposed upper bound and approximation were proved to be asymptotically equivalent. We also proved that the average achievable rates with correlated and uncorrelated channels are asymptotically equivalent for a large number of elements. It was shown that channel correlations lead to performance degradation, and the performance loss in terms of the average achievable rates can be offset by increasing the number of elements.

## 4.6 Appendices

### 4.6.1 Proof of the Proposition 3

To begin with, a Lemma regarding the sum of correlated random variables is presented as follows.

**Lemma 3.** *Consider a sequence of random variables* $\{W_k\}$*. If* $\{W_k\}$ *satisfies*

- $\mathbb{E}[W_k] = a$,
- $\mathrm{Var}[W_k]$ *is bounded,*
- $\mathrm{Cov}\{W_i, W_j\} \to 0$ *as* $|i-j| \to \infty$,

*then,*

$$\frac{1}{K}\sum_{k=1}^{K} W_k \xrightarrow{P} a,\ K \to \infty, \tag{4.95}$$

*with the convergence in probability.*

*Proof.* Since the variance is bounded, the covariance of $W_i$ and $W_j$ is bounded as

$$\mathrm{Cov}\left\{W_i, W_j\right\} \leq c_0, \tag{4.96}$$

where $c_0$ is a constant. Denoting $V_K = \sum_{k=1}^{K} W_k$, the variance of $V_K$ can be written as

$$\begin{aligned}\mathrm{var}[V_K] &= \sum_{k=1}^{K} \mathrm{Cov}\left\{W_k, W_k\right\} + 2\sum_{i=1}^{K-1}\sum_{j=i+1}^{K} \mathrm{Cov}\left\{W_i, W_j\right\} \\ &\leq Kc_0 + 2\sum_{i=1}^{K-1}\sum_{j=i+1}^{K} \mathrm{Cov}\left\{W_i, W_j\right\}. \end{aligned} \tag{4.97}$$

Since $\mathrm{Cov}\left\{W_i, W_j\right\} \to 0$ when $|i-j| \to \infty$, we can find $K_0$ such that for $|i-j| > K_0$, $\mathrm{Cov}\left\{W_i, W_j\right\} < \varepsilon$, for any $\varepsilon > 0$. Hence,

$$\begin{aligned}&\left|\sum_{i=1}^{K-1}\sum_{j=i+1}^{K} \mathrm{Cov}\left\{W_i, W_j\right\}\right| \\ \leq &\left|\sum_{i=1}^{K-1}\sum_{j=i+1}^{i+K_0} \mathrm{Cov}\left\{W_i, W_j\right\}\right| + \left|\sum_{i=1}^{K-1}\sum_{j=i+K_0+1}^{K} \mathrm{Cov}\left\{W_i, W_j\right\}\right| \\ \leq &KK_0c_0 + K^2\varepsilon. \end{aligned} \tag{4.98}$$

Therefore, the variance of $V_K/K$ satisfies

$$\mathrm{Var}\left[\frac{V_K}{K}\right] \leq \frac{c_0}{K} + \frac{2K_0c_0}{K} + 2\varepsilon. \tag{4.99}$$

It can be seen that $\mathrm{Var}\left[\frac{V_K}{K}\right] \to 0$, as $K \to \infty$. Thus, the proof of Lemma 3 is complete. □

The composite channel gain of the Rayleigh fading model $H_A$ is analyzed first. Let $Y_n = |h_{A,n}||g_{A,n}|$. We can have

$$\mathbb{E}[Y_n] = \frac{\pi}{4}, \tag{4.100}$$

and the variance of $Y_n$ is bounded. Covariance of $\{Y_i, Y_j\}$ can be written as

$$\mathrm{Cov}\{Y_i, Y_j\} = \mathbb{E}\left[|h_{A,i}||g_{A,i}||h_{A,j}||g_{A,j}|\right] - \mathbb{E}\left[|h_{A,i}||g_{A,i}|\right]\mathbb{E}\left[|h_{A,j}||g_{A,j}|\right]. \tag{4.101}$$

It can be learned that

$$\mathbb{E}\left[|w_{A,i}||w_{A,j}|\right] \to \mathbb{E}\left[|w_{A,i}|\right]\mathbb{E}\left[|w_{A,j}|\right] = \frac{\pi}{4}, \quad |i-j| \to \infty, \tag{4.102}$$

where $w \in \{h, g\}$. Thus, it can be proved that

$$\mathrm{Cov}\{Y_i, Y_j\} \to 0, \quad |i-j| \to \infty. \tag{4.103}$$

Hence, using Lemma 3, we obtain

$$\frac{1}{N}\sum_{n=1}^{N} |h_{A,n}|\,|g_{A,n}| \xrightarrow{P} \frac{\pi}{4}, \quad N \to \infty. \tag{4.104}$$

Following the similar procedures, (4.79b) can be also obtained for the correlated Nakagami-$m$ fading channel model.

# Chapter 5

# RIS-Assisted Spectral Efficiency Techniques

The impacts of phase errors and channel correlations have been discussed and analyzed in Chapter 3 and Chapter 4, respectively. Furthermore, we have shown that the performance degradation due to phase errors and channel correlations can be decreased by increasing the phase shifting levels and the number of RIS elements, respectively. However, apart from the above analysis focusing on the scenario with a single transmitter and a single receiver, RIS-assisted communication systems should be considered and studied in more sophisticated and practical scenarios to incorporate more realistic factors into next-generation wireless communication network models. Specifically, a wide range of physical layer technologies have been applied in wireless communication networks to improve spectral efficiency and enhance communication reliability. As a potential technology for next generation wireless networks, whether the RIS can be applied in these existing technologies seamlessly remains an open problem.

Among various spectral efficiency technologies, non-orthogonal multiple access (NOMA) has been regarded as a superior multiple access technology in future wire-

less networks due to its promising advantages in terms of spectrum efficiency [91–93]. For example, multiple users could share the same resource block simultaneously in NOMA [94]. As pointed out in [95], NOMA has better performance than orthogonal multiple access (OMA) when the channels gains of users are remarkably different. Conventionally, the channel gains of the users are determined by the uncontrollable wireless propagation environment [96, 97]. Hence, the applications of NOMA are limited in conventional wireless networks [98]. To further improve the performance of NOMA, RIS has been integrated into NOMA communication systems to broaden the applications of NOMA due to the ability of RIS to reconfigure the channels. For example, the authors in [99] proposed a RIS-assisted NOMA network where each element of the RIS applies 1-bit coding scheme to serve the cell-edge users. The authors in [100] proposed a priority oriented design where the RIS is controlled to boost the channel of the prioritized NOMA user and evaluated the system performance. Considering coherent and random phase shifting, the authors in [101] examined the impact of these two phase-shifting schemes on the outage performance of a RIS-assisted NOMA system using the central limit theorem (CLT). The authors in [102] designed a passive beamforming algorithm for a RIS-assisted NOMA network to minimize the power consumption of the transmitter. Apart from designing beamforming algorithms to optimize the system performance, a direct performance analysis of RIS-assisted NOMA systems requires more investigation. Furthermore, as a counterpart of RIS-assisted NOMA, the performance of RIS-assisted time-division multiple access (TDMA) should be carefully compared with RIS-assisted NOMA to figure out which technology can provide better performance.

Apart from NOMA, full-duplex (FD) communication technology is regarded as another promising wireless communication technology for future networks, even though the idea of FD communication is old. Contrary to the conventional half-duplex (HD) system, the FD system enables signal transmission and reception with the

same time and frequency resource block, thus boosting spectral efficiency. Therefore, RIS-assisted FD communication has become an attractive research topic in academia and has been regarded as an important supplement in future wireless communication networks. RIS-assisted FD communication was first proposed in [103]. The authors maximized the sum rate by jointly optimizing the beamforming vectors at users and the phase shifting matrix at the RIS for a RIS-assisted FD multiple-input multiple-output (MIMO) communication system. The authors in [63] proposed a RIS-assisted FD system, where an FD transceiver simultaneously serves a downlink user and an uplink user over the same frequency band. The total power consumption was minimized by jointly optimizing the transmit power of uplink and downlink transmissions and the reflecting coefficients of the RISs. The authors in [104] proposed a RIS-assisted FD communication system where two RISs were deployed to serve two end users separately. Outage probability and symbol error probability were then derived in closed form. However, it is worth noting that self-interference (SI) from the transmit antenna to the receive antenna of a device can only partially be eliminated in practice, which will lead to performance degradation. If the residual SI is significant, an FD communication system may perform even worse than an HD communication system. Therefore, it is necessary to model the SI appropriately, carry out a performance analysis of RIS-assisted FD communication systems, and study the residual SI threshold below which the FD communication outperforms its HD counterpart.

Therefore, in this chapter, we study the performance of a RIS-assisted NOMA communication system and a RIS-assisted FD communication system to advance our knowledge of practical applications of RIS technology. The main contributions are listed as follows:

- A downlink RIS-assisted NOMA communication system is presented. Assuming that a priority-oriented phase shifting scheme is applied at the RIS, the outage probability of the users with strong and weak channel conditions are derived.

The performance of RIS-assisted NOMA and RIS-assisted TDMA are compared in terms of the average achievable rates, and it is proved that RIS-assisted NOMA does not always perform better than OMA due to the reconfigurability of RIS in different time slots. The mathematical condition at which RIS-assisted NOMA has a higher sum rate is given through theoretical analysis.

- A RIS-assisted FD communication network is also proposed, where an FD transceiver communicates with a downlink user and an uplink user simultaneously within the same frequency band. Two RISs are set to serve the uplink and downlink users individually. The outage probability of the uplink and downlink transmissions are obtained in closed form. The impact of the residual SI is discussed, and the residual SI threshold below which the FD communication outperforms the HD counterpart is given.

## 5.1 System Framework

In this section, a RIS-assisted NOMA communication system and a RIS-assisted FD communication system are introduced.

### 5.1.1 RIS-Assisted NOMA Communication

As shown in Fig. 5.1, a single-antenna transmitter (TX) communicates with two single-antenna users, i.e., $U_t$ and $U_r$. Two users are located on the same side of the RIS. It is assumed that obstacles block the direct links from the TX to the users. Each RIS element is able to adjust the phase shift independently without energy dissipation. Denoting the phase shift imposed on the incident signal by the $n$th element as $\theta_n$, the RIS coefficients matrix can be written as

$$\mathbf{\Theta} = \text{diag}\left(e^{j\theta_1}, ..., e^{j\theta_N}\right). \tag{5.1}$$

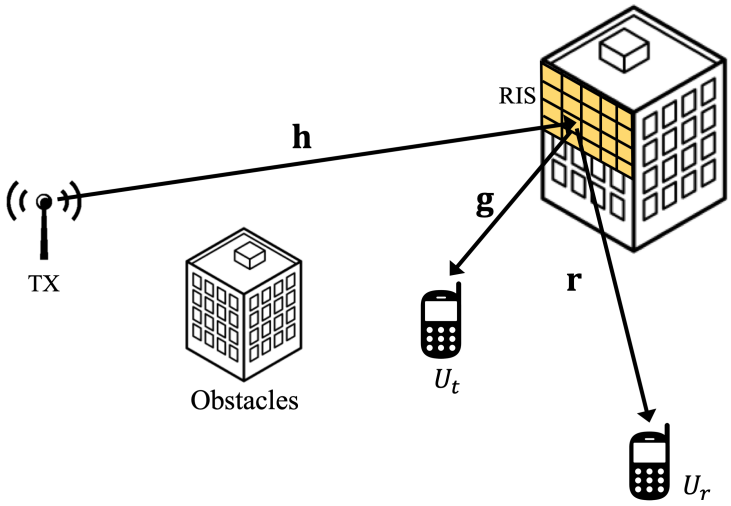



Figure 5.1: System model of RIS-assisted NOMA communication system.

Let $\mathbf{h} = (h_1, ..., h_N)^T \in \mathbb{C}^{N\times 1}$, $\mathbf{g} = (g_1, ..., g_N)^T \in \mathbb{C}^{N\times 1}$ and $\mathbf{r} = (r_1, ..., r_N)^T \in \mathbb{C}^{N\times 1}$ denote the normalized small scale fading of the TX-RIS, RIS-$U_t$ and RIS-$U_r$ channels, respectively. RIS operates in the far-field of TX and users. An i.i.d. Nakagami-$m$ fading channel model is applied. Specifically,

$$|h_n| \sim \text{Nakagami}(a_h, 1), \tag{5.2a}$$

$$|g_n| \sim \text{Nakagami}(a_g, 1), \tag{5.2b}$$

$$|r_n| \sim \text{Nakagami}(a_r, 1), \tag{5.2c}$$

where $n \in \{1, ..., N\}$; $a_h$, $a_g$ and $a_r$ are the shape parameters of the corresponding channels. All the channels in the proposed system are independent to each other. The path loss of the TX-RIS-$U_t$ and TX-RIS-$U_r$ links can be written as [62]

$$\beta_t = \frac{\Lambda_t}{d_h^\chi d_g^\chi}, \ \beta_r = \frac{\Lambda_r}{d_h^\chi d_r^\chi}, \tag{5.3}$$

where $\Lambda_t$ and $\Lambda_r$ stand for the path loss at a reference distance of 1 m of the TX-RIS-$U_t$ and TX-RIS-$U_r$ links, respectively; $\chi$ is the path loss exponent; $d_h$, $d_g$ and $d_r$ denote the distances of the TX-RIS, RIS-$U_t$ and RIS-$U_r$ links, respectively.

In the NOMA transmission scheme, TX broadcasts the superimposed signals of the two users[1] as

$$s = \sqrt{P}\left(q_t s_t + q_r s_r\right), \tag{5.4}$$

where $s_t$ and $s_r$ denote the signals of $U_t$ and $U_r$ with unit power, i.e., $\mathbb{E}[|s_t|^2] = \mathbb{E}[|s_r|^2] = 1$. $P$ is the total transmit power of TX; $q_t$ and $q_r$ are the transmit amplitude coefficients for $U_t$ and $U_r$ at TX, satisfying

$$q_t^2 + q_r^2 = 1. \tag{5.5}$$

Hence, the received signals at $U_t$ and $U_r$ can be written as

$$y_t = \sqrt{\beta_t}\mathbf{g}^T\mathbf{\Theta}\mathbf{h}\sqrt{P}\left(q_t s_t + q_r s_r\right) + n_t, \tag{5.6a}$$

$$y_r = \sqrt{\beta_r}\mathbf{r}^T\mathbf{\Theta}\mathbf{h}\sqrt{P}\left(q_t s_t + q_r s_r\right) + n_r, \tag{5.6b}$$

where $n_t$ and $n_r$ are the additive white Gaussian noise (AWGN) at $U_t$ and $U_r$ with zero mean and variance $\sigma_0^2$.

In the NOMA transmission scheme, one of the two users performs successive interference cancellation (SIC) by decoding the other user's signal, subtracting it from the received signal, and decoding its own signal. The optimal decoding order corresponds to the ascending order of the channel gains of the two users. However, the order of the channel gains is dictated by the small scale fading which fluctuates quickly and renders the analysis and implementation complicated. It is worth highlighting that we do not aim to investigate the optimal decoding order in this work. Alternatively, we assume the distance of the RIS-$U_t$ channel is smaller than that of the RIS-$U_r$ chan-

[1]Note that more than two users can be selected to perform NOMA, but the performance might be degraded since the co-channel interference of the NOMA scheme can be severe and the SIC can be very complex. To optimize the performance of NOMA, hybrid NOMA can be implemented, by combining NOMA with conventional OMA, such as TDMA, FDMA.

nel[2], and the decoding order is fixed as ($U_r$, $U_t$). Specifically, $U_r$ decodes its signal directly by treating the signal of $U_t$ as interference, and $U_t$ performs SIC. This assumption is also adopted in many other similar works, such as [94, 98, 99, 106]. Based on the principles of NOMA transmission scheme, $U_r$ is allocated with more transmit power to ensure that $U_t$ could perform SIC successfully, i.e., $q_t < q_r$. Hence, the signal-to-interference-plus-noise ratio (SINR) of $U_t$ decoding the signal of user $U_r$ in the SIC process can be written as

$$\gamma_s = \frac{\gamma_{t\to r}^{(s)}}{\gamma_{t\to r}^{(i)}} = \frac{Pq_r^2\beta_t \left|\mathbf{g}^T\mathbf{\Theta}\mathbf{h}\right|^2}{Pq_t^2\beta_t \left|\mathbf{g}^T\mathbf{\Theta}\mathbf{h}\right|^2 + \sigma_0^2}. \tag{5.7}$$

After subtracting the signal of $U_r$ from the received signal, $U_t$ is able to decode its own signal with signal-to-noise ratio (SNR)

$$\gamma_t = \gamma_0 q_t^2\beta_t \left|\mathbf{g}^T\mathbf{\Theta}\mathbf{h}\right|^2, \tag{5.8}$$

where $\gamma_0 = P/\sigma_0^2$ is the transmit SNR at TX. On the other hand, $U_r$ decodes its own signal directly with SINR

$$\gamma_r = \frac{\gamma_r^{(s)}}{\gamma_r^{(i)}} = \frac{Pq_r^2\beta_r \left|\mathbf{r}^T\mathbf{\Theta}\mathbf{h}\right|^2}{Pq_t^2\beta_r \left|\mathbf{r}^T\mathbf{\Theta}\mathbf{h}\right|^2 + \sigma_0^2}. \tag{5.9}$$

By using the priority oriented NOMA scheme proposed in [100, 107], the phase shifts of RIS are adjusted to boost the composite channel gain of the user with better channel gain, namely, $U_t$. Hence, the phase shift of each RIS element can be given as

$$\theta_n = -\arg\left(h_n\right) - \arg\left(g_n\right),\ n \in \{1, ..., N\}. \tag{5.10}$$

[2]In practice, the locations of different users can be readily obtained from a location information system, such as GPS [105].

After phase adjustment, $\gamma_t$, $\gamma_s$ and $\gamma_r$ can be rewritten as

$$\gamma_t = \gamma_0 q_t^2 \beta_t H_t^2, \tag{5.11a}$$

$$\gamma_s = \frac{\gamma_{t\to r}^{(s)}}{\gamma_{t\to r}^{(i)}} = \frac{P q_r^2 \beta_t H_t^2}{P q_t^2 \beta_t H_t^2 + \sigma_0^2}, \tag{5.11b}$$

$$\gamma_r = \frac{\gamma_r^{(s)}}{\gamma_r^{(i)}} = \frac{P q_r^2 \beta_r H_r^2}{P q_t^2 \beta_r H_r^2 + \sigma_0^2}, \tag{5.11c}$$

where

$$H_t = \sum_{n=1}^{N} |g_n| \, |h_n| \,, \tag{5.12}$$

$$H_r = |\tilde{H}_r| = \left| \sum_{n=1}^{N} |r_n| \, |h_n| \, e^{j\phi_n^r} \right|. \tag{5.13}$$

Since the channels $\mathbf{h}$, $\mathbf{g}$ and $\mathbf{r}$ are independent with each other, and the phase shifts of the RIS are manipulated to boost the TX-RIS-$U_t$ channel, it can be observed that $\phi_n^r$, $n \in \{1, 2, ..., N\}$, are i.i.d. random variables that follow the uniform distribution over $[-\pi, \pi)$.

### 5.1.2 RIS-Assisted FD Communication

As shown in Fig. 5.2, a RIS-assisted FD wireless communication network is studied, in which an uplink (UL) user $U_A$ and a downlink (DL) user $U_B$ are served by a transceiver simultaneously. $U_A$ and $U_B$ are equipped with a single transmit antenna and a single receive antenna respectively, while TX has two antennas, one each for signal transmission and reception, operating in the FD mode. Since both users are assumed to be cell-edge users, two RISs, $S_A$ and $S_B$, are deployed in close proximity to $U_A$ and $U_B$ respectively for improving the wireless propagation environment by tuning the phases of the corresponding channels. The direct links between TX and users are assumed to be absent due to obstacles, large path loss and/or shadowing

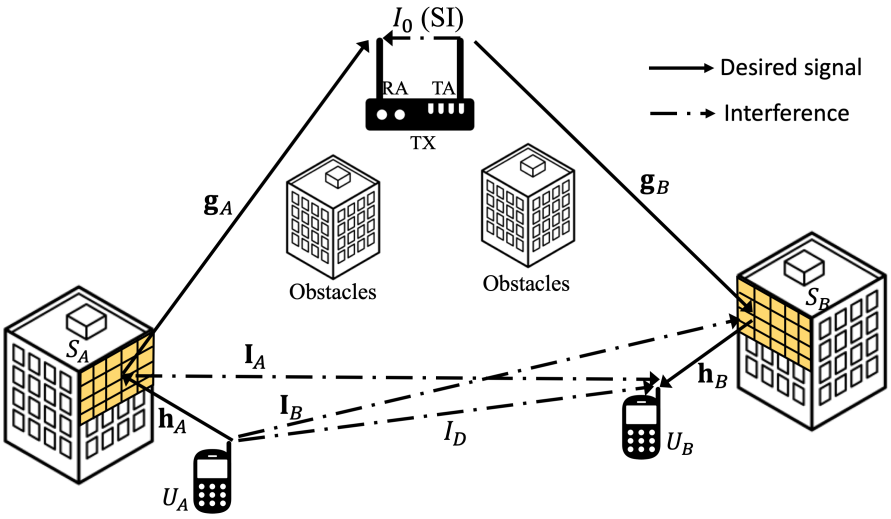



Figure 5.2: System model of RIS-assisted FD communication system.

effects. Two RISs, $S_A$ and $S_B$, are placed near their corresponding users to enhance the communication performance. $S_u$, $u \in \{A, B\}$ contains $N_u$ elements. Assuming that each element of $S_u$ is able to perform independent passive phase shifting without energy dissipation, the passive beamforming matrix of $S_u$ can be given as

$$\mathbf{\Theta}_u = \text{diag}\left(e^{j\theta_{1,u}}, ..., e^{j\theta_{N_u,u}}\right), \tag{5.14}$$

where $\theta_{n,u}$, $n \in \{1, 2, ..., N_u\}$ is the phase shift angle of the $n$th element of $S_u$.

Let $\mathbf{h}_u = (h_{1,u}, ..., h_{N_u,u})^T \in \mathbb{C}^{N_u \times 1}$, $\mathbf{g}_u = (g_{1,u}, ..., g_{N_u,u})^T \in \mathbb{C}^{N_u \times 1}$ and $\mathbf{I}_u = (I_{1,u}, ..., I_{N_u,u})^T \in \mathbb{C}^{N_u \times 1}$ represent the normalized small scale fading of the $S_u$-$U_u$, $S_u$-TX and $S_u$-$U_{u'}$ channels, respectively, where $u \in \{A, B\}$ and $u' \in \{A, B\} \backslash u$. Both RISs work in the far field of TX and users, and the i.i.d. Nakagami-$m$ fading model is applied. Specifically,

$$|h_{n,u}| \sim \text{Nakagami}(a_{h,u}, 1), \tag{5.15a}$$

$$|g_{n,u}| \sim \text{Nakagami}(a_{g,u}, 1), \tag{5.15b}$$

$$|I_{n,u}| \sim \text{Nakagami}(a_{I,u}, 1), \tag{5.15c}$$

where $n \in \{1, ..., N_u\}$; $a_{h,u}$, $a_{g,u}$ and $a_{I,u}$ are the shape parameters of the corresponding channels. $|h_{n,u}|$, $|g_{n,u}|$ and $|I_{n,u}|$ have the same unit scale parameters.

The normalized small scale fading of the $U_A$-$U_B$ channel and the SI channel from the transmit antenna (TA) to the receive antenna (RA) at TX are denoted as $I_D$ and $I_0$, respectively. $I_D$ is circularly symmetric complex Gaussian (CSCG) distributed with unit power such that $I_D \sim \mathcal{CN}(0, 1)$, thus $|I_D|$ is Rayleigh distributed, i.e., $|I_D| \sim \mathcal{R}(\sqrt{2}/2)$. It is assumed that $S_A$ and $S_B$ are sufficiently far from $U_B$ and $U_A$, respectively [108]. Furthermore, $U_A$ and $U_B$ are assumed to be two cell-edge users assisted by RISs which are sufficiently far from TX [109]. Therefore, the channel that $S_A$ reflects the signal from TX to $U_B$, the channel that $S_B$ reflects the signal from $U_A$ to TX, and the channel that $S_B$ reflects back the signal from TX to itself can be ignored due to the long distances [63].

The path loss of the $U_u$-$S_u$-TX, $U_A$-$S_u$-$U_B$ and $U_A$-$U_B$ channels, where $u \in \{A, B\}$, can be given respectively as [110]

$$\beta_u = \frac{\Lambda_u}{d_{h,u}^{\chi} d_{g,u}^{\chi}}, \quad \beta_{I,u} = \frac{\Lambda_{I,u}}{d_{h,u}^{\chi} d_{I,u}^{\chi}}, \quad \beta_D = \frac{\Lambda_D}{d_0^{\chi}}. \tag{5.16}$$

where $\Lambda_u$, $\Lambda_{I,u}$ and $\Lambda_D$ are the path loss per unit distance of the $U_u$-$S_u$-TX, $U_A$-$S_u$-$U_B$ and $U_A$-$U_B$ channels, respectively; $d_{h,u}$, $d_{g,u}$, $d_{I,u}$ and $d_0$ denote respectively the distances of the $S_u$-$U_u$, $S_u$-TX, $S_u$-$U_{u'}$ and $U_A$-$U_B$ links, where $u \in \{A, B\}$ and $u' \in \{A, B\} \backslash u$; $\chi$ stands for the path loss exponent.

The received signal at TX from the uplink transmission and received by $U_B$ from the downlink transmission are introduced separately. The received signal at TX can be given as

$$y_T = \mathbf{g}_A^T \mathbf{\Theta}_A \mathbf{h}_A \sqrt{P_A \beta_A} s_A + I_0 \sqrt{P_T} s_T + n_T, \tag{5.17}$$

where the first term and the second term refer to the desired signal and the SI, respectively; $P_A$ and $P_T$ are the transmit power of $U_A$ and TX, respectively; $s_A$ and

$s_T$ are the independent transmit constellation symbols of $U_A$ and TX with unit power such that $\mathbb{E}[|s_A|^2] = \mathbb{E}[|s_T|^2] = 1$ and $\mathbb{E}[s_A s_T] = 0$; $n_T \sim \mathcal{CN}(0, \sigma_T^2)$ is the AWGN with zero mean and variance $\sigma_T^2$. Similar to [108] and [104], it is assumed that $S_A$ only has the channel state information (CSI) of the channels associated with its pairing user $U_A$, which are $\mathbf{g}_A$ and $\mathbf{h}_A$. Therefore, the phase shift of each element on $S_A$ is adjusted to co-phase the reflecting links such that

$$\theta_{n,A} = -\arg(g_{n,A}) - \arg(h_{n,A}), \quad n \in \{1, 2, ..., N_A\}. \tag{5.18}$$

After proper phase shifting, the received signal at TX can be rewritten as

$$y_T = H_A \sqrt{P_A \beta_A} s_A + I_0 \sqrt{P_T} s_T + n_T, \tag{5.19}$$

where

$$H_A = \sum_{n=1}^{N_A} |g_{n,A}||h_{n,A}|. \tag{5.20}$$

Thus, the received SINR of the uplink transmission from $U_A$ to TX can be written as

$$\gamma_A = \frac{P_A \beta_A H_A^2}{P_T |I_0|^2 + \sigma_T^2}. \tag{5.21}$$

In practice, several SI cancellation techniques can be applied to alleviate the SI and lead to the residual SI [111]. Among different frameworks used in existing works to model the residual SI for FD communication, in this paper, we adopt the model where the residual SI is modelled as a Gaussian random variable with zero mean and variance $\sigma_l^2$ [112]. The variance depends on the transmit power and is modeled as

$$\sigma_l^2 = \varpi P_T^{\epsilon}, \tag{5.22}$$

where the two parameters, $\varpi > 0$ and $\epsilon \in [0, 1]$, depend on the SI cancellation method

used at TX [113]. After several stages of SI cancellation, the received SINR of TX can be rewritten as

$$\gamma_A = \frac{P_A \beta_A H_A^2}{\sigma_l^2 + \sigma_T^2}. \tag{5.23}$$

The received signal at $U_B$ can be expressed as

$$y_B = \mathbf{h}_B^T \mathbf{\Theta}_B \mathbf{g}_B \sqrt{P_T \beta_B} s_T + \tilde{I} \sqrt{P_A} s_A + n_B, \tag{5.24}$$

where

$$\tilde{I} = \sqrt{\beta_{I,A}} \mathbf{I}_A^T \mathbf{\Theta}_A \mathbf{h}_A + \sqrt{\beta_{I,B}} \mathbf{h}_B^T \mathbf{\Theta}_B \mathbf{I_B} + \sqrt{\beta_D} I_D, \tag{5.25}$$

in which the first and second terms denote the interference from $U_A$ reflected by $S_A$ and $S_B$, respectively; the third term stands for the interference from $U_A$ transmitted through the direct link. $n_B \sim \mathcal{CN}(0, \sigma_B^2)$ is the AWGN with zero mean and variance $\sigma_B^2$. Similar to $S_A$, $S_B$ can only obtain the CSI of the channels $\mathbf{g}_B$ and $\mathbf{h}_B$ which are the signal transmission channels regarding its pairing user $U_B$, and the phase shifts of elements on $S_B$ are controlled to boost the signal transmission through the channel TX-$S_B$-$U_B$, i.e.,

$$\theta_{n,B} = -\arg(g_{n,B}) - \arg(h_{n,B}), \quad n \in \{1, 2, ..., N_B\}. \tag{5.26}$$

After phase shifting, the received signal at $U_B$ can be rewritten as

$$y_B = H_B \sqrt{P_T \beta_B} s_T + \tilde{I} \sqrt{P_A} s_A + n_B, \tag{5.27}$$

where

$$H_B = \sum_{n=1}^{N_B} |h_{n,B}||g_{n,B}|, \tag{5.28a}$$

$$\tilde{I} = \sqrt{\beta_{I,A}} \sum_{n=1}^{N_A} |I_{n,A}||h_{n,A}| e^{j\phi_{n,A}} + \sqrt{\beta_{I,B}} \sum_{n=1}^{N_B} |h_{n,B}||I_{n,B}| e^{j\phi_{n,B}} + \sqrt{\beta_D}|I_D| e^{j\phi_D}. \tag{5.28b}$$

Since the channels $\mathbf{h}_u$, $\mathbf{g}_u$ and $\mathbf{I}_u$, $u \in \{A, B\}$ are independent with each other, and the phase shifts of $S_A$ and $S_B$ are manipulated respectively to boost the $U_A$-$S_A$-TX and TX-$S_B$-$U_B$ channels, it can be observed that $\phi_{n,u}$, $u \in \{A, B\}$, $n \in \{1, 2, ..., N_u\}$, are i.i.d. random variables which follow the uniform distribution over $[-\pi, \pi)$. Further, due to the distribution of $I_D$, $\phi_D$ is also uniformly distributed over $[-\pi, \pi)$. Hence, the SINR of $U_B$ can be written as

$$\gamma_B = \frac{P_T \beta_B H_B^2}{P_A I + \sigma_B^2}, \tag{5.29}$$

where $I = |\tilde{I}|^2$.

## 5.2 Analysis of RIS-Assisted NOMA

In this section, the performance of a pair of users in the proposed RIS-assisted downlink NOMA network is studied. The closed form expressions of the outage probability of the two users are derived, followed by comparing the performance of RIS-assisted NOMA with RIS-assisted OMA with regard to the average achievable rates.

### 5.2.1 Outage Probability Analysis

To evaluate the outage probability of $U_t$ and $U_r$, the channel distributions of $H_t$ and $H_r$ are first derived, based on which the outage probability expressions of $U_t$ and $U_r$ are obtained.

#### 5.2.1.1 Channel Distribution Analysis

Since $H_t$ is the sum of the products of Nakagami-$m$ random variables, the exact distribution of $H_t$ cannot be obtained in closed form. Hence, we propose a moment matching method based on gamma distribution to fit the distribution of $H_t$.

Since $|h_n|$ and $|g_n|$, $n \in \{1, ..., N\}$ are independent and identically distributed (i.i.d.) Nakagami-$m$ random variables, the mean and second order raw moment of $H_t$ are derived as:

$$\mathbb{E}\left[H_t\right] = \sum_{n=1}^{N} \mathbb{E}\left[|h_n|\right] \mathbb{E}\left[|g_n|\right] = N \frac{\Gamma\left(a_h + \frac{1}{2}\right)}{\Gamma(a_h)} \frac{\Gamma\left(a_g + \frac{1}{2}\right)}{\Gamma(a_g)} \left(\frac{1}{a_h a_g}\right)^{\frac{1}{2}}, \tag{5.30a}$$

$$\begin{aligned} \mathbb{E}\left[H_t^2\right] &= \mathbb{E}\left[\sum_{n=1}^{N} |h_n|^2 |g_n|^2\right] + 2\,\mathbb{E}\left[\sum_{n=1}^{N-1} \sum_{i=n+1}^{N} |h_n|\,|g_n|\,|h_i|\,|g_i|\right] \\ &= N + N(N-1) \left(\frac{\Gamma\left(a_h + \frac{1}{2}\right)}{\Gamma(a_h)} \frac{\Gamma\left(a_g + \frac{1}{2}\right)}{\Gamma(a_g)}\right)^2 \frac{1}{a_h a_g}. \end{aligned} \tag{5.30b}$$

Hence, $H_t$ can be approximated by a gamma random variable with shape and scale parameters:

$$\kappa_t = \frac{\mathbb{E}^2[H_t]}{\mathbb{E}[H_t^2] - \mathbb{E}^2[H_t]}, \tag{5.31a}$$

$$\omega_t = \frac{\mathbb{E}[H_t^2] - \mathbb{E}^2[H_t]}{\mathbb{E}[H_t]}. \tag{5.31b}$$

And, the probability density function (PDF) and cumulative distribution function

(CDF) of $H_t$ can be written as

$$f_{H_t}(x) = \frac{x^{\kappa_t - 1} \exp\left(-x/\omega_t\right)}{\Gamma(\kappa_t)\, \omega_t^{\kappa_t}}, \tag{5.32a}$$

$$F_{H_t}(x) = \frac{\gamma\left(\kappa_t, x/\omega_t\right)}{\Gamma(\kappa_t)}. \tag{5.32b}$$

Regarding the composite channel gain of $U_r$, i.e., $H_r$, a different approach based on the CLT is applied to model the distribution. Since $\phi_n^r$ is uniformly distributed over $[-\pi, \pi)$, the expectation and variance of $|h_n||r_n|\cos(\phi_n^r)$ and $|h_n||r_n|\sin(\phi_n^r)$ can be obtained as

$$\mathbb{E}\left[|h_n||r_n|\cos(\phi_n^r)\right] = \mathbb{E}\left[|h_n||r_n|\sin(\phi_n^r)\right] = 0, \tag{5.33a}$$

$$\mathrm{Var}\left[|h_n||r_n|\cos(\phi_n^r)\right] = \mathrm{Var}\left[|h_n||r_n|\sin(\phi_n^r)\right] = \frac{1}{2}. \tag{5.33b}$$

Using the central limit theorem, for a large number of elements $N$, $\tilde{H}_r$ follows the CSCG distribution

$$\tilde{H}_r = \sum_{n=1}^{N} |r_n|\,|h_n|\, e^{j\phi_n^r} \sim \mathcal{CN}\left(0, N\right). \tag{5.34}$$

Thus, $H_r = |\tilde{H}_r|$ follows the Rayleigh distribution with the distribution parameter

$$\zeta_r = \sqrt{\frac{N}{2}}. \tag{5.35}$$

The PDF and CDF of $H_r$ can be given as

$$f_{H_r}(x) = \frac{2x}{N} e^{-\frac{x^2}{N}}, \tag{5.36a}$$

$$F_{H_r}(x) = 1 - e^{-\frac{x^2}{N}}. \tag{5.36b}$$

**Remark 8.** *Different from the moment matching method based on the gamma distribution used in the analysis of the distribution of $H_t$, the CLT method is used in*

*the analysis of $H_r$. There are several reasons for this change. First, $H_t$ is the sum of positive random variables. Approximating $H_t$ with the gamma distribution is more reasonable because a gamma random variable is also positive. However, the support of a Gaussian random variable is the set of reals. Hence, using the CLT to analyze $H_t$ will lead to significant errors especially in the lower tail of the distribution. This point is also illustrated in [67]. In contrast to $H_t$, the phase of each term in $\tilde{H}_r$ is uniformly distributed over $[-\pi, \pi)$. Therefore, the real and imaginary parts of $\tilde{H}_r$ are both supported on the real line, and using the CLT to approximate $\tilde{H}_r$ as a CSCG random variable is more accurate.*

**Remark 9.** *With the CLT, the PDF and CDF of $H_r$ is unrelated to the scale parameter of the Nakagami-m distribution.*

#### 5.2.1.2 Outage Probability of $U_t$

According to the principle of NOMA, the outage occurs at $U_t$ when it cannot decode the signal of $U_r$ or its own signal, or both. Thus, the outage probability of $U_t$ is defined as

$$P_t = 1 - \Pr\left(\gamma_s > \bar{\gamma}_s, \gamma_t > \bar{\gamma}_t\right), \tag{5.37}$$

where $\bar{\gamma}_s$ and $\bar{\gamma}_t$ are the SINR threshold of SIC and SNR threshold after SIC, respectively. When $q_r \leq \sqrt{\bar{\gamma}_s} q_t$, it is clear to learn that $P_t = 1$. When $q_r > \sqrt{\bar{\gamma}_s} q_t$, the outage probability of $U_t$ can be given as

$$P_t = 1 - \Pr\left(H_t > \hat{\gamma}_t\right) = \frac{1}{\Gamma(\kappa_t)} \gamma\left(\kappa_t, \frac{\hat{\gamma}_t}{\omega_t}\right), \tag{5.38}$$

where

$$\hat{\gamma}_t = \max\left\{\sqrt{\frac{\bar{\gamma}_s}{\gamma_0 \beta_t \left(q_r^2 - \bar{\gamma}_s q_t^2\right)}}, \sqrt{\frac{\bar{\gamma}_t}{\gamma_0 \beta_t q_t^2}}\right\}. \tag{5.39}$$

#### 5.2.1.3 Outage Probability of $U_r$

An outage will happen at $U_r$ when its received SINR falls below a threshold. Hence, the outage probability of $U_r$ is defined as

$$P_r = \Pr\left(\gamma_r < \bar{\gamma}_r\right), \tag{5.40}$$

where $\bar{\gamma}_r$ is the SINR threshold. Following a similar procedure as in the analysis of $U_t$, the outage probability of $U_r$ can be studied as follows. Under the case of $q_r \leq \sqrt{\bar{\gamma}_r} q_t$, we have $P_r = 1$. Under the case of $q_r > \sqrt{\bar{\gamma}_r} q_t$, the outage probability of $U_r$ can be approximated as

$$P_r = 1 - e^{-\frac{\hat{\gamma}_r^2}{N}}, \tag{5.41}$$

where

$$\hat{\gamma}_r = \sqrt{\frac{\bar{\gamma}_r}{\gamma_0 \beta_r \left(q_r^2 - \bar{\gamma}_r q_t^2\right)}}. \tag{5.42}$$

### 5.2.2 NOMA and OMA Comparison

For comparison, the OMA scheme using TDMA is introduced here. In the OMA scheme, TX communicates to $U_t$ and $U_r$ consecutively over two identical time slots. In each time slot, the phase shifts of the RIS are adjusted to enhance the link of one of the users. Conventionally, the performance characteristics of NOMA and OMA are compared regarding the sum rate. Therefore, the average achievable rates of $U_t$ and $U_r$ in the NOMA and OMA schemes are introduced, then the sum rates of these two schemes are compared.

#### 5.2.2.1 Average Achievable Rates of NOMA

In the NOMA scheme, the average achievable rates of $U_t$ and $U_r$ can be given as [94]

$$R_t = \mathbb{E}[\log_2(1+\gamma_t)], \tag{5.43a}$$

$$R_r = \mathbb{E}\left[\min\left\{\log_2(1+\gamma_s), \log_2(1+\gamma_r)\right\}\right]. \tag{5.43b}$$

By using Jensen's inequality, an upper bound on the average achievable rate of $U_t$ can be given as

$$\begin{aligned} R_t^* &= \log_2\left(1+\mathbb{E}[\gamma_t]\right) \\ &= \log_2\left(1+\frac{\gamma_0 q_t^2 \beta_t \omega_t^2 \Gamma(\kappa_t+2)}{\Gamma(\kappa_t)}\right). \end{aligned} \tag{5.44}$$

Invoking [88, Theorem 4], it can be proved that $R_t$ and $R_t^*$ are asymptotically equivalent for a large number of RIS elements.

Regarding the average achievable rate of $U_r$, Jensen's inequality can still be applied to obtain an upper bound. However, the upper bound is not asymptotic equivalent since it does not satisfy the condition given in [88, Theorem 4]. Therefore, Jensen's inequality is not applied here to analyze the average achievable rate of $U_r$. Alternatively, it can be shown that $\gamma_s$, defined in (5.11b), can be rewritten as

$$\gamma_s = \frac{q_r^2}{q_t^2 + (\gamma_0 \beta_t H_t^2)^{-1}}. \tag{5.45}$$

As $\gamma_0 \to \infty$, we can have

$$\gamma_s \to \frac{q_r^2}{q_t^2}. \tag{5.46}$$

The same conclusion can be derived for $\gamma_r$ such that

$$\gamma_r \to \frac{q_r^2}{q_t^2}, \quad \gamma_0 \to \infty. \tag{5.47}$$

Hence, the average achievable rate of $U_r$ in the large transmit SNR regime can be well approximated as

$$R_r \to R_r^* = \log_2\left(1 + \frac{q_r^2}{q_t^2}\right), \quad \gamma_0 \to \infty. \tag{5.48}$$

#### 5.2.2.2 Average Achievable Rates of OMA

In the OMA scenario, the average achievable rate of $U_t$ can be given as

$$\tilde{R}_t = \frac{1}{2}\mathbb{E}[\log_2(1 + \tilde{\gamma}_t)], \tag{5.49}$$

where $\tilde{\gamma}_t = \gamma_0 \beta_t H_t^2$. By using Jensen's inequality, an upper bound on the average achievable rate of $U_t$ in the OMA scheme is given by

$$\begin{aligned} \tilde{R}_t^* &= \frac{1}{2}\log_2(1 + \mathbb{E}[\tilde{\gamma}_t]) \\ &= \frac{1}{2}\log_2\left(1 + \frac{\gamma_0 \beta_t \omega_t^2 \Gamma(\kappa_t + 2)}{\Gamma(\kappa_t)}\right). \end{aligned} \tag{5.50}$$

On the other hand, since the RIS is able to change the phase shifts to boost the composite channel gain of $U_r$ in its time slot with the OMA scheme, the average achievable rate of $U_r$ can be written as

$$\tilde{R}_r = \frac{1}{2}\mathbb{E}[\log_2(1 + \gamma_0 \beta_r \hat{H}_r^2)], \tag{5.51}$$

where

$$\hat{H}_r = \sum_{n=1}^{N} |r_n| \, |h_n| \, . \tag{5.52}$$

With Jensen's inequality, an upper bound on $R_r$ is given by

$$\begin{aligned}\tilde{R}_r^* &= \frac{1}{2}\log_2(1+\gamma_0\beta_r\mathbb{E}[\hat{H}_r^2]) \\ &= \frac{1}{2}\log_2(1+\gamma_0\beta_r m_0),\end{aligned} \tag{5.53}$$

where

$$m_0 = N + N(N-1)\left(\frac{\Gamma\left(a_h+\frac{1}{2}\right)}{\Gamma(a_h)}\frac{\Gamma\left(a_r+\frac{1}{2}\right)}{\Gamma(a_r)}\right)^2\frac{1}{a_h a_r}. \tag{5.54}$$

#### 5.2.2.3 Sum Rate Comparison

It can be observed that $U_t$ obtains a higher SNR in OMA at the penalty of a 1/2 pre-log factor. It can be shown that $R_t^* > \tilde{R}_t^*$ if

$$\gamma_0 > \frac{(1-2q_t^2)\Gamma(\kappa_t)}{q_t^4\beta_t\omega_t^2\Gamma(\kappa_t+2)}. \tag{5.55}$$

Further, comparing (5.48) with (5.53), it can be learned that $\tilde{R}_r^* > R_r^*$ in the large transmit SNR regime, since $R_r^*$ converges to a constant as $\gamma_0$ goes large.

The approximate sum rates of NOMA and OMA, i.e, $S_{NOMA}$ and $S_{OMA}$, are given by

$$S_{NOMA} = R_t^* + R_r^*, \tag{5.56a}$$

$$S_{OMA} = \tilde{R}_t^* + \tilde{R}_r^*. \tag{5.56b}$$

After some mathematical manipulations, it can be shown that $S_{NOMA}$ and $S_{OMA}$ comply with the following relationship in the large transmit SNR regime:

$$S_{NOMA} > S_{OMA}, \quad \frac{\beta_t\omega_t^2\Gamma(\kappa_t+2)}{\Gamma(\kappa_t)} > \beta_r m_0, \tag{5.57a}$$

$$S_{NOMA} < S_{OMA}, \quad \frac{\beta_t\omega_t^2\Gamma(\kappa_t+2)}{\Gamma(\kappa_t)} < \beta_r m_0. \tag{5.57b}$$

**Remark 10.** *It can be observed that the performance of NOMA surpasses that of OMA when the average channel gain of $U_t$ is greater than that of $U_r$, which aligns with the fundamental principle of NOMA. However, it is crucial to note that we assume a fixed decoding order of $(U_r, U_t)$ based on the assumption that the distance of the $U_t$-RIS channel is shorter than that of the $U_r$-RIS channel. If, in contrast, the average channel gain of $U_t$ is smaller than that of $U_r$, even when $U_t$ is closer to the RIS, the performance of NOMA degrades compared to OMA due to the wrong decoding order. In such cases, switching the decoding order becomes necessary to achieve better performance for NOMA.*

## 5.3 Analysis of RIS-Assisted FD

In this section, we analyze the outage probability of UL user $U_A$ and DL user $U_B$, respectively. The distribution of the composite channel gain $H_u$, $u \in \{A, B\}$ is characterized first, followed by deriving the outage probability expressions of the two users. The performance of FD and HD communications are also compared and discussed, relaying on upper bounds on the average achievable rates.

### 5.3.1 Channel Distribution Analysis

Similar to the analysis of RIS-assisted NOMA, the mean and variance of $H_u$ are

$$\mathbb{E}[H_u] = N_u \frac{\Gamma\left(a_{h,u} + \frac{1}{2}\right)\Gamma\left(a_{g,u} + \frac{1}{2}\right)}{\Gamma(a_{h,u})\Gamma(a_{g,u})} \left(\frac{1}{a_{h,u}a_{g,u}}\right)^{\frac{1}{2}}, \tag{5.58a}$$

$$\mathrm{Var}[H_u] = N_u - \frac{N_u}{a_{h,u}a_{g,u}} \left(\frac{\Gamma\left(a_{h,u} + \frac{1}{2}\right)\Gamma\left(a_{g,u} + \frac{1}{2}\right)}{\Gamma(a_{h,u})\Gamma(a_{g,u})}\right)^2. \tag{5.58b}$$

With the mean and variance of $H_u$, $u \in \{A, B\}$, we can use the moment-matching method to fit the distribution of $H_u$ to a gamma distribution, of which the shape

parameter $\kappa_u$ and the scale parameter $\omega_u$ are provided as follows:

$$\kappa_u = \frac{\mathbb{E}^2[H_u]}{\mathrm{Var}[H_u]}, \quad \omega_u = \frac{\mathrm{Var}[H_u]}{\mathbb{E}[H_u]}. \tag{5.59}$$

Hence, the PDF and CDF of $H_u$ can be written as

$$f_{H_u}(x) = \frac{x^{\kappa_u - 1} \exp\left(-x/\omega_u\right)}{\Gamma(\kappa_u)\, \omega_u^{\kappa_u}}, \quad F_{H_u}(x) = \frac{\gamma\left(\kappa_u, x/\omega_u\right)}{\Gamma(\kappa_u)}. \tag{5.60}$$

### 5.3.2 Outage Probability of UL and DL Users

#### 5.3.2.1 Outage Probability of $U_A$

The outage probability of $U_A$ can be expressed as

$$\bar{P}_A(\bar{\gamma}) = \mathbb{P}\left(\gamma_A < \bar{\gamma}\right) = \mathbb{P}\left(\frac{P_A \beta_A H_A^2}{\sigma_l^2 + \sigma_T^2} < \bar{\gamma}\right) = F_{H_A}\left(\sqrt{\frac{\bar{\gamma}(\sigma_l^2 + \sigma_T^2)}{P_A \beta_A}}\right) \tag{5.61}$$

Since the CDF of $H_A$ has been given in (5.60), the outage probability of $U_A$ is written as

$$\bar{P}_A(\bar{\gamma}) = \frac{1}{\Gamma(\kappa_A)}\, \gamma\left(\kappa_A, \sqrt{\frac{\bar{\gamma}(\sigma_l^2 + \sigma_T^2)}{P_A \beta_A \omega_A^2}}\right). \tag{5.62}$$

**Remark 11.** *Considering the case of $P_A = P_T$, the impact of the residual SI on the outage probability depends on the residual SI exponent $\epsilon$. If $0 \leq \epsilon < 1$, the outage probability will decrease with the increase of $P_A$, and smaller $\epsilon$ will lead to lower outage probability. If $\epsilon = 1$ and $P_A$ is large, the outage probability will be independent of $P_A$, such that*

$$\bar{P}_A(\bar{\gamma}) = \frac{1}{\Gamma(\kappa_A)}\, \gamma\left(\kappa_A, \sqrt{\frac{\bar{\gamma}\varpi}{\beta_A \omega_A^2}}\right). \tag{5.63}$$

#### 5.3.2.2 Outage Probability of $U_B$

As per the expressions of the received SINR of $U_B$ and the CDF of $H_B$, the outage probability of $U_B$ is computed as

$$\begin{aligned}\bar{P}_B(\bar{\gamma}) &= \mathbb{P}(\gamma_B < \bar{\gamma}) \\ &= \mathbb{P}\left(\frac{P_T \beta_B H_B^2}{P_A I + \sigma_B^2} < \bar{\gamma}\right) \\ &= \int_0^\infty F_{H_B}\left(\sqrt{\frac{\bar{\gamma}\left(P_A x + \sigma_B^2\right)}{P_T \beta_B}}\right) f_I(x)\,\mathrm{d}x \\ &= \int_0^\infty \frac{1}{\Gamma(\kappa_B)} \gamma\left(\kappa_B, \sqrt{\frac{\bar{\gamma}\left(P_A x + \sigma_B^2\right)}{P_T \beta_B \omega_B^2}}\right) f_I(x)\,\mathrm{d}x. \end{aligned} \tag{5.64}$$

To further simplify the outage probability of $U_B$, it is required to characterize the distribution of $I$. According to the system model, the aggregate interference power $I$ is written as

$$I = |\tilde{I}|^2 = \left|\sqrt{\beta_{I,A}}\tilde{I}_A + \sqrt{\beta_{I,B}}\tilde{I}_B + \sqrt{\beta_D} I_D\right|^2, \tag{5.65}$$

where

$$\tilde{I}_A = \sum_{n=1}^{N_A} |I_{n,A}||h_{n,A}| e^{j\phi_{n,A}}, \quad \tilde{I}_B = \sum_{n=1}^{N_B} |h_{n,B}||I_{n,B}| e^{j\phi_{n,B}}. \tag{5.66}$$

The distribution of $\tilde{I}_A$ is characterized first. Since $\phi_{n,A}$ follows the uniform distribution within $[-\pi, \pi)$, the expectation and variance of $|I_{n,A}||h_{n,A}|\cos(\phi_{n,A})$ and $|I_{n,A}||h_{n,A}|\sin(\phi_{n,A})$ are derived as

$$\mathbb{E}\left[|I_{n,A}||h_{n,A}|\cos(\phi_{n,A})\right] = \mathbb{E}\left[|I_{n,A}||h_{n,A}|\sin(\phi_{n,A})\right] = 0, \tag{5.67a}$$

$$\mathrm{Var}\left[|I_{n,A}||h_{n,A}|\cos(\phi_{n,A})\right] = \mathrm{Var}\left[|I_{n,A}||h_{n,A}|\sin(\phi_{n,A})\right] = \frac{1}{2}. \tag{5.67b}$$

Moreover, these two terms are proved to be uncorrelated with each other due to the relation:

$$\begin{aligned}&\mathbb{E}\left[|I_{n,A}|^2|h_{n,A}|^2\cos(\phi_{n,A})\sin(\phi_{n,A})\right]\\=&\mathbb{E}\left[|I_{n,A}||h_{n,A}|\cos(\phi_{n,A})\right]\mathbb{E}\left[|I_{n,A}||h_{n,A}|\sin(\phi_{n,A})\right].\end{aligned}\tag{5.68}$$

Hence, with the CLT, $\tilde{I}_A$ can be approximated as a CSCG random variable with zero mean and variance $N_A$, such that

$$\tilde{I}_A \sim \mathcal{CN}(0, N_A).\tag{5.69}$$

Following the same method, we can observe that $\tilde{I}_B$ also follows the CSCG distribution with zero mean and variance $N_B$, i.e.,

$$\tilde{I}_B \sim \mathcal{CN}(0, N_B).\tag{5.70}$$

Since $I_D$ is also CSCG distributed, and applying the property of the sum of CSCG random variables, we can obtain the distribution of $\tilde{I}$ as

$$\tilde{I} \sim \mathcal{CN}(0, \beta_{I,A}N_A + \beta_{I,B}N_B + \beta_D).\tag{5.71}$$

Recalling the relationship between exponential and CSCG distributions, we can learn that the aggregate interference power $I$ approximately follows the exponential distribution with the distribution parameter

$$\xi_I = \frac{1}{\beta_{I,A}N_A + \beta_{I,B}N_B + \beta_D}\tag{5.72}$$

Hence, the PDF and CDF of $I$ are given by

$$f_I(x) = \xi_I e^{-\xi_I x}, \quad F_I(x) = 1 - e^{-\xi_I x}. \tag{5.73}$$

Thus, the outage probability of $U_B$ can be rewritten as

$$\bar{P}_B(\bar{\gamma}) = \int_0^\infty \frac{\xi_I}{\Gamma(\kappa_B)} \gamma\left(\kappa_B, \sqrt{\frac{\bar{\gamma}\left(P_A x + \sigma_B^2\right)}{P_T \beta_B \omega_B^2}}\right) e^{-\xi_I x}\, \mathrm{d}x. \tag{5.74}$$

The above integral can be evaluated numerically in efficient ways. On the other hand, we propose to use the Gaussian Chebyshev quadrature (GCQ) method to approximate (5.74), and derive an accurate closed form expression, which is provided in the following proposition.

**Proposition 7.** *Using the GCQ method, an approximation to the outage probability of $U_B$ is given in closed form as*

$$\bar{P}_B^{+}(\bar{\gamma}) = \frac{\pi}{2K\Gamma(\kappa_B)} \sum_{k=1}^{K} \sqrt{1-\varphi_k^2}\, \gamma\left(\kappa_B, \sqrt{\frac{\bar{\gamma}\left(\frac{P_A}{\xi_I} \ln\left(\frac{1}{b_k}\right) + \sigma_B^2\right)}{P_T \beta_B \omega_B^2}}\right), \tag{5.75}$$

*where*

$$\varphi_k = \cos\left(\frac{\pi}{2K}(2k-1)\right), \tag{5.76a}$$

$$b_k = \frac{\varphi_k}{2} + \frac{1}{2}; \tag{5.76b}$$

*$K$ is the complexity-accuracy trade-off factor, and the approximation error is negligible for large value of $K$.*

*Proof.* Based on the integral form of the outage probability of $U_B$, by changing the

integration variable of (5.74) as $t = e^{-\xi_I x}$, we can obtain that

$$\bar{P}_B(\bar{\gamma}) = \int_0^1 \frac{1}{\Gamma(\kappa_B)} \gamma\left(\kappa_B, \sqrt{\frac{\bar{\gamma}\left(\frac{P_A}{\xi_I}\ln\left(\frac{1}{t}\right)+\sigma_B^2\right)}{P_T\beta_B\omega_B^2}}\right) \mathrm{d}t$$
$$\overset{(a)}{\approx} \frac{\pi}{2K\Gamma(\kappa_B)} \sum_{k=1}^{K} \sqrt{1-\varphi_k^2}\, \gamma\left(\kappa_B, \sqrt{\frac{\bar{\gamma}\left(\frac{P_A}{\xi_I}\ln\left(\frac{1}{b_k}\right)+\sigma_B^2\right)}{P_T\beta_B\omega_B^2}}\right), \tag{5.77}$$

where $(a)$ follows from the GCQ method as introduced in [72]; $\varphi_k$ and $b_k$ have been defined in (5.76a) and (5.76b), respectively. □

**Remark 12.** *The GCQ-based approximation is demonstrated to be highly accurate, even for small values of $K$. The relative error between $\bar{P}_B(\bar{\gamma})$ and $\bar{P}_B^{+}(\bar{\gamma})$ for different values of $K$ will be presented numerically in the section of numerical results.*

### 5.3.3 Discussion of HD Communication

Since a main feature of the FD communication is the residual SI, which affects the performance of $U_A$, we compared the performance of $U_A$ with the FD and HD communication schemes here. Firstly, a tight upper bound on the average achievable rate of $U_A$ with FD communication is derived with the well-known Jensen's inequality [87], such that

$$\mathbb{E}[f(X)] \leq f\left(\mathbb{E}[X]\right), \tag{5.78}$$

for any random variable $X$ and concave function $f(x)$.

With Jensen's inequality, an upper bound on the average achievable rate of $U_A$

can be written as

$$\begin{aligned}\hat{R}_A &= \log_2\left(1+\mathbb{E}[\gamma_A]\right)\\ &= \log_2\left(1+\frac{P_A\beta_A\mathbb{E}[H_A^2]}{\sigma_l^2+\sigma_T^2}\right)\\ &= \log_2\left(1+\frac{P_A\beta_A\omega_A^2\Gamma(\kappa_A+2)}{(\sigma_l^2+\sigma_T^2)\,\Gamma(\kappa_A)}\right)\end{aligned} \tag{5.79}$$

For comparison, the performance of the HD communication scheme is introduced here. Specifically, TX serves the uplink and downlink users consecutively in two identical time slots. In the first time slot, TX receives the signal coming from $U_A$. And, TX transmits the signal towards $U_B$ in the second time slot. In each time slot, the phases of the corresponding RIS are shifted to maximize the composite gain of the corresponding channels. Therefore, the average achievable rate of $U_A$ in the HD communication scheme can be written as

$$R_A^* = \frac{1}{2}\mathbb{E}\left[\log_2\left(1+\gamma_A^*\right)\right], \tag{5.80}$$

where

$$\gamma_A^* = \frac{P_A\beta_A H_A^2}{\sigma_T^2}. \tag{5.81}$$

By using Jensen's inequality, an upper bound on the average achievable rate of $U_A$ in the HD communication scheme is given by

$$\hat{R}_A^* = \frac{1}{2}\log_2\left(1+\frac{P_A\beta_A\omega_A^2\Gamma(\kappa_A+2)}{\sigma_T^2\Gamma(\kappa_A)}\right). \tag{5.82}$$

Compared (5.79) with (5.82), it can be learned that the received SINR of the uplink transmission is larger with the HD communication scheme due to the lack of SI. However, the average achievable rate of the HD communication scheme is with the

penalty of a 1/2 pre-log coefficient. The superiority of FD and HD communication schemes depends on the level of the residual SI after the SI cancellation procedures. It can be shown that $\hat{R}_A > \hat{R}_A^*$ if

$$\sigma_l^2 < \sqrt{\sigma_T^4 + P_A \beta_A \omega_A^2 \sigma_T^2 \frac{\Gamma(\kappa_A + 2)}{\Gamma(\kappa_A)}}. \tag{5.83}$$

As expected, the FD communication scheme performs better as long as the power of the residual SI is lower than the threshold given in (5.83).

## 5.4 Numerical Results

In this section, numerical results are provided to verify the effectiveness of the proposed analysis by Monte Carlo (MC) simulations, and illustrate the impacts of different system parameters on the communication performance.

For the RIS-assisted NOMA communication system, the distances of the TX-RIS, RIS-$U_t$ and RIS-$U_r$ links are set to be $d_h = 10\,\text{m}$, $d_g = 10\,\text{m}$ and $d_r = 15\,\text{m}$. The path loss exponent is $\chi = 3$. The transmit amplitude coefficients at TX are $q_t = 0.6$ and $q_r = 0.8$, such that $q_t^2 + q_r^2 = 1$.[3] The SNR/SINR thresholds are $\bar{\gamma}_s = \bar{\gamma}_t = \bar{\gamma}_r = 0\,\text{dB}$. The path loss per unit distance of the TX-RIS-$U_t$ and TX-RIS-$U_r$ channels are $\Lambda_t = \Lambda_r = -20\,\text{dB}$. The noise power is $\sigma_0^2 = -50\,\text{dBm}$.

For the RIS-assisted FD communication system, the distances of the $U_A$-$S_A$ and $S_A$-TX links are given as $d_{h,A} = 5\,\text{m}$ and $d_{g,A} = 20\,\text{m}$, respectively. The path loss per unit distance of the uplink channel is set to be $\Lambda_A = -20\,\text{dB}$. Regarding the downlink transmission, the distances of the TX-$S_B$ and $S_B$-$U_B$ are set as $d_{h,B} = 4\,\text{m}$ and $d_{g,B} = 20\,\text{m}$, respectively. The path loss per unit distance of the downlink channel is $\Lambda_B = -20\,\text{dB}$. This reflects the scenario where $S_A$ and $S_B$ are placed closed to

[3]In practice, $q_t$ and $q_r$ can be adjusted to meet different performance requirement of each user. For example, if $U_r$ needs better performance, we can increase $q_r$.

$U_A$ and $U_B$, respectively. Regarding the interference channel, the distances of the $S_A$-$U_B$ and $S_B$-$U_A$ links are set to be $d_{I,A} = d_{I,B} = 30\,\text{m}$. The distance of the $U_A$-$U_B$ link is $d_0 = 25\,\text{m}$. The path loss per unit distance of the interference channels are $\Lambda_{I,A} = \Lambda_{I,B} = \Lambda_D = -25\,\text{dB}$. The path loss exponent is $\chi = 3$. The AWGN noise power at TX and $U_B$ are set to be $\sigma_T^2 = \sigma_B^2 = -50\,\text{dBm}$.

### 5.4.1 RIS-Assisted NOMA

The outage probability of $U_t$ versus the transmit power $P$ is presented in Fig. 5.3. The number of RIS elements varies in $N \in \{16, 32, 64\}$, and the Nakagami-$m$ shape parameters varies in $a_h, a_g \in \{1, 2, 4\}$. As shown in Fig. 5.3, it turns out that the proposed outage probability expression matches very well with the simulation results. Increasing the number of elements can significantly reduce the outage probability of $U_t$. For example, when the transmit power is $P = 13\,\text{dBm}$ and $a_h = a_g = 1$, the outage probability is 0.65 and $1.8 \times 10^{-5}$ for $N = 16$ and $N = 32$, respectively. Furthermore, larger Nakagami-$m$ shape parameters correspond to better channel conditions, leading to lower outage probability. On the other hand, the outage probability of $U_r$ versus the transmit power $P$ is presented in Fig. 5.4. The shape parameter of the Nakagami-$m$ distribution will not affect the interference distribution due to the lack of passive beamforming. Compared with Fig. 5.3, the performance of $U_r$ is much worse than $U_t$ due to the larger distance between RIS and $U_r$, and the phase shifts of RIS are adjusted to boost the composite channel gain of $U_t$. Another important point is that the outage probability of $U_r$ will not decrease as rapidly with the increase of the elements as the case of $U_t$.

The relation between the average achievable rate of $U_t$ and the transmit power is explored in Fig. 5.5. The Nakagami-$m$ scale parameters are $a_h = a_g = 2$. The number of RIS elements varies in $N \in \{16, 32, 64\}$. As expected, the average achievable rate of $U_t$ increases with the transmit power. The proposed upper bounds are very close

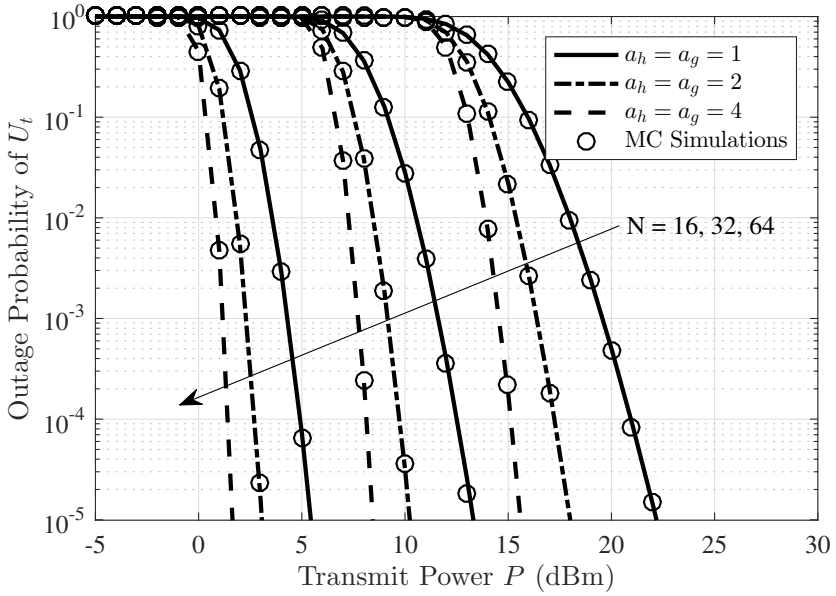



Figure 5.3: Outage probability of $U_t$ versus the transmit power $P$ for different Nakagami-$m$ shape parameters and number of RIS elements $N$.

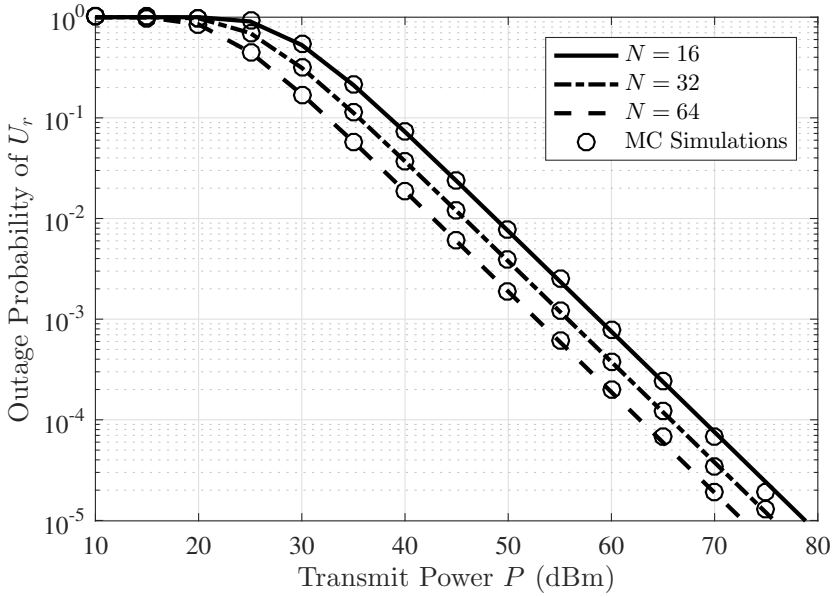



Figure 5.4: Outage probability of $U_r$ versus the transmit power $P$ for different number of RIS elements $N$.

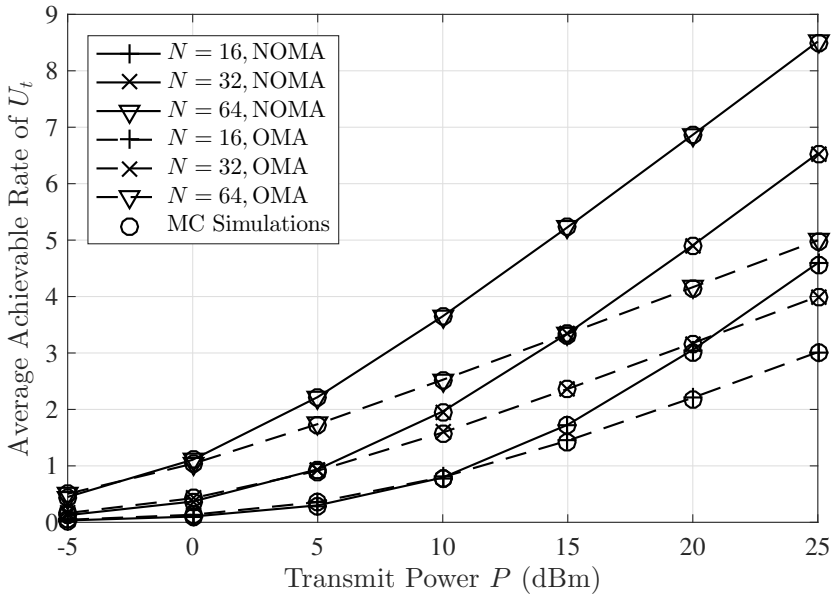



Figure 5.5: Average achievable rate of $U_t$ versus the transmit power $P$ for different number of RIS elements $N$.

to the numerical results. The results of OMA are also given for comparison. We can see that the average achievable rate of $U_t$ in NOMA outperforms that of OMA in the large transmit SNR regime. In addition, in Fig. 5.6, the average achievable rate of $U_r$ grows and converges to the upper bound $\log_2(1 + q_r^2/q_t^2)$ with the increase of the transmit power. This observation corroborates our discussion. However, the average achievable rate of $U_r$ in NOMA is inferior to that of OMA because it converges to a constant value. As a step further, we compare the system sum rates of NOMA and OMA in Fig. 5.7. The large transmit SNR regime is focused and $\Lambda_r$ varies in $\Lambda_r \in \{-20\,\text{dB}, -10\,\text{dB}\}$. For $\Lambda_r = -10\,\text{dB}$, $\frac{\beta_t \omega_t^2 \Gamma(\kappa_t+2)}{\Gamma(\kappa_t)} < \beta_r m_0$, and OMA is better[4]; For $\Lambda_r = -20\,\text{dB}$, NOMA has larger sum rate. Numerical results confirm our analysis.

### 5.4.2 RIS-Assisted FD

Fig. 5.8 shows the outage probability of $U_A$ versus the transmit power of $U_A$. $S_A$ is equipped with $N_A = 64$ elements. The Nakagami-$m$ shape parameters are set to

[4]OMA is better since the decoding order is fixed as $(U_r, U_t)$. If the decoding order is switched, NOMA will be better.

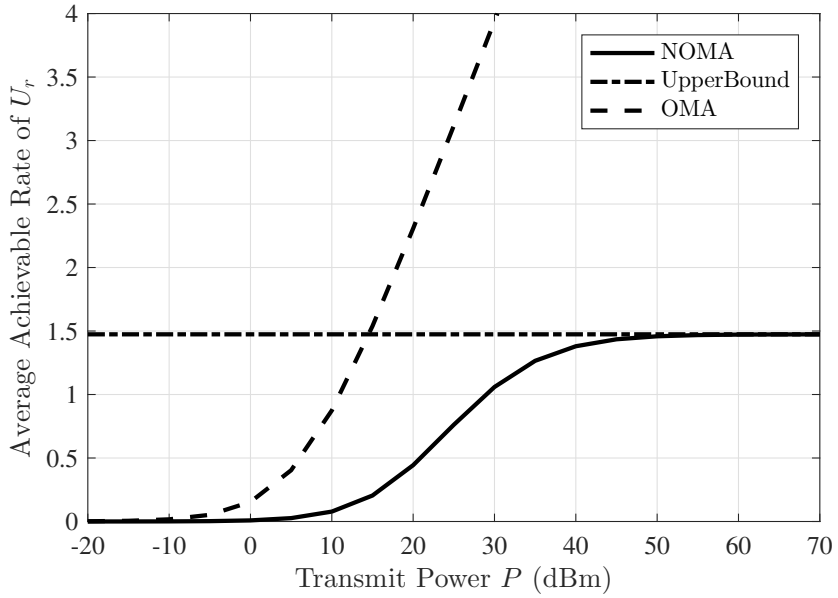



Figure 5.6: Average achievable rate of $U_r$ versus the transmit power $P$.

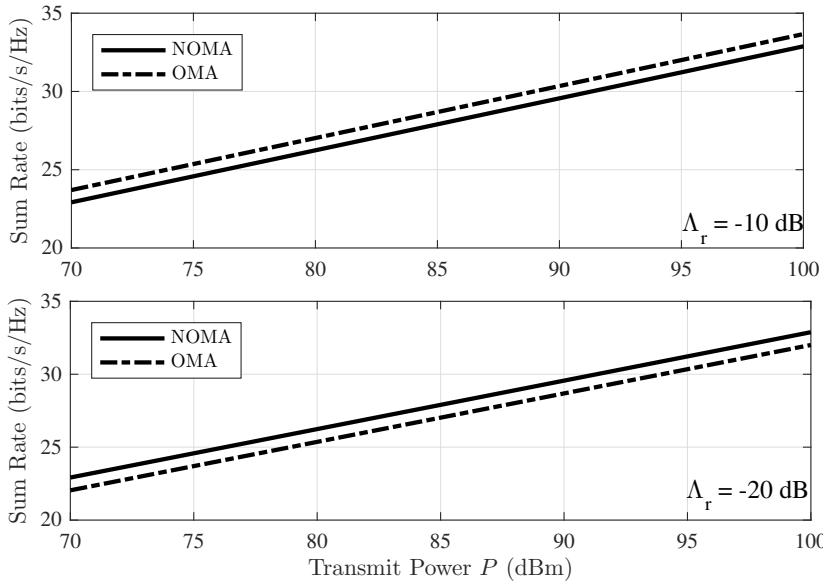



Figure 5.7: Sum rate versus the transmit power $P$ for NOMA and OMA.

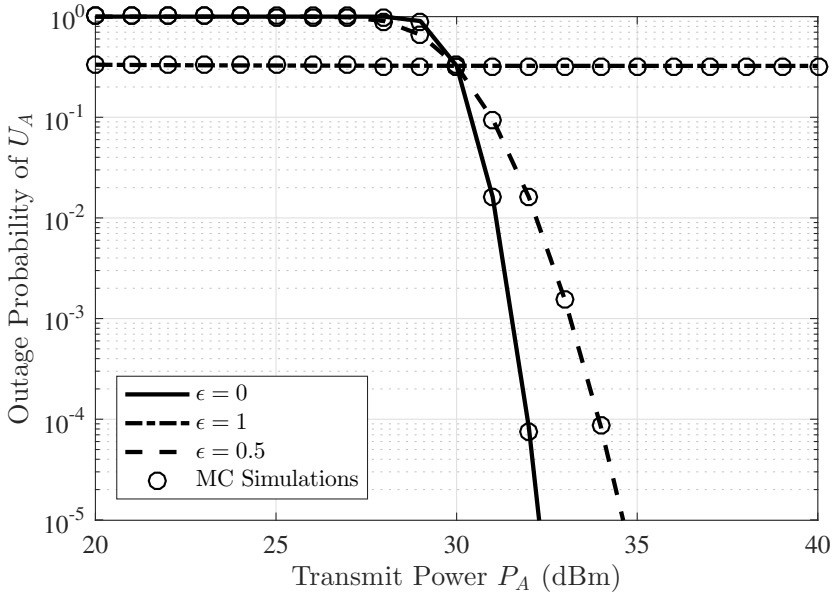



Figure 5.8: Outage probability of $U_A$ versus the transmit power $P_A$ with different $\epsilon$.

be $a_{h,A} = a_{g,A} = 2$. It is assumed that the transmit power of $U_A$ and TX are equal, i.e., $P_A = P_T$. Regarding the residual SI, we set $\varpi = 3 \times 10^{-5}$, and $\epsilon \in \{0, 0.5, 1\}$. $\epsilon = 0$ and $\epsilon = 1$ stand for the cases where the residual SI is independent and linearly dependent of the transmit power, respectively. For different residual SI exponent $\epsilon$, it can be observed that the outage probability converges to a constant for $\epsilon = 1$, and decreases with the increase of the transmit power for $0 \leq \epsilon < 1$ in the large transmit power regime. This confirms our analysis in Remark 11. Furthermore, if $0 < \epsilon < 1$, the system performance falls between the cases of $\epsilon = 0$ and $\epsilon = 1$.

Fig. 5.9 illustrates the outage probability of $U_B$ versus the transmit power of TX. The number of elements of $S_A$ and $S_B$ are: $N_A = 32$; $N_B \in \{16, 32\}$. The transmit power of $U_A$ varies in $P_A \in \{20\,\text{dBm}, 30\,\text{dBm}\}$. As can be seen from the figures, increasing the number of elements on $S_B$ and reducing the transmit power of $U_A$ are both beneficial for the system performance due to the increased desired signal power and the decreased interference power, respectively. For example, when the transmit power of TX is $P_T = 10\,\text{dBm}$ and $P_A = 20\,\text{dBm}$, the outage probability of $U_B$ are $10^{-2}$ and 0.35 for $N_B = 32$ and $N_B = 16$, respectively.

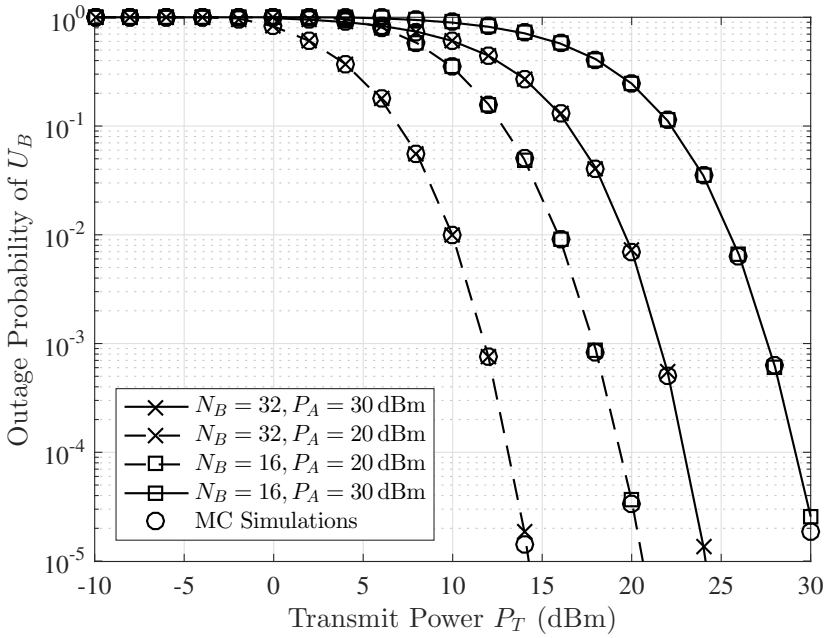



Figure 5.9: Outage probability of $U_B$ versus the transmit power $P_T$ with different number of elements.

The relative error between $\bar{P}_B(\bar{\gamma})$ and its GCQ-based approximation $\bar{P}_B^+(\bar{\gamma})$ for different values of the complexity-accuracy trade-off factor $K$ is depicted in Fig. 5.10. The relative error is defined as

$$\tau = \frac{|\bar{P}_B(\bar{\gamma}) - \bar{P}_B^+(\bar{\gamma})|}{\bar{P}_B(\bar{\gamma})}. \tag{5.84}$$

It is assumed that the number of elements of $S_A$ and $S_B$ are $N_A = 32$ and $N_B = 16$, and that the transmit power of the UA and TX are $P_A = 30\,\text{dBm}$ and $P_T = 10\,\text{dBm}$. The results show that the GCQ-based approximation is accurate even for small values of $K$. For instance, the relative error is less than $10^{-3}$ when $K$ is larger than 15.

Fig. 5.11 is presented to verify the boundary at which the FD communication scheme is better than the HD communication given in (5.83). The number of elements of $S_A$ is $N_A = 32$. The transmit power of $U_A$ varies in $P_A \in \{20\,\text{dBm}, 30\,\text{dBm}\}$. The residual SI lies in $\sigma_l^2 \in (-70\,\text{dBm}, -20\,\text{dBm})$. As can be seen from Fig. 5.11, the FD communication outperforms the HD communication when the residual SI is lower

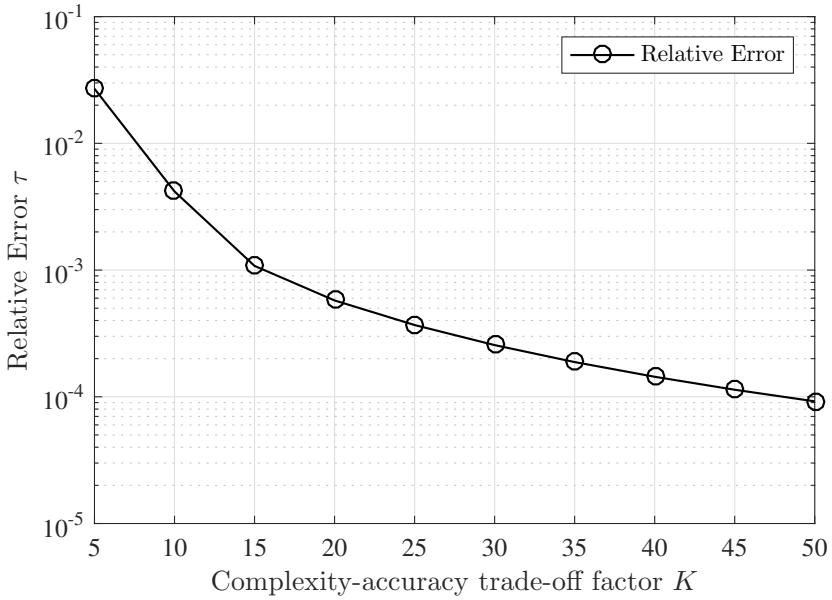



Figure 5.10: Relative error of the GCQ based approximation.

than a threshold value. The boundary given by (5.83) is very precise as proven by the simulations. In the current simulation setup, even with a high transmit power value of $P_A = 30\,\text{dBm}$ and a low residual SI level of $\sigma_l^2 = -20\,\text{dBm}$, the FD communication is still worse than the HD communication due to the weakness of the composite channel gain in the $U_A$-$S_A$-TX channel. The presence of fading leads to a low received signal power at the TX, thus, the SI significantly degrades the uplink performance. However, it should be noted that for a system with a larger number of elements and better channel conditions, the FD will outperforms the HD counterpart with a less stringent requirement on the SI level.

## 5.5 Summary

In this chapter, we studied the performance of two spectral efficiency techniques in RIS-assisted communication systems, i.e., RIS-assisted NOMA and RIS-assisted FD. For a RIS-assisted NOMA communication system, the distributions of the composite channel gains of a pair of NOMA users were investigated, and then new closed form

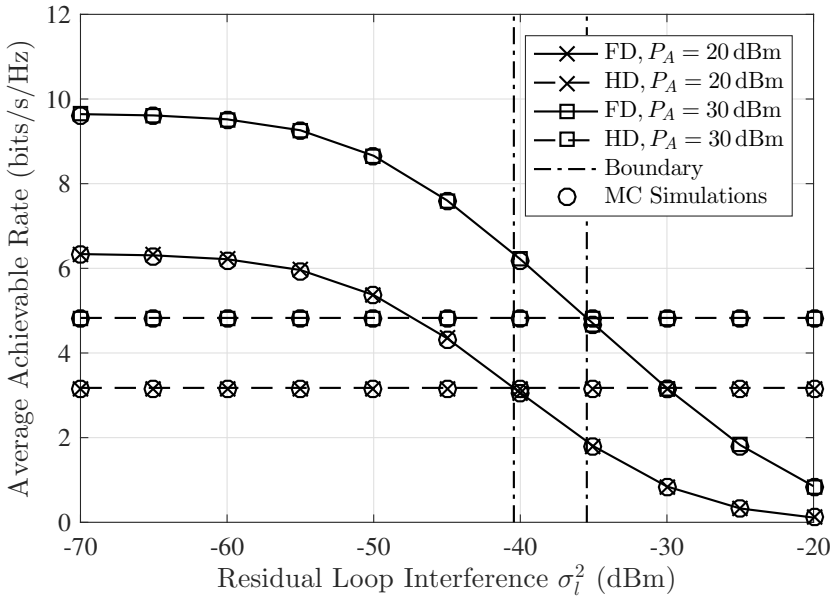



Figure 5.11: FD and HD Communications Comparison. Average achievable rate of $U_A$ with FD and HD schemes.

outage probability expressions were derived. Upper bounds on the average achievable rates of the two users with NOMA and OMA transmission schemes were also derived with the same framework, and the sum rates of RIS-assisted NOMA and RIS-assisted OMA were explored. It was confirmed that NOMA is not always superior to OMA due to the reconfigurability of RIS over different time slots. The condition at which NOMA performs better was given and verified through numerical results.

In a RIS-assisted FD communication system, an uplink user and a downlink user were served by an FD transceiver over the same time and frequency resource block. The outage probability of the uplink and downlink users were derived in closed form. The impact of the residual SI was explored. Floors of outage probability can appear due to the linear relationship between the transmit power and the residual SI. Furthermore, the residual SI threshold below which the FD communication performs better than the HD counterpart was given in the closed form and verified by simulations.

# Chapter 6

# RIS-Assisted Large-Scale Networks

The aforementioned works all consider single-cell networks. However, a real RIS-assisted communication network comprises multiple transmitters, receivers and RISs, and they may share the same resource block, i.e., time and frequency, in a multi-cell environment. Thus, in the performance analysis of RIS-assisted communication systems, it is essential to model the RIS-assisted multi-cell network subjected to inter-cell interference. Stochastic geometry has been widely used to model and characterize the performance of large-scale wireless networks, which can provide useful performance bounds and practical insights regarding practical wireless systems [48, 114]. Performance analysis of RIS-assisted multi-cell networks using stochastic geometry has been carried out in recent works. In [115], the authors investigated the coverage probability of a large-scale RIS-assisted millimeter-wave (mmWave) communication network using stochastic geometry. The authors in [116] modelled the blockages as boolean line segments, and the RISs are attached to the blockages with a probability. The probability that a given user is associated with a transmitter (TX) via a RIS is derived, which shows that RISs can enlarge the coverage in a multi-cell network by providing indirect line-of-sight (LoS) paths. In [117], the authors modelled the locations of TXs and RISs as two independent homogeneous Poisson point process (HPPP) in a

multi-cell mmWave network and derived the average achievable rate as a multi-fold integral. With a similar system setup, the authors in [58] analyzed the distributions of the signal power and interference power, respectively, and derived a two-fold integral expression for the coverage probability of the typical user when it is connected with the nearest TX and RIS. RIS-assisted multi-cell non-orthogonal multiple access (NOMA) networks were investigated in [110], in which the authors modelled the locations of TXs and users as HPPP and assumed the interference from other RISs that are not associated with the typical user could be ignored. The coverage probability and average achievable rate of the typical user were both derived in integral form. The performance of two different types of users, i.e., served by the TX with and without RIS-assisted transmissions, were analyzed in a more recent work [118], where the authors derived the coverage probability of the network conditioned on the proportions of the two types of users.

All the aforementioned works use independent HPPP to model the locations of TXs and RISs, because HPPP not only can model randomly located nodes but also makes the analysis mathematically tractable [48]. However, the HPPP may not be an accurate model for large-scale RIS-assisted systems since it does not capture the spatial correlations between TXs and RISs [60]. Since RIS is a passive device and its locations have to be appropriately designed according to the location of the TX, the locations of TXs and RISs exhibit significant spatial correlations [15]. To describe this characteristic of a large-scale RIS-assisted network, the Gauss-Poisson process (GPP) can be applied because the GPP is a clustering process that can capture the correlations of the node locations, in which each cluster has one or two points with the spatial correlations [59].

Therefore, we use a GPP to model a large-scale RIS-assisted network to represent the spatial correlations between TXs and RISs. Furthermore, the general Nakagami-$m$ fading channel model and the RIS-assisted transmission with the direct link between

the user and the TX are considered in the analysis. The main contributions of this chapter are listed as follows:

1. To provide an accurate system-level performance analysis, we propose an analytical framework to characterize the performance of a RIS-assisted large-scale network by using stochastic geometry. The locations of user equipments (UEs) are modelled by an HPPP, while the locations of TXs and RISs are modelled by a cluster process GPP to characterize the spatial correlations between TXs and RISs. The channels related to the RIS are Nakagami-$m$ fading. Moreover, we consider the fixed association and nearest association strategies between the TX and the typical user in the analysis.

2. We obtain expressions for the coverage probability and the average achievable rate in the downlink for the typical user with the fixed and nearest association strategies. The expressions for the coverage probability have closed forms for both association strategies in terms of elementary and/or special functions for all path loss exponents. The expressions for the average achievable rate have integral forms, which are further simplified to closed forms for certain path loss exponents.

3. The numerical results verify the effectiveness of the theoretical analysis, and practical insights are extracted from the analytical and numerical results. For the fixed association strategy, increasing the density of TXs and the RIS association probability will both impair the system performance due to the enhanced interference power. While for the nearest association strategy, a larger density of TXs and RIS association probability is beneficial since the typical user is more likely to be served by a closer TX with an assisting RIS. Furthermore, we prove that the coverage probability and the average achievable rate are unrelated to the density of TXs when the nearest association strategy is applied in

the large transmit signal-to-noise ratio (SNR) regime.

## 6.1 System Framework

This chapter studies a RIS-assisted multi-cell wireless communication network with multiple single-antenna TXs, RISs, and single-antenna UEs shown in Fig. 6.1. The performance of the downlink communication from the TXs to UEs is analyzed. The locations of UEs are modelled by a HPPP $\Lambda_u$ with density $\lambda_u$. We consider the spatial correlations between the locations of TXs and RISs, and model the locations of TXs and RISs as a GPP $\Lambda_c$, which is a clustering process that can capture the correlations of the node locations [60]. $\Lambda_c$ is a Poisson cluster process where the locations of TXs are the parent process and follow a HPPP $\Lambda_t$ with density $\lambda_t$. Each cluster in $\Lambda_c$ has one or two points. If a cluster has one point, it is at the location of the parent point. Otherwise, one of them is the parent point, and the daughter point, which represents the location of an assisting RIS of the corresponding TX, is uniformly distributed on a circle with a radius $d_0$ centred at the parent point[1]. The probabilities of each cluster having one or two points are $1-p$ and $p$, respectively. In other words, for a typical TX, the probability that it has an assisting RIS is $p$. In this chapter, we study the system where each TX can be served by one RIS at most. For notational simplicity, we denote the cluster processes with one point and two points as $\Lambda_1$ and $\Lambda_2$, respectively. Based on the definition of GPP, we have

$$\Lambda_c = \Lambda_1 \cup \Lambda_2. \tag{6.1}$$

[1]In this chapter, we consider the standard GPP where $d_0$ is fixed for clarity. The proposed results can be easily extended to the generalized GPP model by averaging the derived coverage probability and average achievable rate over the distribution of $d_0$.

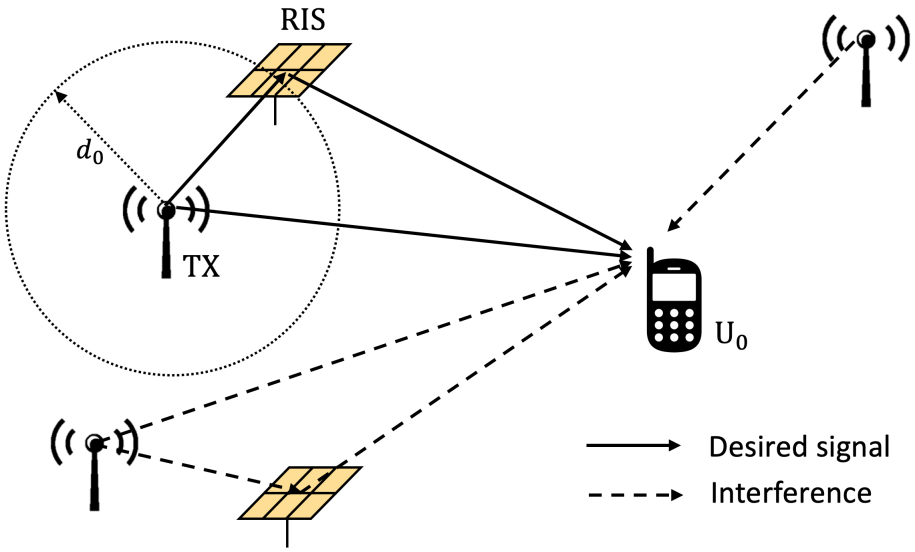



Figure 6.1: System model of RIS assisted large-scale network.

Furthermore, the parent and daughter point processes of the clusters with two points are respectively denoted as $\Lambda_2^{(P)}$ and $\Lambda_2^{(D)}$ such that

$$\Lambda_2 = \Lambda_2^{(P)} \cup \Lambda_2^{(D)}. \tag{6.2}$$

Since the locations of UEs are assumed to follow a HPPP, we can randomly select a typical UE $U_0$ from $\Lambda_u$ and fix it at the origin of the considered plane. As per Slivnyak's theorem, the performance of $U_0$ represents the average UE performance.

### 6.1.1 Channel Model

It is assumed that each RIS has $N$ elements and can perform continuous phase adjustment to increase the composite channel gain of its serving UE, which gives an upper bound on the system performance [119]. Furthermore, we have proved that only two-bit phase shifting leads to the performance close to upper bound in practice. The transmit power of each TX is $P$. The normalized small scale fading of the $T_i$-$U_0$ channel is denoted as $g_i \in \mathbb{C}$ where $i \in \Lambda_t$. The direct links between TXs and UEs are assumed to be Rayleigh fading channels, i.e., $|g_i| \sim \mathcal{R}(\sqrt{2}/2)$. The Rayleigh

fading model applies to rich scattering urban environments and stable LoS paths do not exist between TXs and UEs [120]. The path loss of the direct link $T_i$-$U_0$ can be expressed as

$$\eta_{g,i} = C_d d_{g,i}^{-\alpha}, \tag{6.3}$$

where $d_{g,i}$ is the distance of the $T_i$-$U_0$ channel; $C_d$ is the path loss per unit distance of the direct link; $\alpha$ is the path loss exponent. Similar to [121–123], it is assumed that the horizontal distances of different channels are much larger than the vertical distances and the heights of TXs, RISs and UEs are ignored.

It is assumed that each RIS receives the signal from its associated TX and the signals from other TXs impinging on the RIS can be ignored[2]. For $T_j$, $j \in \Lambda_2^{(P)}$ that has an assisting RIS $R_{j'}$, $j' \in \Lambda_2^{(D)}$, the normalized small scale fading of the $T_j$-$R_{j'}$ and $R_{j'}$-$U_0$ channels are denoted as $\mathbf{h}_j = (h_{j,1}, ..., h_{j,N})^T \in \mathbb{C}^{N\times 1}$, and $\mathbf{r}_j = (r_{j,1}, ..., r_{j,N})^T \in \mathbb{C}^{N\times 1}$, respectively. $T_j$ and $R_{j'}$ are the parent and daughter points in the same two-point cluster. RISs operate in the far field of both TXs and UEs. We assume the reflected links associated with RISs are Nakagami-$m$ fading channels. To be specific, $|h_{j,n}| \sim$ Nakagami$(m_h, 1)$ and $|r_{j,n}| \sim$ Nakagami$(m_r, 1)$, where $n \in \{1, ..., N\}$. $m_h$ and $m_r$ are the shape parameters of $|h_{j,n}|$ and $|r_{j,n}|$, respectively. The path loss of the reflected path $T_j$-$R_{j'}$-$U_0$ can be expressed as

$$\eta_{h,j} = C_r \left(d_0 d_{r,j}\right)^{-\alpha}, \tag{6.4}$$

where $d_{r,j}$ is the distance of the $R_{j'}$-$U_0$ channel; $C_r$ is the path loss per unit distance of the reflected link.

[2]In this chapter, we consider the spatial correlation between the locations of TXs and RISs. This assumption is particularly valid when the distances among different TXs are significantly larger than the distance between a TX and its associated RIS. A similar assumption is also applied in [110,118].

### 6.1.2 Signal Model

The received signal at $U_0$ depends on whether its associated TX $T_0$ has an assisting RIS or not. If $T_0$ has an assisting RIS, the received signal at $U_0$ can be expressed as

$$y_0^+ = \left(\sqrt{\eta_{g,0}} g_0 + \sqrt{\eta_{h,0}} \mathbf{h}_0^T \mathbf{\Phi}_0 \mathbf{r}_0\right) \sqrt{P} s_0 + \tilde{I} + n_0, \tag{6.5}$$

where

$$\tilde{I} = \sum_{k \in \Lambda_t \backslash \{0\}} (1 - b_k) \sqrt{\eta_{g,k} P} g_k s_k + b_k \left(\sqrt{\eta_{g,k}} g_k + \sqrt{\eta_{h,k}} \mathbf{h}_k^T \mathbf{\Phi}_k \mathbf{r}_k\right) \sqrt{P} s_k, \tag{6.6}$$

representing the interference from all other TXs. $\mathbf{\Phi}_k = \text{diag}\left(e^{j\phi_{k,1}}, ..., e^{j\phi_{k,N}}\right)$ is the phase shifting matrix of $R_{k'}$, and $R_{k'}$ is the assisting RIS of $T_k$ in a two-point cluster; $b_k \in \{0, 1\}$ represents if $T_k$ is without or with an assisting RIS; $s_k$ is the unit power transmit symbol from $T_k$, satisfying $\mathbb{E}[s_k^2] = 1$ and $\mathbb{E}[s_k s_l] = 0$ for $k \neq l$; $n_0 \sim \mathcal{CN}(0, \sigma_0^2)$ is the additive white Gaussian noise (AWGN) with zero mean and variance $\sigma_0^2$. If $T_0$ does not have an assisting RIS, the received signal at $U_0$ can be expressed as

$$y_0^* = \sqrt{\eta_{g,0} P} g_0 s_0 + \tilde{I} + n_0. \tag{6.7}$$

If $T_0$ has an assisting RIS, the phase shifts of $R_0$ should be adjusted to align the phases of the reflected paths to the phase of the direct link, i.e.,

$$\phi_{0,n} = -\arg(h_{0,n}) - \arg(r_{0,n}) + \arg(g_0). \tag{6.8}$$

On the other hand, the phases of the composite channels $T_l$-$R_{l'}$-$U_0$, $l \in \Lambda_2^{(P)} \backslash \{0\}$ can be regarded as uniformly distributed over $[-\pi, \pi)$. Following the above discussions,

(6.5) can be written as

$$y_0^+ = \left( \sqrt{\eta_{g,0}}|g_0| + \sqrt{\eta_{h,0}} \sum_{n=1}^{N} |h_{0,n}||r_{0,n}| \right) e^{j \arg(g_0)} \sqrt{P} s_0 + \sqrt{P} \tilde{I} + n_0, \tag{6.9}$$

where

$$\tilde{I} = \sum_{k \in \Lambda_t \setminus \{0\}} b_k \tilde{I}_{1,k} + (1 - b_k) \tilde{I}_{2,k}; \tag{6.10a}$$

$$\tilde{I}_{1,k} = \left( \sqrt{\eta_{g,k}} g_k + \sqrt{\eta_{h,k}} \sum_{n=1}^{N} |h_{k,n}||r_{k,n}| e^{j\theta_{k,n}} \right) s_k; \tag{6.10b}$$

$$\tilde{I}_{2,k} = \sqrt{\eta_{g,k}} g_k s_k, \tag{6.10c}$$

and $\theta_{k,n}$ is uniformly distributed over $[-\pi, \pi)$.

We will give the signal-to-interference-plus-noise ratio (SINR) of $U_0$ at different association strategies as follows:

1. With the fixed association strategy, the SINR of $U_0$ with an assisting RIS is given by

$$\gamma_0^+ = \frac{S_0^+}{I + \gamma_t^{-1}}, \tag{6.11}$$

where $\gamma_t = P/\sigma_0^2$. The signal power $S_0^+$ is

$$S_0^+ = \left( \sqrt{\eta_{g,0}}|g_0| + \sqrt{\eta_{h,0}} \sum_{n=1}^{N} |h_{0,n}||r_{0,n}| \right)^2. \tag{6.12}$$

The interference power is

$$I = |\tilde{I}|^2 = \sum_{k \in \Lambda_t \setminus \{0\}} b_k I_{1,k} + (1 - b_k) I_{2,k}, \tag{6.13}$$

in which

$$I_{1,k} = |\tilde{I}_{1,k}|^2 = \left| \sqrt{\eta_{g,k}} g_k + \sqrt{\eta_{h,k}} \sum_{n=1}^{N} |h_{k,n}||r_{k,n}| e^{j\theta_{k,n}} \right|^2, \tag{6.14a}$$

$$I_{2,k} = |\tilde{I}_{2,k}|^2 = \left| \sqrt{\eta_{g,k}} g_k \right|^2. \tag{6.14b}$$

2. With the fixed association strategy, the SINR of $T_0$ without an assisting RIS can be given by

$$\gamma_0^* = \frac{S_0^*}{I + \gamma_t^{-1}}, \tag{6.15}$$

where

$$S_0^* = \eta_{g,0} |g_0|^2. \tag{6.16}$$

3. With the nearest association strategy, the SINR of $U_0$ is given by[3]

$$\gamma_0 = \begin{cases} \gamma_0^+, & \text{w.p.} \quad p, \\ \gamma_0^*, & \text{w.p.} \quad 1-p, \end{cases} \tag{6.17}$$

### 6.1.3 Performance Metrics

In this chapter, we will analyze the coverage probability and average achievable rate of the typical user $U_0$.

#### 6.1.3.1 Coverage Probability

Coverage probability is defined as the probability that the received SINR is larger than a threshold, i.e.,

$$P_c(\bar{\gamma}) = \mathbb{P}\left(\gamma > \bar{\gamma}\right), \tag{6.18}$$

[3] $\gamma_0$ is a function of the distance between $T_i$ and $U_0$, $i \in \Lambda_t$, i.e., $d_{g,i}$. With the nearest association strategy, $U_0$ is associated with the TX with the minimum $d_{g,i}$.

where $\gamma \in \{\gamma_0^+, \gamma_0^*, \gamma_0\}$; $\bar{\gamma}$ is the coverage SINR threshold.

#### 6.1.3.2 Average Achievable Rate

The average achievable rate of the typical user is defined as

$$R = \int_0^\infty \log_2(1+x)\, f_\gamma(x)\, \mathrm{d}x, \tag{6.19}$$

where $f_\gamma(x)$ is the probability density function (PDF) of $\gamma$.

## 6.2 Signal Power Analysis

In this section, we characterize the signal power distributions with and without RIS reflect beamforming, which are denoted as $S_0^+$ and $S_0^*$, respectively.

### 6.2.1 Distribution with RIS-Assisted Transmission

The received signal power with RIS-assisted transmission $S_0^+$ can be rewritten as

$$S_0^+ = \left(\sqrt{\eta_{g,0}}|g_0| + \sqrt{\eta_{h,0}}S_r\right)^2, \tag{6.20}$$

where

$$S_r = \sum_{n=1}^{N} |h_{0,n}||r_{0,n}|, \tag{6.21}$$

which is the sum of the products of Nakagami-$m$ random variables. The exact distribution of $S_r$ cannot be obtained in closed form. Hence, we propose a moment matching method based on gamma distribution to fit the distribution of $S_r$.

Since $|h_{0,n}|$ and $|r_{0,n}|$, $n \in \{1, ..., N\}$ are independent and identically distributed (i.i.d.) Nakagami-$m$ random variables, the mean and second order raw moment of $S_r$

are derived as:

$$\mathbb{E}\left[S_r\right] = \sum_{n=1}^{N} \mathbb{E}\left[|h_{0,n}|\right] \mathbb{E}\left[|r_{0,n}|\right] = N \frac{\Gamma\left(m_h + \frac{1}{2}\right)}{\Gamma(m_h)} \frac{\Gamma\left(m_r + \frac{1}{2}\right)}{\Gamma(m_r)} \left(\frac{1}{m_h m_r}\right)^{\frac{1}{2}}, \tag{6.22a}$$

$$\begin{aligned}\mathbb{E}\left[S_r^2\right] &= \mathbb{E}\left[\sum_{n=1}^{N} |h_{0,n}|^2 |r_{0,n}|^2\right] + 2\,\mathbb{E}\left[\sum_{n=1}^{N-1} \sum_{i=n+1}^{N} |h_{0,n}|\,|r_{0,n}|\,|h_{0,i}|\,|r_{0,i}|\right] \\ &= N + N(N-1)\left(\frac{\Gamma\left(m_h + \frac{1}{2}\right)}{\Gamma(m_h)} \frac{\Gamma\left(m_r + \frac{1}{2}\right)}{\Gamma(m_r)}\right)^2 \frac{1}{m_h m_r}. \end{aligned} \tag{6.22b}$$

Hence, $S_r$ can be approximated by a gamma random variable with shape and scale parameters:

$$\kappa_r = \frac{\mathbb{E}^2[S_r]}{\mathbb{E}[S_r^2] - \mathbb{E}^2[S_r]}, \tag{6.23a}$$

$$\omega_r = \frac{\mathbb{E}[S_r^2] - \mathbb{E}^2[S_r]}{\mathbb{E}[S_r]}. \tag{6.23b}$$

The moment matching approach can be applied to fit the distribution of $S_0^+$. Then the mean and second order moment of $S_0^+$ can be derived as

$$\mathbb{E}[S_0^+] = \eta_{g,0}\chi_1, \tag{6.24a}$$

$$\mathbb{E}\left[\left(S_0^+\right)^2\right] = \eta_{g,0}^2\chi_2, \tag{6.24b}$$

where

$$\beta = \sqrt{\eta_{h,0}/\eta_{g,0}}, \tag{6.25a}$$

$$\chi_1 = \mu_2^g + 2\beta\mu_1^g\,\mu_1^\varsigma + \beta^2\mu_2^\varsigma, \tag{6.25b}$$

$$\chi_2 = \mu_4^g + 4\beta\mu_3^g\mu_1^\varsigma + 6\beta^2\mu_2^g\mu_2^\varsigma + 4\beta^3\mu_1^g\mu_3^\varsigma + \beta^4\mu_4^\varsigma. \tag{6.25c}$$

$\mu_q^\epsilon$, $\epsilon \in \{g, \varsigma\}$, $q \in \{1, 2, 3, 4\}$ denotes the $q$th order raw moment of $|g_0|$ and $S_r$, respectively. Since $|g_0| \sim \mathcal{R}(\sqrt{2}/2)$ and $S_r$ has been fitted by a gamma random

variable, $\mu_q^g$ and $\mu_q^s$ are given by

$$\mu_q^g = \Gamma\left(1 + \frac{1}{2}q\right), \tag{6.26a}$$

$$\mu_q^\varsigma = \omega_r^q \frac{\Gamma(q + \kappa_r)}{\Gamma(\kappa_r)}. \tag{6.26b}$$

Therefore, $S_0^+$ can be approximated by a gamma random variable with shape and scale parameters as

$$\kappa_s = \frac{\chi_1^2}{\chi_2 - \chi_1^2}, \tag{6.27a}$$

$$\omega_s = \eta_{g,0}\bar{\chi} = \eta_{g,0}\frac{\chi_2 - \chi_1^2}{\chi_1}. \tag{6.27b}$$

Furthermore, the approximate PDF and cumulative distribution function (CDF) of $S_0^+$ are given by

$$f_{S_0^+}(x) = \frac{x^{\kappa_s - 1}\,\exp\left(-x/\omega_s\right)}{\Gamma(\kappa_s)\,\omega_s^{\kappa_s}}, \tag{6.28a}$$

$$F_{S_0^+}(x) = \frac{\gamma\left(\kappa_s, x/\omega_s\right)}{\Gamma(\kappa_s)}. \tag{6.28b}$$

### 6.2.2 Distribution without RIS Beamforming

Since $|g_0| \sim \mathcal{R}(\sqrt{2}/2)$, $S_0^*$ follows the exponential distribution with the distribution parameter $\zeta_g = 1/\eta_{g,0}$. The PDF and CDF of $S_0^*$ are respectively given by

$$f_{S_0^*}(x) = \frac{1}{\eta_{g,0}} e^{-\frac{x}{\eta_{g,0}}}, \tag{6.29a}$$

$$F_{S_0^*}(x) = 1 - e^{-\frac{x}{\eta_{g,0}}}. \tag{6.29b}$$

## 6.3 Interference Power Analysis

In this section, the interference power $I$ is analyzed. Referring to (6.13), (6.14a) and (6.14b), we first characterize the distributions of $I_{1,k}$ and $I_{2,k}$, respectively. Then, the Laplace transform of $I$ is computed, which is used in analyzing the coverage probability and the average achievable rate of the typical user.

### 6.3.1 Interference Power Distribution Analysis

#### 6.3.1.1 Interference from TX with Assisting RIS

The interference power from a TX with an assisting RIS $I_{1,k}$ is rewritten by

$$I_{1,k} = \left|\sqrt{\eta_{g,k}} g_k + \sqrt{\eta_{h,k}} I_{r,k}\right|^2, \tag{6.30}$$

where

$$I_{r,k} = \sum_{n=1}^{N} |h_{k,n}||r_{k,n}| e^{j\theta_{k,n}}. \tag{6.31}$$

Then, the distribution of $I_{r,k}$ is analyzed. Since $\theta_{k,n}$ is uniformly distributed over $[-\pi, \pi)$, the expectation and variance of $|h_{k,n}||r_{k,n}|\cos(\theta_{k,n})$ and $|h_{k,n}||r_{k,n}|\sin(\theta_{k,n})$ can be shown to be

$$\mathbb{E}\left[|h_{k,n}||r_{k,n}|\cos(\theta_{k,n})\right] = \mathbb{E}\left[|h_{k,n}||r_{k,n}|\sin(\theta_{k,n})\right] = 0, \tag{6.32a}$$

$$\mathrm{Var}\left[|h_{k,n}||r_{k,n}|\cos(\theta_{k,n})\right] = \mathrm{Var}\left[|h_{k,n}||r_{k,n}|\sin(\theta_{k,n})\right] = \frac{1}{2}. \tag{6.32b}$$

Further, it can be proved that $|h_{k,n}||r_{k,n}|\cos(\varphi_{k,n})$ and $|h_{k,n}||r_{k,n}|\sin(\varphi_{k,n})$ are uncorrelated with each other, since

$$\begin{aligned} &\mathbb{E}[|h_{k,n}|^2|r_{k,n}|^2\cos(\varphi_{k,n})\sin(\varphi_{k,n})] \\ &= \mathbb{E}\left[|h_{k,n}||r_{k,n}|\cos(\theta_{k,n})\right]\mathbb{E}\left[|h_{k,n}||r_{k,n}|\sin(\theta_{k,n})\right]. \end{aligned} \tag{6.33}$$

Using the central limit theorem, for a large number of elements $N$, $I_{r,k}$ follows the circularly symmetric complex Gaussian (CSCG) distribution

$$I_{r,k} \sim \mathcal{CN}\left(0, N\right). \tag{6.34}$$

Since $g_k$ follows the CSCG distribution, i.e., $g_k \sim \mathcal{CN}(0,1)$, it can be observed that

$$\sqrt{\eta_{g,k}} g_k + \sqrt{\eta_{h,k}} I_{r,k} \sim \mathcal{CN}\left(0, \eta_{g,k} + N\eta_{h,k}\right). \tag{6.35}$$

Thus, $I_{1,k}$ follows the exponential distribution with the distribution parameter

$$\zeta_k = \frac{1}{\eta_{g,k} + N\eta_{h,k}}. \tag{6.36}$$

#### 6.3.1.2 Interference from TX without Assisting RIS

As defined in (6.14a), Since $|g_k| \sim \mathcal{R}(\sqrt{2}/2)$, $I_{2,k}$ follows the exponential distribution with the distribution parameter $\zeta_{g,k} = 1/\eta_{g,k}$. The PDF and CDF of $I_{2,k}$ are given by

$$f_{I_{2,k}}(x) = \frac{1}{\eta_{g,k}} e^{-\frac{x}{\eta_{g,k}}}, \tag{6.37a}$$

$$F_{I_{2,k}}(x) = 1 - e^{-\frac{x}{\eta_{g,k}}}. \tag{6.37b}$$

### 6.3.2 Laplace Transform of the Interference Power

The Laplace transform of the interference power is useful in the analysis of the coverage probability in the next section. Hence, the Laplace transform of the interference power with the fixed and nearest association strategies can be obtained as follows.

#### 6.3.2.1 Fixed Association Strategy

If $U_0$ is associated with a TX at a fixed location, i.e, $d_{g,0}$ is a fixed value, the Laplace transform of the interference power is summarized in the following proposition.

**Proposition 8.** *The Laplace transform of the interference power $I$ with the fixed association strategy is*

$$\mathcal{L}_{I,f}(s) = E_{f,1}(s)\, E_{f,2}(s), \tag{6.38}$$

*where*

$$E_{f,1}(s) = \exp\left(-\frac{2\pi^2\lambda_t p \csc\left(\frac{2\pi}{\alpha}\right)(e_1 s)^{\frac{2}{\alpha}}}{\alpha}\right), \tag{6.39a}$$

$$E_{f,2}(s) = \exp\left(-\frac{2\pi^2\lambda_t (1-p) \csc\left(\frac{2\pi}{\alpha}\right)(C_d s)^{\frac{2}{\alpha}}}{\alpha}\right), \tag{6.39b}$$

$$e_1 = \left(C_d + NC_r d_0^{-\alpha}\right). \tag{6.39c}$$

*Proof.* See Appendix 6.7.1. □

#### 6.3.2.2 Nearest Association Strategy

If $U_0$ is associated with the nearest TX, the Laplace transform of the interference power is given in the following proposition.

**Proposition 9.** *The Laplace transform of the interference power $I$ with nearest association strategy is*

$$\mathcal{L}_{I,n}(s) = E_{n,1}(s)\, E_{n,2}(s), \tag{6.40}$$

*where*

$$E_{n,1}(s) = \exp\left(\pi\lambda_t p d_{g,0}^2 \left(1 - {}_2F_1\left(1, -\frac{2}{\alpha}; 1 - \frac{2}{\alpha}; -e_1 d_{g,0}^{-\alpha} s\right)\right)\right), \tag{6.41a}$$

$$E_{n,2}(s) = \exp\left(\pi\lambda_t (1-p) d_{g,0}^2 \left(1 - {}_2F_1\left(1, -\frac{2}{\alpha}; 1 - \frac{2}{\alpha}; -C_d d_{g,0}^{-\alpha} s\right)\right)\right). \tag{6.41b}$$

*$d_{g,0}$ is the distance between $U_0$ and the associated TX that is closest to $U_0$.*

*Proof.* The proof is similar to that used in Proposition 8 by changing lower limit of the integration to $d_{g,0}$, as

$$\begin{aligned}\mathcal{L}_{I,n}(s) &= \exp\left(2\pi\lambda_t \int_{d_{g,0}}^{\infty} \left(\frac{p}{1 + s e_1 r^{-\alpha}} + \frac{1-p}{1 + s C_d r^{-\alpha}} - 1\right) r \, \mathrm{d}r\right) \\ &= E_{n,1}(s)\, E_{n,2}(s).\end{aligned} \tag{6.42}$$

□

## 6.4 Performance Analysis

In this section, we analyze the coverage probability and the average achievable rate of the typical user with the fixed and nearest association strategies.

### 6.4.1 Coverage Probability Analysis

#### 6.4.1.1 Fixed Association with Assisting RIS

The main result is concluded in the following proposition.

**Proposition 10.** *If $U_0$ is associated with a TX at a fixed location and the TX has an assisting RIS, the coverage probability of $U_0$ is*

$$P_1(\bar{\gamma}) = \sum_{i=0}^{\hat{\kappa}_s - 1} \frac{(-1)^i}{i!} \left[\frac{\partial^i}{\partial s^i} \exp\left(V(s)\right)\right]_{s=1}, \tag{6.43}$$

*where*

$$\hat{\kappa}_s = \lfloor \kappa_s \rceil, \tag{6.44a}$$

$$V(s) = -\frac{s\bar{\gamma}}{\omega_s}\gamma_t^{-1} - \frac{2\pi^2\lambda_t p \csc\left(\frac{2\pi}{\alpha}\right)\left(\frac{e_1\bar{\gamma}}{\omega_s}s\right)^{\frac{2}{\alpha}}}{\alpha} - \frac{2\pi^2\lambda_t(1-p)\csc\left(\frac{2\pi}{\alpha}\right)\left(\frac{C_d\bar{\gamma}}{\omega_s}s\right)^{\frac{2}{\alpha}}}{\alpha}. \tag{6.44b}$$

*Proof.* See Appendix 6.7.2. □

**Remark 13.** *We take another step to round $\kappa_s$ to its nearest positive integer. We will study errors introduced by the rounding operation through simulations.*

#### 6.4.1.2 Fixed Association without Assisting RIS

If the associated TX does not have an assisting RIS, the coverage probability is derived in the following proposition.

**Proposition 11.** *If $U_0$ is associated with a TX at a fixed location and the TX does not have an assisting RIS, the coverage probability of $U_0$ is*

$$P_2(\bar{\gamma}) = \exp\left(-\frac{\bar{\gamma}}{\eta_{g,0}}\gamma_t^{-1} - \frac{2\pi^2\lambda_t p \csc\left(\frac{2\pi}{\alpha}\right)\left(\frac{e_1\bar{\gamma}}{\eta_{g,0}}\right)^{\frac{2}{\alpha}}}{\alpha} - \frac{2\pi^2\lambda_t(1-p)\csc\left(\frac{2\pi}{\alpha}\right)\left(\frac{C_d\bar{\gamma}}{\eta_{g,0}}\right)^{\frac{2}{\alpha}}}{\alpha}\right). \tag{6.45}$$

*Proof.* Since $S_0^*$ is exponentially distributed, we can write

$$\begin{aligned} P_2 &= \mathbb{P}\left(\gamma_0^* > \bar{\gamma}\right) \\ &= \mathbb{P}\left(S_0^* > \bar{\gamma}(I + \gamma_t^{-1})\right) \\ &= \mathbb{E}_I\left[\bar{F}_{S_0^*}(\bar{\gamma}(I + \gamma_t^{-1}))\right] \\ &= \mathbb{E}_I\left[\exp\left(-\frac{\bar{\gamma}}{\eta_{g,0}}\left(I + \gamma_t^{-1}\right)\right)\right] \\ &= \exp\left(-\frac{\bar{\gamma}}{\eta_{g,0}}\gamma_t^{-1}\right)\mathcal{L}_{I,f}\left(\frac{\bar{\gamma}}{\eta_{g,0}}\right). \end{aligned} \tag{6.46}$$

Thus, the proof is complete. □

**Remark 14.** *As can be seen from* (6.45)*, increasing the density of TXs will lead to lower coverage probability due to the increased interference power.*

#### 6.4.1.3 Nearest Association Strategy

If $U_0$ is associated with the nearest TX, the PDF of $d_{g,0}$ is given by

$$f_{d_{g,0}}(x) = 2\pi\lambda_t x e^{-\lambda_t \pi x^2}. \tag{6.47}$$

Then, the coverage probability of $U_0$ is given in the following proposition

**Proposition 12.** *With the nearest association strategy, the coverage probability of* $U_0$ *is given in an integral form as*

$$P_{c,n}(\bar{\gamma}) = p\int_0^\infty q^+(r) f_{d_{g,0}}(r)\,\mathrm{d}r + (1-p)\int_0^\infty q^*(r) f_{d_{g,0}}(r)\,\mathrm{d}r, \tag{6.48}$$

*where*

$$q^+(r) = \sum_{i=0}^{\hat{\kappa}_s - 1} \frac{(-1)^i}{i!} \left[ \frac{\partial^i}{\partial s^i} \exp\left(W(s,r)\right) \right]_{s=1}, \tag{6.49a}$$

$$\begin{aligned} W(s,r) = &-\frac{\bar{\gamma}\gamma_t^{-1}}{C_d \bar{\chi}} r^\alpha s + \pi\lambda_t r^2 - \pi\lambda_t p r^2 {}_2F_1\left(1, -\frac{2}{\alpha}; 1 - \frac{2}{\alpha}; -\frac{e_1\bar{\gamma}}{C_d\bar{\chi}} s\right) \\ &- \pi\lambda_t (1-p) r^2 {}_2F_1\left(1, -\frac{2}{\alpha}; 1 - \frac{2}{\alpha}; -\frac{\bar{\gamma}}{\bar{\chi}} s\right), \end{aligned} \tag{6.49b}$$

$$\begin{aligned} q^*(r) = \exp\Bigg( &-\frac{\bar{\gamma}\gamma_t^{-1}}{C_d} r^\alpha + \pi\lambda_t r^2 - \pi\lambda_t p r^2 {}_2F_1\left(1, -\frac{2}{\alpha}; 1 - \frac{2}{\alpha}; -\frac{e_1\bar{\gamma}}{C_d}\right) \\ &- \pi\lambda_t (1-p) r^2 {}_2F_1\left(1, -\frac{2}{\alpha}; 1 - \frac{2}{\alpha}; -\bar{\gamma}\right)\Bigg). \end{aligned} \tag{6.49c}$$

*Proof.* See Appendix 6.7.3. □

For $\alpha = 4$, the above expression in Proposition 12 can be further simplified to a closed form expression, which is summarized in the following Corollary.

**Corollary 1.** *For $\alpha = 4$, the coverage probability of $U_0$ with the nearest association strategy is given in closed form as*

$$P_{c,n}(\bar{\gamma}) = \frac{\pi\lambda_t p}{2} \sum_{i=0}^{\hat{\kappa}_s - 1} \frac{(-1)^i}{i!} \left[ \frac{\partial^i}{\partial s^i} X^+(s) \right]_{s=1} + \frac{\pi\lambda_t (1-p)}{2} X^*, \tag{6.50}$$

*where*

$$X^+(s) = \frac{\sqrt{\pi} \exp\left(\frac{X_2^2(s)}{4X_1(s)}\right) \operatorname{erfc}\left(\frac{X_2(s)}{2\sqrt{X_1(s)}}\right)}{\sqrt{X_1(s)}}, \quad X_1(s) = \frac{\bar{\gamma}\gamma_t^{-1}}{C_d\bar{\chi}} s, \tag{6.51a}$$

$$X_2(s) = \pi\lambda_t p \, {}_2F_1\left(1, -\frac{1}{2}; \frac{1}{2}; -\frac{e_1\bar{\gamma}}{C_d\bar{\chi}} s\right) + \pi\lambda_t (1-p) {}_2F_1\left(1, -\frac{1}{2}; \frac{1}{2}; -\frac{\bar{\gamma}}{\bar{\chi}} s\right), \tag{6.51b}$$

$$X^* = \frac{\sqrt{\pi} \exp\left(\frac{X_4^2}{4X_3}\right) \operatorname{erfc}\left(\frac{X_4}{2\sqrt{X_3}}\right)}{\sqrt{X_3}}, \quad X_3 = \frac{\bar{\gamma}\gamma_t^{-1}}{C_d}, \tag{6.51c}$$

$$X_4 = \pi\lambda_t p \, {}_2F_1\left(1, -\frac{1}{2}; \frac{1}{2}; -\frac{e_1\bar{\gamma}}{C_d}\right) + \pi\lambda_t (1-p) {}_2F_1\left(1, -\frac{1}{2}; \frac{1}{2}; -\bar{\gamma}\right). \tag{6.51d}$$

*Proof.* This corollary can be proved by using the interchangeable property of differentiation and integration. □

Then, we consider the interference-limited case where the noise power is negligible compared to the transmit power $P$, such that $\gamma_t^{-1} \approx 0$. This is common in a practical wireless communication system where the transmit power is usually much larger than the noise power. In this case, the closed form outage probability expression can be derived, which is summarized in the following Proposition.

**Proposition 13.** *If $P \gg \sigma_0^2$, the coverage probability of $U_0$ can be expressed as*

$$\tilde{P}_{c,n}(\bar{\gamma}) = p \sum_{i=0}^{\hat{\kappa}_s - 1} \frac{(-1)^i}{i!} \left[ \frac{\partial^i}{\partial s^i} \left( Y_1(s) \right)^{-1} \right]_{s=1} + (1-p)(Y_2)^{-1} \tag{6.52}$$

*where*

$$Y_1(s) = p\, {}_2F_1\left(1, -\frac{2}{\alpha}; 1 - \frac{2}{\alpha}; -\frac{e_1 \bar{\gamma}}{C_d \bar{\chi}} s\right) + (1-p)\, {}_2F_1\left(1, -\frac{2}{\alpha}; 1 - \frac{2}{\alpha}; -\frac{\bar{\gamma}}{\bar{\chi}} s\right), \tag{6.53a}$$

$$Y_2 = p\, {}_2F_1\left(1, -\frac{2}{\alpha}; 1 - \frac{2}{\alpha}; -\frac{e_1 \bar{\gamma}}{C_d}\right) + (1-p) {}_2F_1\left(1, -\frac{2}{\alpha}; 1 - \frac{2}{\alpha}; -\bar{\gamma}\right). \tag{6.53b}$$

*Proof.* As $\gamma_t^{-1} \to 0$, $W(s)$ and $q^*(r)$ defined in Proposition 12 can be simplified as

$$\begin{aligned} W(s,r) = {} & \pi \lambda_t r^2 - \pi \lambda_t p r^2 {}_2F_1\left(1, -\frac{2}{\alpha}; 1 - \frac{2}{\alpha}; -\frac{e_1 \bar{\gamma}}{C_d \bar{\chi}} s\right) \\ & - \pi \lambda_t (1-p) r^2 {}_2F_1\left(1, -\frac{2}{\alpha}; 1 - \frac{2}{\alpha}; -\frac{\bar{\gamma}}{\bar{\chi}} s\right), \end{aligned} \tag{6.54a}$$

$$\begin{aligned} q^*(r) = \exp\Bigg( & \pi \lambda_t r^2 - \pi \lambda_t p r^2 {}_2F_1\left(1, -\frac{2}{\alpha}; 1 - \frac{2}{\alpha}; -\frac{e_1 \bar{\gamma}}{C_d}\right) \\ & - \pi \lambda_t (1-p) r^2 {}_2F_1\left(1, -\frac{2}{\alpha}; 1 - \frac{2}{\alpha}; -\bar{\gamma}\right) \Bigg). \end{aligned} \tag{6.54b}$$

Recalling the definition of $P_{c,n}(\bar{\gamma})$ in Proposition 12 and using the interchangeable property of integration and differentiation, we can obtain the result in Proposition 13.

□

**Remark 15.** *It turns out the coverage probability of $U_0$ does not depend on $\lambda_t$ in the interference-limited scenario. With the nearest association strategy, increasing the density of TXs will help $U_0$ connect with a closer TX. On the other hand, the larger density of TXs will lead to enhanced interference. Proposition 13 shows that these two effects can perfectly offset each other. This point will be further illustrated by numerical results.*

### 6.4.2 Average Achievable Rate Analysis

The average achievable rate of the typical user can be derived from the coverage probability expression. A lemma regarding the relationship between the average achievable rate and the coverage probability is first provided.

**Lemma 4.** *If the coverage probability of the typical user is $P_c(\bar{\gamma})$, where $\bar{\gamma}$ is the coverage SINR threshold, the average achievable rate of the typical user can be written as*

$$R = \frac{1}{\ln(2)} \int_0^\infty \frac{P_c(x)}{1+x} \, \mathrm{d}x. \tag{6.55}$$

*Proof.* As defined in (6.19), the average achievable rate of the typical user can be

rewritten as

$$\begin{aligned} R &\overset{(a)}{=} \int_0^\infty \log_2(1+\bar{\gamma}) \frac{\partial(1-P_c(\bar{\gamma}))}{\partial\bar{\gamma}} \mathrm{d}\bar{\gamma} \\ &= -\frac{1}{\ln(2)} \int_0^\infty \int_0^{\bar{\gamma}} \frac{1}{1+x} \mathrm{d}x \frac{\partial P_c(\bar{\gamma})}{\partial\bar{\gamma}} \mathrm{d}\bar{\gamma} \\ &\overset{(b)}{=} -\frac{1}{\ln(2)} \int_0^\infty \frac{1}{1+x} \int_x^\infty \frac{\partial P_c(\bar{\gamma})}{\partial\bar{\gamma}} \mathrm{d}\bar{\gamma}\, \mathrm{d}x \\ &= \frac{1}{\ln(2)} \int_0^\infty \frac{P_c(x)}{1+x} \mathrm{d}x, \end{aligned} \tag{6.56}$$

where $(a)$ is due to the mathematical relationship between the PDF and CDF; $(b)$ is obtained by changing the integration order. □

**Corollary 2.** *For the fixed association strategy, the average achievable rate of $U_0$ with and without an assisting RIS can be respectively given as*

$$R_1 = \frac{1}{\ln(2)} \int_0^\infty \frac{P_1(x)}{1+x} \mathrm{d}x, \tag{6.57a}$$

$$R_2 = \frac{1}{\ln(2)} \int_0^\infty \frac{P_2(x)}{1+x} \mathrm{d}x, \tag{6.57b}$$

*where $P_1(x)$ and $P_2(x)$ are defined in Proposition 10 and Proposition 11, respectively.*

If $\alpha = 4$, $R_1$ and $R_2$ in the interference-limited scenario can be further transformed in the following Corollary.

**Corollary 3.** *In an interference-limited scenario with $\alpha = 4$, $R_1$ and $R_2$ are given by*

$$\tilde{R}_1 = \frac{1}{\ln(2)} \sum_{i=0}^{\hat{\kappa}_s - 1} \frac{(-1)^i}{i!} \left[ \frac{\partial^i}{\partial s^i} V^+(s) \right]_{s=1} \tag{6.58a}$$

$$\tilde{R}_2 = \frac{1}{\ln(2)} \left( (\pi - 2\mathrm{Si}(V_2(s))) \sin(V_2(s)) - 2\mathrm{Ci}(V_2(s)) \cos(V_2(s)) \right) \tag{6.58b}$$

*where*

$$V^{+}(s) = (\pi - 2\mathrm{Si}(V_1(s)))\sin(V_1(s)) - 2\mathrm{Ci}(V_1(s))\cos(V_1(s)), \tag{6.59a}$$

$$V_1(s) = \frac{\pi^2}{2}\lambda_t \left( p\left(\frac{e_1}{\omega_s}s\right)^{\frac{1}{2}} + (1-p)\left(\frac{C_d}{\omega_s}s\right)^{\frac{1}{2}} \right), \tag{6.59b}$$

$$V_2(s) = \frac{\pi^2}{2}\lambda_t \left( p\left(\frac{e_1}{\eta_{g,0}}\right)^{\frac{1}{2}} + (1-p)\left(\frac{C_d}{\eta_{g,0}}\right)^{\frac{1}{2}} \right). \tag{6.59c}$$

*Proof.* This can be proved by using the interchangeable property of differentiation and integration. □

**Corollary 4.** *For the nearest association strategy, the average achievable rate of $U_0$ is given by*

$$R_{c,n} = \frac{1}{\ln(2)} \int_0^{\infty} \frac{P_{c,n}(\bar{\gamma})}{1+\bar{\gamma}} \, \mathrm{d}\bar{\gamma}, \tag{6.60}$$

*where $P_{c,n}(\bar{\gamma})$ is defined in Proposition 12.*

**Corollary 5.** *For the nearest association strategy, the average achievable rate of $U_0$ in the interference-limited scenario is given by*

$$\tilde{R}_{c,n} = \frac{1}{\ln(2)} \int_0^{\infty} \frac{\tilde{P}_{c,n}(x)}{1+x} \, \mathrm{d}x, \tag{6.61}$$

*where $\tilde{P}_{c,n}(x)$ is defined in Proposition 13.*

## 6.5 Numerical Results

In this section, we present numerical results to validate the effectiveness of the above analysis, including the approximate signal power distribution, coverage probability and average achievable rate. We also explore several insights regarding the impacts of different system parameters on the communication performance. Unless otherwise

mentioned, the parameters of the MC simulations are listed as follows. The GPP for the distribution of TXs and RISs is generated in a disk area of radius 5000 m. The path loss per unit distance of the direct link and the reflected path are given by $C_d = C_r = -30\,\text{dB}$. $U_0$ is located at the origin. The AWGN power is $\sigma_0^2 = -70\,\text{dBm}$. Similar simulation parameters setting has been applied in [118, 121].

### 6.5.1 Fixed Association Strategy Analysis

Fig. 6.2 illustrates the coverage probability versus the transmit power with different densities of TXs. $U_0$ is associated with a fixed TX that has an assisting RIS. The path loss exponent is $\alpha = 2.5$. The number of elements of each RIS is $N = 32$, and the RIS association probability is $p = 0.5$. The Nakagami-$m$ shape parameters are set to be $m_h = m_r = 2$. The distance between a RIS and its corresponding TX varies in $d_0 \in \{3, 5\}$. The location of $U_0$'s corresponding TX is fixed at $(20, 0)$, while the locations of its assisting RIS are $(20, 3)$ and $(20, 5)$ for $d_0 = 3$ and $d_0 = 5$, respectively. To illustrate the impact of interfering TXs, the coverage probability curve without interfering TXs, labelled as 'No Interference', is also given for $d_0 = 3$. We can see that, even though several approximations are applied to obtain the closed form coverage probability in Proposition 10, the proposed analytical result is still accurate for a large density of TXs, e.g., $\lambda_t = 10^{-3}$. Interfering TXs sharing the same resource block will always deteriorate the system performance, but the influence is only significant when the density of TXs is large. For example, when the transmit power is $P = -24\text{dBm}$ and $d_0 = 3$, the coverage probability is 0.53 and 0.93 for $\lambda_t = 10^{-3}$ and $\lambda_t = 10^{-4}$, respectively. However, the impact of interfering TXs is negligible when $\lambda_t < 10^{-4}$ as the curves are close to the ideal case without interference. Further, it can be observed that increasing the distance between TX and its associating RIS has negative impact on the system performance due to the double fading effect of RIS assisted transmission. Increasing $d_0$ will lead to lower desired signal power received at $U_0$.

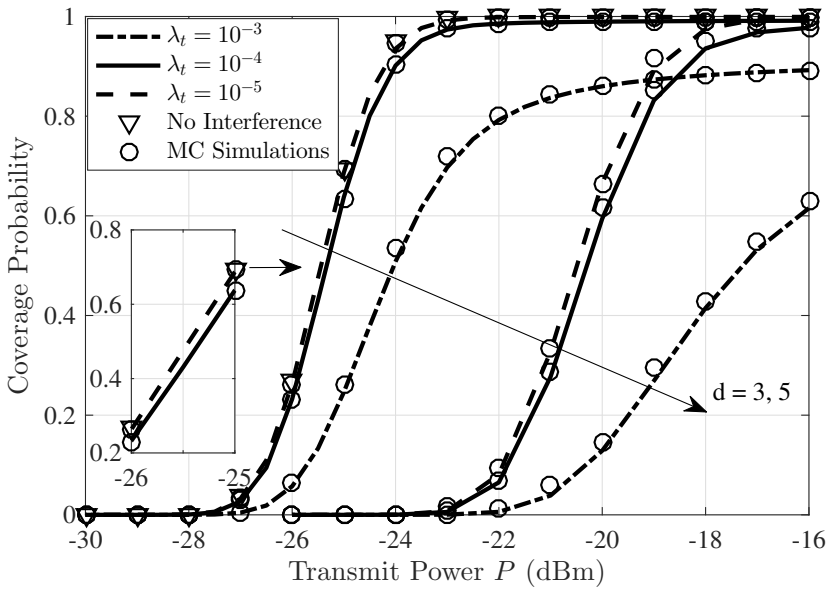



Figure 6.2: Coverage probability versus transmit power with different densities of TXs. Fixed association strategy with assisting RIS.

Fig. 6.3 shows the coverage probability versus the transmit power when $U_0$ is associated with a fixed TX without an assisting RIS. $d_0 = 3$. To illustrate the impact of path loss exponent on the system performance, the path loss exponent varies in $\alpha \in \{2.5, 3, 3.5, 4\}$ for $\lambda_t = 10^{-5}$. The performance degradation due to interfering TXs is negligible if $\lambda_t < 10^{-6}$. Compared with Fig. 6.2, we can learn that associating $U_0$ with a TX that has an assisting RIS can significantly improve the performance. For example, if $\lambda_t = 10^{-5}$ and $\alpha = 2.5$, achieving the coverage probability of 0.9 requires the transmit power of $P = -24\,\text{dBm}$ and $10\,\text{dBm}$ for the cases with and without assisting RIS, respectively.

The impact of the RIS association probability $p$ is explored in Fig. 6.4. $U_0$ is associated with a fixed TX with an assisting RIS. The path loss exponent is $\alpha = 2.5$, and $d_0 = 3$. The RIS association probability and the number of elements vary in $p \in \{0, 0.5, 1\}$ and $N \in \{32, 64\}$, respectively. As expected, increasing $p$ will lead to lower coverage probability if the fixed associations strategy is applied since the desired signal power is fixed and the interference power scattered by RISs is enhanced due to

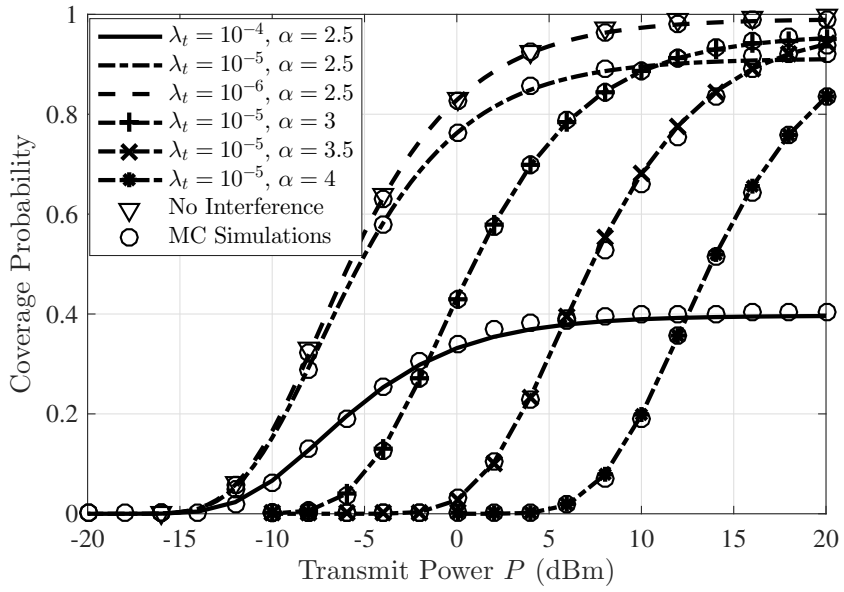



Figure 6.3: Coverage probability versus transmit power with different densities of TXs. Fixed association strategy without assisting RIS.

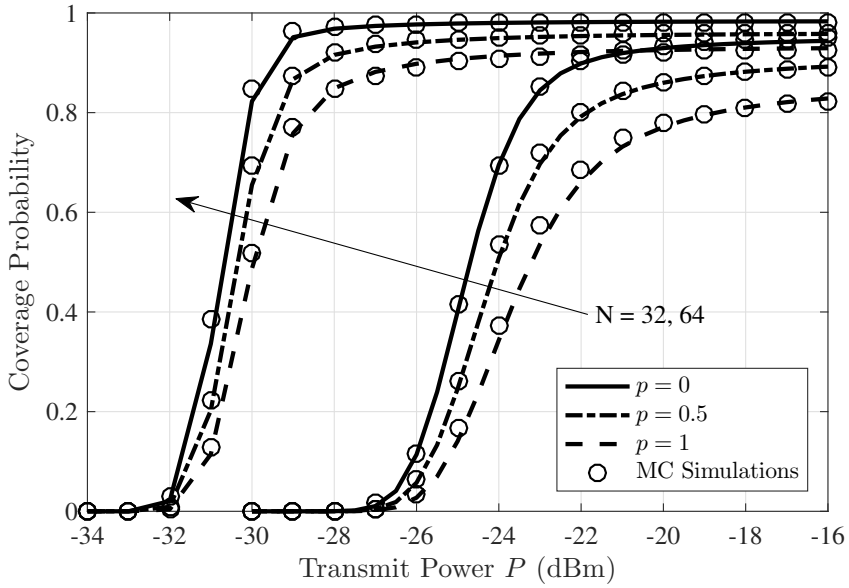



Figure 6.4: Coverage probability versus transmit power with different RIS association probabilities. Fixed association strategy with assisting RIS.

the larger RIS association probability.

Fig. 6.5 shows the average achievable rate versus the transmit power with different densities of TXs. $U_0$ is connected with a fixed TX that has an assisting RIS. Similar to the setup in Fig. 6.2, the distance between a RIS and its corresponding TX lies

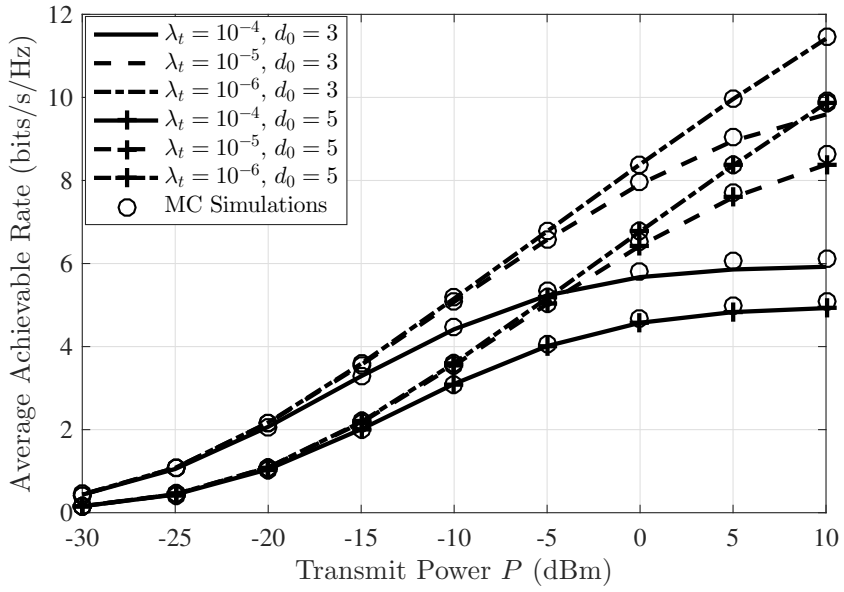



Figure 6.5: Average achievable versus transmit power with different densities of TXs. Fixed association strategy.

in $d_0 \in \{3, 5\}$. The RIS association probability and the path loss exponent are respectively $p = 0.5$ and $\alpha = 2.5$, and the number of elements per RIS is $N = 32$. The density of TXs varies in $\lambda_t \in \{10^{-6}, 10^{-5}, 10^{-4}\}$. As expected, increasing the transmit power and reducing the density of TXs will lead to better performance of $U_0$. Similar to result regarding the coverage probability, the larger distance between TX and its connected RIS results in the lower average achievable rate due to the double fading effect.

### 6.5.2 Nearest Association Strategy Analysis

Fig. 6.6 illustrates the coverage probability against the transmit power when $U_0$ is associated with the nearest TX and $\alpha = 2.5$. The density of TXs varies in $\lambda_t \in \{10^{-5}, 5 \times 10^{-5}, 10^{-4}, 10^{-3}\}$, and the RIS association probability is $p = 0.9$. The number of elements per RIS is $N = 32$, and the distance between TX and its connected RIS is $d_0 = 3$. To verify the analysis in Corollary 1, the curves for $\alpha = 4$ are also given for $\lambda_t = 10^{-4}$. Increasing the density of TXs is beneficial for $U_0$ within certain transmit

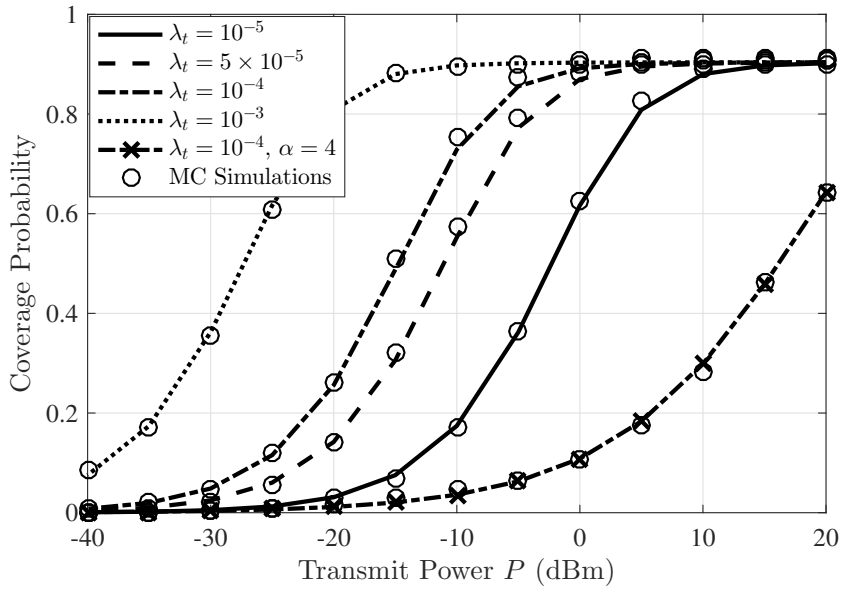



Figure 6.6: Coverage probability versus transmit power with different densities of TXs. Nearest association strategy.

power regime, since $U_0$ is more likely to be connected with a closer TX with the nearest association strategy. Furthermore, we can observe that the coverage probability is independent with the density of TXs when the noise power is negligible, which proves our analysis in Remark 15. As a step further, we investigate the impact of the RIS association probability $p$ on the average achievable rate and the coverage probability in the interference-limited scenario, i.e., $\gamma_t \to \infty$, with the nearest association strategy in Fig. 6.7. The path loss exponent lies in $\alpha \in \{2.5, 4\}$. In the current simulation setup, it turns out that increasing the RIS association probability can also improve the system performance since $U_0$ is more likely to be served by a RIS-assisted TX.

## 6.6 Summary

This chapter proposed a RIS-assisted multi-cell network with large-scale randomly deployed TXs, RISs and UEs. The locations of TXs and RISs were modeled by a GPP. We investigated the coverage probability and the average achievable rate of the typical user. The analytical results showed that increasing the density of TXs has

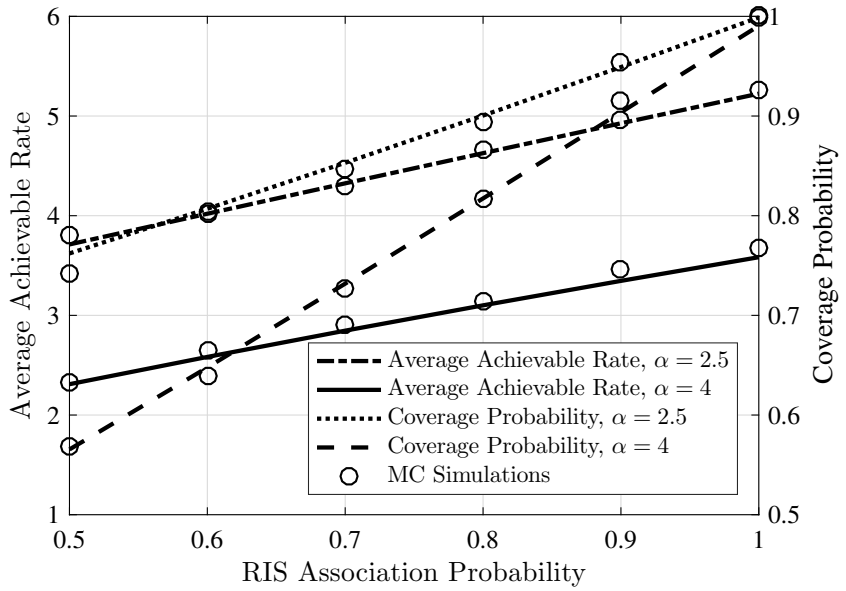



Figure 6.7: Average achievable rate and coverage probability versus RIS association probability. Nearest association strategy.

no influence on the coverage probability and the average achievable rate in the large transmit SNR regime with the nearest association strategy. The analysis was validated by the numerical results, which also demonstrated the significant performance gain brought by the RIS-assisted transmission with passive beamforming. With different association strategies, the impact on system performance differed when the density of TXs and the RIS association probability were increased. Specifically, with the fixed association strategy, increasing the density of TXs and the association probability was found to be detrimental to system performance. On the other hand, with the nearest association strategy, increasing the density of TXs and the association probability was found to be beneficial to system performance. It is essential to highlight that the system model represents a wireless communication network where each transmitter has equal power, and no interference suppression techniques are employed within the network. In practice, the performance of a wireless network is expected to surpass the analysis based on stochastic geometry since transmitters can cooperate with each other, and interference can be effectively suppressed. Incorporating

interference suppression techniques and modeling varying transmit powers among different transmitters will constitute an important future work when utilizing stochastic geometry to analyze the performance of wireless networks.

## 6.7 Appendices

### 6.7.1 Proof of the Proposition 8

The Laplace transform of the interference power $I$ with the fixed association strategy can be written as

$$
\begin{aligned}
&\mathcal{L}_{I,f}(s) = \mathbb{E}\left[e^{-sI}\right] \qquad (6.62)\\
&= \mathbb{E}\left[\exp\left(-s\left(\sum_{k\in\Lambda_t\setminus\{0\}} I_{1,k}b_k + I_{2,k}(1-b_k)\right)\right)\right]\\
&\overset{(a)}{=} \mathbb{E}\left[\prod_{k\in\Lambda_t\setminus\{0\}} \left(p\exp\left(-sI_{1,k}\right) + (1-p)\exp\left(-sI_{2,k}\right)\right)\right]\\
&\overset{(b)}{=} \mathbb{E}\left[\prod_{k\in\Lambda_t\setminus\{0\}} \left(\frac{p}{1+\left(\eta_{g,k}+N\eta_{h,k}\right)s} + \frac{1-p}{1+\eta_{g,k}s}\right)\right],\\
&\overset{(c)}{\approx} \mathbb{E}\left[\prod_{k\in\Lambda_t\setminus\{0\}} \left(\frac{p}{1+e_1 d_{g,k}^{-\alpha}s} + \frac{1-p}{1+C_d d_{g,k}^{-\alpha}s}\right)\right]\\
&\overset{(d)}{=} \exp\left(2\pi\lambda_t\int_0^\infty \left(\frac{p}{1+se_1r^{-\alpha}} + \frac{1-p}{1+sC_dr^{-\alpha}} - 1\right) r\,\mathrm{d}r\right)\\
&= \exp\left(2\pi\lambda_t p\int_0^\infty \left(\frac{1}{1+se_1r^{-\alpha}} - 1\right) r\,\mathrm{d}r\right)\\
&\quad\times \exp\left(2\pi\lambda_t(1-p)\int_0^\infty \left(\frac{1}{1+sC_dr^{-\alpha}} - 1\right) r\,\mathrm{d}r\right),
\end{aligned}
$$

where $(a)$ follows from Lemma 2 in [60]; $(b)$ is obtained by the fact that $I_{1,k}$ and $I_{2,k}$ both follow the exponential distribution. From the Slivnyak's theorem, conditioning on a TX at a fixed location does not influence the distribution of other clusters; $(c)$

is due to the distance approximation. Considering the spatial correlation between the locations of a TX and its associated RIS where a separate link is required to pass the CSI, $d_{g,j}$ can be significantly larger than $d_0$. A similar assumption is also applied in [58]. Besides, $(d)$ holds by using the probability generating functional lemma (PGFL). Thus, the result in Proposition 8 can be obtained.

### 6.7.2 Proof of the Proposition 10

We have used the moment matching approach to fit the distribution of $S_0^+$ to a gamma random variable with shape parameter $\kappa_s$ and scale parameter $\omega_s$. Here, we round $\kappa_s$ to its nearest integer $\hat{\kappa}_s$. Then, we can have

$$\begin{aligned} P_1(\bar{\gamma}) &= \mathbb{P}\left(\gamma_0^+ > \bar{\gamma}\right) \\ &= \mathbb{P}\left(S_0^+ > \bar{\gamma}(I + \gamma_t^{-1})\right) \\ &= \mathbb{E}_I\left[\bar{F}_{S_0^+}(\bar{\gamma}(I + \gamma_t^{-1}))\right] \\ &= \mathbb{E}_X\left[\frac{\Gamma\left(\hat{\kappa}_s, X\right)}{\Gamma(\hat{\kappa}_s)}\right], \end{aligned} \tag{6.63}$$

where

$$X = \frac{\bar{\gamma}}{\omega_s}\left(I + \gamma_t^{-1}\right). \tag{6.64}$$

Since $\hat{\kappa}_s$ is an integer, using the series expansion of the upper incomplete gamma function, we can write

$$\begin{aligned}
P_1(\bar{\gamma}) &= \sum_{i=0}^{\hat{\kappa}_s-1} \frac{(-1)^i}{i!} \mathbb{E}_X \left[(-1)^i X^i e^{-X}\right] \\
&= \sum_{i=0}^{\hat{\kappa}_s-1} \frac{(-1)^i}{i!} \mathbb{E}_X \left[\left[\frac{\partial^i}{\partial s^i} e^{-sX}\right]_{s=1}\right] \\
&\overset{(a)}{=} \sum_{i=0}^{\hat{\kappa}_s-1} \frac{(-1)^i}{i!} \left[\frac{\partial^i}{\partial s^i} \mathbb{E}_X \left[e^{-sX}\right]\right]_{s=1} \\
&= \sum_{i=0}^{\hat{\kappa}_s-1} \frac{(-1)^i}{i!} \left[\frac{\partial^i}{\partial s^i} \mathcal{L}_X(s)\right]_{s=1}, \qquad (6.65)
\end{aligned}$$

where $(a)$ follows by interchanging differentiation and expectation.

The Laplace transform of $X$ can be derived directly from the Laplace transform of $I$:

$$\begin{aligned}
\mathcal{L}_X(s) &= \mathbb{E}_I \left[\exp\left(-\frac{s\bar{\gamma}}{\omega_s}(I + \gamma_t^{-1})\right)\right] \\
&= \exp\left(-\frac{s\bar{\gamma}}{\omega_s}\gamma_t^{-1}\right) \mathcal{L}_{I,f}\left(\frac{s\bar{\gamma}}{\omega_s}\right). \qquad (6.66)
\end{aligned}$$

Using the result in Proposition 8, we arrive at the expression of $P_1$ given in the proposition.

### 6.7.3 Proof of the Proposition 12

The coverage probability of $U_0$ can be transformed as

$$\begin{aligned} P_{c,n}(\bar{\gamma}) &= \mathbb{E}_{d_{g,0}}\left[\mathbb{P}\left(\gamma_0 > \bar{\gamma}\right)\right] \\ &= \mathbb{E}_{d_{g,0}}\left[p\mathbb{P}\left(\gamma_0^+ > \bar{\gamma}\right) + (1-p)\mathbb{P}\left(\gamma_0^* > \bar{\gamma}\right)\right] \\ &= p\int_0^\infty \mathbb{P}\left(\gamma_0^+ > \bar{\gamma}\right) f_{d_{g,0}}(r)\,\mathrm{d}r \\ &\quad + (1-p)\int_0^\infty \mathbb{P}\left(\gamma_0^* > \bar{\gamma}\right) f_{d_{g,0}}(r)\,\mathrm{d}r. \end{aligned} \tag{6.67}$$

The distance approximation used in the proof of Proposition 8 such that $d_{g,j} \approx d_{r,j}$, $j \in \Lambda_2^{(P)}$ is applied here. Then, following a similar procedure to Proposition 10 and Proposition 11, using the result in Proposition 9, and recalling the definitions of $\omega_s$ and $\eta_{g,0}$, we can directly derive $\mathbb{P}\left(\gamma_0^+ > \bar{\gamma}\right)$ and $\mathbb{P}\left(\gamma_0^* > \bar{\gamma}\right)$ as $q^+(r)$ and $q^*(r)$, respectively.

# Chapter 7

# Conclusions and Future Work

## 7.1 Thesis Summary

In conclusion, this thesis presented a comprehensive analysis of the performance of various RIS-assisted wireless communication systems, considering practical RIS characteristics and different scenarios. The research focused on four distinct RIS systems, each with a different system model and practical RIS characteristics. The primary aim of this work was to better understand the potential and limitations of RIS technology in future wireless networks.

More specifically, Chapter 1 briefly introduced the development of wireless communications and stated the motivation of studying the RIS-assisted communications. Then, we provided a research background in Chapter 2 by introducing the concept of smart radio environments and exploring the fundamental principles of RIS technology. It also briefly covered stochastic geometry, a mathematical approach for analyzing large-scale wireless networks.

Chapter 3 was the first technical chapter, focusing on the performance analysis of RIS-assisted wireless communication systems with phase errors in both line-of-sight (LoS) and Rayleigh fading scenarios. The chapter derived the outage probability of

the system with Von Mises distributed phase errors over LoS channels, as well as the outage probability and diversity orders of perfect phase alignment and one-bit phase adjustment schemes over Rayleigh fading channels. The impact of different types of phase errors and other system parameters on the system performance was explored and discussed in detail. The study showed that increasing the number of RIS elements and improving the accuracy of phase adjustment can significantly improve the system performance. By comparing the performance of perfect phase alignment and one-bit phase adjustment, it was revealed that one-bit phase adjustment can result in a penalty of approximately 5 dB, while two-bit phase adjustment can lead to nearly optimal performance.

Chapter 4 examined the impact of channel correlations on RIS-assisted communication systems, which is a critical issue in practical scenarios due to the small distances among adjacent RIS elements. The chapter analyzed the performance of RIS systems under two channel models, correlated Rayleigh fading and correlated Nakagami-$m$ fading, deriving closed-form expressions of outage probability and average achievable rates for both models. The channel hardening effect in the RIS-assisted communication system with correlated channels was also investigated. The study demonstrated that channel correlations can lead to performance degradation. However, it was proved that the average achievable rates with correlated channels were asymptotically equivalent to those with uncorrelated channels for a large number of elements. This key conclusion indicated that the performance loss can be compensated by implementing large-scale RISs. The research provided valuable insights into the impact of channel correlations on RIS systems and offered useful guidance for the design of practical RIS-assisted communication systems.

Chapter 5 studied the application of RIS technology in more intricate wireless communication systems, specifically concentrating on two spectrum efficiency techniques: non-orthogonal multiple access (NOMA) and full-duplex (FD) communications. In

the RIS-assisted NOMA, the chapter derived closed-form expressions for the outage probability of users with strong and weak channel conditions. Moreover, it investigated the circumstances under which RIS-assisted NOMA surpassed RIS-assisted time-division multiple access (TDMA) performance by calculating upper bounds on the average achievable rates for both NOMA and TDMA transmission schemes. Regarding the RIS-assisted FD system, the chapter proposed a setup where an FD transceiver simultaneously served an uplink user and a downlink user, with two RISs dedicated to assisting each user individually. The outage probability of uplink and downlink transmissions was derived in a closed form, and the impact of residual self-interference (SI) was examined by identifying the residual SI threshold, below which FD communication proved superior to its HD counterpart.

Chapter 6 examined the performance of a RIS-assisted large-scale network by assessing coverage probability and average achievable rate through stochastic geometry. Transmitter (TX) and RIS locations, modeled by a Gauss-Poisson process (GPP), accounted for spatial correlation. The study discussed two association strategies: nearest and fixed association. The coverage probability and average achievable rate of a typical user were derived. The results revealed that increasing TX density did not impact coverage probability or average achievable rate with the nearest association strategy in a high transmit signal-to-noise ratio (SNR) regime. RIS-assisted transmission with passive beamforming demonstrated substantial performance gains, and increasing TX density and RIS association probability had mixed effects on system performance depending on the association strategy.

The approaches and techniques presented in this thesis offer valuable understanding and analytical resources regarding the performance of RIS-assisted wireless communications, serving as a foundation for continued research and potential application in the future.

## 7.2 Future Directions

The studies conducted on the performance analysis of RIS-assisted communications in this thesis have revealed several promising research directions for future exploration. These potential avenues are briefly outlined in the subsequent subsections.

### 7.2.1 Analysis of RIS-Assisted MIMO Systems

Much of the existing research on the performance analysis of RIS-assisted communications focuses on scenarios with single-antenna transmitters and receivers. However, multiple-input multiple-output (MIMO) technology, which employs multiple antennas at both the transmitter and receiver, has been widely adopted in contemporary wireless networks. As such, the study of RIS-assisted MIMO systems is of paramount importance in the field of wireless communication.

RIS-assisted MIMO systems can effectively harness spatial diversity through the use of multiple antennas at both ends, thereby improving spectral efficiency and capacity. Additionally, RIS technology enables passive beamforming, which can reduce energy consumption, enhance signal quality, and expand coverage. This combination of features positions RIS-assisted MIMO systems as a promising solution for future wireless communication networks.

While many existing works have investigated the joint optimization of active and passive beamforming schemes in RIS-assisted MIMO systems, rigorous performance analysis in this area is still lacking. A thorough examination of the performance of RIS-assisted MIMO systems is essential for understanding their potential benefits, limitations, and trade-offs. This analysis should encompass various aspects such as channel estimation, interference management, and deployment strategies.

By delving deeper into the performance analysis of RIS-assisted MIMO systems, researchers can obtain valuable insights and develop innovative techniques to optimize

system performance. These findings will ultimately guide the development of future communication networks that fully leverage the capabilities of RIS-assisted MIMO technology, contributing to the emergence of more intelligent and efficient wireless communication systems.

### 7.2.2 New Designs of RIS to Achieve Full Coverage

Exploring new RIS designs is of paramount importance, particularly focusing on developing prototypes or test machines. Conventional designs mainly concentrate on reflecting-only RIS, which requires users to be located on the same side as the transmitter. As a result, users on the opposite side of the reflecting-only RIS experience obstruction, leading to limitations in service coverage. To tackle this challenge and achieve full coverage, it is crucial to explore innovative RIS designs capable of overcoming these constraints.

The concept of simultaneously transmitting and reflecting reconfigurable intelligent surface (STAR-RIS) has been proposed, which allows independent phase shifting for both reflected and refracted signals. However, no prototype has been developed thus far. New RIS designs enabling full coverage offer significant potential in expanding the capabilities of wireless communication systems. By ensuring that all users, regardless of their location, can access the system, these groundbreaking designs can substantially enhance connectivity and reliability. Furthermore, improved coverage can result in more consistent user experiences and heightened overall network performance. Exploring new RIS designs that facilitate full coverage is, therefore, an essential step towards realizing the complete potential of RIS technology, ultimately contributing to the development of more comprehensive and efficient wireless communication networks in the future.

### 7.2.3 Analysis of RIS-Assisted OFDM

The study of RIS-assisted orthogonal frequency-division multiplexing (OFDM) systems is of great importance in the field of wireless communication, as most existing works on the performance analysis of RIS-assisted communications have primarily assumed flat fading channels. However, when transmitting signals with large bandwidths, frequency-selectivity of the occupied channels is likely to occur, resulting in variations in channel conditions across different subcarriers. Consequently, it is essential to consider frequency-selective channels when analyzing the performance of RIS-assisted systems. OFDM, as a widely adopted technique for combating frequency-selective fading, enables efficient utilization of spectrum resources and mitigates inter-symbol interference. By investigating RIS-assisted OFDM systems, researchers can develop a more comprehensive understanding of the potential benefits and limitations associated with the integration of RIS technology into frequency-selective channel environments. Furthermore, exploring RIS-assisted OFDM systems can lead to the development of novel techniques for optimizing system performance in practical scenarios, thereby contributing to the advancement of next-generation wireless communication networks.

### 7.2.4 Standardization and Regulation

Standardization and regulation are critical for the successful implementation of RIS-assisted communications in real-world applications, as they provide a structured framework for the development, deployment, and integration of this emerging technology. The transition of RIS from a theoretical concept to a practical solution demands significant time and resources. Standardization ensures that the technology is consistent, compatible, and efficiently utilized across various wireless communication systems. Meanwhile, regulation guarantees that RIS-assisted communications adhere to industry requirements and guidelines, promoting a safe and reliable communication

environment.

By emphasizing the importance of standardization and regulation of RIS-assisted communications, researchers can contribute to a more efficient integration of this innovative technology to the existing wireless communication systems. This will also expedite the deployment of RIS-assisted systems in next-generation wireless networks, leading to improved communication capabilities and overall network performance.

## 7.3 Outlook on RIS Technology

From the theoretical analysis of the performance of RIS-assisted wireless communications presented in this thesis, we have developed a general outlook on the potential of this new technology in enhancing future wireless communication systems. RIS is an effective means of improving spectrum efficiency and enlarging wireless coverage by employing passive elements of low hardware cost. It has been demonstrated that RIS can be deployed in various wireless network scenarios to improve the overall performance of wireless communication systems.

Looking toward the future, RIS technology is expected to have potential in various wireless network applications. One such application is in millimeter-wave (mmWave) communication systems, where RIS can offer a viable solution to the challenges posed by the use of higher frequency bands. With the proliferation of fifth-generation (5G) networks and the upcoming sixth-generation (6G) networks, the use of higher frequency bands will become more prevalent, and the need for effective means of enhancing the signal strength in these bands will become critical, given that the channels for high-frequency signals are very vulnerable to blockages. By using RIS technology, these signals can be redirected and enhanced to overcome blockages and improve communication performance. Moreover, RIS technology is also well-suited for indoor environments that require stable wireless connections, such as virtual conference rooms

and factories. In these scenarios, RIS can be used to enhance signal coverage and link stability, thus improving overall communication performance.

However, to fully realize the potential of RIS technology, it is essential to address the challenges associated with its implementation. For example, the joint active and passive beamforming design in RIS-assisted MIMO systems and the STAR-RIS development are listed as future directions above. These challenges need to be addressed through ongoing research and development efforts in the field. Despite these challenges, RIS technology offers a promising solution for improving communication performance with low hardware cost and high energy efficiency. As such, we expect RIS technology to become a feature in future wireless communication systems, contributing to the development of more efficient and reliable wireless networks.

# Bibliography


[1] G. Marconi, "Wireless telegraphic communication," *Nobel Lecture*, vol. 11, pp. 198–222, 1909.

[2] R. Simons, "Guglielmo marconi and early systems of wireless communication," *Gec Review*, vol. 11, no. 1, pp. 37–55, 1996.

[3] T. M. Cover, *Elements of information theory*. John Wiley & Sons, 1999.

[4] C. E. Shannon, "A mathematical theory of communication," *The Bell system technical journal*, vol. 27, no. 3, pp. 379–423, 1948.

[5] P. Nicopolitidis, M. S. Obaidat, G. I. Papadimitriou, and A. S. Pomportsis, *Wireless networks*. John Wiley & Sons, 2003.

[6] M. Zeng, A. Annamalai, and V. K. Bhargava, "Recent advances in cellular wireless communications," *IEEE Commun. Mag.*, vol. 37, no. 9, pp. 128–138, 1999.

[7] C. Smith and D. Collins, *3G wireless networks*. McGraw-Hill Education, 2002.

[8] U. Varshney and R. Jain, "Issues in emerging 4G wireless networks," *Computer*, vol. 34, no. 6, pp. 94–96, 2001.

[9] A. Gupta and R. K. Jha, "A survey of 5G network: Architecture and emerging technologies," *IEEE Access*, vol. 3, pp. 1206–1232, 2015.

[10] F. Tariq, M. R. Khandaker, K.-K. Wong, M. A. Imran, M. Bennis, and M. Debbah, "A speculative study on 6G," *IEEE Wireless Commun.*, vol. 27, no. 4, pp. 118–125, 2020.

[11] A. Jovicic, J. Li, and T. Richardson, "Visible light communication: opportunities, challenges and the path to market," *IEEE Commun. Mag.*, vol. 51, no. 12, pp. 26–32, 2013.

[12] Y. Cui, F. Liu, X. Jing, and J. Mu, "Integrating sensing and communications for ubiquitous IoT: Applications, trends, and challenges," *IEEE Network*, vol. 35, no. 5, pp. 158–167, 2021.

[13] X. Luo, H.-H. Chen, and Q. Guo, "Semantic communications: Overview, open issues, and future research directions," *IEEE Wireless Commun.*, vol. 29, no. 1, pp. 210–219, 2022.

[14] G. Maral, J.-J. de Ridder, B. G. Evans, and M. Richharia, "Low earth orbit satellite systems for communications," *Int. J. Satell. Commun. Netw.*, vol. 9, no. 4, pp. 209–225, 1991.

[15] Q. Wu and R. Zhang, "Towards smart and reconfigurable environment: Intelligent reflecting surface aided wireless network," *IEEE Commun. Mag.*, vol. 58, no. 1, pp. 106–112, 2020.

[16] C. Liaskos, S. Nie, A. Tsioliaridou, A. Pitsillides, S. Ioannidis, and I. Akyildiz, "A new wireless communication paradigm through software-controlled metasurfaces," *IEEE Commun. Mag.*, vol. 56, no. 9, pp. 162–169, 2018.

[17] Q. Wu and R. Zhang, "Intelligent reflecting surface enhanced wireless network via joint active and passive beamforming," *IEEE Trans. Wireless Commun.*, vol. 18, no. 11, pp. 5394–5409, 2019.

[18] C. Pan, H. Ren, K. Wang, J. F. Kolb, M. Elkashlan, M. Chen, M. Di Renzo, Y. Hao, J. Wang, A. L. Swindlehurst, *et al.*, "Reconfigurable intelligent surfaces for 6G systems: Principles, applications, and research directions," *IEEE Commun. Mag.*, vol. 59, no. 6, pp. 14–20, 2021.

[19] C. Huang, A. Zappone, G. C. Alexandropoulos, M. Debbah, and C. Yuen, "Reconfigurable intelligent surfaces for energy efficiency in wireless communication," *IEEE Trans. Wireless Commun.*, vol. 18, no. 8, pp. 4157–4170, 2019.

[20] J. Zhang, Z. Zheng, Z. Fei, and Z. Han, "Energy-efficient multiuser localization in the RIS-assisted IoT networks," *IEEE Internet Things J.*, vol. 9, no. 20, pp. 20651–20665, 2022.

[21] E. Basar, M. Di Renzo, J. De Rosny, M. Debbah, M.-S. Alouini, and R. Zhang, "Wireless communications through reconfigurable intelligent surfaces," *IEEE Access*, vol. 7, pp. 116753–116773, 2019.

[22] M. A. ElMossallamy, H. Zhang, L. Song, K. G. Seddik, Z. Han, and G. Y. Li, "Reconfigurable intelligent surfaces for wireless communications: Principles, challenges, and opportunities," *IEEE Trans. Cogn. Commun. Netw.*, vol. 6, no. 3, pp. 990–1002, 2020.

[23] Y. Liu, X. Liu, X. Mu, T. Hou, J. Xu, M. Di Renzo, and N. Al-Dhahir, "Reconfigurable intelligent surfaces: Principles and opportunities," *IEEE Commun. Surv. Tutor.*, vol. 23, no. 3, pp. 1546–1577, 2021.

[24] Y. Niu, Y. Li, D. Jin, L. Su, and A. V. Vasilakos, "A survey of millimeter wave communications (mmwave) for 5G: opportunities and challenges," *Wireless networks*, vol. 21, pp. 2657–2676, 2015.

[25] S. Gong, X. Lu, D. T. Hoang, D. Niyato, L. Shu, D. I. Kim, and Y.-C. Liang, "Toward smart wireless communications via intelligent reflecting surfaces: A

contemporary survey," *IEEE Commun. Surv. Tutor.*, vol. 22, no. 4, pp. 2283–2314, 2020.

[26] D. Tse and P. Viswanath, *Fundamentals of wireless communication*. Cambridge university press, 2005.

[27] L. Lu, G. Y. Li, A. L. Swindlehurst, A. Ashikhmin, and R. Zhang, "An overview of massive MIMO: Benefits and challenges," *IEEE J. Sel. Top. Signal Process.*, vol. 8, no. 5, pp. 742–758, 2014.

[28] V. Stankovic, A. Host-Madsen, and Z. Xiong, "Cooperative diversity for wireless ad hoc networks," *IEEE Signal Process. Mag.*, vol. 23, no. 5, pp. 37–49, 2006.

[29] S. Dang, O. Amin, B. Shihada, and M.-S. Alouini, "What should 6G be?," *Nat. Electron.*, vol. 3, no. 1, pp. 20–29, 2020.

[30] M. Di Renzo, M. Debbah, D.-T. Phan-Huy, A. Zappone, M.-S. Alouini, C. Yuen, V. Sciancalepore, G. C. Alexandropoulos, J. Hoydis, H. Gacanin, *et al.*, "Smart radio environments empowered by reconfigurable AI meta-surfaces: An idea whose time has come," *EURASIP J. Wireless Commun. Net.*, vol. 2019, no. 1, pp. 1–20, 2019.

[31] X. Yu, D. Xu, Y. Sun, D. W. K. Ng, and R. Schober, "Robust and secure wireless communications via intelligent reflecting surfaces," *IEEE J. Sel. Areas Commun.*, vol. 38, no. 11, pp. 2637–2652, 2020.

[32] X. Zhou, R. Zhang, and C. K. Ho, "Wireless information and power transfer: Architecture design and rate-energy tradeoff," *IEEE Trans. Commun.*, vol. 61, no. 11, pp. 4754–4767, 2013.

[33] W. Tang, M. Z. Chen, X. Chen, J. Y. Dai, Y. Han, M. Di Renzo, Y. Zeng, S. Jin, Q. Cheng, and T. J. Cui, "Wireless communications with reconfigurable

intelligent surface: Path loss modeling and experimental measurement," *IEEE Trans. Wireless Commun.*, vol. 20, no. 1, pp. 421–439, 2020.

[34] N. Yu, P. Genevet, M. A. Kats, F. Aieta, J.-P. Tetienne, F. Capasso, and Z. Gaburro, "Light propagation with phase discontinuities: generalized laws of reflection and refraction," *Science*, vol. 334, no. 6054, pp. 333–337, 2011.

[35] W. Tang, X. Li, J. Y. Dai, S. Jin, Y. Zeng, Q. Cheng, and T. J. Cui, "Wireless communications with programmable metasurface: Transceiver design and experimental results," *China Commun.*, vol. 16, no. 5, pp. 46–61, 2019.

[36] X. Pei, H. Yin, L. Tan, L. Cao, Z. Li, K. Wang, K. Zhang, and E. Björnson, "RIS-aided wireless communications: Prototyping, adaptive beamforming, and indoor/outdoor field trials," *IEEE Trans. Commun.*, vol. 69, no. 12, pp. 8627–8640, 2021.

[37] S. Koziel and L. Leifsson, *Surrogate-based modeling and optimization*. Springer, 2013.

[38] S. Abeywickrama, R. Zhang, Q. Wu, and C. Yuen, "Intelligent reflecting surface: Practical phase shift model and beamforming optimization," *IEEE Trans. Commun.*, vol. 68, no. 9, pp. 5849–5863, 2020.

[39] X. Tan, Z. Sun, J. M. Jornet, and D. Pados, "Increasing indoor spectrum sharing capacity using smart reflect-array," in *Proc. IEEE Int. Conf. Commun. (ICC)*, pp. 1–6, Kuala Lumpur, Malaysia, 2016.

[40] T. J. Cui, M. Q. Qi, X. Wan, J. Zhao, and Q. Cheng, "Coding metamaterials, digital metamaterials and programmable metamaterials," *Light: science & applications*, vol. 3, no. 10, pp. e218–e218, 2014.

[41] E. Björnson and L. Sanguinetti, "Power scaling laws and near-field behaviors of massive MIMO and intelligent reflecting surfaces," *IEEE Open J. Commun. Soc.*, vol. 1, pp. 1306–1324, 2020.

[42] D. Mishra and H. Johansson, "Channel estimation and low-complexity beamforming design for passive intelligent surface assisted MISO wireless energy transfer," in *Proc. IEEE Int. Conf. Acoust. Speech Signal Process. (ICASSP)*, pp. 4659–4663, Brighton, UK, 2019.

[43] Y. Yang, B. Zheng, S. Zhang, and R. Zhang, "Intelligent reflecting surface meets OFDM: Protocol design and rate maximization," *IEEE Trans. Commun.*, vol. 68, no. 7, pp. 4522–4535, 2020.

[44] T. L. Jensen and E. De Carvalho, "An optimal channel estimation scheme for intelligent reflecting surfaces based on a minimum variance unbiased estimator," in *Proc. IEEE Int. Conf. Acoust. Speech Signal Process. (ICASSP)*, pp. 5000–5004, Virtual, 2020.

[45] B. Zheng and R. Zhang, "Intelligent reflecting surface-enhanced OFDM: Channel estimation and reflection optimization," *IEEE Wireless Commun. Lett.*, vol. 9, no. 4, pp. 518–522, 2020.

[46] M. Xu, S. Zhang, J. Ma, and O. A. Dobre, "Deep learning-based time-varying channel estimation for RIS assisted communication," *IEEE Commun. Lett.*, vol. 26, no. 1, pp. 94–98, 2021.

[47] N. K. Kundu and M. R. McKay, "Channel estimation for reconfigurable intelligent surface aided MISO communications: From LMMSE to deep learning solutions," *IEEE Open J. Commun. Soc.*, vol. 2, pp. 471–487, 2021.

[48] M. Haenggi, *Stochastic geometry for wireless networks.* Cambridge University Press, 2012.

[49] M. Haenggi, J. G. Andrews, F. Baccelli, O. Dousse, and M. Franceschetti, "Stochastic geometry and random graphs for the analysis and design of wireless networks," *IEEE J. Sel. Areas Commun.*, vol. 27, no. 7, pp. 1029–1046, 2009.

[50] F. Baccelli, B. Błaszczyszyn, *et al.*, "Stochastic geometry and wireless networks: Volume II applications," *Found. Trends Netw.*, vol. 4, no. 1–2, pp. 1–312, 2010.

[51] H. ElSawy, E. Hossain, and M. Haenggi, "Stochastic geometry for modeling, analysis, and design of multi-tier and cognitive cellular wireless networks: A survey," *IEEE Commun. Surv. Tutor.*, vol. 15, no. 3, pp. 996–1019, 2013.

[52] Y. Hmamouche, M. Benjillali, S. Saoudi, H. Yanikomeroglu, and M. Di Renzo, "New trends in stochastic geometry for wireless networks: A tutorial and survey," *Proceedings of the IEEE*, vol. 109, no. 7, pp. 1200–1252, 2021.

[53] X. Lu, M. Salehi, M. Haenggi, E. Hossain, and H. Jiang, "Stochastic geometry analysis of spatial-temporal performance in wireless networks: A tutorial," *IEEE Commun. Surv. Tutor.*, vol. 23, no. 4, pp. 2753–2801, 2021.

[54] M. Afshang and H. S. Dhillon, "Fundamentals of modeling finite wireless networks using binomial point process," *IEEE Trans. Wireless Commun.*, vol. 16, no. 5, pp. 3355–3370, 2017.

[55] V. V. Chetlur and H. S. Dhillon, "Downlink coverage analysis for a finite 3-D wireless network of unmanned aerial vehicles," *IEEE Trans. Commun.*, vol. 65, no. 10, pp. 4543–4558, 2017.

[56] D. Stoyan, W. S. Kendall, S. N. Chiu, and J. Mecke, *Stochastic geometry and its applications*. John Wiley & Sons, 2013.

[57] T. X. Brown, "Cellular performance bounds via shotgun cellular systems," *IEEE J. Sel. Areas Commun.*, vol. 18, no. 11, pp. 2443–2455, 2000.

[58] J. Lyu and R. Zhang, "Hybrid active/passive wireless network aided by intelligent reflecting surface: System modeling and performance analysis," *IEEE Trans. Wireless Commun.*, vol. 20, no. 11, pp. 7196–7212, 2021.

[59] N. Deng and M. Haenggi, "The benefits of hybrid caching in Gauss–Poisson D2D networks," *IEEE J. Sel. Areas Commun.*, vol. 36, no. 6, pp. 1217–1230, 2018.

[60] A. Guo, Y. Zhong, W. Zhang, and M. Haenggi, "The Gauss–Poisson process for wireless networks and the benefits of cooperation," *IEEE Trans. Commun.*, vol. 64, no. 5, pp. 1916–1929, 2016.

[61] D. Kudathanthirige, D. Gunasinghe, and G. Amarasuriya, "Performance analysis of intelligent reflective surfaces for wireless communication," in *Proc. IEEE Int. Conf. Commun. (ICC)*, pp. 1–6, Dublin, Ireland, Jun. 2020.

[62] Ö. Özdogan, E. Björnson, and E. G. Larsson, "Intelligent reflecting surfaces: Physics, propagation, and pathloss modeling," *IEEE Wireless Commun. Lett.*, vol. 9, no. 5, pp. 581–585, 2019.

[63] Y. Cai, M.-M. Zhao, K. Xu, and R. Zhang, "Intelligent reflecting surface aided full-duplex communication: Passive beamforming and deployment design," *IEEE Trans. Wireless Commun.*, vol. 21, no. 1, pp. 383–397, 2021.

[64] K. V. Mardia and P. E. Jupp, *Directional statistics*, vol. 494. John Wiley & Sons, 2009.

[65] R. B. Paris and D. Kaminski, *Asymptotics and mellin-barnes integrals*, vol. 85. Cambridge University Press, 2001.

[66] Z. Wang and G. B. Giannakis, "A simple and general parameterization quantifying performance in fading channels," *IEEE Trans. Commun.*, vol. 51, no. 8, pp. 1389–1398, 2003.

[67] S. Atapattu, R. Fan, P. Dharmawansa, G. Wang, J. Evans, and T. A. Tsiftsis, "Reconfigurable intelligent surface assisted two–way communications: Performance analysis and optimization," *IEEE Trans. Wireless Commun.*, vol. 68, no. 10, pp. 6552–6567, 2020.

[68] B. Grigelionis, *Student's t-distribution and related stochastic processes*. Springer, 2013.

[69] J. L. Snell, *Introduction to probability*. Random House New York, 1988.

[70] S. Kotz, T. Kozubowski, and K. Podgorski, *The Laplace distribution and generalizations: a revisit with applications to communications, economics, engineering, and finance*. Springer Science & Business Media, 2012.

[71] I. S. Gradshteyn and I. M. Ryzhik, *Table of integrals, series, and products*. Academic press, 2014.

[72] M. Abramowitz and I. A. Stegun, *Handbook of mathematical functions with formulas, graphs, and mathematical tables*, vol. 55. US Government printing office, 1964.

[73] L. Landau, "Bessel functions: monotonicity and bounds," *J. London Math. Soc.*, vol. 61, no. 1, pp. 197–215, 2000.

[74] M. Hwang, Y. Youn, S. Chang, D. Kim, C. Lee, D. An, and W. Hong, "Sensor-integrated RIS unit element featuring mutual coupling reduction," in *Proc. IEEE Int. Symp. Radio-Frequency Integr. Technol. (RFIT)*, pp. 159–160, IEEE, 2022.

[75] X. Qian and M. Di Renzo, "Mutual coupling and unit cell aware optimization for reconfigurable intelligent surfaces," *IEEE Wireless Commun. Lett.*, vol. 10, no. 6, pp. 1183–1187, 2021.

[76] E. Björnson and L. Sanguinetti, "Rayleigh fading modeling and channel hardening for reconfigurable intelligent surfaces," *IEEE Wireless Commun. Lett.*, vol. 10, no. 4, pp. 830–834, 2020.

[77] T. Van Chien, A. K. Papazafeiropoulos, L. T. Tu, R. Chopra, S. Chatzinotas, and B. Ottersten, "Outage probability analysis of IRS-assisted systems under spatially correlated channels," *IEEE Wireless Commun. Lett.*, vol. 10, no. 8, pp. 1815–1819, 2021.

[78] A. Goldsmith, *Wireless communications*. Cambridge university press, 2005.

[79] T. Aulin, "A modified model for the fading signal at a mobile radio channel," *IEEE Trans. Veh. Technol.*, vol. 28, no. 3, pp. 182–203, 1979.

[80] E. Björnson, J. Hoydis, and L. Sanguinetti, "Massive MIMO networks: Spectral, energy, and hardware efficiency," *Found. Trends Signal Process.*, vol. 11, no. 3-4, pp. 154–655, 2017.

[81] G. K. Karagiannidis, D. A. Zogas, and S. A. Kotsopoulos, "Performance analysis of triple selection diversity over exponentially correlated Nakagami-m fading channels," *IEEE Trans. Commun.*, vol. 51, no. 8, pp. 1245–1248, 2003.

[82] P. Sahu and A. K. Chaturvedi, "Performance analysis of predetection EGC in exponentially correlated Nakagami-m fading channel," *IEEE Trans. Commun.*, vol. 53, no. 8, pp. 1252–1256, 2005.

[83] G. K. Karagiannidis, D. A. Zogas, and S. A. Kotsopoulos, "On the multivariate Nakagami-m distribution with exponential correlation," *IEEE Trans. Commun.*, vol. 51, no. 8, pp. 1240–1244, 2003.

[84] W. C. Jakes and D. C. Cox, *Microwave mobile communications*. Wiley-IEEE press, 1994.

[85] M. Nakagami, "The m-distribution—a general formula of intensity distribution of rapid fading," in *Statistical methods in radio wave propagation*, pp. 3–36, Elsevier, 1960.

[86] L. Debnath, "The double laplace transforms and their properties with applications to functional, integral and partial differential equations," *Int. J. Appl. Comput. Math.*, vol. 2, no. 2, pp. 223–241, 2016.

[87] S. Boyd and L. Vandenberghe, *Convex Optimization*. Cambridge university press, 2004.

[88] S. Sanayei, A. Nosratinia, *et al.*, "Opportunistic beamforming with limited feedback," *IEEE Trans. Wireless Commun.*, vol. 6, no. 8, pp. 2765–2771, 2007.

[89] B. Natarajan, C. R. Nassar, and V. Chandrasekhar, "Generation of correlated Rayleigh fading envelopes for spread spectrum applications," *IEEE Commun. Lett.*, vol. 4, no. 1, pp. 9–11, 2000.

[90] Q. Zhang, "A decomposition technique for efficient generation of correlated Nakagami fading channels," *IEEE J. Sel. Areas Commun.*, vol. 18, no. 11, pp. 2385–2392, 2000.

[91] J. Tang, J. Luo, M. Liu, D. K. So, E. Alsusa, G. Chen, K.-K. Wong, and J. A. Chambers, "Energy efficiency optimization for NOMA with SWIPT," *IEEE J. Sel. Areas Commun.*, vol. 13, no. 3, pp. 452–466, 2019.

[92] M. Alkhawatrah, Y. Gong, G. Chen, S. Lambotharan, and J. A. Chambers, "Buffer-aided relay selection for cooperative NOMA in the internet of things," *IEEE Internet Things J.*, vol. 6, no. 3, pp. 5722–5731, 2019.

[93] L. Dai, B. Wang, Y. Yuan, S. Han, I. Chih-Lin, and Z. Wang, "Non-orthogonal multiple access for 5G: solutions, challenges, opportunities, and future research trends," *IEEE Commun. Mag.*, vol. 53, no. 9, pp. 74–81, 2015.

[94] J. Zhu, Y. Huang, J. Wang, K. Navaie, and Z. Ding, "Power efficient IRS-assisted NOMA," *IEEE Trans. Commun.*, vol. 69, no. 2, pp. 900–913, 2020.

[95] W. Wang, X. Liu, J. Tang, N. Zhao, Y. Chen, Z. Ding, and X. Wang, "Beamforming and jamming optimization for IRS-aided secure NOMA networks," *IEEE Trans. Wireless Commun.*, Early Access, 2021.

[96] M. Badiu and J. P. Coon, "Communication through a large reflecting surface with phase errors," *IEEE Wireless Commun. Lett.*, vol. 9, no. 2, pp. 184–188, 2020.

[97] C. Huang, G. Chen, Y. Gong, P. Xu, Z. Han, and J. A. Chambers, "Buffer-aided relay selection for cooperative hybrid NOMA/OMA networks with asynchronous deep reinforcement learning," *IEEE J. Sel. Areas Commun.*, Early Access, 2021.

[98] Z. Chen, Z. Ding, X. Dai, and G. K. Karagiannidis, "On the application of quasi-degradation to MISO-NOMA downlink," *IEEE Trans. Signal Process.*, vol. 64, no. 23, pp. 6174–6189, 2016.

[99] Z. Ding and H. V. Poor, "A simple design of IRS-NOMA transmission," *IEEE Commun. Lett.*, vol. 24, no. 5, pp. 1119–1123, 2020.

[100] T. Hou, Y. Liu, Z. Song, X. Sun, Y. Chen, and L. Hanzo, "Reconfigurable intelligent surface aided NOMA networks," *IEEE J. Sel. Areas Commun.*, vol. 38, no. 11, pp. 2575–2588, 2020.

[101] Z. Ding, R. Schober, and H. V. Poor, "On the impact of phase shifting designs on IRS-NOMA," *IEEE Wireless Commun. Lett.*, vol. 9, no. 10, pp. 1596–1600, 2020.

[102] B. Zheng, Q. Wu, and R. Zhang, "Intelligent reflecting surface-assisted multiple access with user pairing: NOMA or OMA?," *IEEE Commun. Lett.*, vol. 24, no. 4, pp. 753–757, 2020.

[103] Y. Zhang, C. Zhong, Z. Zhang, and W. Lu, "Sum rate optimization for two way communications with intelligent reflecting surface," *IEEE Commun. Lett.*, vol. 24, no. 5, pp. 1090–1094, 2020.

[104] P. K. Sharma and P. Garg, "Intelligent reflecting surfaces to achieve the full-duplex wireless communication," *IEEE Commun. Lett.*, vol. 25, no. 2, pp. 622–626, 2020.

[105] X. Hu, C. Zhong, Y. Zhang, X. Chen, and Z. Zhang, "Location information aided multiple intelligent reflecting surface systems," *IEEE Trans. Commun.*, vol. 68, no. 12, pp. 7948–7962, 2020.

[106] F. Fang, Y. Xu, Q.-V. Pham, and Z. Ding, "Energy-efficient design of IRS-NOMA networks," *IEEE Trans. Veh. Technol.*, vol. 69, no. 11, pp. 14088–14092, 2020.

[107] B. Tahir, S. Schwarz, and M. Rupp, "Analysis of uplink IRS-assisted NOMA under Nakagami-m fading via moments matching," *IEEE Wireless Commun. Lett.*, vol. 10, no. 3, pp. 624–628, 2020.

[108] S. Dhok and P. K. Sharma, "Infinite and finite block-length FD transmissions with spatially-correlated RIS channels," *IEEE Trans. Wireless Commun.*, 2022, Early Access.

[109] Q. Wu, S. Zhang, B. Zheng, C. You, and R. Zhang, "Intelligent reflecting surface-aided wireless communications: A tutorial," *IEEE Trans. Commun.*, vol. 69, no. 5, pp. 3313–3351, 2021.

[110] C. Zhang, W. Yi, Y. Liu, K. Yang, and Z. Ding, "Reconfigurable intelligent surfaces aided multi-cell NOMA networks: A stochastic geometry model," *IEEE Trans. Commun.*, vol. 70, no. 2, pp. 951–966, 2022.

[111] S. Atapattu, P. Dharmawansa, M. Di Renzo, C. Tellambura, and J. S. Evans, "Multi-user relay selection for full-duplex radio," *IEEE Trans. Commun.*, vol. 67, no. 2, pp. 955–972, 2018.

[112] A. Sabharwal, P. Schniter, D. Guo, D. W. Bliss, S. Rangarajan, and R. Wichman, "In-band full-duplex wireless: Challenges and opportunities," *IEEE J. Sel. Areas Commun.*, vol. 32, no. 9, pp. 1637–1652, 2014.

[113] L. J. Rodriguez, N. H. Tran, and T. Le-Ngoc, "Performance of full-duplex AF relaying in the presence of residual self-interference," *IEEE J. Sel. Areas Commun.*, vol. 32, no. 9, pp. 1752–1764, 2014.

[114] G. Chen, J. P. Coon, and M. Di Renzo, "Secrecy outage analysis for downlink transmissions in the presence of randomly located eavesdroppers," *IEEE Trans. Inf. Forensics Security*, vol. 12, no. 5, pp. 1195–1206, 2017.

[115] M. Nemati, J. Park, and J. Choi, "RIS-assisted coverage enhancement in millimeter-wave cellular networks," *IEEE Access*, vol. 8, pp. 188171–188185, 2020.

[116] M. A. Kishk and M.-S. Alouini, "Exploiting randomly located blockages for large-scale deployment of intelligent surfaces," *IEEE J. Sel. Areas Commun.*, vol. 39, no. 4, pp. 1043–1056, 2020.

[117] Y. Zhu, G. Zheng, and K.-K. Wong, "Stochastic geometry analysis of large intelligent surface-assisted millimeter wave networks," *IEEE J. Sel. Areas Commun.*, vol. 38, no. 8, pp. 1749–1762, 2020.

[118] T. Shafique, H. Tabassum, and E. Hossain, "Stochastic geometry analysis of IRS-assisted downlink cellular networks," *IEEE Trans. Commun.*, vol. 70, no. 2, pp. 1442–1456, 2022.

[119] T. Wang, M.-A. Badiu, G. Chen, and J. P. Coon, "Outage probability analysis of RIS-assisted wireless networks with Von Mises phase errors," *IEEE Wireless Commun. Lett.*, vol. 10, no. 12, pp. 2737–2741, 2021.

[120] T. Wang, M.-A. Badiu, G. Chen, and J. P. Coon, "Performance analysis of IOS-assisted NOMA system with channel correlation and phase errors," *IEEE Trans. Veh. Technol.*, vol. 71, no. 11, pp. 11861–11875, 2022.

[121] Z. Xie, W. Yi, X. Wu, Y. Liu, and A. Nallanathan, "STAR-RIS aided NOMA in multi-cell networks: A general analytical framework with gamma distributed channel modeling," *IEEE Trans. Commun.*, 2022, Early Access.

[122] T. Hou, Y. Liu, Z. Song, X. Sun, Y. Chen, and L. Hanzo, "MIMO assisted networks relying on intelligent reflective surfaces: A stochastic geometry based analysis," *IEEE Trans. Veh. Technol.*, vol. 71, no. 1, pp. 571–582, 2021.

[123] Z. Xie, W. Yi, X. Wu, Y. Liu, and A. Nallanathan, "Modeling and coverage analysis for RIS-aided NOMA transmissions in heterogeneous networks," 2020. [Online]. Available: https://arxiv.org/abs/2104.13182.